UNIVERSITY OF CALIFORNIA
RIVERSIDE

The Properties of Gas Flows and Their Connection to $z \sim 2$ Star-Forming Galaxies

A Dissertation submitted in partial satisfaction
of the requirements for the degree of

Doctor of Philosophy

in

Physics

by

Andrew J. Weldon

June 2024

Dissertation Committee:

Dr. Naveen A. Reddy, Chairperson
Dr. Brian Siana
Dr. Bahram Mobasher

The Dissertation of Andrew J. Weldon is approved:

Committee Chairperson

University of California, Riverside

Acknowledgments

First and foremost, I want to thank my research advisor, Prof. Naveen Reddy. Your constant support, thought-provoking questions, and guidance have been invaluable during my PhD journey. In addition, completing this work would not have been possible without the support of my many collaborators – both within and outside the MOSDEF collaboration – for their contributions and valuable feedback. I particularly thank Prof. Alice Shapely and Dr. Michael Topping for their work in obtaining and reducing the LRIS observations, which provided the basis for this work. I am also grateful to the astronomy faculty and my fellow astronomy graduate students for creating a supportive culture and sense of community in the department at UCR. Lastly, but most importantly, I would like to thank my family, especially my parents and sister. Your support and encouragement over the years gave me the confidence to follow my passion in life.

The observations for this work utilized the MOSFIRE multi-object spectrograph and the Low-Resolution Imaging Spectrometer on the Keck I telescope, and the Keck Cosmic Web Imager on the Keck II telescope at the W. M. Keck Observatory. The W. M. Keck Observatory is a private 501(c)3 non-profit organization operated as a scientific partnership among the California Institute of Technology, the University of California, and the National Aeronautics and Space Administration. The Observatory was made possible by the generous financial support of the W. M. Keck Foundation. I also wish to recognize and acknowledge the very significant cultural role and reverence that the summit of Maunakea has always had within the indigenous Hawaiian community. We are most fortunate to have the opportunity to conduct observations from this mountain. In addition, some of the data presented herein

is based on observations taken by the CANDELS Multi-Cycle Treasury Program and the 3D-HST Treasury Program (GO 12177 and 12328) with the NASA/ESA Hubble Space Telescope (HST), operated by the Association of Universities for Research in Astronomy, Inc., under NASA contract NAS5-26555.

The MOSDEF team acknowledges support from an NSF AAG collaborative grant (AST-1312780, 1312547, 1312764, and 1313171), grant AR-13907 from the Space Telescope Science Institute, and grant NNX16AF54G from the NASA ADAP program.

I acknowledge the following open-source Python packages in the analyses of this work: Astropy (Astropy Collaboration et al., 2013, 2018, 2022), Matplotlib (Hunter, 2007), NumPy (Harris et al., 2020), SciPy (Virtanen et al., 2020), emcee, (Foreman-Mackey et al., 2013), specline (Shivaei et al., 2018), and the radiative transfer model code zELDA (Gurung-López et al., 2022).

This dissertation contains drafts of papers published (Chapters 2 and 3) or submitted for publication (Chapters 4 and 5) by the Oxford University Press in the Monthly Notices of the Royal Astronomical Society and the American Astronomical Society in the Astrophysical Journal.

To my parents for all the support.

ABSTRACT OF THE DISSERTATION

The Properties of Gas Flows and Their Connection to $z \sim 2$ Star-Forming Galaxies

by

Andrew J. Weldon

Doctor of Philosophy, Graduate Program in Physics
University of California, Riverside, June 2024
Dr. Naveen A. Reddy, Chairperson

The cycling of gas into and out of galaxies is a crucial ingredient in their evolution. The incidence rate and effects of these gas flows are expected to be common and pronounced at redshifts of $z \sim 2$, the peak of star formation and quasar activity in the history of the Universe. In this work, I characterize cool low-ionized ($\sim 10^3$ K) and warm ionized ($\sim 10^4$ K) gas outflows and inflows from individual and stacks of star-forming galaxies during this epoch. I utilize rest-optical spectroscopic data from the MOSFIRE Deep Evolution Field survey and rest-UV follow-up campaigns with Keck LRIS and KCWI. Using Lyα emission, low-ionization interstellar metal absorption lines, and broad components of strong rest-optical emission lines, I measure the properties of outflows and inflows, how their properties scale with the global properties of galaxies, and the driving mechanisms behind outflows. My results indicate that mechanical energy from supernova explosions primarily drives cool gas outflows, while a combination of mechanical energy and radiation pressure acting on dusty material drives warm gas outflows. In addition, I find that warm outflows have modest mass-loss rates and are likely negligible, even during the peak of cosmic star-formation history.

By comparing galaxies with robust measurements of cool low-ionized gas inflows to those without inflows, I explore the low detection rate of inflowing gas. My results reveal that galaxies with inflows have higher star-formation activity and that the covering fraction of inflowing gas is enhanced among galaxies with higher specific star-formation rates. Lastly, I utilize integral field spectroscopy to measure the spectral variation of Lyα emission across stacked Lyα halos of $z \sim 2$ star-forming galaxies. Redshifted single-peaked Lyα profiles are ubiquitous down-the-barrel of galaxies, while farther out, the shape of the profile varies with outflow velocity and star-formation activity. Overall, my dissertation work provides a glimpse into the complex multi-phase nature of gas cycling around star-forming galaxies at $z \sim 2$ when feedback from star-formation activity was at its highest.

Contents

List of Figures

List of Tables

Chapter 1

Introduction

In simple terms, galaxies are gravitationally bound systems consisting of many stars and gas, which represent the basic unit of observable structure in the Universe. At the same time, galaxies are incredibly diverse, displaying an astonishing range of shapes, sizes, colors, brightness, masses, and surroundings. One of the greatest open questions in modern extragalactic astrophysics is how various interconnected processes operating on scales that vary over orders of magnitude result in the diverse galaxy population we see today. Over the past two decades, a general framework of galaxy evolution has emerged: accreted pristine cold gas from large-scale filaments in the intergalactic medium (IGM) fuels star formation in galaxies, which, in turn, results in feedback that ejects metal-enriched gas and imparts energy and momentum back into the surrounding gas. Understanding this competition between inflowing gas and feedback is crucial in developing a complete picture of galaxy evolution.

1.1 The Impact of Gas Flows

Galaxies are not isolated systems, sitting out in Universe, passively evolving along a well-established path. Instead, and far more interestingly, galaxies are open systems that exchange gas, energy, momentum, and metals between their interstellar medium (ISM), their surrounding circumgalactic medium (CGM), and farther out into the vast intergalactic medium between galaxies. Understanding this cycling of gas is crucial for developing a complete description of galaxy evolution.

Large-scale outflows of material from galaxies, of course, are the negative part of this cycle. Driven by energy and momentum injected into the ISM (i.e., feedback) from stars and active galactic nuclei (AGN), these outflows have many effects on their host galaxy. Outflows suppress star formation in galaxies directly by removing the necessary cold gas and indirectly through heating gas in the ISM and CGM (e.g., Scannapieco et al., 2005; Croton et al., 2006). As they move through their host, outflows can carve low-column-density channels in the ISM, which may be an important factor in the escape of ionizing photons from galaxies (e.g., Gnedin et al., 2008; Leitet et al., 2013; Ma et al., 2016; Reddy et al., 2016; Gazagnes et al., 2018; Reddy et al., 2022). If the velocity of an outflow is below the escape velocity of their host, the outflow will be retained and eventually recycle back onto the galaxy as part of a galactic fountain. This recycling gas may fuel a significant fraction of star-formation in galaxies at late-times (Oppenheimer et al., 2010; Henriques et al., 2013; Anglés-Alcázar et al., 2017). Outflows that escape their host are expected to be metal-enriched relative to the ISM, thus they modulate the metallicity of galaxies, and pollute the CGM and IGM with metals (e.g., Tremonti et al., 2004; Dalcanton, 2007).

As the counterpart to outflows, inflows of gas into galaxies are perhaps more fundamental, as gas accretion is required, but the launching of large-scale outflows is optional. The accretion and conversion of cold into stars is a key process for the growth of galaxies. The gas reservoir around galaxies, however, can only sustain their star-formation rates for a few gigayears (Leroy et al., 2008; Saintonge et al., 2017; Tacconi et al., 2018), thus galaxies must continuously accrete pristine gas from the IGM to replenish these reservoirs throughout their evolution (Kennicutt, 1983; Prochaska & Wolfe, 2009; Bauermeister et al., 2010). In addition, the accretion of metal-poor gas may also resolve the discrepancy between the number of low metallicity stars observed in the Milky Way and predictions from "closed-box" chemical evolution models, known as the G-Dwarf problem (van den Bergh, 1962; Schmidt, 1963; Sommer-Larsen, 1991).

1.2 Gas Flows at $z \sim 2$

An important epoch in the history of the Universe occurred about 2 – 3 Gyr after the Big Bang (redshifts $z \sim 2$ – 3). Over this relatively short period, the cosmic star-formation rate (SFR) density peaked, with galaxies experiencing intense episodes of star formation and assembling most of their stellar mass (see Madau & Dickinson, 2014). Many of the structural patterns observed among galaxies today were established during this epoch, and feedback from star-formation and AGN was maximized.

The intense star formation of this era is well suited for studying the cycling of gas into and out of galaxies. Inflows of gas should be common, providing the fuel for galaxies to maintain their observed SFRs. At the same time, the increase in star-formation and

AGN feedback should naturally give rise to large-scale galactic outflows. In addition, at these redshifts, there is access to a wealth of multi-wavelength observations. In particular, the far-UV is shifted to wavelengths where the sky background is extremely low, and the rest-optical is shifted into near-infrared atmospheric transmission windows. These two wavelength regimes contain multiple absorption and emission lines that trace gas flows and probe the physical conditions in galaxies.

Indeed, tremendous progress has been made in characterizing gas flows around star-forming galaxies at $z \sim 2$ (see reviews by Heckman & Thompson, 2017; Rupke, 2018; Veilleux et al., 2020). At these redshifts, information on gas flows come from kinematic offsets in interstellar absorption, Lyα emission, and stellar photospheric/nebular emission lines towards galaxies ("down-the-barrel"; e.g., Steidel et al., 2010; Newman et al., 2012) and absorption lines along sightlines through foreground galaxy halos towards bright background quasars or galaxies ("transverse absorption-line"; e.g., Steidel et al., 2010; Rudie et al., 2012). Down-the-barrel and transverse spectroscopic surveys have revealed that outflows are a common feature of star-forming galaxies, with moderate velocities (on average a few hundred of km/s) that correlate with stellar mass, star-formation rate (SFR), and star-formation-rate surface density ($\Sigma_{\rm SFR}$), extending up to $\sim$50–100 kpc. On the other hand, direct observational detections of inflowing gas are sparse, with implied covering fractions of $\sim$5% (Rubin et al., 2012; Martin et al., 2012).

1.3 Dissertation Outline

The work presented in the chapters that follow address the following questions regarding gas flows of $z \sim 2$ star-forming galaxies.

1. What are the properties of their outflows?

2. What is the primary driving mechanism of their outflows?

3. What is the frequency of inflows?

4. What are the kinematics and distribution of neutral gas within their circumgalatic mediums?

These questions are difficult to address observationally. The range of scales that flows operate over is enormous: from ∼Mpc scales of the environment surrounding galaxies, down through the size of galaxies, and to the sub-parsec scales where star-formation takes place. Multi-wavelength observations show that outflows possess a complex, multi-phase structure spanning from very hot ($\sim 10^{6-7}$ K; e.g., Strickland & Stevens, 2000; Strickland & Heckman, 2009), to warm ($\sim 10^4$ K; e.g., Heckman et al., 2015; Du et al., 2016) and cool ($\sim 10^3$ K; e.g., Weiner et al., 2009; Kornei et al., 2012) ionized gas and down to cold (100 K; e.g., Leroy et al., 2015; Meléndez et al., 2015) molecular gas and dust. Furthermore, observations of high-redshift galaxies are also subject to the effects of cosmological dimming (see Barden et al., 2008), limiting previous studies to small samples of gravitationally lensed galaxies, very luminous galaxies, or creating high signal-to-noise composite spectra to infer average properties (e.g., Pettini et al., 2002; Shapley et al., 2003; Rubin et al., 2010; Jones

et al., 2012; Bordoloi et al., 2016). While the multi-scale and multi-phase nature of flows cannot be avoided, deep spectroscopy can reveal gas flows of typical, individual galaxies.

In this dissertation, gas flows of $z \sim 2$ star-forming galaxies are examined on (1) an individual galaxy basis using down-the-barrel rest-optical and rest-UV spectroscopy from the MOSFIRE Deep Evolution Field (MOSDEF; Kriek et al., 2015) survey and the Keck Low Resolution Imagining Spectrograph (LRIS; Oke et al., 1995); and (2) stacked galaxies using rest-UV spectroscopy from the Keck Cosmic Web Imager (KCWI; Morrissey et al., 2018) integral field spectrograph. The MOSDEF survey is a large spectroscopic program targeting objects at $1.4 \leq z \leq 3.8$ in well-studied extragalactic legacy survey fields to study their stellar, gaseous, metal, dust, and black hole content. The survey obtained moderate-resolution ($R \sim 3000 - 3600$) rest-optical spectroscopy of ∼1500 typical star forming galaxies using the MOSFIRE multi-object spectrograph (McLean et al., 2010, 2012a) on the Keck I telescope. Galaxies with detections of several strong rest-optical emission lines (e.g., Hβ, [O III], Hα, [N II]) were followed-up with LRIS and KCWI to obtain deep rest-UV spectra.

The outline of this dissertation is as follows. In Chapter 2, we investigate the primary driving mechanisms of cool, neutral/low-ionization outflows traced by rest-UV interstellar absorption lines. The frequency of inflowing gas is explored in Chapter 3 using three galaxies with significantly redshifted low-ionization absorption lines. In Chapter 4, we study the properties and driving mechanism of warm, ionized outflows traced by broad rest-optical emission line components. In Chapter 5, spectral variations in the Lyα line profile across Lyα halos are explored to quantify the distribution and kinematics of neutral CGM gas. The main conclusions of the dissertation and future work are presented in Chapter 6.

Chapter 2

The MOSDEF-LRIS Survey: Connection between Galactic-scale Outflows and the Properties of $z \sim 2$ Star-forming Galaxies[1]

Abstract We investigate the conditions that facilitate galactic-scale outflows using a sample of 155 typical star-forming galaxies at $z \sim 2$ drawn from the MOSFIRE Deep Evolution Field (MOSDEF) survey. The sample includes deep rest-frame UV spectroscopy from the Keck Low-Resolution Imaging Spectrometer (LRIS), which provides spectral coverage of several low-ionization interstellar (LIS) metal absorption lines and Lyα emission. Outflow velocities are calculated from the centroids of the LIS absorption and/or Lyα emission, as

[1] A version of this chapter was published in Weldon et al. (2022)

well as the highest-velocity component of the outflow from the blue wings of the LIS absorption lines. Outflow velocities are found to be marginally correlated or independent of galaxy properties, such as star-formation rate (SFR) and star-formation rate surface density ($\Sigma_{\rm SFR}$). Outflow velocity scales with SFR as a power-law with index 0.24, which suggests that the outflows may be primarily driven by mechanical energy generated by supernovae explosions, as opposed to radiation pressure acting on dusty material. On the other hand, outflow velocity and $\Sigma_{\rm SFR}$ are not significantly correlated, which may be due to the limited dynamic range of $\Sigma_{\rm SFR}$ probed by our sample. The relationship between outflow velocity and $\Sigma_{\rm SFR}$ normalized by stellar mass ($\Sigma_{\rm sSFR}$), as a proxy for gravitational potential, suggests that strong outflows (e.g., > 200 km s^{-1}) become common above a threshold of $\log(\Sigma_{\rm sSFR}/{\rm yr}^{-1}\ {\rm kpc}^{-2}) \sim -11.3$, and that above this threshold, outflow velocity uncouples from $\Sigma_{\rm sSFR}$. These results highlight the need for higher resolution spectroscopic data and spatially resolved imaging to test the driving mechanisms of outflows predicted by theory.

2.1 Introduction

The evolution of galaxies is influenced by the flow of baryons. Galaxies accrete cold gas from filaments in the cosmic web, convert the gas into stars, and eject metal-enriched gas from the interstellar medium (ISM) into the circumgalactic medium (CGM) or possibly beyond into the intergalactic medium (IGM). One important component of this cycle is galactic-scale outflows, which enriches the CGM and IGM with metals, modulates the metallicity within galaxies (e.g., Tremonti et al., 2004; Dalcanton, 2007; Finlator & Davé, 2008), and depletes the availability of cold gas causing a suppression of star formation (e.g.,

Scannapieco et al., 2005; Croton et al., 2006). Outflows also appear to be an important factor in the creation of low-column-density channels in the ISM, allowing for the escape of ionizing photons (e.g., Gnedin et al., 2008; Leitet et al., 2013; Ma et al., 2016; Reddy et al., 2016; Gazagnes et al., 2018; Reddy et al., 2022).

Galactic outflows are a common feature of actively star-forming galaxies, with observations of such flows in local galaxies (e.g., Heckman et al., 2000; Chen et al., 2010; Roberts-Borsani et al., 2020) and high-redshift galaxies (e.g., Shapley et al., 2003; Steidel et al., 2010; Davies et al., 2019). However, the physical mechanisms that generate and sustain outflows remain an open question. In star-forming galaxies, outflows are theorized to be driven by energy injected into the ISM by supernovae; radiation pressure acting on cool, dusty material; or a combination of these mechanisms (Chevalier & Clegg, 1985; Murray et al., 2005, 2011). Outflow velocity should then scale with star formation properties as the level of star formation activity, which peaks at $z \sim 1-3$ (Madau & Dickinson, 2014), sets the effectiveness of these mechanisms.

Galactic outflows are often probed by either blueshifted interstellar absorption or redshifted resonantly-scattered emission of cool, diffuse interstellar and circumgalactic gas. Observations of blueshifted interstellar absorption lines for both local and high-redshift galaxies have found that outflow velocity ($v_{\rm out}$) increases with several galactic properties such as stellar mass, star-formation rate (SFR), and star-formation-rate surface density ($\Sigma_{\rm SFR}$) (e.g., Sato et al., 2009; Weiner et al., 2009; Chen et al., 2010; Rubin et al., 2010; Steidel et al., 2010; Law et al., 2012; Martin et al., 2012; Rubin et al., 2014; Chisholm et al., 2015; Heckman et al., 2015; Bordoloi et al., 2016; Förster Schreiber & Wuyts, 2020; Prusinski

et al., 2021). However, the existence of a $v_{\rm out}-$SFR or $v_{\rm out}-\Sigma_{\rm SFR}$ relation is still debated. There is general agreement at low redshifts ($z \lesssim 0.3$) that the relations are significant, weak power laws ($v_{\rm out} \propto {\rm SFR}^{0.15-0.35}$; Martin, 2005; Chisholm et al., 2015; Sugahara et al., 2017, $v_{\rm out} \propto {\Sigma_{\rm SFR}}^{0.1}$; Chen et al. 2010). At higher redshifts ($1 \lesssim z \lesssim 2$) there is disagreement on the significance of the $v_{\rm out}-\Sigma_{\rm SFR}$ relation (Steidel et al., 2010; Kornei et al., 2012; Law et al., 2012; Rubin et al., 2014; Prusinski et al., 2021). This tension may be due to the use of ions (e.g., C IV, Si IV, Si II, and Mg II) that trace different components of the outflowing gas, different methods to parameterize outflow kinematics, and differences in the methodology used to estimate $\Sigma_{\rm SFR}$ (see discussions in Ho et al., 2016; Heckman & Thompson, 2017).

Rest-UV spectra of $z \sim 2$ star forming galaxies contain a wealth of emission and low-ionization interstellar (LIS) absorption metal lines (e.g., Si II, O I, C II, and Fe II) of cool, diffuse interstellar gas transported by galactic-scale outflows. Due to the difficulty of obtaining rest-UV spectra with sufficient S/N for typically faint high-redshift galaxies, previous studies have been primarily limited to gravitationally-lensed Lyman Break galaxies (LBGs), very luminous LBGs, or high S/N composite spectra to infer average outflow properties (Pettini et al., 2002; Shapley et al., 2003; Rubin et al., 2010; Jones et al., 2012; Bordoloi et al., 2016; Du et al., 2018). Here, we use a sample of 155 galaxies drawn from the MOSFIRE Deep Evolution Field (MOSDEF; Kriek et al., 2015) Survey with additional deep ($\sim$7.5 hrs) rest-UV observations from the Keck Low Resolution Imaging Spectrometer (LRIS; Oke et al., 1995; Steidel et al., 2003). The combination of rest-optical spectra from the MOSFIRE near-IR spectrograph and rest-UV spectra from LRIS creates an ideal dataset for investigating the relationship between outflows and the physical properties of the host

galaxy at high redshift on an individual galaxy basis. The primary objectives of this study are to (1) explore which, if any, galactic properties correlate with outflow properties; and (2) determine the primary driving mechanisms of outflows in $z \sim 2 - 3$ galaxies.

The outline of this paper is as follows. In Section 2.2, we introduce the sample and stellar population models used in this work. Section 2.3 describes the approach for estimating SFR, $\Sigma_{\rm SFR}$, outflow velocity, and other galaxy properties. In Section 2.4, we present our main results on the correlations between outflow velocities and measured galaxy properties. We discuss the physical context behind these results in Section 2.5 and summarize our conclusions in Section 2.6. Throughout this paper, we adopt a standard cosmology with $\Omega_\Lambda = 0.7$, $\Omega_{\rm M} = 0.3$, and $\rm H_0 = 70$ km s^{-1}Mpc^{-1}. All wavelengths are presented in the vacuum frame.

2.2 Data

2.2.1 MOSDEF Spectroscopy

Our analysis utilizes rest-optical spectra from the MOSDEF Survey which targeted ≈1500 H-band selected galaxies in the CANDELS fields (Grogin et al., 2011; Koekemoer et al., 2011). The survey used the MOSFIRE spectrograph (McLean et al., 2012a) on the 10m Keck I telescope over 48.5 nights from 2012 – 2016 to obtain moderate-resolution ($R \sim 3000$–3600) near-infrared spectra. Galaxies were targeted for spectroscopy based on pre-existing spectroscopic, grism, or photometric redshifts that placed them into one of three redshift ranges ($z = 1.37 - 1.70$, $z = 2.09 - 2.61$, and $z = 2.95 - 3.80$) where strong

rest-frame optical emission lines lie in the $YJHK$ transmission windows. For full details regarding the survey (targeting, data reduction, and sample properties), we refer readers to Kriek et al. (2015).

Emission line fluxes were measured from the MOSFIRE spectra by simultaneously fitting a line with a Gaussian function and a linear continuum component. Two Gaussian functions were used to fit the [O II] doublet, while three were used to fit Hα and the [N II] doublet. Systemic redshifts were derived from the strongest emission line, usually Hα or [O III]λ5008, and were used to fit the other rest-frame optical nebular emission lines. Line fluxes and errors were derived by perturbing the spectra by its error spectrum to generate 1000 realizations, remeasuring the line fluxes from these realizations, and calculating the average line fluxes and their dispersion from the realizations. Further details on emission line measurements and slit loss corrections are given in Kriek et al. (2015) and Reddy et al. (2015).

Galaxy sizes and inclinations were estimated from the effective radius ($R_{\rm E}$), within which half the total light of the galaxy is contained, and the axis ratio (b/a), respectively, measured by van der Wel et al. (2014)[2] using GALFIT (Peng et al., 2010) on HST/F160W images from the CANDELS survey.

2.2.2 MOSDEF-LRIS Spectroscopy

In this study, we use a sample of 155 galaxies drawn from the MOSDEF survey with follow-up rest-UV frame LRIS observations. Here, we briefly summarize the sample and

[2] https://users.ugent.be/~avdrwel/research.html

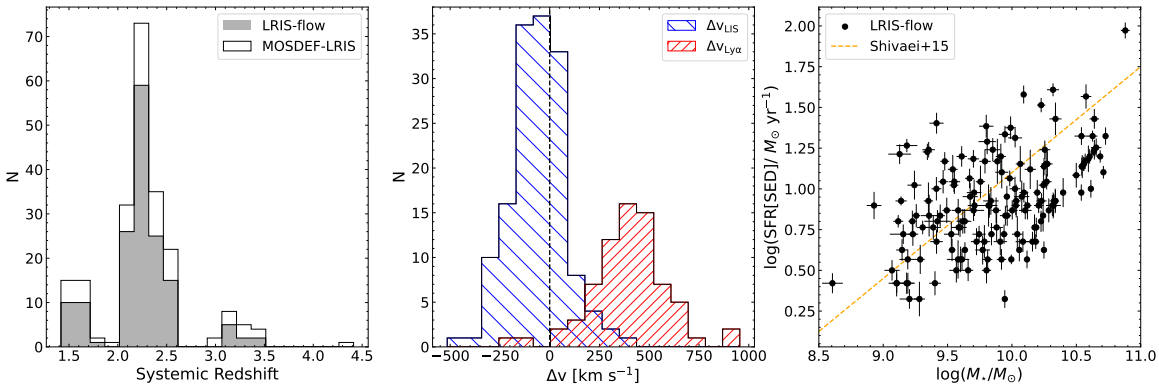

Figure 2.1: Properties of the LRIS-flow sample. *Left*: Redshift distribution. Open black and solid gray histograms represent the MOSDEF-LRIS sample with systemic redshift measurements (215 objects) and the LRIS-flow sample with additional LIS or Lyα redshifts (155 objects), respectively. *Center*: Velocity distribution. Blue and red hashed histograms denote the distribution of centroid velocities of the LIS absorption lines (149 objects) and Lyα emission (72 objects), respectively. *Right*: SFR versus stellar mass. SFRs and stellar masses are derived from SED modeling (Section 2.2.4). For comparison, the SFR–stellar mass relation derived in Shivaei et al. (2015) the parent MOSDEF sample is shown as an orange dash line. The SFRs in the study are derived from dust-corrected Hα fluxes.

refer readers to Topping et al. (2020) for more details. From the MOSDEF Survey, objects were prioritized for LRIS spectroscopy based on detections of rest-optical emission lines (Hβ, [OIII], Hα, and [NII]). Higher priority was given to objects with confirmed spectroscopic redshifts at $1.90 \leq z \leq 2.65$. Additional objects were selected in the following order of priority: objects with Hα, Hβ, and [OIII] detected at $\geq 3\sigma$ and an upper limit on [NII]; objects with a confirmed systemic redshift from MOSDEF; objects observed as part of the MOSDEF survey without a successful systemic redshift measurement, but with a prior spectroscopic or photometric redshift; and finally, objects not observed with MOSFIRE, but with a prior redshift from the 3D-HST survey that placed them within the redshift ranges and magnitude limit of the MOSDEF survey. In total, 260 galaxies were selected for follow-up observations with LRIS.[3]

[3]Systemic redshift measured by MOSDEF were obtained for 214 galaxies, while the remaining 45 galaxies either have a spectroscopic redshift prior to the MOSDEF survey or a photometric redshift.

LRIS observations were obtained over nine nights in 2017 and 2018 in the COSMOS, GOODS-S, GOODS-N, and AEGIS fields using nine multi-object slit masks milled with 1.″2 slits. The instrumental setup included a dichroic to split the incoming beam at ∼5000Å into the blue and red arms of LRIS. We configured the blue side with the 400 lines/mm grism, and the red side with the 600 lines/mm grating. This configuration provided continuous spectral coverage from the atmospheric cut-off at 3100Å up to a typical wavelength of ∼7000Å, depending on the position of the slit within the spectroscopic field of view. The seeing ranged from 0.″6 to 1.″2 with a typical value of 0.″8. The process to create the 1D spectra used in this study is described in Topping et al. (2020) and we refer readers there for more details. The rest-frame spectra were continuum normalized around each LIS absorption line. The local continuum was determined by fitting a linear model between the average flux in two spectral windows, bluewards and redwards of the LIS absorption line. The spectral windows, listed in Table 2.1, were chosen to bracket the line and free of other spectral features.

2.2.3 Redshift Measurements

Due to large-scale galaxy outflows, low-ionization interstellar absorption lines and the Lyα emission are Doppler shifted away from the MOSDEF systemic redshift ($z_{\rm sys}$) measured from strong rest-frame optical emission lines. LIS absorption line ($z_{\rm LIS}$) and Lyα ($z_{\rm Ly\alpha}$) redshifts and uncertainties were measured using the procedures described in Topping et al. (2020). Briefly, these redshifts were obtained by fitting lines with Gaussian functions and a quadratic function for the local continuum and calculating the centroids of the Gaussians. Redshift uncertainties were determined by perturbing the LRIS spectra by

the corresponding error spectra, refitting lines, and recalculating the centroids. Any LIS absorption lines with poor fits were excluded in the calculation of the average $z_{\rm LIS}$, typically based on two lines, for a given galaxy.

2.2.4 Sample Selection

For our analysis of outflows, 167 galaxies were initially selected with $z_{\rm sys}$ determined from MOSDEF observations, $z_{\rm LIS}$ and/or $z_{\rm Ly\alpha}$ measurements from LRIS observations. Additionally, as we are interested in star-forming galaxies, 12 galaxies were removed for possible AGNs based based on IR emission, X-ray emission, and the [NII]/Hα line ratio (Coil et al., 2015; Azadi et al., 2017, 2018; Leung et al., 2019). These requirements reduced the sample of 260 MOSDEF-LRIS galaxies to 155 galaxies (hereafter the "LRIS-flow" sample). For nine galaxies, the MOSDEF or LRIS slit includes close, unresolved galaxies such that there may be a mismatch between the measured redshifts. These galaxies are included in the LRIS-flow sample, and we note that our final results are not affected by their inclusion. As shown in Figure 2.1, the LRIS-flow sample has a redshift range of $1.42 \leq z \leq 3.48$ with a median redshift of 2.24, centroid LIS absorption line velocities ($\Delta v_{\rm LIS}$) from -510 km s^{-1} to 380 km s^{-1} with a mean of -60 ± 10 km s^{-1}, and centroid Lyα emission velocities ($\Delta v_{\rm Ly\alpha}$) from -190 km s^{-1} to 950 km s^{-1} with a mean of 400 ± 23 km s^{-1}.

Table 2.1: Spectral Windows

Line	λ (Å)[a]	Blue Window (Å)[b]	Red Window (Å)[b]
Lyα	1215.67	1195 - 1202	1225 - 1235
SiII	1260.42	1245 - 1252	1270 - 1275
OI	1302.17	1285 - 1293	1312 - 1318
CII	1334.53	1320 - 1330	1342 - 1351
SiII	1526.71	1512 - 1520	1535 - 1540
FeII	1608.45	1590 - 1600	1616 - 1620

[a] Rest-frame vacuum wavelength, taken from the Atomic Spectra Database website of the National Institute of Standards and Technology (NIST; Kramida et al., 2022).
[b] Wavelength window over which continuum fitting was performed.

2.3 Measurements

2.3.1 Stellar Population Properties

Stellar masses ($M_\star$) and SFRs of the LRIS-flow sample were derived from spectral energy distribution (SED) modeling. Here, we briefly describe the models used and refer readers to Reddy et al. (2015) for more details. The models were created adopting a Bruzual & Charlot (2003a, hereafter BC03) stellar population synthesis model, Chabrier (2003) initial mass function, constant star formation histories (SFH), Small Magellanic Cloud (SMC) attenuation curve (Fitzpatrick & Massa, 1990; Gordon et al., 2003), and sub-solar metallicity $Z = 0.28 Z_\odot$.[4] A lower age limit of 50 Myr was imposed, based on the typical dynamical timescale of $z \sim 2$ galaxies (Reddy et al., 2012). The combination of the steeper SMC attenuation curve, which has been found to best reproduce the dust obscurations of typical star-forming galaxies at $z \sim 2$ based on far-infrared data (Reddy et al., 2018a), and

[4] Recent MOSDEF studies have suggested that a Calzetti et al. (2000) attenuation curve and solar metallicities provide a better description for high-mass ($\log(M_\star/M_\odot) \geq 10.04$) star-forming galaxies at z $\sim$ 2, compared to an SMC attenuation curve with sub-solar metallicities (Reddy et al., 2018a; Shivaei et al., 2020). If instead we assume a Calzetti et al. (2000) attenuation curve and solar metallicities for high-mass galaxies, on average, stellar masses are lower and SFRs are higher. However, our main results do not significantly change if we were to alter the assumed attenuation curve.

sub-solar metallicity provide self-consistent SFRs with those derived using other methods (Reddy et al., 2018b; Theios et al., 2019).[5] The best-fit stellar population parameters and their errors were obtained by perturbing the photometry, refitting the models, and taking the median and dispersion in the resulting parameters, respectively. As shown in the right panel of Figure 2.1, the LRIS-flow sample covers a range of typical star-forming galaxies. The LRIS-flow sample has a stellar mass range of $8.61 < \log(M_\star/M_\odot) < 10.88$ with a median $\log(M_\star/M_\odot)$ of 9.89 and SFR[SED] range from $0.32 < \log(\mathrm{SFR}/M_\odot\ \mathrm{yr}^{-1}) < 1.97$ with a median $\log(\mathrm{SFR}/M_\odot\ \mathrm{yr}^{-1})$ of 0.9.

2.3.2 SFR and SFR Surface Densities

We calculate Hα SFRs (SFR[Hα]) from Hα and Hβ flux measurements corrected for dust using the Balmer decrement. Following the methodology presented in Reddy et al. (2015), Hα luminosities are corrected for attenuation assuming a Cardelli et al. (1989) Galactic extinction curve[6] and converted to SFRs using the conversion factor from Reddy et al. (2018b), $3.236 \times 10^{-42}\ M_\odot\ \mathrm{yr}^{-1}\ \mathrm{ergs}^{-1}\ \mathrm{s}$, for a BC03 stellar population synthesis model and sub-solar metallicity adopted for the SED fitting (see Section 2.3.1). SFR[Hα] is calculated for objects with significant detections (S/N > 3) of Hα and Hβ. For objects where Hβ is undetected, 3σ upper limits are assigned. In the LRIS-flow sample, 25% of the galaxies do not have significant Hα and/or Hβ detections. To make full use of the statistical power of the sample, we have chosen to focus on SFR[SED] when discussing SFR. However, as the SFR[SED] is tightly correlated with stellar mass (i.e., both quantities are sensitive

[5] See also Appendix A of Reddy et al. (2022).

[6] Reddy et al. (2020) found that the nebular attenuation curve is similar in shape to that of the Galactic extinction curve (Cardelli et al., 1989).

to the normalisation of the best-fit SED), SFR[Hα] is used instead for the specific star-formation rate (sSFR = SFR[Hα]/$M_\star$). As discussed in previous studies, there is a general agreement between SFR[SED] and SFR[Hα] for MOSDEF galaxies (e.g., Reddy et al., 2015; Shivaei et al., 2016; Azadi et al., 2018; Reddy et al., 2022).

Along with the star-formation rate, the mechanisms that drive outflows may be enhanced in regions of compact star formation, so we define the star-formation-rate surface density ($\Sigma_{\rm SFR}$) as

$$\Sigma_{\rm SFR} = \frac{\rm SFR[SED]}{2\pi R_{\rm E}^2}. \tag{2.1}$$

At a given $\Sigma_{\rm SFR}$, outflows may be more effectively launched from a shallow galaxy potential (i.e., low stellar mass) relative to a deep potential. To examine the dependence of outflow velocity on both $\Sigma_{\rm SFR}$ and the galaxy potential, we compute the specific star-formation-rate surface density ($\Sigma_{\rm sSFR}$):

$$\Sigma_{\rm SFR}/M_X = \frac{\Sigma_{\rm SFR[H\alpha]}}{M_X} = \frac{\rm SFR[H\alpha]}{2\pi R_{\rm E}^2 M_X}, \tag{2.2}$$

where M_X can be stellar, dynamical, or baryonic mass (Section 2.3.3). As discussed in Price et al. (2020), the stellar mass of MOSDEF galaxies correlates with their dynamical mass, thus stellar mass can be used as a rough proxy for the gravitational potential well. For simplicity, we have retained the factor of 2 in the denominator as the impact that feedback has on the ISM is likely sensitive to the entire galaxy mass, not just the mass contained within the half-light radius.

2.3.3 Dynamical and Baryonic Masses

In addition to stellar masses, we also consider dynamical ($M_{\rm dyn}$), and baryonic ($M_{\rm bar} = M_\star + M_{\rm gas}$) masses, as these masses may better trace the gravitational potential well of the galaxies. The procedure to calculate $M_{\rm dyn}$ and $M_{\rm gas}$ is described in Price et al. (2020) and we refer readers there for more details. Briefly, $M_{\rm dyn}$ was calculated as

$$M_{\rm dyn} = k_{\rm tot}(R_{\rm E}) \frac{V_{circ}(R_{\rm E})^2 R_{\rm E}}{G}, \tag{2.3}$$

where $R_{\rm E}$ is the effective radii, $k_{\rm tot}(R_{\rm E})$ is the virial coefficient and G is the gravitational constant. For galaxies with resolved and detected rotation measured from 2D spectra, circular velocities can be calculated as: $V_{\rm circ}(R_{\rm E}) = \sqrt{V(R_{\rm E})^2 + 3.35\sigma_{V,0}^2}$, where $\sigma_{V,0}$ is the intrinsic galaxy velocity dispersion (Price et al., 2020). Otherwise, circular velocities are calculated by assuming a fixed value of intrinsic rotation velocity divided by intrinsic galaxy velocity dispersion. Gas masses are estimated using the Kennicutt-Schmidt (Kennicutt, 1989) relation between $\Sigma_{\rm SFR} = {\rm SFR}/(2\pi R_{\rm E}^2)$ and $\Sigma_{\rm gas} = M_{\rm gas}/(2\pi R_{\rm E}^2)$, where SFRs are derived from Hα and Hβ observations (if available) or SED fitting. In the LRIS-flow sample, 136 galaxies have measured dynamical and baryonic masses[7], with ranges of 9.1 $< \log(M_{\rm dyn}/M_\odot) <$ 11.9 and 9.5 $< \log(M_{\rm bar}/M_\odot) <$ 11.2, and medians $\log(M_{\rm dyn}/M_\odot) =$ 10.3 and $\log(M_{\rm bar}/M_\odot) = 10.4$.

[7]Galaxies without a robustly measured $R_{\rm E}$ do not have a measured $M_{\rm dyn}$ or $M_{\rm bar}$.

2.3.4 Outflow Velocity

Using systemic redshifts, LIS absorption line redshifts, and Lyα emission redshifts, we measure centroid outflow velocities from the redshift difference:

$$\Delta v_{\rm LIS} = \frac{c(z_{\rm LIS} - z_{\rm sys})}{1 + z_{\rm sys}} \quad \text{and} \quad \Delta v_{{\rm Ly}\alpha} = \frac{c(z_{{\rm Ly}\alpha} - z_{\rm sys})}{1 + z_{\rm sys}}, \tag{2.4}$$

where $z_{\rm sys}$ is the systemic redshift from optical emission lines. In addition to centroid outflow velocities, another technique for estimating outflow velocity uses the blue wings of the absorption line profile. In general, $\Delta v_{\rm LIS}$ may include both outflowing gas and interstellar gas at or near $z_{\rm sys}$. The interstellar gas could then shift the line profile to lower velocities, so that the true outflowing gas is better traced by the blue wings of the absorption line profile.

To estimate the velocity of the blue wings, previous studies have either used the outflow velocity where the absorption feature reaches some percent of the continuum level (Martin, 2005; Weiner et al., 2009; Chisholm et al., 2015) or the maximum velocity where the absorption feature returns to the continuum level (Steidel et al., 2010; Kornei et al., 2012; Rubin et al., 2014; Prusinski et al., 2021). We consider both the outflow velocity at 80% of the continuum (v_{80}) and maximum outflow velocity ($v_{\rm max}$) following a similar approach as Kornei et al. (2012). Using the normalized spectra, we identify the absolute minimum of a detected absorption feature, then move towards shorter wavelengths, checking the sum of the flux and its uncertainty at each wavelength step. We record the first wavelengths at which this sum exceeds 0.8 and 1.0, perturb the spectrum by its error spectrum, and repeat the same procedure many times. The average and standard deviation, after 3σ clipping,

of the trials are then used to calculate v_{80}, $v_{\rm max}$, and their uncertainties. This process was repeated for each detected LIS feature, listed in Table 2.1, adopting v_{80} and $v_{\rm max}$ as the average of the detected LIS features. A similar bootstrap method for calculating uncertainties is applied for apparent optical depth (Section 2.3.5) and equivalent width (Section 2.3.6). For objects in the LRIS-flow sample, v_{80} ($v_{\rm max}$) ranges from -26 to -990 km s^{-1} (-47 to -1090 km s^{-1}) with a median of -428 ± 29 km s^{-1} (-574 ± 29 km s^{-1}).

2.3.5 Apparent Optical Depth

The LIS absorption lines analyzed in this work are typically saturated, as observed in other studies of $z \sim 2-3$ galaxies (Shapley et al., 2003; Trainor et al., 2015; Du et al., 2018). As the LIS lines are saturated, the line depth provides a measure of the metal covering fraction along the line of sight, rather than the metal column density. Furthermore, with the LIS absorption lines falling on the flat part of the curve of growth, we cannot measure their optical depth. Instead, we measure the apparent optical depth (τ_a) directly from the flux ratio:

$$\tau_a = -\ln\left[\frac{F_\lambda}{F_{\lambda,\ \rm cont}}\right], \tag{2.5}$$

where F_λ is the observed flux and $F_{\lambda,\ \rm cont}$ is the continuum flux.[8] For each detected LIS feature listed in Table 2.1, the flux at the rest wavelength is calculated by weighting the flux from the two nearest pixels. If the weighted flux is negative, then the τ_a of that line is not calculated. The average τ_a from individually-detected LIS lines is adopted as τ_a for the galaxy.

[8]We note that τ_a is sensitive to the spectral resolution; i.e., a lower "optical depth" would be measured in a lower-resolution spectrum.

2.3.6 Equivalent Width

The equivalent widths of the LIS features (W_λ) are measured by summing the normalized absorbed flux enclosed between the edges of a feature's spectral window (Table 2.1). The average equivalent width of individually-detected LIS lines is taken as $W_{\rm LIS}$ and its uncertainty is estimated by adding the 1σ error bar of the detected LIS lines in quadrature. The equivalent width of Lyα ($W_{\rm Ly\alpha}$) is measured following the procedures given in Kornei et al. (2010) and Du et al. (2018). Throughout this work, W_λ refers to the rest-frame value and is negative for absorption features.

2.3.7 Composite Spectra

To evaluate the average outflow velocities in bins of other galaxy properties, we construct composite spectra by sorting the galaxies into equal-number bins according to various physical properties (e.g., SFR, mass, $\Sigma_{\rm SFR}$, inclination, τ_a, and W_λ). The composite spectrum is computed by shifting each galaxy's blue and red spectra into the rest-frame, converting to luminosity density, interpolating onto a new wavelength grid, and taking the unweighted average of the spectra for all galaxies contributing to the composite. We refer readers to Topping et al. (2020) and Reddy et al. (2022) for more details on how the composite and associated error spectra were calculated.[9] Using the same techniques described for individual objects, v_{80}, $v_{\rm max}$, τ_a, and $W_{\rm LIS}$ were measured from the composite spectra. Centroid velocities ($\Delta v_{\rm LIS}$ and $\Delta v_{\rm Ly\alpha}$) for the composite were measured in a similar way as v_{80} and $v_{\rm max}$ (Section 2.3.4), using the normalized spectra to measure the wavelength

[9]The code used to create the composite spectra is adapted from Shivaei et al. (2018); https://github.com/IreneShivaei/specline/

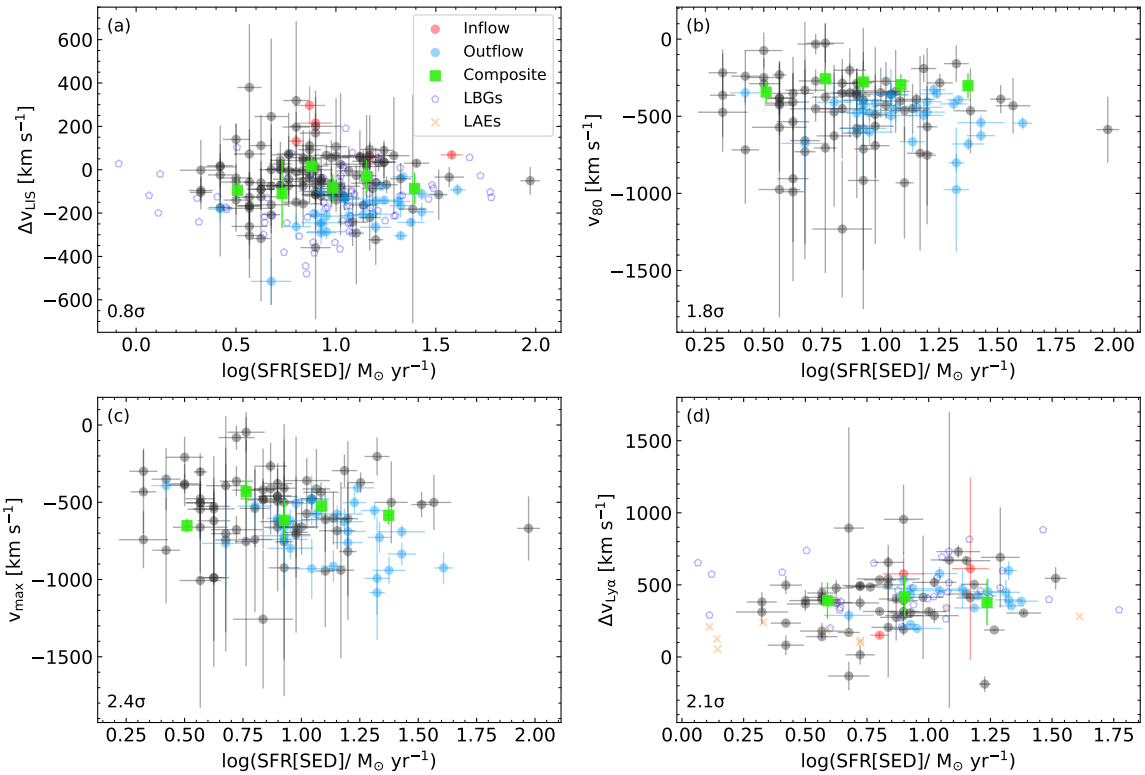

Figure 2.2: Outflow velocity versus log(SFR[SED]). Panel (a) $\Delta v_{\rm LIS}$, Panel (b) v_{80}, Panel (c) $v_{\rm max}$, and Panel (d) $\Delta v_{{\rm Ly}\alpha}$. Significant detections of outflows ($\Delta v_{\rm LIS}$ - $3\sigma_{\Delta v_{\rm LIS}} < 0$ km s^{-1}) or inflows ($\Delta v_{\rm LIS}$ - $3\sigma_{\Delta v_{\rm LIS}} > 0$ km s^{-1}) are shown as blue and red circles, respectively. gray circles are galaxies with non-significant measured flows. Results from composite spectra, binning the galaxies by log(SFR[SED]), are shown as green squares. Blue pentagons are Lyman Break galaxies from Erb et al. (2006) and orange crosses are Lyα Emitter galaxies from Erb et al. (2016). In the lower left corners, σ is the number of standard deviations from the null hypothesis that the quantities are uncorrelated, based on a Spearman rank correlation test of the blue, red, and gray circles.

at the absolute minimum of the detected LIS absorption trough or at the maximum of the Lyα peak.

2.4 Results

In this section, we present the relations between outflow velocity and several galactic properties. Table 2.7 summarizes the results of Spearman correlation tests between

$\Delta v_{\rm LIS}$, v_{80}, $v_{\rm max}$, $\Delta v_{{\rm Ly}\alpha}$, and the galaxy properties analyzed in this work. Note that, when SFR[Hα] is considered, 16 galaxies without robust measurements of the nebular dust attenuation, i.e. Hβ detections, are not used in the correlation test.

2.4.1 SFR and sSFR

A key property is SFR, which sets the amount of mechanical energy and radiation pressure available in star-forming galaxies to drive outflows. Figure 2.2 shows outflow velocity against SFR[SED]. We find that $v_{\rm max}$ and $\Delta v_{{\rm Ly}\alpha}$ are marginally correlated with SFR[SED], such that higher SFR[SED] galaxies appear to have gas at larger velocities than lower SFR[SED] galaxies. While this trend is in agreement with the picture of galactic outflows driven by supernova or radiation pressure (Chevalier & Clegg, 1985; Murray et al., 2011), it is surprising that these relations are found, given the small range of SFR[SED] probed by the LRIS-flow sample (SFR[SED]: 2 – 93 $M_{\odot}$ yr^{-1}). On the other hand, these marginal correlations are not seen for the composite spectra (green squares), with the correlations decreasing to 0.5σ and 0.6σ for $v_{\rm max}$ and $\Delta v_{{\rm Ly}\alpha}$, respectively. This suggests that the average outflow properties measured from composite spectra may not accurately reflect those of the individual galaxies.

To increase our sample size, we include $z \sim 2$ Lyman Break galaxies (LBGs) and Lyα-emitters (LAEs) from the literature (Erb et al., 2006, 2016).[10] Including LBGs in the Spearman test, the correlation between $\Delta v_{\rm LIS}$ and SFR[SED] decreases to 0.2σ. The lack of a correlation with $\Delta v_{\rm LIS}$ suggests, at a given SFR[SED], that $\Delta v_{\rm LIS}$ may be biased to

[10] We recalculate the SFRs of the LBGs and LAEs using the same SED models as described in Section 2.3.1.

lower average outflow velocities possibly due to gas at rest near $z_{\rm sys}$. In this case, v_{80} and $v_{\rm max}$ are likely more robust indicators of the outflow velocity (see Section 2.3.4), thus a correlation is more likely to be seen over a smaller range in SFR. For $\Delta v_{{\rm Ly}\alpha}$, the larger SFR[SED] range of LBGs increases the correlation with SFR[SED] slightly to 2.2σ, while the correlation increases to 3σ when LAEs are included. However, the LAEs appear to have lower velocities at a given SFR[SED], as seen in studies of LAEs (Hashimoto et al., 2013; Shibuya et al., 2014), complicating a direct comparison between these LAEs and the LRIS-flow sample.

Next, we investigate the dependence of outflow velocity on specific SFR (sSFR). As sSFR is a tracer of both mechanical energy and gravitational potential energy (the latter due to the dependence of specific SFR on $M_\star$), one might expect a correlation with outflow velocity. Of the four combinations of outflow velocities and SFR[Hα]/$M_\star$, only a very marginal correlation is found between v_{80} and SFR[Hα]/$M_\star$ at 2σ (panel (a) of Figure 2.3). These findings appear to contradict previous studies which have found no correlation between SFR[Hα]/$M_\star$ and outflow velocity (Rubin et al., 2010; Chisholm et al., 2015; Prusinski et al., 2021). However, the finding of a marginal correlation with v_{80}, but not $v_{\rm max}$, is suspicious, as both should trace the high-velocity component of the outflow. If we restrict the correlation test to include only those galaxies for which the uncertainties in $\Delta v_{\rm LIS}$ imply that there are outflows with $>3\sigma$ significance, the correlation between v_{80} and SFR[Hα]/$M_\star$ drops to 1.6σ. We conclude that the apparent marginal correlation between SFR[Hα]/$M_\star$ and v_{80} is likely the result of galaxies with large uncertainties in v_{80} (gray points), rather than having a physical origin.

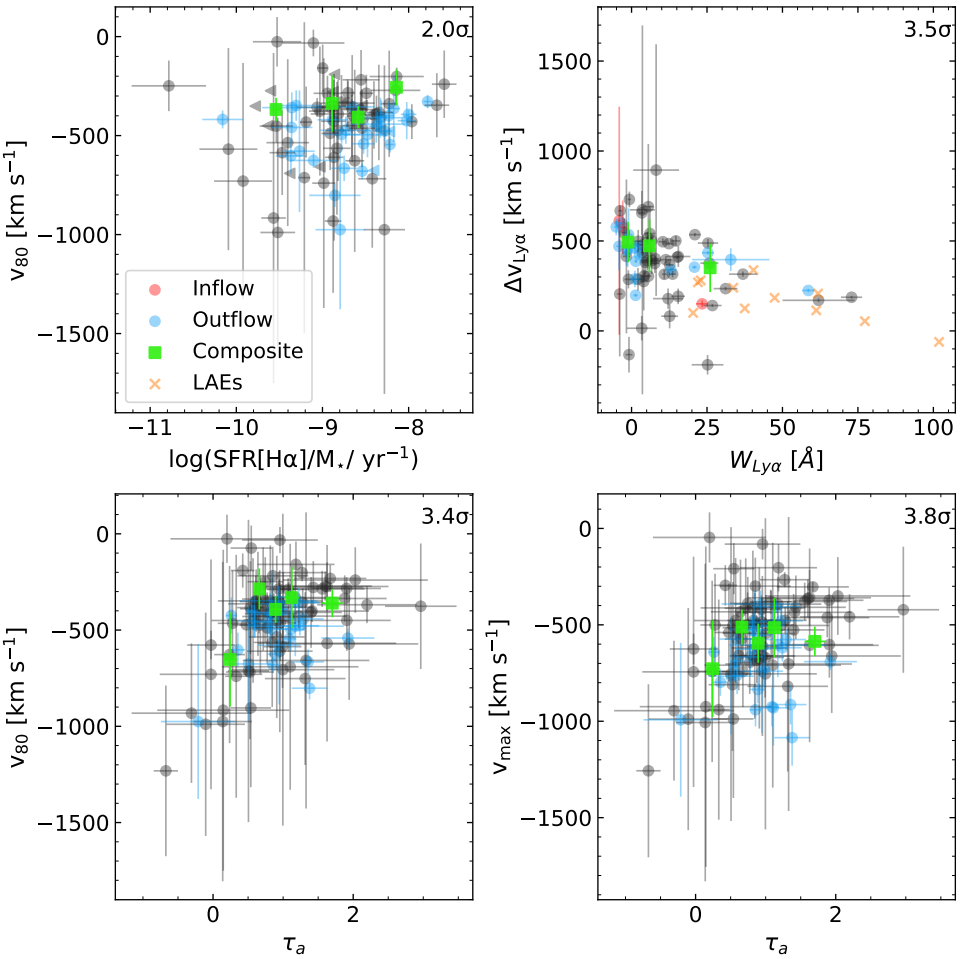

Figure 2.3: Panel (a): v_{80} versus $\log(\mathrm{SFR}[\mathrm{H}\alpha]/M_\star)$. Panel (b): $\Delta v_{\mathrm{Ly}\alpha}$ versus $W_{\mathrm{Ly}\alpha}$. Panel (c): v_{80} versus τ_a. Panel (d): $v_{\max}$ versus τ_a. Triangles are upper limits for galaxies without H_β detections. Same point and style as Figure 2.2.

2.4.2 Lyα Equivalent Width

Panel (b) of Figure 2.3 shows the relation between $W_{\mathrm{Ly}\alpha}$ and outflow velocity $\Delta v_{\mathrm{Ly}\alpha}$. There is a clear anti-correlation between the two, such that objects with a larger Lyα equivalent width tend to have smaller outflow velocities. As shown in previous studies of LAEs at $z \sim 2 - 3$ (Erb et al., 2014; Trainor et al., 2015; Nakajima et al., 2018), this anti-correlation is likely tied to the column density of neutral hydrogen. For high column densities of gas at systemic redshift, Lyα photons resonantly scatter farther out in the wings to escape, increasing $\Delta v_{\mathrm{Ly}\alpha}$ while decreasing $W_{\mathrm{Ly}\alpha}$. While we find a high significance of 3.7σ, this is weaker than the correlation reported by studies of LAEs. This is likely due to the smaller dynamic range in $W_{\mathrm{Ly}\alpha}$ covered in the LRIS-flow sample, where only 5% of objects have $W_{\mathrm{Ly}\alpha} > 40$ Å compared to 42% of LAEs in Erb et al. (2016). When LAEs are included in the Spearman test, the correlation between $\Delta v_{\mathrm{Ly}\alpha}$ and $W_{\mathrm{Ly}\alpha}$ increases, as expected, to 6.7σ.

2.4.3 Apparent Optical Depth

Panels (c) and (d) of Figure 2.3 show the relation between τ_a and outflow velocity. As the LIS absorption lines are saturated, τ_a is sensitive to the metal covering fraction along the line of sight rather than metal column density. For both v_{80} and v_{max}, there is a positive correlation with τ_a, such that objects with lower τ_a have faster outflow velocities. This correlation is also seen in studies of Green Pea galaxies (e.g., Alexandroff et al., 2015; Jaskot et al., 2017), where it is argued that extreme feedback (i.e., high v_{out}) creates holes

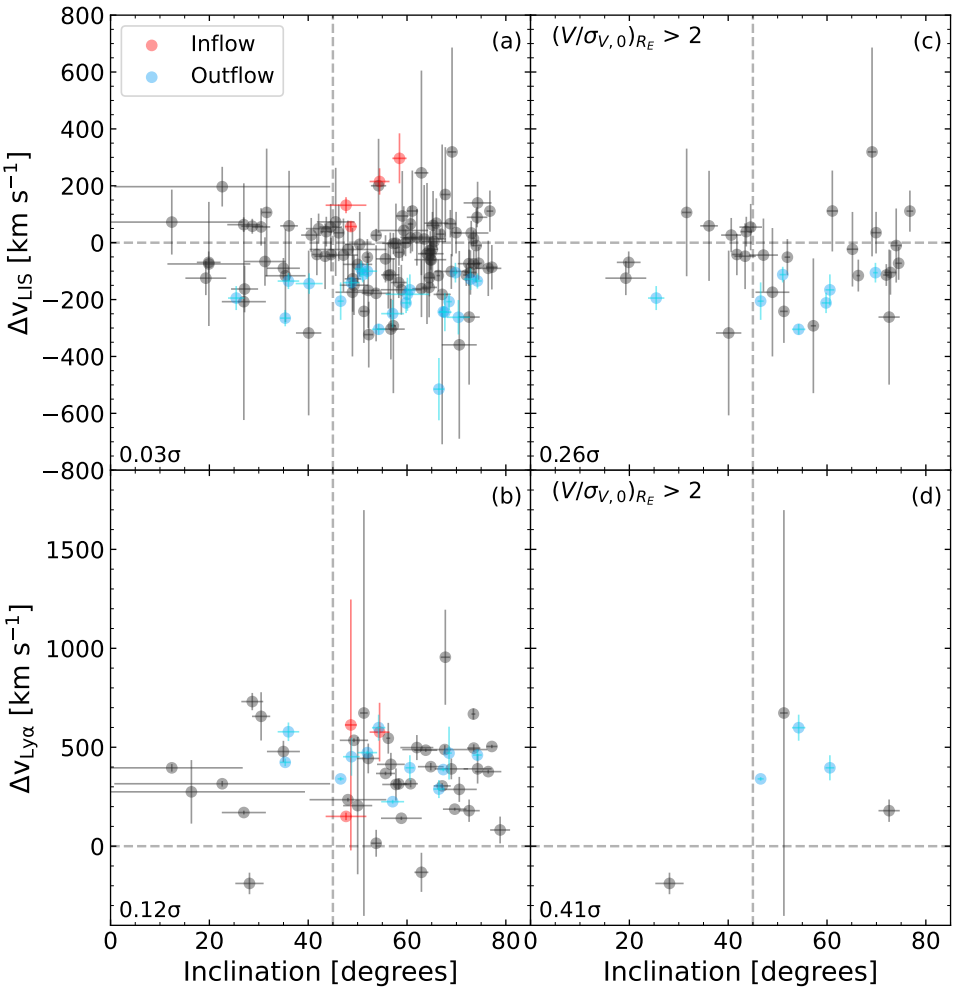

Figure 2.4: *Top*: $\Delta v_{\rm LIS}$ versus inclination. *Bottom*: $\Delta v_{{\rm Ly}\alpha}$ versus inclination. Panels (a) and (b) include all galaxies with a measured inclination, while panels (c) and (d) are limited to galaxies with $(V/\sigma_{V,0})_{R_E} > 2$. Same point and style as Fig. 2.2.

in the neutral ISM, which decreases τ_a. A full investigation into the structure of the ISM/CGM is beyond the scope of this paper, and we refer interested readers to Du et al. (2021).

2.4.4 Inclination

In the canonical picture of galaxy flows, outflows emerge perpendicular to the disk in a biconical structure, while inflows occur along the major axis of the galaxy (Heckman et al., 1990; Katz & White, 1993). Within this picture, measured outflow velocities would strongly depend on inclination, with low-inclination (face-on) galaxies exhibiting faster outflows and weaker inflows compared to high-inclination (edge-on) galaxies. Studies of low-redshift galaxies have found a strong correlation of decreasing outflow velocity with increasing inclination, consistent with the physical picture described above (e.g., Chen et al., 2010; Concas et al., 2019; Roberts-Borsani & Saintonge, 2019). At intermediate redshifts ($z \sim 1$), no strong correlation has been observed likely due to the difficulty of measuring inclination robustly for high-redshift galaxies with low-spatial-resolution observations and complicated morphologies. Despite these complications, studies have shown that low-inclination galaxies tend to exhibit outflowing gas, while inflowing gas is typically found in high-inclination ($i > 50$) galaxies (Kornei et al., 2012; Rubin et al., 2012, 2014). Additionally, at high redshifts ($z \gtrsim 2$), gaseous disks to neatly collimate galactic outflows are only found in massive galaxies, which could explain the lack of a correlation between inclination and $v_{\rm out}$ (Law et al., 2012).

Here, we investigate the dependence of outflow velocity on galaxy inclination, where the inclination is calculated as the ratio of a galaxy's semi-minor to semi-major axes, $i = \cos(b/a)^{-1}$. As shown in panels (a) and (b) of Figure 2.4, galaxies with significant inflows are only found at $i > 45°$, consistent with the physical picture of inflowing gas entering along the major axis of the galactic disk. For galaxies with significant outflows, 18/22 have

inclinations above 45° (edge-on), which, at face value, is inconsistent with the canonical picture of bi-polar outflows.[11] In part, the large fraction of outflowing galaxies in edge-on galaxies may reflect the lack of thin disks and/or the difficulty of measuring structural properties robustly for high redshift galaxies. Without established disks, the path with the lowest ambient gas pressure may not be along the minor axis, allowing outflows to escape at various angles, thus there would be no relation between inclination and $v_{\rm out}$. van der Wel et al. (2012) found that the structural properties of galaxies in the CANDELS fields were accurate within ∼10° of the 'true' properties using simulated galaxies images with known light distributions.

To explore this issue further, we investigate a rotation-dominated subsample, with $(V/\sigma_{V,0})_{R_E} > 2$ (Price et al., 2020). This subsample should resemble local star-forming disks more closely than clumpy, irregular galaxies with large velocity dispersions, such that inclination may be better measured from the axis ratio. Panels (c) and (d) of Figure 2.4 show outflow velocity against inclination for the subsample. Significant outflows are still primarily found in high inclination galaxies, with 6/7 of the galaxies inclined above 45°. As with the full sample, there is no significant correlation between inclination and outflow velocity for the significantly outflowing galaxies. These results may suggest that the covering fraction of outflowing material is quite large, such that outflows are measurable even at high inclinations. Recently, Chen et al. (2021) stacked Lyα spectral profiles of 59 star-forming galaxies at $z = 2 - 3$ galaxies and found an excess emission in the blueshifted component of Lyα along the minor axis, indicating a high covering fraction of outflowing gas.[12]

[11] We note that the lack of galaxies with low inclinations is unlikely due to selection effects. In the parent MOSDEF sample, about 4% of the sample has an inclination below 25°, which is very similar to the 5% of galaxies in the LRIS-flow sample.

[12] Reichardt Chu et al. (2022a) analyzed IFS observations of a starbursting disk galaxy at $z \sim 0.02$, and

2.4.5 SFR Surface Density

The connection between $\Sigma_{\rm SFR}$ and galactic outflows has been investigated in several studies (Steidel et al., 2010; Kornei et al., 2012; Rubin et al., 2014; Chisholm et al., 2015; Davies et al., 2019; Prusinski et al., 2021). Specifically, it has been suggested that regions with higher $\Sigma_{\rm SFR}$, which traces the concentration of star formation in a galaxy, will be more efficient at injecting energy and momentum into the ISM from overlapping supernovae or stellar winds from massive stars, resulting in conditions amenable for launching outflows. Additionally, in this study, we consider a possible $v_{\rm out}$-$\Sigma_{\rm sSFR}$ relation. A correlation between $\Sigma_{\rm sSFR}$ and $v_{\rm out}$ may be expected if galaxies with high $\Sigma_{\rm SFR}$ and low gravitational potential (or low stellar mass) are more efficient in launching outflows (Reddy et al., 2022). We investigate both $\Sigma_{\rm SFR}$ and $\Sigma_{\rm sSFR}$, and find no significant correlations (see Figure 2.9), which may be due to the limited dynamic range and/or the spatial resolution of our data (see Section 2.5.2).

There is a debate in the literature about the existence of a $v_{\rm out}-\Sigma_{\rm SFR}$ relation. Kornei et al. (2012) used a sample of 72 star-forming galaxies at z $\sim$ 1 and found that galaxies with higher $\Sigma_{\rm SFR}$ had faster outflow velocities. However, Kornei et al. (2012) proposed that such a relation is only present when inflowing and outflowing galaxies are considered together, with no significant trend between $\Sigma_{\rm SFR}$ and velocity among galaxies where the latter is negative (indicating outflows). Davies et al. (2019) found that outflow velocity is related to $\Sigma_{\rm SFR}$ as $v_{\rm out} \propto \Sigma_{\rm SFR}^{0.34}$, using integral field unit observations of 28 star-forming galaxies at z $\sim$ 2. The Davies et al. (2019) study traced denser, ionized outflowing gas using

found a high covering fraction of $\sim$0.7 $-$ 1.

the narrow and broad components of Hα emission, which may be partially broadened by shocks or turbulent mixing layers potentially making Hα less reliable for measuring outflow velocities. Both Steidel et al. (2010) and Rubin et al. (2014) found no correlation between outflow velocity with $\Sigma_{\rm SFR}$. The limited dynamic range of SFR probed in these studies, similar to the range in our sample, is likely a contributing factor to their results.

2.5 Discussion

2.5.1 Outflow Driving Mechanisms

The physical picture underlying observed trends among star-formation properties and outflow velocities have been considered in several theoretical and observational studies (Chevalier & Clegg, 1985; Ferrara & Ricotti, 2006; Steidel et al., 2010; Murray et al., 2011; Sharma & Nath, 2012). There are two commonly invoked mechanism for launching galactic-scale outflows in star-forming galaxies: (1) mechanical energy injected by supernovae ("energy-driven"; Chevalier & Clegg, 1985); and (2) momentum injected by supernovae or radiation pressure from massive stars acting on dust grains ("momentum-driven"; Murray et al., 2005, 2011). In the energy-driven case, mechanical energy from multiple, overlapping supernovae thermalizes a large fraction of nearby gas into a hot over-pressured bubble. As the bubble expands adiabatically through the disk, it sweeps up ambient ISM material until it is ejected from the galaxy. Within the hot wind, ram pressure accelerates entrained cold gas clouds. Outflows driven by mechanical energy are predicted to scale weakly with star formation: $v_{\rm out} \propto {\rm SFR}^{0.2}$ (Ferrara & Ricotti, 2006) or $v_{\rm out} \propto {\rm SFR}^{0.25}$ (Heckman et al., 2000) and $v_{\rm out} \propto \Sigma_{\rm SFR}^{0.1}$ (Chen et al., 2010). In the momentum-driven case,

momentum is injected into the ISM by supernovae that accelerates cold gas, or radiation pressure from the absorption and scattering of photons on dust grains accelerating cold gas coupled to the dust. If the outflows are purely radiatively driven, the outflow velocity is predicted to scale strongly with star formation activity: $v_{\rm out} \propto {\rm SFR}$ (Sharma & Nath, 2012) and $v_{\rm out} \propto \Sigma_{\rm SFR}^2$ (Murray et al., 2011). As these mechanisms are likely dominate under different galactic conditions, outflows could be driven by a combination of mechanical energy and radiation pressure. The power law scaling between outflow velocity and star formation activity would then fall between the energy- and momentum-driven cases. Murray et al. (2011) used 1-D models to investigate this case, and found that radiation pressure initially drives cold gas to about the scale height of the galaxy. After $\sim$3 – 5 Myr, the lifetime of massive stars, supernovae begin to occur, and cold gas is then driven by radiation pressure and ram pressure to hundreds of kiloparsecs from the galaxy.

Along with energy and momentum, cosmic rays produced by supernovae may drive large-scale galactic outflows in star-forming galaxies (see discussions in Heckman & Thompson, 2017; Zhang, 2018). As they diffuse out of the galaxy, cosmic rays scatter several times off of magnetic inhomogeneities in the ISM, transferring momentum to the surrounding gas. Based on the diffusion timescale of cosmic rays in the Milky Way, the total momentum deposited by cosmic rays is comparable to the momentum injected by radiation (Zhang, 2018). However, despite the promising potential of cosmic rays to drive outflows, there are many open questions. Cosmic rays can be destroyed by scattering off of ISM gas, creating pions. If this destruction timescale is significantly shorter than the diffusion timescale, then the total cosmic ray momentum available to drive outflows would

be severely limited. Additionally, the coupling between cosmic rays and multiphase gas is unclear, with some simulations finding that cosmic rays can decouple from cold gas clouds (Everett & Zweibel, 2011).

There is tension between studies of low and high-redshift galaxies regarding the existence of a relation between SFR and outflow velocity. At low redshifts, Martin (2005) found that outflow velocity traced by the Na I absorption line scales as $v_{\rm out} \propto {\rm SFR}^{0.35}$, covering four orders-of-magnitude in SFR. Chen et al. (2010) and Sugahara et al. (2017) found no significant relation with the Na I centroid velocity over smaller ranges in SFR. However, Sugahara et al. (2017) found a similar power-law scaling ($v_{\rm out} \propto {\rm SFR}^{0.25}$) when outflow velocity is defined using the blue wings of the absorption profile, rather than centroid velocities. Studies at higher redshift are often limited to a smaller dynamic range of SFR and fail to find a significant correlations between SFR and centroid or maximum outflow velocities (Steidel et al., 2010; Law et al., 2012; Kornei et al., 2012; Rubin et al., 2014).

Here, we investigate the marginally-correlated trend of $v_{\rm max}$ with SFR[SED]. The power-law relations discussed above can be generalized as

$$\log(|{\rm V}|) = \alpha + \beta \log({\rm SFR[SED]}/{\rm M}_\odot\ {\rm yr}^{-1}), \tag{2.6}$$

where V is the outflow velocity, α is the scaling factor, and β is the power-law index. We adopt a Bayesian approach for calculating the linear regression to simultaneously fit possible combinations of α and β to equation 2.6, while accounting for the uncertainties in $v_{\rm max}$ and SFR[SED]. The results of the fitting are shown in Figure 2.5. The best-fit power-

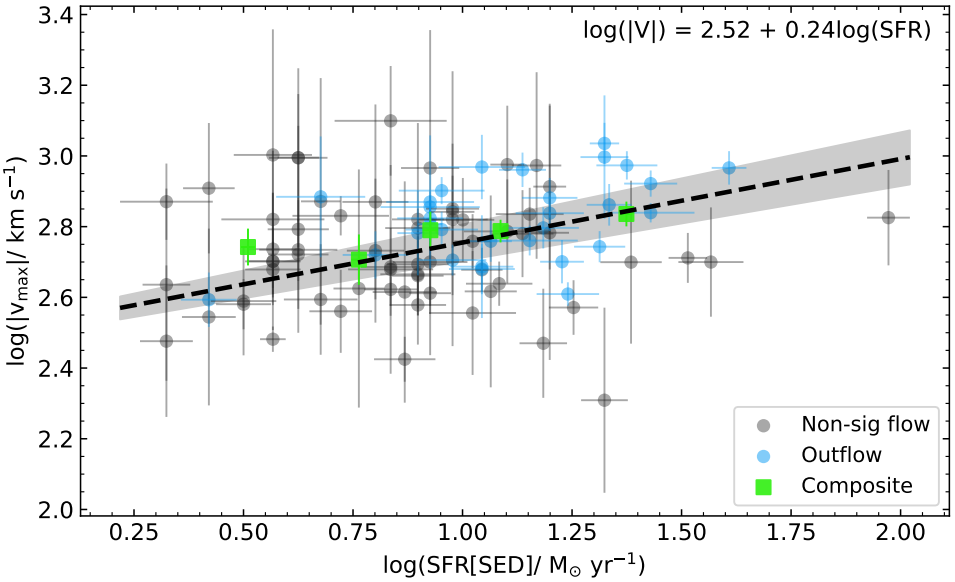

Figure 2.5: $\log(|v_{\rm max}|)$ versus log(SFR[SED]). Blue circles are galaxies with 3σ-measured outflows. gray circles are non-significant measured flows. The dashed black line and shaded region (68% confidence intervals) is the best-fit line to the galaxies (blue and gray). The functional form of the line is listed in the upper-right corner.

law index is $\beta = 0.24 \pm 0.03$. Our measurements of β are consistent with the energy-driven case, suggesting that in these galaxies cool outflows are driven primarily from mechanical energy injected into the ISM from supernovae. However, we caution that β is determined from a *marginal correlation* between outflow velocity and SFR[SED]. In the next section, we explore the contribution of radiation pressure on outflow velocity.

Radiation Pressure

While it appears that the outflows studied here are driven primarily by mechanical energy, these outflows may be driven by a combination of ram and radiation pressure. To explore the contribution of radiation pressure in driving outflows, we divided the sample into groups according to the dustiness of the galaxies. Dust is the cornerstone of momentum-

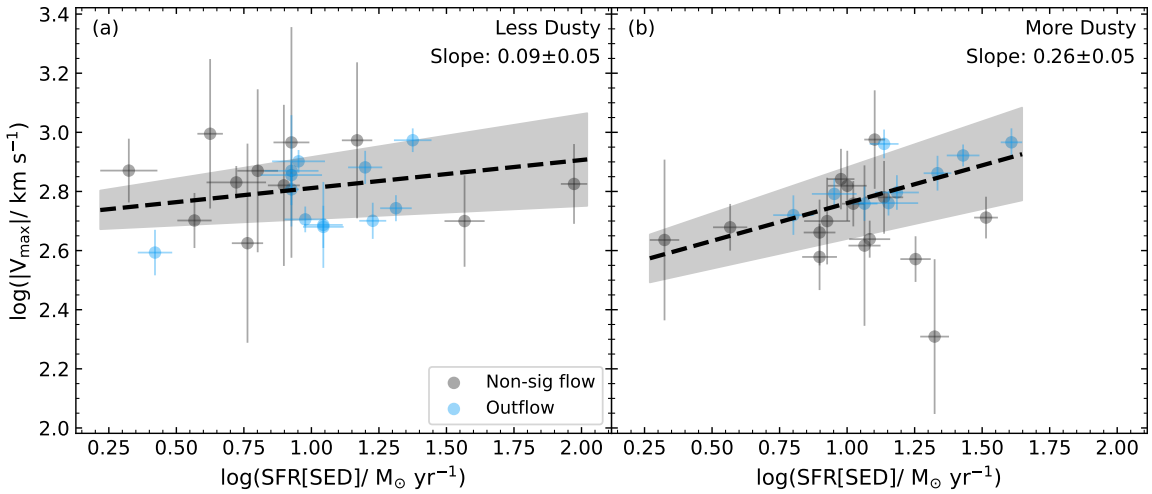

Figure 2.6: $\log(|v_{\rm max}|)$ versus log(SFR[SED]). Panel (a) are "less dusty" galaxies ($\tau_b + \sigma_{\tau_b} < \tau_{b,\rm median}$), while panel (b) are "more dusty" (τ_b - $\sigma_{\tau_b} \geq \tau_{b,\rm median}$). Blue circles are galaxies with 3σ-measured outflows. gray circles are non-significant measured flows. The dashed black line and shaded region (68% confidence intervals) is the best-fit line to the sample. The slope and uncertainty of the line are listed in the upper-right corner.

driven outflows; without dust coupling to gas, radiation pressure on dust grains could not drive large amounts of gas out of galaxies (Murray et al., 2005). If radiation pressure is negligible, then the slope of the $v_{\rm max}$-SFR relation will remain consistent with the energy-driven case for galaxies with low and high dust content.

We parameterize the dustiness of galaxies using the Balmer optical depth (Calzetti et al., 1994):

$$\tau_b = \ln\left(\frac{\rm H\alpha/H\beta}{2.86}\right), \tag{2.7}$$

where Hα/Hβ is the Hα to Hβ line luminosity ratio and τ_b, the Balmer optical depth, is the difference in optical depths for Hβ and Hα. The Balmer optical depth is chosen over other dust metrics (e.g., E(B-V) or UV continuum slope) as it is sensitive to the reddening towards the ionized regions surrounding massive stars, which are more likely to have sufficient radiation pressure to drive outflows. We require that galaxies have 3σ

detections of Hα and Hβ to calculate τ_b. Galaxies with measured Hα/Hβ < 2.86, the theoretical minimum value in the absence of dust for Case B recombination and T = 10000 K (Osterbrock, 1989), are assigned $\tau_b = 0$. Galaxies are divided into "less dusty" ($\tau_b + \sigma_{\tau_b} < \tau_{b,\mathrm{median}}$) and "more dusty" ($\tau_b$ - $\sigma_{\tau_b} > \tau_{b,\mathrm{median}}$) groups.[13] The average τ_b of the "less dusty" and "more dusty" groups are 0.06 and 0.54, respectively. Figure 2.6 shows that the slopes of the v_{max}-SFR relation between the two groups differ marginally (2σ), with "less dusty" galaxies having a weaker slope (0.10±0.05), while "more dusty" galaxies have a steeper slope (0.26±0.06). The difference in the slopes suggests that radiation pressure plays a minor role, along with ram pressure, in driving cool outflows. However, the dustiness traced by τ_b may not reflect the dust content of the outflows themselves, and without constraints on the other outflow phases (i.e., ionized and molecular), we cannot fully separate the contributions of ram and radiation pressure on galactic-scale outflows.

Lastly, it is useful to discuss the energy- vs. momentum-driven outflows in the context of simulations. A complete description of galactic-scale outflows and their impacts on galaxy evolution is challenging for simulations due to the different length scales of outflows. Both the ISM and large-scale galaxy features must be adequately resolved to capture relevant physical processes that generate outflows and how outflows interact with the CGM and IGM. These resolution requirements have led simulations of outflows to be performed in a relatively new generation of cosmological "zoom-in" simulations (Hopkins et al., 2014; Christensen et al., 2016; Hopkins et al., 2018), where an individual galaxy is simulated to a high resolution within a larger, coarser cosmological volume. As simulations are not limited

[13] We note that the different ranges spanned by the "less dusty" and "more dusty" subsamples is primarily due to one outlier "less dusty" galaxy at $\log(\mathrm{SFR[SED]}/M_\odot\ \mathrm{yr}^{-1}) = 1.9$. After removing the outlier, the median SFR[SED] and interquartile range of the subsamples are similar, thus a comparison of the slopes is reasonable.

by observational constraints, one can directly probe the mass loading factor (η), the gas mass outflow rates normalized by SFR, and how it scales with the circular velocity (V_{circ}) of the halo. In contrast to the v_{out}-SFR relation, the $\eta-V_{circ}$ relation is predicted to be steeper in the energy-driven case ($\eta \propto V_{circ}^{-2}$) and shallower in the momentum-driven case ($\eta \propto V_{circ}^{-1}$) (Murray et al., 2005).

We have found that the outflows in the LRIS-flow sample are most consistent with an energy-driven scenario, which is supported by results from zoom-in simulations. Muratov et al. (2015) used the Feedback in Realistic Environments (FIRE-1; Hopkins et al., 2014) zoom-in simulations to analyse galactic-scale outflows and found a broken power law for the $\eta-V_{circ}$ relation spanning the energy- and momentum-driven cases. Muratov et al. (2015) concluded that the broken power law represented a transition from energy-driven outflows in dwarfs to momentum-driven outflows in higher mass halos. In a recent study, Pandya et al. (2021) investigated outflows in the updated FIRE-2 simulations (Hopkins et al., 2018) and found that $z \sim 2$ galaxies from low-mass dwarf halos to Milky Way-mass halos galaxies follow a $\eta-V_{circ}^{-2}$, in agreement with the energy-driven case. However, in both the FIRE-1 and FIRE-2 simulations, missing physics (e.g., radiation pressure from infrared multiple-scattering, type Ia SNe, cosmic rays, etc.) and the lower resolution of the ISM, compared to "resolved" ISM simulations, may lead to overestimated of mass-loading factors, thus radiation pressure could play a role in driving cool outflows.

2.5.2 Significance of SFR Surface Densities on Outflows

As discussed in Section 2.4.5, outflow velocity does not appear to correlate significantly with the star-formation-rate surface density over the dynamic range of our sample.

This result appears to be in tension with several other studies at low and intermediate redshifts, which find a weak $v_{\rm out}$-$\Sigma_{\rm SFR}$ relationship (Chen et al., 2010; Kornei et al., 2012; Chisholm et al., 2015). However, there are three possible reasons for the lack of an observed relation: (1) there is ambiguity regarding the actual location of the gas and its coupling to the star formation activity, (2) $\Sigma_{\rm SFR}$ and outflow velocity may be correlated on spatial scales that are unresolved by the LRIS observations, and (3) the relationship between outflow velocity and $\Sigma_{\rm SFR}$ may be weak over the dynamic range of $\Sigma_{\rm SFR}$ probed in our sample. We discuss each of these possibilities below.

Where is the Absorbing Gas?

Using starlight from the galaxy as the background light source against which interstellar absorption and Lyα emission is measured (i.e., down-the-barrel observations) provides valuable information about gas flows. However, these observations tell us very little about the spatial location of the absorbing gas. To gain a better insight into the physical mechanisms that drive galactic outflows, and their effects on their host galaxies, we would require precise measurements of the physical location of the gas, so that position and velocity could be simultaneously constrained.

The LRIS spectra, which probe down the barrel of the galaxy, only provide a surface-brightness weighted absorption profile for each observed LIS line, integrated along the entire line of sight. Although the different LIS lines appear to have similar profiles after integrating along the line of sight, there is no way of knowing where the bulk of the absorption is occurring relative to the galaxy. Furthermore, after integration, material from both past and current outflows affects the shape of the absorption line profiles. This

indicates that the observed absorption may originate from regions far enough away from the galaxy that the outflow velocity traced by LIS absorption has uncoupled from changes in $\Sigma_{\rm SFR}$. However, using a sample of close angular pairs of galaxies at $z \sim 2-3$, Steidel et al. (2010) found that LIS absorption line profiles are dominated by gas within ∼10 kpc of the galaxy. Based on $\langle \Delta v_{\rm LIS} \rangle$ and $\langle v_{\rm max} \rangle$ of the LRIS-flow sample, outflowing gas could exceed that distance in a roughly 50 Myr dynamical timescale, travelling 10 to 36 kpc. The observed absorption line profiles are likely originating in gas that is dynamically connected to recent star formation, thus the location ambiguity introduced by the down-the-barrel observations is unlikely the reason why we find no correlation between $v_{\rm out}$ and $\Sigma_{\rm SFR}$.

Limited Spatial Resolution

Another possible explanation for the observed lack of correlation between outflow velocity and $\Sigma_{\rm SFR}$ is the limited spatial resolution probed by the LRIS spectroscopy. In particular, if the velocity of outflowing gas is coupled to $\Sigma_{\rm SFR}$ on scales smaller than a few kpc, then such a coupling may be masked by seeing-limited spectroscopy. Several studies have suggested that $\Sigma_{\rm SFR}$ and outflow velocity are correlated on small ∼kpc spatial scales. Bordoloi et al. (2016) found that outflow velocities from individual star-forming knots in a lensed galaxy at $z \sim 1.7$ are correlated to the $\Sigma_{\rm SFR}$ of the knots, suggesting that outflows are 'locally sourced'. Similarly, Davies et al. (2019) created high S/N stacks of IFU Hα observations from 28 $z \sim 2.3$ galaxies in bins of resolved physical properties. From their analysis, Davies et al. (2019) concluded that $\Sigma_{\rm SFR}$ and outflows are closely related on 1 – 2 kpc scales. In the LRIS-flow sample, ∼54% of the galaxies have an effective radius, as

measured from HST imaging, >2 kpc, thus the seeing-limited observations could "wash-out" the small scale structure where $\Sigma_{\rm SFR}$ and outflows may be correlated.

Strength of $v_{\rm out}$-$\Sigma_{\rm SFR}$

A final consideration is the predicted strength of the $v_{\rm out}$-$\Sigma_{\rm SFR}$ relation. As discussed in Section 2.5.1, outflow velocity is predicted to scale as $v_{\rm out} \propto \Sigma_{\rm SFR}^{0.1}$ in the energy-driven case up to $v_{\rm out} \propto \Sigma_{\rm SFR}^{2}$ in the momentum-driven case.

While we do not find a correlation between outflow velocity and $\Sigma_{\rm SFR}$, here we investigate which case could be consistent with the observed $\Delta v_{\rm LIS}$-$\Sigma_{\rm SFR}$ correlation. Two samples of outflowing galaxies ($\Delta v_{\rm LIS} < 0$ km s^{-1}) are simulated following the predicted scaling relations of the energy- and momentum-driven cases over the dynamic range in $\Sigma_{\rm SFR}$ probed by the sample. Each value of $\Sigma_{\rm SFR}$ and $\Delta v_{\rm LIS}$ is perturbed assuming typical uncertainties of the measured values ($\sigma_{\Sigma_{\rm SFR}} = 0.1$ M$_\odot$ yr^{-1} kpc^{-2}, $\sigma_{v_{\rm LIS}} = 100$ km s^{-1}) and the intrinsic scatter in the observed $\Delta v_{\rm LIS}$-$\Sigma_{\rm SFR}$ relation ($\sigma_{\rm int} = 0.09$). This is repeated for 10,000 realizations in the energy- and momentum-driven cases. We find that none of the momentum-driven realizations yield a correlation as insignificant as the one that is observed, while 65% of the energy-driven realizations are $\leq 1.77\sigma$ correlated. These results suggest that the LRIS-flow sample more likely follows a weak relation as in the energy-driven case, rather than a steep relation predicted by the momentum-driven case. As outflow velocity is likely only weakly dependent on $\Sigma_{\rm SFR}$, a correlation between the two would require a large dynamic range in $\Sigma_{\rm SFR}$ to be observable. Our simulations imply that the small dynamic range of $\Sigma_{\rm SFR}$ of the LRIS-flow sample is likely responsible for the lack of an observed correlation between outflow velocity and $\Sigma_{\rm SFR}$.

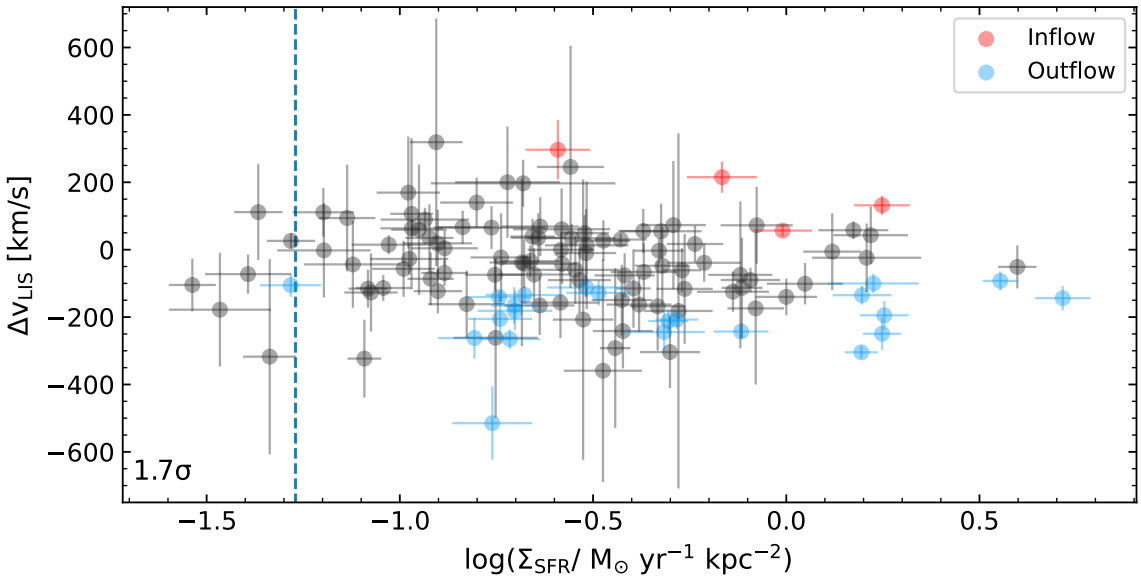

Figure 2.7: $\Delta v_{\rm LIS}$ vs $\log(\Sigma_{\rm SFR})$. Blue, red, and gray circles are galaxies with significant outflows, significant inflows, and non-significant flows, respectively. σ is the number of standard deviations from the null hypothesis that the quantities are uncorrelated, based on a Spearman rank correlation test. The dashed line marks the threshold $\Sigma_{\rm SFR}$ from Heckman (2002).

2.5.3 SFR Surface Density Threshold

Starting with McKee & Ostriker (1977), theoretical studies have long predicted that there exists a threshold $\Sigma_{\rm SFR}$ to launch galactic-scale outflows. Specifically, if the concentration of star formation is sufficiently high, then enough energy can be injected into surrounding gas allowing the gas to overcome its binding energy and escape the galaxy. Based on the $v_{\rm out}$-$\Sigma_{\rm SFR}$ relation observed in local starbursts galaxies, Heckman (2002) proposed a $\Sigma_{\rm SFR}$ threshold of ~ 0.1 ${\rm M}_\odot$ ${\rm yr}^{-1}$ ${\rm kpc}^{-2}$.

We investigated if the LRIS-flow sample supports this threshold. The Heckman (2002) threshold is $\sim$0.05 ${\rm M}_\odot$ ${\rm yr}^{-1}$ ${\rm kpc}^{-2}$ for the Chabrier (2003) IMF assumed here. As shown in Figure 2.7, nearly every significant outflowing galaxy exceeds the Heckman

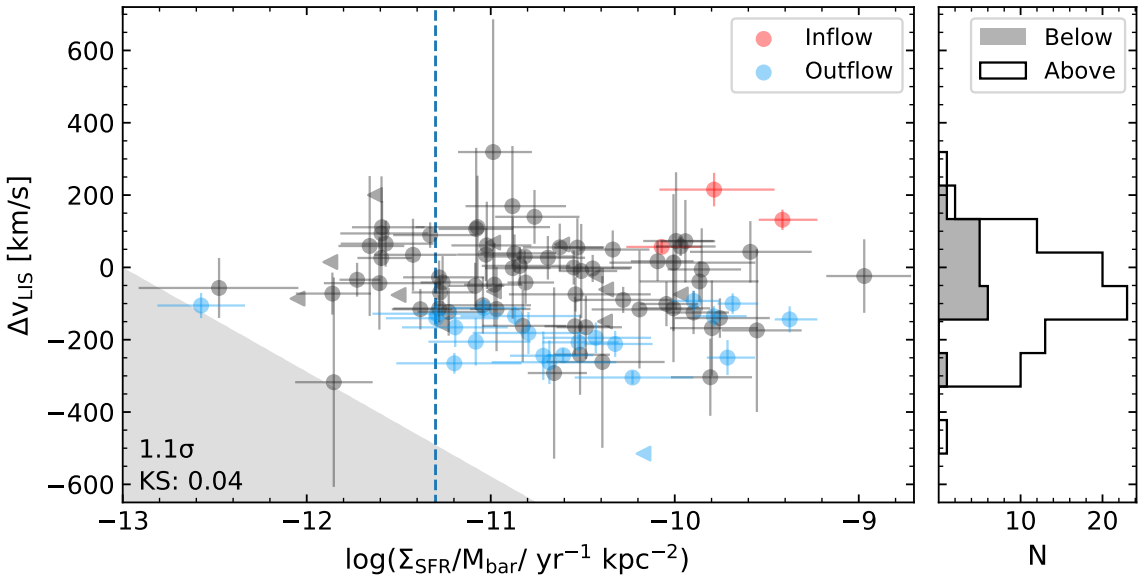

Figure 2.8: *Left*: $\Delta v_{\rm LIS}$ vs $\log(\Sigma_{\rm sSFR})$. Blue, red, and gray circles are galaxies with significant outflows, significant inflows, and non-significant flows, respectively. σ is the number of standard deviations from the null hypothesis that the quantities are uncorrelated, based on a Spearman rank correlation test. KS is the p-value of a Kolmogorov-Smirnov test (excluding significant inflowing galaxies) above and below $\log(\Sigma_{\rm sSFR}/{\rm yr}^{-1}\ {\rm kpc}^{-2}) = -11.3$, marked with a dashed line. *Right*: Distribution of outflow velocities below (gray) and above (black outline) $\log(\Sigma_{\rm sSFR}/{\rm yr}^{-1}\ {\rm kpc}^{-2}) = -11.3$.

(2002) threshold, with only one significant outflowing galaxy within the threshold given the measurement uncertainties. It is not surprising that our galaxies lie above this threshold, as the threshold itself is only approximate and the LRIS-flow sample does not probe to $\Sigma_{\rm SFR}$ significantly lower than the threshold. However, there is debate around the Heckman (2002) threshold, with some studies reporting galaxies with measurable outflow velocities down to $\sim 0.01\ {\rm M}_\odot\ {\rm yr}^{-1}\ {\rm kpc}^{-2}$ (Rubin et al., 2014; Chisholm et al., 2015; Roberts-Borsani et al., 2020).

In addition to $\Sigma_{\rm SFR}$, the mass of the galaxy, as a measure of the gravitational potential, may play an important role in launching outflows (e.g., Reddy et al., 2022). In this case, one might observe faster outflows in galaxies with a high $\Sigma_{\rm SFR}$ and low potential

(or mass). In Figure 2.8, nearly all of the galaxies with significant outflows have a high $\Sigma_{\rm sSFR}$, with only one found below $\log(\Sigma_{\rm sSFR}/{\rm yr}^{-1}\ {\rm kpc}^{-2}) = -11.3$. A Kolmogorov-Smirnov test (excluding the three galaxies with significant inflows) indicates a 4% probability that galaxies below and above this threshold are drawn from the same parent distribution. Thus, outflows may only become common for galaxies with $\log(\Sigma_{\rm sSFR}/{\rm yr}^{-1}\ {\rm kpc}^{-2}) > -11.3$, while below this outflows tend to be weak.[14] Above $\log(\Sigma_{\rm sSFR}/{\rm yr}^{-1}\ {\rm kpc}^{-2}) = -11.3$, outflow velocity appears to uncouple from $\Sigma_{\rm sSFR}$ suggestive of a limit in the maximum allowable outflow speed, probably tied to the Eddington limit from radiation pressure on dust grains (Murray et al., 2005; Thompson et al., 2005; Hopkins et al., 2010). This behaviour in $\Sigma_{\rm sSFR}$ is seen regardless of whether $\Sigma_{\rm SFR}$ is normalized by stellar, dynamical, or baryonic mass (see Figure 2.9).

2.6 Conclusions

We use a sample of 155 typical star-forming galaxies at redshifts $z = 1.42 - 3.48$ to investigate how outflows vary with a number of galactic properties (e.g., SFR, mass, $\Sigma_{\rm SFR}$, inclination, $\Sigma_{\rm sSFR}$). The sample includes deep optical and FUV spectra obtained with the MOSFIRE and the Keck/LRIS spectrographs providing spectral covering of several LIS absorption lines and Lyα emission. The combination of MOSFIRE and LRIS spectra allow us to study outflows on an individual galaxy basis. Centroid velocities are measured from the redshift difference between $z_{\rm sys}$, $z_{\rm LIS}$, and/or $z_{{\rm Ly}\alpha}$, while fractional (v_{80}) and maximum

[14] We note that the lack of galaxies in the lower left corner is unlikely due to selection effects. In the parent MOSDEF sample, about 8% of the sample has a $\Sigma_{\rm sSFR}$ below $\log(\Sigma_{\rm sSFR}/{\rm yr}^{-1}\ {\rm kpc}^{-2}) = -11.3$ (using the same definition of $\Sigma_{\rm sSFR}$ given in equation 2.2), which is very similar to the 7% of galaxies in the LRIS-flow sample.

($v_{\rm max}$) outflow velocities are measured from the blue wings of LIS lines that may better trace outflowing gas. The galaxies exhibit blueshifted absorption features with a mean outflow velocities of $\Delta v_{\rm LIS} = -60\pm10$ km s^{-1}, $v_{80} = -468\pm29$ km s^{-1}, $v_{\rm max} = -591\pm29$ km s^{-1}, and redshifted Lyα emission with a mean velocity of $\Delta v_{{\rm Ly}\alpha} = 400\pm23$ km s^{-1}. We combined SFRs from SED modeling, Hα SFRs, and masses with galaxy areas based on effective radii to measure $\Sigma_{\rm SFR}$ and $\Sigma_{\rm sSFR}$. Our main conclusions are as follows:

- We find marginal correlations between SFR[SED] and outflow velocities measured by $v_{\rm max}$ and $\Delta v_{{\rm Ly}\alpha}$, such that higher SFR[SED] galaxies appear to have gas at larger velocities than lower SFR[SED] galaxies (Section 2.4.1).

- Galaxies with significant outflows or inflows are found primarily at high inclinations ($i > 45°$). There appears to be no correlation between $v_{\rm out}$ and inclination, which may be due to the difficulty of measuring inclination for these galaxies, the lack of established disks, or large covering fractions of outflowing gas (Section 2.4.4).

- Outflow velocity scales as $v_{\rm max} \propto {\rm SFR[SED]}^{0.24\pm0.03}$. This scaling is in agreement with predictions for outflows driven by mechanical energy from supernovae, suggesting that supernovae are the primary driver of outflows in these $z \sim 2$ galaxies (Section 2.5.1). Radiation pressure acting on dusty material may play a minor role in the $v_{\rm max}$-SFR relation.

- Outflow velocity is not correlated with $\Sigma_{\rm SFR}$ or $\Sigma_{\rm sSFR}$, which may be due to limitations in the LRIS observations. After integrating along the entire line of sight, we lose vital spatial information about the absorbing gas. However, distant gas that has

uncoupled from changes in $\Sigma_{\rm SFR}$ likely only provides a minor contribution to the measured outflow velocity (Section 2.5.2). The LRIS observations are not resolved, limiting our study to global $\Sigma_{\rm SFR}$. Outflowing gas and $\Sigma_{\rm SFR}$ may be related on small spatial scales, such that any correlation between outflow velocity and global $\Sigma_{\rm SFR}$ disappears (Section 2.5.2). Simulations suggest that the $v_{\rm out}$-$\Sigma_{\rm SFR}$ relation follows a weak scaling, as predicted by the energy-driven case, thus the small dynamic range of $\Sigma_{\rm SFR}$ probed by the LRIS-flow sample is likely the contributing factor for the absence of an observed correlation between $v_{\rm out}$ and $\Sigma_{\rm SFR}$ (Section 2.5.2).

- Our sample agrees with the Heckman (2002) $\Sigma_{\rm SFR}$ threshold, and suggests a threshold in $\Sigma_{\rm sSFR}$ above which outflows are commonly detected. In the $v_{\rm out}$-$\Sigma_{\rm sSFR}$ relation, a KS-test indicates a 4% probability that galaxies below and above $\log(\Sigma_{\rm sSFR}/{\rm yr}^{-1}\ {\rm kpc}^{-2}) = -11.3$ are drawn from the same parent distribution. Above this threshold, strong outflows are common, however, there appears to be a limit in the maximum allowable outflow speed, resulting in an insignificant correlation between outflow speed and $\Sigma_{\rm sSFR}$ above the aforementioned threshold (Section 2.5.3).

Galactic-scale outflows are a critical component of the baryon cycle, influencing the environment and mass build-up of galaxies across cosmic time. Here, we have studied outflows in a large sample of $z \sim 2$ galaxies that push the limits of current ground-based facilities, with full night ($\sim$7.5 hrs) observations needed to obtain sufficiently high S/N spectra. We find that global galaxy properties and outflows are only weakly correlated and exhibit large scatter. However, outflows may be related to properties (e.g., $\Sigma_{\rm SFR}$) across larger dynamical ranges or on smaller kpc scales. To build a better understanding of

outflows, higher resolution spectroscopic data and spatially resolved imaging are necessary to constrain the geometry of outflowing gas. The increased sensitivity and field-of-view of the *James Webb Space Telescope* and next generation of 30-m class telescopes will enable observations of galaxies with lower masses, lower star-formation rates, and higher star-formation-rate surface densities, allowing for studies of galactic outflows across orders of magnitude in galaxy properties.

2.7 Appendix

Here we provide a table of statistical tests between $v_{\rm out}$ and the galaxy properties analyzed in this work (Table 2.7), and plots of $v_{\rm out}$ versus $\Sigma_{\rm SFR}$ and $\Sigma_{\rm sSFR}$ (Figure 2.9).

Attribute	Quantity	N	ρ_s	σ	P_s	KS	Attribute	Quantity	N	ρ_s	σ	P_s	KS
(1)	(2)	(3)	(4)	(5)	(6)	(7)	(1)	(2)	(3)	(4)	(5)	(6)	(7)
$\Delta v_{\rm LIS}$	log(SFR[SED])	147	-0.07	0.81	0.42	0.33	v_{80}	log(SFR[SED])	100	-0.18	1.84	0.07	0.19
	log(sSFR[Hα])	112	0.08	0.89	0.38	0.98		log(sSFR[Hα])	77	0.23	2.04	0.04	0.04
	log($M_\star$)	147	-0.07	0.78	0.43	0.94		log($M_\star$)	100	-0.20	1.90	0.06	0.40
	log($M_{\rm dyn}$)	129	0.07	0.76	0.45	0.12		log($M_{\rm dyn}$)	88	-0.07	0.67	0.51	0.94
	log($M_{\rm bar}$)	129	0.04	0.42	0.68	0.88		log($M_{\rm bar}$)	88	-0.03	0.31	0.75	0.81
	log($\Sigma_{\rm SFR[SED]}$)	119	-0.16	1.70	0.09	0.15		log($\Sigma_{\rm SFR[SED]}$)	79	-0.10	0.90	0.37	0.72
	log($\Sigma_{\rm SFR[H\alpha]}/M_\star$)	91	-0.05	0.49	0.62	0.67		log($\Sigma_{\rm SFR[H\alpha]}/M_\star$)	61	0.10	0.76	0.45	0.39
	log($\Sigma_{\rm SFR[H\alpha]}/M_{\rm dyn}$)	90	-0.10	0.95	0.34	0.33		log($\Sigma_{\rm SFR[H\alpha]}/M_{\rm dyn}$)	60	-0.01	0.08	0.94	0.60
	log($\Sigma_{\rm SFR[H\alpha]}/M_{\rm bar}$)	90	-0.12	1.13	0.26	0.22		log($\Sigma_{\rm SFR[H\alpha]}/M_{\rm bar}$)	60	0.02	0.12	0.90	0.96
	i	119	0.00	0.03	0.97	0.68		i	79	0.02	0.14	0.89	0.81
	$W_{\rm LIS}$	112	0.00	0.01	0.99	0.62		$W_{\rm LIS}$	75	0.23	1.97	0.05	0.08
	$\tau_{\rm LIS}$	145	0.07	0.86	0.39	0.27		$\tau_{\rm LIS}$	100	0.30	3.10	0.00	0.18
$v_{\rm max}$	log(SFR[SED])	100	-0.25	2.50	0.01	0.08		log(SFR[SED])	71	0.25	2.15	0.04	0.20
	log(sSFR[Hα])	77	0.08	0.65	0.52	0.24		log(sSFR[Hα])	52	0.12	0.85	0.40	0.31
	log($M_\star$)	100	-0.12	1.23	0.22	0.55		log($M_\star$)	71	0.11	0.90	0.37	0.41
	log($M_{\rm dyn}$)	88	-0.01	0.09	0.93	0.94		log($M_{\rm dyn}$)	62	0.11	0.82	0.41	0.08
	log($M_{\rm bar}$)	88	-0.04	0.37	0.71	0.84		log($M_{\rm bar}$)	62	0.22	1.76	0.06	0.15
	log($\Sigma_{\rm SFR[SED]}$)	79	-0.18	1.62	0.11	0.33		log($\Sigma_{\rm SFR[SED]}$)	53	0.05	0.34	0.74	0.43
	log($\Sigma_{\rm SFR[H\alpha]}/M_\star$)	61	-0.04	0.30	0.76	0.59		log($\Sigma_{\rm SFR[H\alpha]}/M_\star$)	38	0.11	0.67	0.51	0.98
	log($\Sigma_{\rm SFR[H\alpha]}/M_{\rm dyn}$)	60	-0.12	0.94	0.35	0.59		log($\Sigma_{\rm SFR[H\alpha]}/M_{\rm dyn}$)	37	0.08	0.50	0.62	0.92
	log($\Sigma_{\rm SFR[H\alpha]}/M_{\rm bar}$)	60	-0.10	0.76	0.45	0.96		log($\Sigma_{\rm SFR[H\alpha]}/M_{\rm bar}$)	37	0.04	0.21	0.84	0.92
	i	79	0.03	0.25	0.80	0.42		i	53	-0.02	0.12	0.90	0.26
	$W_{\rm LIS}$	75	0.14	1.20	0.23	0.35		$W_{\rm Ly\alpha}$	69	-0.40	3.53	0.00	0.03
	$\tau_{\rm LIS}$	100	0.33	3.49	0.00	0.07		$\tau_{\rm LIS}$	...	...	...	...	...
$W_{\rm LIS}$	log(SFR[SED])	112	-0.05	0.57	0.57	0.47	$W_{\rm Ly\alpha}$	log(SFR[SED])	69	-0.30	2.59	0.01	0.03
	log(sSFR[Hα])	88	-0.03	0.28	0.78	0.32		log(sSFR[Hα])	50	-0.03	0.19	0.85	0.99
	log($\Sigma_{\rm SFR[SED]}$)	90	-0.07	0.70	0.49	0.48		log($\Sigma_{\rm SFR[SED]}$)	51	0.01	0.09	0.93	0.70
	log($\Sigma_{\rm SFR[H\alpha]}/M_\star$)	70	-0.05	0.38	0.71	0.32		log($\Sigma_{\rm SFR[H\alpha]}/M_\star$)	36	-0.04	0.24	0.81	0.78
	log($\Sigma_{\rm SFR[H\alpha]}/M_{\rm dyn}$)	70	-0.08	0.67	0.50	0.20		log($\Sigma_{\rm SFR[H\alpha]}/M_{\rm dyn}$)	35	0.00	0.03	0.98	0.88
	log($\Sigma_{\rm SFR[H\alpha]}/M_{\rm bar}$)	70	-0.08	0.62	0.54	0.12		log($\Sigma_{\rm SFR[H\alpha]}/M_{\rm bar}$)	35	0.07	0.39	0.70	0.88
$\tau_{\rm LIS}$	log(SFR[SED])	145	0.10	1.24	0.22	0.04							
	log(sSFR[Hα])	110	0.03	0.27	0.79	0.46							
	log($\Sigma_{\rm SFR[SED]}$)	118	0.06	0.62	0.54	0.65							
	log($\Sigma_{\rm SFR[H\alpha]}/M_\star$)	90	0.04	0.39	0.70	0.48							
	log($\Sigma_{\rm SFR[H\alpha]}/M_{\rm dyn}$)	89	0.10	0.99	0.34	0.49							
	log($\Sigma_{\rm SFR[H\alpha]}/M_{\rm bar}$)	89	0.02	0.22	0.83	0.54							

(1): Attribute is galactic property on the y-axis, (2): Quantity is galactic property on the x-axis, (3) Number of galaxies used to evaluate the correlation, (4): Spearman rank correlation coefficient, (5): Number of standard deviations by which the correlation deviates from the null hypothesis of no correlation, (6): Spearman p-value, (7): Kolmogorov–Smirnov test p-value from dividing the galaxies into two groups, above and below the median Quantity, and testing against the Attribute.

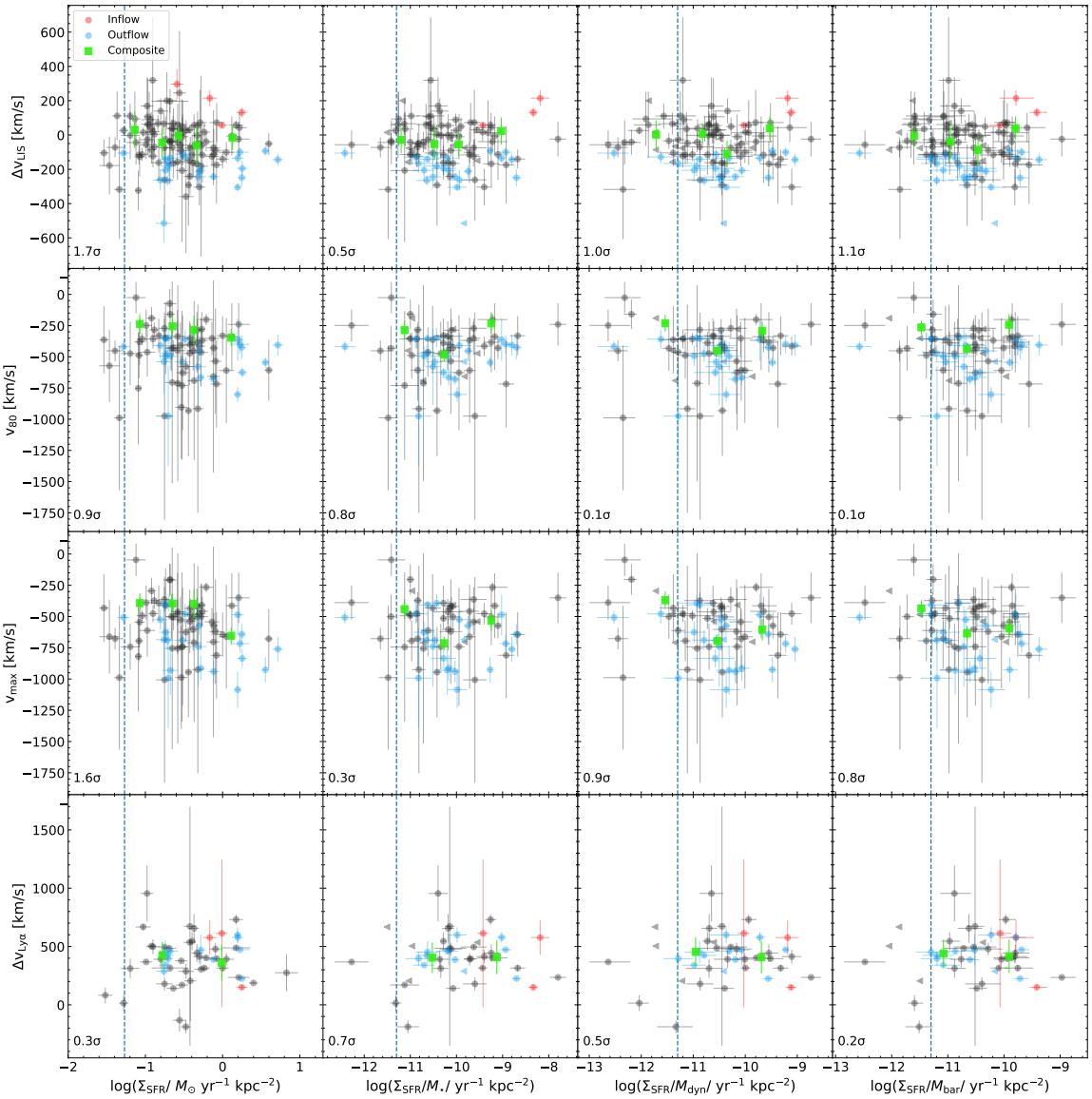
Inflow
Outflow
Composite
Δv_{LIS} [km/s]
v_{80} [km/s]
v_{max} [km/s]
$\Delta v_{Ly\alpha}$ [km/s]
1.7σ
0.5σ
1.0σ
1.1σ
0.9σ
0.8σ
0.1σ
0.1σ
1.6σ
0.3σ
0.9σ
0.8σ
0.3σ
0.7σ
0.5σ
0.2σ
log(Σ_{SFR}/ $M_\odot$ yr^{-1} kpc^{-2})
log(Σ_{SFR}/M_*/ yr^{-1} kpc^{-2})
log(Σ_{SFR}/M_{dyn}/ yr^{-1} kpc^{-2})
log(Σ_{SFR}/M_{bar}/ yr^{-1} kpc^{-2})

Figure 2.9: Plots of outflow velocity versus $\Sigma_{\rm SFR}$ and $\Sigma_{\rm sSFR}$. Blue, red, and gray circles represent galaxies with significant ($\Delta v_{\rm LIS}$ - $3\sigma_{\Delta v_{\rm LIS}} < 0$ km s^{-1}) outflows, significant ($\Delta v_{\rm LIS}$ - $3\sigma_{\Delta v_{\rm LIS}} > 0$ km s^{-1}) inflows, and non-significant flows, respectively. Triangles (in $\Sigma_{\rm sSFR}$ panels) are upper limits for galaxies without Hβ detections. Results from composite spectra are shown as green squares. In the lower left corners, σ is the number of standard deviations from the null hypothesis that the quantities are uncorrelated, based on a Spearman rank correlation test. For $\Sigma_{\rm SFR}$, the dashed line marks the threshold $\Sigma_{\rm SFR}$ from Heckman (2002). For $\Sigma_{\rm sSFR}$, the dashed line marks our proposed $\Sigma_{\rm sSFR}$ threshold; $\log(\Sigma_{\rm sSFR}/{\rm yr}^{-1}\ {\rm kpc}^{-2}) = -11.3$ (Section 2.5.3).

Chapter 3

The MOSDEF-LRIS Survey: Detection of Inflowing Gas Towards Three Star-forming Galaxies at $z \sim 2$[1]

Abstract We report on the discovery of cool gas inflows towards three star-forming galaxies at $\langle z \rangle \sim 2.30$. Analysis of Keck Low-Resolution Imaging Spectrometer spectroscopy reveals redshifted low-ionization interstellar (LIS) metal absorption lines with centroid velocities of 60 – 130 km s^{-1}. These inflows represent some of the most robust detections of inflowing gas into isolated, star-forming galaxies at high redshift. Our analysis suggests that the inflows are due to recycling metal-enriched gas from previous ejections. Comparisons

[1]A version of this chapter was published in Weldon et al. (2023)

between the galaxies with inflows and a larger parent sample of 131 objects indicate that galaxies with detected inflows may have higher specific star-formation rates (sSFR) and star-formation-rate surface densities ($\Sigma_{\rm SFR}$). However, when additional galaxies without robustly detected inflows based on centroid velocity but whose LIS absorption line profiles indicate large red-wing velocities are considered, galaxies with inflows do not show unique properties relative to those lacking inflows. Additionally, we calculate the covering fraction of cool inflowing gas as a function of red-wing inflow velocity, finding an enhancement in high sSFR binned galaxies, likely due to an increase in the amount of recycling gas. Together, these results suggest that the low detection rate of galaxies with cool inflows is primarily related to the viewing angle rather than the physical properties of the galaxies.

3.1 Introduction

A key mechanism for the growth of galaxies is the conversion of cold gas into stars. However, the gas reservoir around galaxies can only sustain their star-formation rates (SFR) for a few gigayears (Leroy et al., 2008; Saintonge et al., 2017; Tacconi et al., 2018). The accretion of pristine gas from the intergalactic medium (IGM) into galaxies is required to replenish their gas reservoirs throughout their evolution (Kennicutt, 1983; Prochaska & Wolfe, 2009; Bauermeister et al., 2010). The continuous accretion of metal-poor gas may also resolve the discrepancy between the number of low metallicity stars observed in the Milky Way and predictions from "closed-box" chemical evolution models, known as the G-Dwarf problem (van den Bergh, 1962; Schmidt, 1963; Sommer-Larsen, 1991). Additionally, cosmological simulations suggest that inflows of recycled gas from past outflows are the

dominant source of accretion at $z < 1$ (Oppenheimer et al., 2010; Henriques et al., 2013; Anglés-Alcázar et al., 2017). While inflows are commonly invoked to reconcile observations with theory, how gas accretes onto galaxies remains an open question, and is a top priority for astronomers in the coming decade (see priority area: Unveiling the Drivers of Galaxy Growth, The Astronomy and Astrophysics Decadal Survey, 2021).

The problem of gas accretion from the IGM into galaxies has been studied extensively by simulations. In the 'classical' theory of galaxy formation, cold gas from the IGM falls into a dark matter potential well, shock heats to the virial temperature of the dark matter halo, forming a hot, gas-pressure-supported atmosphere in quasi-hydrostatic equilibrium, which can then radiatively cool and fall to the halo center (Rees & Ostriker, 1977; Silk, 1977; White & Rees, 1978a). More recently, a new theoretical paradigm emerged in which infalling cold gas does not shock heat to the virial temperature of the dark matter halo (e.g., Kereš et al., 2005; Dekel & Birnboim, 2006; Faucher-Giguère et al., 2011). In this picture, galaxies in dark matter halos below $\sim 10^{12} M_{\odot}$ at any redshift freely accrete cold gas from the IGM via a "cold-mode", as the gas cooling times are shorter than the dynamical times. Once inside the dark matter halo, large-scale tidal torques can align the accreting gas with a pre-existing disk, forming a warped, extended "cold-flow disk" that co-rotates with the central disk (e.g., Stewart et al., 2011). Additionally, in massive halos ($M_{\rm halo} \gtrsim 10^{12} M_{\odot}$) at $z \gtrsim 2$, simulations predict that dense, collimated "cold-streams" of gas can penetrate the hot medium surrounding a massive galaxy and feed the central galaxy (e.g., Dekel & Birnboim, 2006; Dekel et al., 2009).

Although simulations suggest that the accretion of cold gas is crucial for the formation and evolution of galaxies, direct observational detections of such inflows are sparse. Fortuitously aligned galaxy–quasar pair studies indicate that gas traced by low-ionization interstellar (LIS) metal absorption lines appears to co-rotate with the host galaxy, which is interpreted as evidence of a "cold-flow disk" (Kacprzak et al., 2010; Bouché et al., 2013, 2016; Diamond-Stanic et al., 2016; Ho et al., 2019; Zabl et al., 2019). However, there are different possible origins for the gas that cause LIS absorption lines, such as outflows that can carry angular momentum when launched from a rotating disk, complicating the tracing of accretion by co-rotating LIS absorption lines. Recently, studies have shown evidence of accretion from cold filamentary streams into the center of massive halos at $z \sim 3$ (Daddi et al., 2021; Fu et al., 2021). Other studies, using down-the-barrel observations, have reported redshifted LIS metal absorption lines in ∼5% of star-forming galaxies at $z \sim 1$ (Rubin et al., 2012; Martin et al., 2012), similar to the small covering fractions predicted by simulations (e.g., Faucher-Giguère & Kereš, 2011; Fumagalli et al., 2011, 2014; Faucher-Giguère et al., 2015). At higher redshifts, $z \sim 2 - 4.5$, Calabrò et al. (2022) found redshifted LIS lines ($v > 0$ km s^{-1}) in 34% of their star-forming galaxies. However, the origin of inflowing gas in down-the-barrel observations is often ambiguous, as the gas must have moderate metallicity to give rise to the LIS absorption lines. The gas could be part of a filament of pristine, low-metallicity gas from the IGM that mixed with metal-enriched gas while moving through the circumgalactic medium (CGM) or the re-accretion of gas previously ejected from the galaxy.

The low detection rate of inflowing gas may be due to (1) the geometry of accretion, and/or (2) weak redshifted absorption line profiles. As simulations and observations have shown, the covering fraction of inflows is relatively small (Faucher-Giguère & Kereš, 2011; Faucher-Giguère et al., 2015). To be observable, a filament would need to be well aligned with the line of sight so that a strong absorption feature is produced. Additionally, inflows may be missed altogether due to weak or absent absorption lines if the filament has low metallicity or a small velocity such that outflows or bulk ISM motions dominate the absorption line profiles (Kimm et al., 2011).

In this paper, we report on the identification of three star-forming galaxies with observed inflows drawn from the MOSFIRE Deep Evolution Field (MOSDEF; Kriek et al., 2015) Survey, which have significant inflows based on LIS absorption lines measured from deep (∼7.5 hrs) rest-UV observations from the Keck Low Resolution Imaging Spectrometer (LRIS; Oke et al., 1995; Steidel et al., 2003). The primary objectives of this study are to (1) explore which, if any, galactic properties differ between galaxies with robust inflows and outflows; and (2) measure the covering fraction of inflowing gas as a function of redwing inflow velocity. The outline of this paper is as follows. Section 3.2 describes the MOSDEF survey, follow-up LRIS spectroscopy, stellar population models, and the approach for measuring inflow velocity and galaxy properties. In Section 3.3, we present our main results on the properties of the inflowing galaxies and discuss the implications in Section 3.4. The conclusions are summarized in Section 3.5. Throughout this paper, we adopt a standard cosmology with $\Omega_\Lambda = 0.7$, $\Omega_M = 0.3$, and $H_0 = 70$ km s^{-1}Mpc^{-1}. All wavelengths are presented in the vacuum frame.

3.2 Data and Measurements

3.2.1 MOSDEF Survey

The galaxies presented in this paper were drawn from the MOSDEF Survey, which targeted ≈1500 H-band selected galaxies and AGNs at redshifts $1.4 \leq z \leq 3.8$. The survey obtained moderate-resolution ($R \sim 3000-3600$) near-infrared spectra using the Multi-Object Spectrometer for Infra-Red Exploration (MOSFIRE; McLean et al., 2012a) spectrograph over 48.5 nights between 2012 – 2016. Galaxies were targeted for spectroscopy based on pre-existing spectroscopic, grism, or photometric redshifts that placed them in three redshift ranges ($z = 1.37$ – 1.70, $z = 2.09$ – 2.61, and $z = 2.95$ – 3.80) where strong rest-frame optical emission lines (e.g., Hβ, [O III], Hα, [N II]) lie in the $YJHK$ transmission windows. For full details regarding the MOSDEF survey (targeting, data reduction, and sample properties), we refer readers to Kriek et al. (2015).

Emission-line fluxes were measured by simultaneously fitting a line with the best-fit SED model for the continuum and a Gaussian function (see Reddy et al. (2022) for a complete description of the SED modeling). For multiple lines that lie in close proximity, multiple Gaussians were fit, such as the [O II] doublet and Hα and the [N II] doublet, which were fitted with two and three Gaussians, respectively. Systemic redshifts were derived from the strongest emission line, usually Hα or [O III]λ5008, and were used to fit the other rest-frame optical nebular emission lines. Further details on emission-line measurements and slit loss corrections are given in Kriek et al. (2015) and Reddy et al. (2015).

Galaxy sizes and inclinations were estimated from the effective radius ($R_{\rm E}$), within which half the total light of the galaxy is contained, and the axis ratio (b/a), respectively,

measured by van der Wel et al. (2014)[2] using GALFIT (Peng et al., 2010) on HST/F160W images from the CANDELS survey.

3.2.2 MOSDEF-LRIS Spectroscopy

In this study, we use a subset of galaxies drawn from the MOSDEF survey with follow-up rest-frame UV spectroscopy, which provides coverage of absorption and emission features from diffuse circumgalactic gas (e.g., Lyα, Si II, O I, C II). Here, we present an overview of the sample and refer readers to Topping et al. (2020) and Reddy et al. (2022) for more details on the sample selection, data collection, and reduction. Objects for follow-up LRIS spectroscopy were prioritized based on strong detections of rest-optical emission lines (Hβ, [O III], Hα, and [N II]), with higher priority given to objects with confirmed spectroscopic redshift at $1.90 \leq z \leq 2.65$. Additional objects were selected in the following order of priority: objects with Hα, Hβ, and [O III] detected at $\geq 3\sigma$ and an upper limit on [N II]; objects with a confirmed systemic redshift from MOSDEF; objects observed as part of the MOSDEF survey without a successful systemic redshift measurement, but with a prior spectroscopic or photometric redshift; and finally, objects not observed with MOSFIRE, but with a prior redshift from the 3D-HST survey that placed them within the redshift ranges and magnitude limit of the MOSDEF survey.

Observations were performed over nine nights in 2017 and 2018 in the COSMOS, GOODS-S, GOODS-N, and AEGIS fields using nine multi-object slit masks milled with 1$''$.2 slits. The instrumental setup included a dichroic to split the incoming beam at ∼5000 Å into

[2] https://users.ugent.be/~avdrwel/research.html

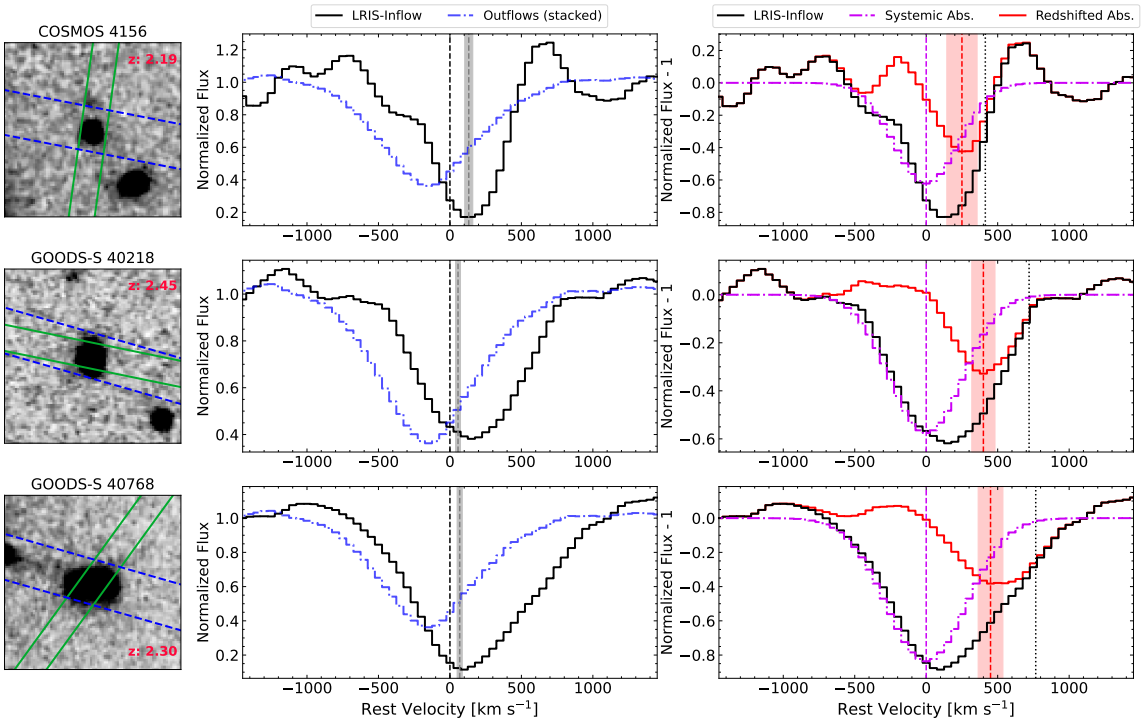

Figure 3.1: The three galaxies with significantly measured inflows. *Left*: F160W HST images. Each image is 4.″8 on a side, which corresponds to an angular distance of 39 kpc at $z = 2.3$, and oriented such that North is up and East is left. The solid green and dashed blue outlines represent the MOSDEF and LRIS slit placements, respectively. *Center*: Comparison between the composite LIS metal absorption line profiles of the three inflow galaxies and a stack of 29 outflow galaxies ($\Delta v_{\rm LIS} + 3\sigma_{v_{\Delta_{\rm LIS}}} < 0$ km s^{-1}) as solid black and blue dot-dashed lines, respectively. The centroid velocity ($\Delta v_{\rm LIS}$) is marked with a dashed vertical line. The dark grey shaded region marks the 1σ confidence interval. *Right*: Decomposition of absoprtion line profile into symmetric, interstellar absorption (purple dashed Gaussian) and inflow absorption (solid red line) components, discussed in Section 3.2.5. The centroid velocity of the inflow component is marked with a red dashed vertical line. The red shaded region marks the 1σ confidence interval. For comparison, the dotted line marks the maximum red-wing velocity (see Section 3.2.4).

the blue and red arms of LRIS. We configured the blue side with the 400 lines/mm grism, and the red side with the 600 lines/mm grating. This configuration provided continuous spectral coverage from the atmospheric cut-off at 3100Å up to a typical wavelength of ∼7000Å, depending on the position of the slit within the spectroscopic field of view. The seeing ranged from 0.″6 to 1.″2 with a typical value of 0.″8. The rest-frame spectra were continuum normalized around each LIS absorption line. The local continuum was determined by fitting a linear function between the average flux in two spectral windows, bluewards and redwards of the LIS absorption line. The spectral windows, listed in Table 3.1, were chosen to bracket the line and exclude other spectral features.

3.2.3 Sample Selection

Several criteria were applied to the parent MOSDEF-LRIS sample to create a sample with robust systemic ($z_{\rm sys}$) and LIS absorption line redshifts ($z_{\rm LIS}$) for our analysis. We select objects with secure systemic redshifts from MOSDEF spectroscopy. Specifically, objects must have more than one emission line with an integrated line flux with S/N $\geq$ 2. Next, any objects for which the LRIS spectra contained irreparable artifacts that were too noisy to yield a robust absorption-line redshift were removed. Active galactic nuclei (AGNs) identified by IR colors, X-ray emission, and/or the [N II]/Hα line ratio were removed (Coil et al., 2015; Azadi et al., 2017, 2018; Leung et al., 2019). Finally, objects for which the MOSFIRE or LRIS spectra indicate that the target may be blended with a foreground object were removed.

These criteria result in a final sample of 134 galaxies, of which 39 galaxies (29%) exhibit redshifted LIS metal absorption lines. For our inflow analysis, galaxies that have red-

shifted absorption lines with centroids statistically consistent with being redshifted ($\Delta v_{\rm LIS}$ - $3\sigma_{v_{\Delta_{\rm LIS}}} > 0$ km s^{-1}, see Section 3.2.4) are considered to have inflowing gas, reducing the sample to three galaxies (hereafter the "LRIS-Inflow" sample). Similarly, 29 galaxies have blueshifted centroids ($\Delta v_{\rm LIS} + 3\sigma_{v_{\Delta_{\rm LIS}}} < 0$ km s^{-1}) indicating outflowing gas. Figure 3.1 presents images, composite and decomposed (see Section 3.2.5) LIS absorption line profiles of the LRIS-Inflow galaxies. Figure 3.7 presents individual optical emission and LIS absorption lines of the LRIS-Inflow galaxies.

As the absorption line centroids reflect the overall velocity distribution of the gas, galaxies may have a large amount of inflowing gas masked by more prevalent outflowing gas or gas at zero systemic velocity. To increase the sample size of "inflowing" galaxies, we consider galaxies whose LIS absorption line profiles are skewed redward, indicating a large fraction of inflowing gas, see Figure 3.2. We define a Skewness Ratio (Vasan G. C. et al., 2022)[3] as

$$\text{Skewness Ratio} = \left| \frac{v_{\rm max,blue}}{v_{\rm max,red}} \right| - 1, \tag{3.1}$$

where $v_{\rm max,blue}$ and $v_{\rm max,red}$ are the outflow and inflow and velocity at 100% of the continuum (Section 3.2.4). A negative Skewness Ratio indicates that the red-wing is more extended than the blue-wing. Galaxies with Skewness Ratio + $2\sigma_{\text{Skewness Ratio}} < 0$ and $v_{\rm max,red} - v_{\rm max,blue} > 300$ km s^{-1}, corresponding to the velocity resolution of the LRIS observations, are added to the LRIS-Inflow sample to create a second, larger sample of galaxies with

[3]The Skewness Ratio presented in this study measures the skewness of the absorption line profile with respect to 0 km s^{-1}, as oppose to Vasan G. C. et al. (2022) which measures skewness with respect to the centroid velocity.

inflowing gas. We adopt these thresholds because they are rather conservative, such that the selected galaxies likely have a substantial amount of inflowing gas.

3.2.4 Velocity Measurements

Using systemic redshifts and LIS absorption line redshifts, we measured centroid velocities from the redshift difference:

$$\Delta v_{\rm LIS} = \frac{c(z_{\rm LIS} - z_{\rm sys})}{1 + z_{\rm sys}}, \tag{3.2}$$

where $z_{\rm LIS}$ is taken from Topping et al. (2020). Briefly, $z_{\rm LIS}$ was obtained by fitting the absorption lines with Gaussian functions and a quadratic function for the local continuum, then determining the centroids of the Gaussians. Uncertainties were determined by perturbing the LRIS spectra by the corresponding error spectra, refitting the lines, and recalculating the centroids. Any LIS absorption lines with poor fits were excluded in the calculation of the average $z_{\rm LIS}$, which is typically based on two lines for a given galaxy. The uncertainties of the centroid velocities ($\sigma_{v_{\Delta_{\rm LIS}}}$) are taken as the standard deviation of many realizations after perturbing $z_{\rm sys}$ and $z_{\rm LIS}$ by their corresponding errors and recalculating $\Delta v_{\rm LIS}$.

In addition to centroid velocities, another technique for estimating velocities uses the wings of the absorption line profile. In the down-barrel-observations, $\Delta v_{\rm LIS}$ represents the sum of all outflowing, inflowing, and interstellar gas at or near $z_{\rm sys}$. Gas near the systemic redshift will naturally shift the centroid towards zero systemic velocity. To better estimate the velocity of inflowing (outflowing) gas, we consider the red (blue) wings of

the absorption line profiles. Previous outflow studies have either used the velocity where the absorption feature reaches some percent of the continuum level (Martin, 2005; Weiner et al., 2009; Chisholm et al., 2015; Du et al., 2016; Weldon et al., 2022) or the maximum velocity where the absorption feature returns to the continuum level (Steidel et al., 2010; Kornei et al., 2012; Rubin et al., 2014; Weldon et al., 2022). We measure the inflow and outflow velocity at 80% ($v_{80,\mathrm{red}}$, $v_{80,\mathrm{blue}}$) and 100% ($v_{\mathrm{max,red}}$, $v_{\mathrm{max,blue}}$) of the continuum following a similar approach as Kornei et al. (2012) and Weldon et al. (2022). Using the normalized spectra, we identify the absolute minimum of a detected absorption feature, then move towards longer (v_{red}) or shorter (v_{blue}) wavelengths, checking the sum of the flux and its uncertainty at each wavelength step. We record the first wavelengths at which this sum exceeds 0.8 and 1.0, for v_{80} and v_{max}, respectively, perturb the spectrum by its error spectrum and repeat the same procedure many times. The average and standard deviation, after 3σ clipping, of the trials are then used to calculate v_{80}, v_{max}, and their uncertainties. This entire process was repeated for each detected LIS feature, listed in Table 3.1, adopting v_{80} and v_{max} as the average of the detected LIS features. For the 134 galaxies, $v_{80,\mathrm{red}}$ ($v_{\mathrm{max,red}}$) ranges from -228 to 662 km s^{-1} (-218 to 766 km s^{-1}) with a mean of 200$\pm$150 km s^{-1} (300$\pm$188 km s^{-1}). For the LRIS-Inflow galaxies, $v_{80,\mathrm{red}}$ ($v_{\mathrm{max,red}}$) ranges from 328 to 662 km s^{-1} (413 to 766 km s^{-1}) with a mean of 525$\pm$143 km s^{-1} (720$\pm$156 km s^{-1}).

3.2.5 Decomposition into Symmetric and Redshifted Absorption

A complementary approach to isolate the inflowing gas is to separate its absorption from the intrinsic absorption of interstellar gas. In the down-barrel-observations, the LIS

Table 3.1: Spectral Windows

Line	$\lambda_{\rm rest}$ (Å)[a]	Blue Window (Å)[b]	Red Window (Å)[b]
Lyα	1215.67	1195 - 1202	1225 - 1235
Si II	1260.42	1245 - 1252	1270 - 1275
O II + Si II	1303.27	1285 - 1293	1312 - 1318
C II	1334.53	1320 - 1330	1342 - 1351
Si II	1526.71	1512 - 1520	1535 - 1540

[a] Rest-frame vacuum wavelength, taken from the Atomic Spectra Database website of the National Institute of Standards and Technology (NIST; Kramida et al., 2022).
[b] Wavelength window over which continuum fitting was performed.

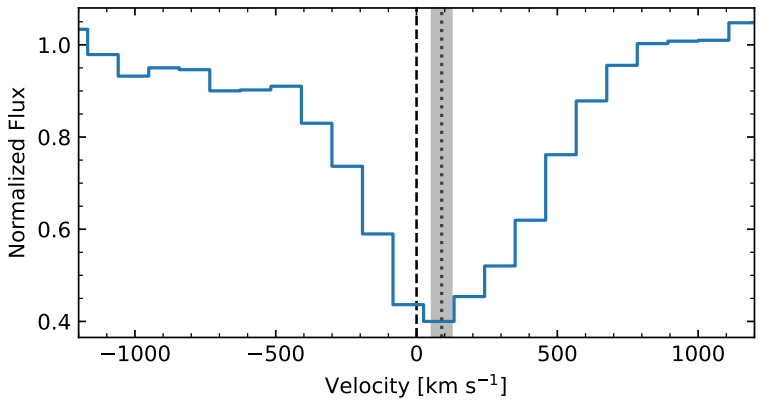

Figure 3.2: Average LIS metal absorption profile of GOODS-N 24328. An example of a galaxy with a negatively skewed profile (Skewness Ratio = -0.47±0.17) added to the LRIS-Inflow galaxies to create a larger "inflow" subsample. The centroid velocity ($\Delta v_{\rm LIS}$) is marked with a dotted vertical line. The dark grey shaded region marks the 1σ confidence on the centroid velocity.

metal absorption lines probe the velocity of gas seen along the line of sight towards a galaxy. Interstellar gas within the galaxy will absorb close to the systemic redshift (i.e., $v \sim 0$ km s^{-1}) with a velocity range set by the galactic rotation curve and velocity dispersion. Inflowing gas gives rise to redshifted absorption (at $v > 0$ km s^{-1}), while outflowing gas produces blueshifted absorption ($v < 0$ km s^{-1}). In principle, the redshifted (blueshifted) absorption is a mixture of interstellar and inflowing (outflowing) absorption. However, without detections of driven outflows from the LRIS-Inflow galaxies, it is difficult to separate outflowing gas from the blue-wing of interstellar absorption. To determine properties of the inflowing gas, we attempt to separate it from the systemic, interstellar gas by adopting a simple three-component model:

$$F_{\rm obs} = C(\lambda) + A_{\rm sys} + A_{\rm inflow}, \tag{3.3}$$

where $F_{\rm obs}$ is the observed flux density, C(λ) is the underlying linear continuum of the galaxy, $A_{\rm sys}$ is the systemic absorption from interstellar gas at or near $z_{\rm sys}$, and $A_{\rm inflow}$ is the absorption from inflowing gas.

We begin by creating a composite LIS absorption line profile. For each galaxy, the flux and error around each detected LIS line are interpolated onto a common velocity grid. The composite flux is then taken as the average flux of the detected lines, and the error is estimated by adding the error of the lines in quadrature. For the decomposition, we perform two preliminary fits and one final fit. The first preliminary fit uses a linear continuum with a Gaussian to fit the absorption profile using `curve fit`, a non-linear least squares fitting routine from the `scipy.optimize` subpackage. We use this fit to divide the

composite spectra by a linear continuum, normalising the spectrum to 1. Next, we fit a Gaussian for the systemic absorption to the blue-side of $F_{\rm obs}/{\rm C} - 1$, using only the pixels at $-1600 < {\rm v} < 0$ km s^{-1}. The free parameters are a constant continuum level, absorption intensity, and velocity dispersion; the central velocity is held fixed at 0 km s^{-1}. We use the resulting values and errors of this second fit as initial values for the final fit, which is done using `emcee`, a Python Markov chain Monte Carlo (MCMC) ensemble sampler. Finally, we subtract the systemic absorption from the normalized spectra to obtain the redshifted absorption of the inflowing gas.

The right panels of Figure 3.1 show the decomposition applied to LRIS-Inflow galaxies. The centroid velocity of the inflowing gas ($v_{\rm cen,red}$; red dashed line) is measured at the absolute minimum of the redshifted absorption component, and its error is estimated by perturbing the composite profile by its error, and repeating the decomposition many times. The velocity of the inflow absorption presents an intermediate case between the centroid of the observed profile and maximum red-wing velocity.

3.2.6 Galaxy Properties

In this study, we analyze several of the global galaxy properties (e.g., SFR, mass, star-formation-rate surface density, inclination) discussed in Weldon et al. (2022). Here, we briefly summarize the measurements and refer readers to Weldon et al. (2022) for more details. Stellar masses ($M_\star$) and SFRs were derived from spectral energy distribution (SED) modeling, adopting a Bruzual & Charlot (2003a, hereafter BC03) stellar population synthesis model, Chabrier (2003) initial mass function, constant star formation histories (SFH), Small Magellanic Cloud (SMC) attenuation curve (Fitzpatrick & Massa, 1990; Gordon et al.,

2003), and sub-solar metallicity ($Z_* = 0.28 Z_\odot$).[4] The sample has a stellar mass range of $8.6 < \log(M_\star/M_\odot) < 10.9$ with a median $\log(M_\star/M_\odot)$ of 9.9 and SFR range from 0.32 $< \log(\mathrm{SFR}/M_\odot\ \mathrm{yr}^{-1}) < 1.97$ with a median $\log(\mathrm{SFR}/M_\odot\ \mathrm{yr}^{-1})$ of 0.93. In addition, dynamical ($M_{\rm dyn}$) and baryonic mass ($M_{\rm bar} = M_{\rm dyn} + M_{\rm gas}$) were calculated following the procedure of Price et al. (2020). Dynamical masses were derived using circular velocities measured from 2D spectra with detected rotation or inferred using integrated velocity dispersions and the best-fit ensemble V/σ from galaxies without detected rotation, while $M_{\rm gas}$ was estimated from the Schmidt-Kennicutt (Kennicutt, 1989) relation between $\Sigma_{\rm SFR}$ and $\Sigma_{\rm gas}$.

Absorption-line studies indicate that outflows are ubiquitous in $z > 2$ star-forming galaxies (e.g., Shapley et al., 2003; Steidel et al., 2010). Observations suggest that outflow velocity increases with the SFR and star-formation-rate surface density ($\Sigma_{\rm SFR}$) of a galaxy (e.g., see Weldon et al., 2022, and references therein). This result implies that detectable inflowing gas may only occur in galaxies with low SFRs or $\Sigma_{\rm SFR}$ when outflows would be weak or absent. We have chosen to focus on SFR[SED] when discussing SFR as of the 134 galaxies 23% lack significant Hα and/or Hβ detections. However, as the SFR[SED] is tightly correlated with stellar mass (i.e., both quantities are sensitive to the normalization of the best-fit SED), Hα SFRs are used to calculate specific SFR (sSFR), using the conversion factor from Reddy et al. (2018b) for a BC03 stellar population synthesis model and sub-

[4] A steep SMC-like attenuation curve and sub-solar metallicities have been found to provide self-consistent SFRs with those derived using other methods (Reddy et al., 2018b, 2022). However, other studies have suggested that a Calzetti et al. (2000) attenuation curve and solar metallicity provide a better description for high-mass ($\log(M_\star/M_\odot) \geq 10.04$) star-forming galaxies at $z \sim 2$ (Reddy et al., 2018a; Shivaei et al., 2020). If instead we assume a Calzetti et al. (2000) attenuation curve and solar metallicities for high-mass galaxies, on average, stellar masses are 0.06 dex higher and SFRs are 0.4 dex higher. Our main results do not significantly change if we were to alter the assumed attenuation curve.

solar metallicity adopted for the SED fitting. The star-formation-rate surface density is then defined as $\Sigma_{\rm SFR} = {\rm SFR[SED]}/(2\pi R_{\rm E}^2)$. Additionally, at a given SFR, outflows may be more effectively launched from a shallow galaxy potential (i.e., low stellar, dynamical, and/or baryonic mass) relative to a deep potential (Reddy et al., 2022). To examine the frequency of galaxies with observed inflows on both $\Sigma_{\rm SFR}$ and the galaxy potential, we define the specific star-formation-rate surface density ($\Sigma_{\rm sSFR}$) as $\Sigma_{\rm sSFR} = {\rm SFR[H}\alpha{\rm]}/(2\pi R_{\rm E}^2 M_X)$, where M_X is the stellar, dynamical, or baryonic mass.

3.3 Properties of Inflowing Galaxies

In this section, we compare the properties of the three LRIS-Inflow galaxies to those of the remaining LRIS galaxies. Of particular interest is whether the star-formation activity or inclination of the two groups differ significantly. In typical star-forming galaxies, inflows are theorized to enter along the major axis, either as part of a filament or "cold-flow disk", while outflows emerge perpendicular to the disk in a biconical structure (e.g., Katz & White, 1993; Bordoloi et al., 2011; Stewart et al., 2011; Bouché et al., 2012; Kacprzak et al., 2012). On the other hand, outflows are theorized to be driven by energy injected into the ISM by supernovae; radiation pressure acting on cool, dusty material; cosmic rays; or a combination of these mechanisms (Ipavich, 1975; Chevalier & Clegg, 1985; Murray et al., 2005, 2011). As galactic outflows are a common feature of actively star-forming galaxies (e.g., Shapley et al., 2003; Steidel et al., 2010; Weldon et al., 2022), observable inflows may be biased towards edge-on galaxies with low star-formation rates, where inflows could potentially dominate over outflows.

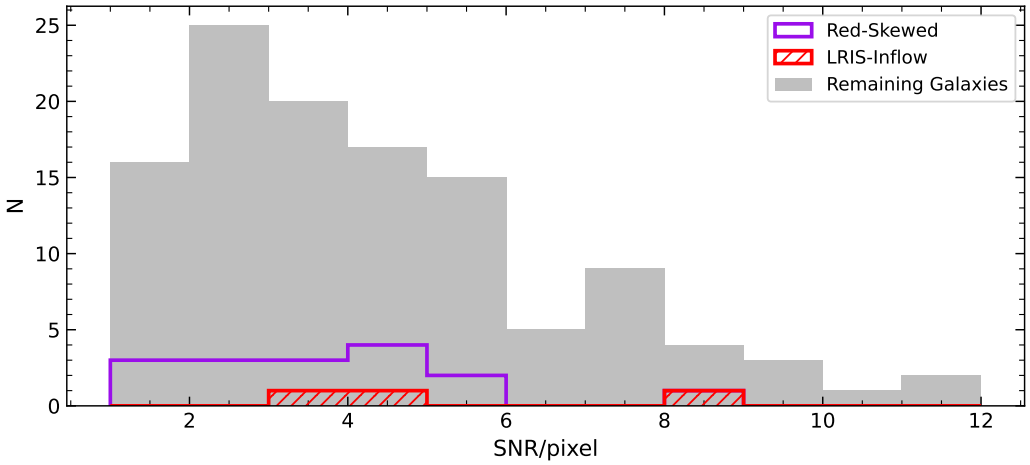

Figure 3.3: Distribution of UV continuum signal-to-noise ratio (SNR) per pixel over the wavelength range 1425Å $\leq \lambda \leq$ 1500Å. Hashed red, open purple, and solid grey bars represent inflowing, redward-skewed, and remaining galaxies, respectively. Neither the LRIS-Inflow nor red-skewed galaxies appear biased towards higher SNRs, suggesting that the SNR does not play a significant role in whether their properties differ from the remaining galaxies.

The detection of LIS metal absorption lines shifted away from systemic redshift requires a high signal-to-noise ratio (SNR) in the UV continuum. However, galaxies with high SNR are also associated with a high SFR. Therefore, it is important to check whether the three LRIS-inflow galaxies may be biased towards higher SFRs relative to the underlying sample. To investigate this possibility, we calculate the SNR per pixel over the wavelength range 1425Å $\leq \lambda \leq$ 1500Å. As shown in Figure 3.3, neither the LRIS-Inflow (red-hashed) nor the red-skewed (open purple) galaxies are biased toward high SNRs. The SNR of the continuum does not appear to play a significant role in whether the properties of these subsamples differ from the remaining galaxies.

For each property (e.g., SFR, mass, $\Sigma_{\rm SFR}$, inclination), we investigate whether the LRIS-Inflow galaxies have unique properties compared to the remaining galaxies. As shown in Figure 3.4, the LRIS-Inflow galaxies appear to have higher sSFR and $\Sigma_{\rm SFR}$ relative to the

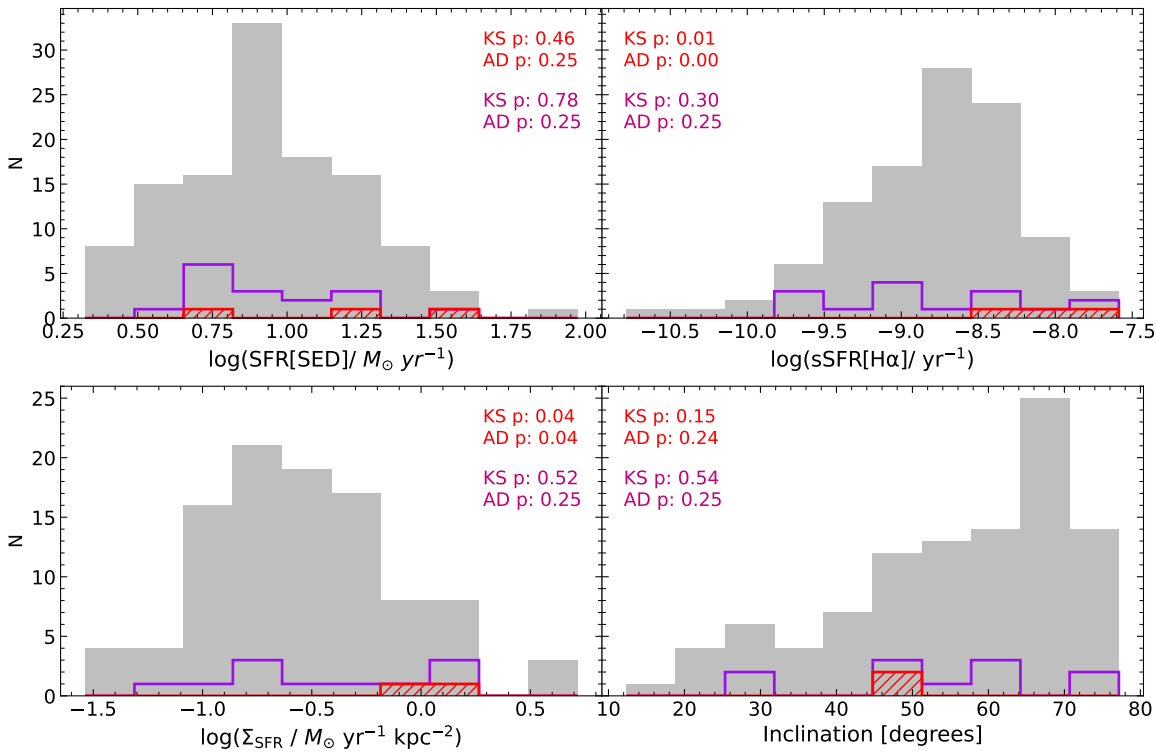

Figure 3.4: The distribution of various galactic properties, with the same style as Figure 3.3. *top left*: log(SFR), *top right*: log(sSFR), *bottom left*: log($\Sigma_{\rm SFR}$), *bottom right*: Inclination. The p-values of the KS and AD tests between the inflowing and remaining galaxies (red) and inflowing, redward-skewed and remaining galaxies (magenta) are shown in the upper corners of each panel. Of the three inflowing galaxies, one does not have a robust $R_{\rm E}$ limiting our analysis to two inflowing galaxies for $\Sigma_{\rm SFR}$ and inclination.

full sample, suggesting that both SFR and the gravitational potential well of a galaxy may be important factors in determining the visibility of inflows. To quantitatively test whether the LRIS-Inflow galaxies are drawn from the same parent distribution as the remaining galaxies, we perform a Kolmogorov–Smirnov (KS) and Anderson-Darling (AD) test. While these statistical tests are similar, the AD test is more sensitive to the tails of the distributions than the KS test, which makes it a more powerful statistic when dealing with small sample sizes (Hou et al., 2009).

Of the properties investigated, both the KS and AD tests indicate a <5% probability that the sSFR and $\Sigma_{\rm SFR}$ of the LRIS-Inflow and remaining galaxies are drawn from the same distribution. On the other hand, the LRIS-Inflow galaxies have moderate ($\sim$45°) inclinations. In part, these inclinations may reflect the lack of thin disks and/or the difficulty of measuring structural properties robustly for high redshift galaxies. The simple picture of biconical outflows along the minor axis and inflows along the major axis may not be applicable for galaxies without established disks. Rather, such galaxies may be fed primarily by filamentary inflows that enter at random angles, resulting in no significant relation between galaxy inclination and the detection of inflows. However, we caution that these results are based on a small number of galaxies.[5]

To extend this analysis towards larger samples, we perform KS and AD tests on the distribution of properties between the inflowing galaxies, redward-skewed galaxies (Section 3.2.3) and the remaining galaxies. The tests indicate that all of the properties investigated are statistically consistent with having been drawn from the same parent distributions.

[5]One LRIS-Inflow galaxy does not have a robust $R_{\rm E}$ limiting our analysis to two inflowing galaxies for $\Sigma_{\rm SFR}$ and inclination.

Table 3.2: Inflow Velocities

Field	V4ID	$\log(M_{\rm halo}/M_\odot)$	$\log(M_\star/M_\odot)$	$v_{\rm cen,red}$[a] [km s^{-1}]	$v_{\rm max,red}$[b] [km s^{-1}]	$V_{\rm stream}$[c] [km s^{-1}]
COSMOS	4156	11.53±0.07	9.11±0.04	250±100	413±51	98±11
GOODS-S	40218	11.90±0.09	9.79±0.04	400±80	720±36	145±13
GOODS-S	40768	12.06±0.06	10.09±0.01	450±87	766±61	158±11

[a] Centroid velocity of the inflowing gas (See Section 3.2.5).
[b] Maximum inflow velocity (See Section 3.2.4).
[c] Cold stream inflow velocity

Given the lack of significantly different properties with this larger subsample, we suggest that the detection of inflowing gas is likely dependent on the geometry and covering fraction of the inflowing gas into a host galaxy's potential well rather than the particular physical properties of the host galaxy. In the next section, we explore the accretion geometry of the galaxies.

3.4 Discussion

3.4.1 Comparison to Simulations

We report on three star-forming galaxies at $\langle z \rangle \sim 2.3$, whose spectra show redshifted LIS metal absorption lines. As these detections were made using LIS metal lines, they likely trace relatively metal-enriched gas rather than pristine gas accreting from the IGM for the first-time. The origin of this gas could be the re-accretion of gas previously ejected from the galaxy or gas-rich satellite dwarf galaxies being stripped and accreted onto the central galaxy. Several cosmological simulations have investigated the origin of gas accreted onto galaxies by considering pristine inflows, recycling gas, and interactions with satellite galaxies (e.g., Anglés-Alcázar et al., 2017; Grand et al., 2019; Mitchell et al., 2020).

While simulations disagree on the relative contributions to total gas accretion, they have found that pristine inflows (Mitchell et al., 2020) or gas recycling (Anglés-Alcázar et al., 2017) dominate the total accretion at $z \sim 2$, with satellite mergers and stripping contributing a non-trivial but minor amount. Without evidence of dwarf satellite galaxies in HST imaging, we adopt the interpretation that the redshifted LIS lines are evidence of the re-accretion of gas previously ejected from the galaxy. However, the LIS absorption lines may also arise from filamentary inflows from the IGM. Several studies have shown that the circumgalactic medium (CGM) has a complex, multiphase structure in which metal-enriched gas may be distributed throughout (e.g., Tumlinson et al., 2017; Pointon et al., 2019). As pristine gas from the IGM moves through the CGM, it may mix with enriched gas before accreting onto the galactic disk, thus giving rise to the LIS absorption lines (Faucher-Giguère et al., 2015). However, the efficiency of mixing in the CGM remains highly uncertain and requires high-resolution simulations to properly resolve the small-scales where this mixing would take place.

To investigate the origin of the inflowing gas in the LRIS-Inflow galaxies, we compared their redshifted centroid velocities and maximum red-wing inflow velocities to their predicted circular halo velocities ($V_{\rm circ,halo}$). Cosmological simulations suggest that the average radial inflow velocity of filamentary streams is between $0.5V_{\rm circ,halo}$ and $0.8V_{\rm circ,halo}$ (e.g., Kereš et al., 2005; Goerdt & Ceverino, 2015). The $V_{\rm circ,halo}$ is calculated using the following equations from Mo & White (2002):

$$V_{\rm circ,halo} = \left(\frac{GM_{\rm halo}}{r_{\rm halo}} \right)^{1/2} \tag{3.4}$$

$$r_{\rm halo} = \left(\frac{GM_{\rm halo}}{100\Omega_m H_0^2}\right)^{1/3} (1+z)^{-1}\,, \tag{3.5}$$

where $M_{\rm halo}$ is the inferred halo mass from the redshift-dependent stellar-halo mass ratio from Behroozi et al. (2019). The conversion factor between $V_{\rm circ,halo}$ and filamentary stream inflow velocity ($V_{\rm stream}$) is calculated using the redshift-$M_{\rm halo}$ dependent function from Goerdt & Ceverino (2015).

As listed in Table 3.2, the LRIS-Inflow galaxies have $v_{\rm cen,red}$ ranging from 250 to 450 km s^{-1} and $v_{\rm max,red}$ ranging from 410 to 770 km s^{-1}, well above the 98 to 158 km s^{-1} predictions for accretion of pristine gas from filamentary streams or the typical velocity dispersion ($\sim$80 km s^{-1}) of galaxies in the MOSDEF sample (Price et al., 2020). These large inflow velocities imply that the LIS metal lines are tracing motion separate from filamentary inflows or large-scale ISM motion. Taken together, the large inflow velocities and metal-enrichment of the gas that gives rise to the redshifted LIS lines suggest that these lines are likely tracing the re-accretion of metal-enriched gas previously ejected from the galaxy.

Simulations have focused on measuring flow properties, such as outflow rates and mass-loading factors, that depend on the geometry of the flows, which makes them notoriously difficult to compare with observations.However, a different approach is to directly compare observed absorption line profiles to "mock spectra" generated from simulations. As the spatial distribution of the gas is known, simulations could separate the outflowing, systemic, inflowing, and recycling gas components and assess their relative contributions to the observed absorption line profile. Tools such as TRIDENT (Hummels et al., 2017), FOGGIE (Peeples et al., 2019), and SALT (Carr & Scarlata, 2022) are promising for such future analyses.

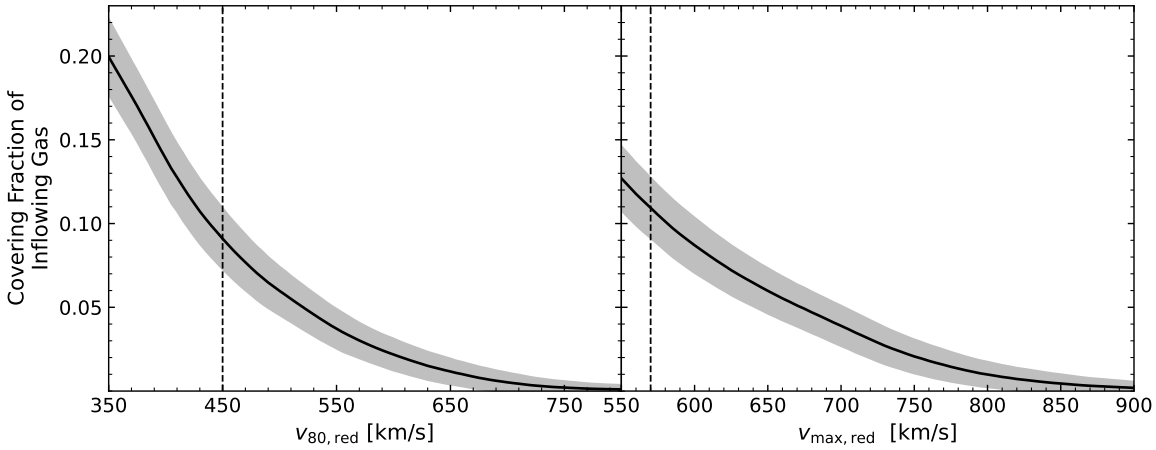

Figure 3.5: *Left*: Covering fraction of inflowing gas versus $v_{80,\mathrm{red}}$. *Right*: Covering fraction of inflowing gas versus $v_{\mathrm{max,red}}$. The covering fraction is taken as the fraction of galaxies with v_{red} equal to or greater than the given velocity. The grey shaded regions mark the 68% confidence interval. The dashed vertical line marks the dividing velocity calculated using a subsample of galaxies with robust red-wing velocities ($v_{\mathrm{red}} - 3\sigma_{v_{\mathrm{red}}} > 0$ km s^{-1}).

3.4.2 Covering Fraction of Inflowing Gas

The LRIS-Inflow galaxies do not exhibit unusual properties compared to other galaxies, suggesting that the frequency of galaxies with observed inflows is related to the geometry and covering fraction of inflowing gas. Specifically, three galaxies with robust inflow velocities in a sample of 134 imply that along a random sightline through a galaxy, the chance of encountering an inflow (i.e., covering fraction) is $\sim$2% $\pm$ 1%. The low detection rate of inflowing gas in the sample is consistent with previous studies at intermediate redshifts. Rubin et al. (2012) traced gas flows using Mg II and Fe II absorption lines in 101 $z \sim$ 0.5 star-forming galaxies of a similar SFR range but smaller stellar mass range compared to our sample (SFRs $\sim 1 - 63\ M_{\odot}$ yr^{-1} and $\log(M_{\star}/M_{\odot}) \sim 9.5$ - 11). They found six galaxies with redshifted absorption lines indicating inflowing gas at a 2σ level. When compared to the remaining galaxies, their inflowing galaxies were highly inclined, suggesting that inflows

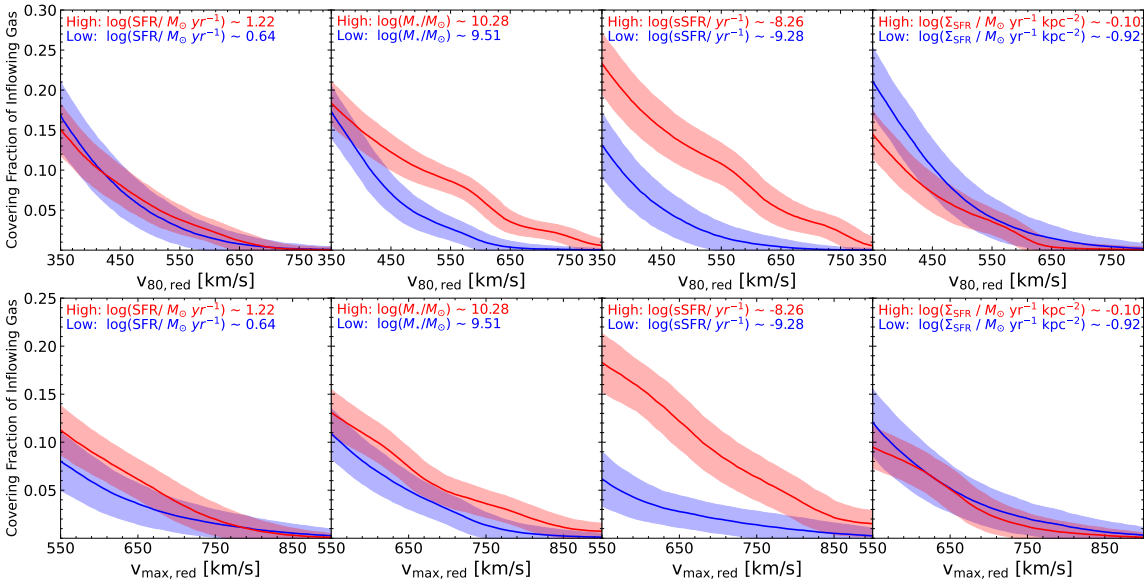

Figure 3.6: The covering fraction of inflowing gas in "lower" (blue) and "higher" (red) bins of *left*: log(SFR), *left center*: log($M_\star/M_\odot$), *right center*: log(sSFR), and *right*: log($\Sigma_{\rm SFR}$). The average value of each bin is listed in the top of each panel. Top panels are plotted against $v_{\rm 80,red}$ and bottom panels are against $v_{\rm max,red}$. The shaded regions mark the 68% confidence interval.

are more likely along the major axis of a galaxy. Similarly, in a sample of 208 star-forming galaxies with SFRs $\sim 1-98\ M_\odot\ {\rm yr}^{-1}$ and stellar masses $\log(M_\star/M_\odot) \sim 9.4-11.5$ at $z \sim 1$, Martin et al. (2012) detected inflowing gas at a 3σ level in $\sim$4% of galaxies. Both of these studies concluded that the low detection rate of inflowing gas was due to the low covering fraction of cold streams or recycled gas circulating in a galactic fountain. Alternatively, Calabrò et al. (2022) analyzed 330 $z \sim 2-4.5$ star-forming galaxies over a broad range of SFRs from 1 to 500 $M_\odot\ {\rm yr}^{-1}$, and stellar masses $\log(M_\star/M_\odot) \sim 8-10$, finding galaxies with redshifted LIS lines ($\Delta v_{\rm LIS} \geq 0\ {\rm km\ s}^{-1}$) in 34% of their sample. The authors suggest that their high detection rate of inflowing gas may be due to the increased role of inflows at earlier cosmic times. Although, we note that the higher detection rate of

Calabrò et al. (2022) may be a matter of definition. In the MOSDEF-LRIS sample, 29% of galaxies have $\Delta v_{\rm LIS} \geq 0$ km s^{-1}, similar to Calabrò et al. (2022).

Using the full statistical power of the MOSDEF-LRIS sample, we investigated the covering fraction of inflowing gas as a function of red-wing inflow velocity. At a given velocity (v), we calculated the fraction of galaxies with red-wing velocities ($v_{\rm 80,red}$ or $v_{\rm max,red}$) equal to or greater than v, perturbed the velocities by their uncertainties, and repeated this calculation many times. The average and standard deviation of the fraction found for each trial were taken as the covering fraction and its uncertainty at each v. This calculation, however, is only meaningful for velocities above which inflows become prominent. Classifying galaxies as "inflowing" or "outflowing" based solely on their red-wing velocity is difficult as different combinations of centroids and line widths can produce the same absorption line wing (i.e., a narrow, redshifted line and a broad, blueshifted line could both have $v_{\rm max,red}$ = 100 km s^{-1}).[6] Due to this ambiguity, we defined a "dividing" velocity as the v that maximized the fraction of galaxies with $v_{\rm red} > v$ and $\Delta v_{\rm LIS} > 0$ km s^{-1} (true positives) or with $v_{\rm red} < v$ and $\Delta v_{\rm LIS} < 0$ km s^{-1} (true negatives). At each v, we calculated the fraction of true positives and negatives, perturbed the red-wing velocities by their uncertainties, and repeated this many times. Figure 3.5 shows the chance of encountering inflowing gas of at least speed v along a random sightline through a galaxy (i.e., covering fraction) as a function of $v_{\rm 80,red}$ and $v_{\rm max,red}$. The covering fraction is roughly 20%, 4%, and 0.3% for $v_{\rm 80,red}$ larger than 350 km s^{-1}, 550 km s^{-1}, and 750 km s^{-1}, respectively. In contrast, the covering fraction is 12% (2%) for galaxies with $v_{\rm max,red}$ larger than 550 km s^{-1} (750 km s^{-1}). The rapid decrease of inflowing gas covering fraction with red-wing velocity suggests

[6] We note that red-wing velocity is also dependent on the spectral resolution of the observations.

that the low detection rate of galaxies with cool inflows is related to the viewing angle. As inflow velocity reaches speeds that may be more easily detected, the covering faction decreases to levels such that observing inflowing gas would be rare.

A complementary question is how, if at all, the inflow covering fraction varies with galactic properties. To investigate this, we divided the full sample into "lower" ($x + \sigma_x < x_{\rm median}$) and "higher" ($x$ - $\sigma_x > x_{\rm median}$) property bins. However, this simple division for star-formation properties introduces significant SNR differences between the two bins. To account for the effect of continuum SNR, we remeasure $v_{\rm red}$ and $v_{\rm blue}$ for galaxies in the "higher" bins after adding random noise to their spectra, so that their SNR falls within the SNR range of galaxies in the "lower" bins. In Figure 3.6, we plot the inflow covering fraction in bins of several galactic properties. The covering fraction appears independent of SFR, stellar mass, and $\Sigma_{\rm SFR}$. On the other hand, in the "higher" sSFR bin, the covering fraction is enhanced by a factor of 1.8±0.6 (3.0±1.2) at the $v_{\rm 80,red}$ ($v_{\rm max,red}$) dividing velocity. It is not surprising that the galaxies with higher sSFR have an increased inflow covering fraction, as higher gas accretion would allow for more star formation per unit mass. The covering fraction could increase due to thicker filaments from the IGM or more recycling gas in the CGM from previous outflows. The down-the-barrel LRIS observations cannot distinguish between these cases. However, in either case, the LIS absorption line profiles would be red-skewed, as both cases increase the fraction of inflowing gas relative to outflowing and interstellar gas. As a test, we compared the skewness-ratio of the LIS absorption line profiles between the "lower" and "higher" bins. A KS-test indicates a 3% probability that galaxies in the lower and higher sSFR bins are drawn from the same parent distribution, with the

"higher" bin having a smaller skewness-ratio (i.e., more red-skewed) than the "lower" bin. Conversely, the SFR, stellar mass, and $\Sigma_{\rm SFR}$ bins each have a >40% probability of being drawn from the same skewness distribution. Thus, the increased inflow covering fraction is likely due to more inflowing gas, such as recycling gas, which in turns increases the star-formation rate per unit mass.

3.5 Conclusions

We report on three star-forming galaxies from the MOSDEF Survey with additional deep rest-UV observations from Keck/LRIS with significantly measured centroid inflow velocities traced by LIS absorption lines. These inflows represent some of the most robust detections of inflowing gas into isolated, star-forming galaxies at $\langle z \rangle \sim 2.3$. Centroid velocities are measured from the redshift difference between $z_{\rm sys}$ and $z_{\rm LIS}$, while fractional (v_{80}) and maximum ($v_{\rm max}$) inflow (outflow) velocities are measured from the red (blue) wings of LIS lines that may better trace inflowing (outflowing) gas. Our main conclusions are as follows:

- The LRIS-Inflow galaxies have higher sSFR and $\Sigma_{\rm SFR}$ compared to the remaining galaxies, suggesting that both SFR and the gravitational potential of a galaxy are important in gas accretion. However, when other galaxies with large amounts of inflowing gas are included, no property is unique. The frequency of galaxies with observed inflows is then likely related to the geometry and covering fraction of inflowing gas (Section 3.3).

- The inflow centroid ($v_{\rm cen,red}$) and maximum inflow velocities ($v_{\rm max,red}$) of the LRIS-inflow galaxies are larger than predictions for the accretion of pristine gas from filamentary streams. We interpret the redshifted LIS absorptions lines of the LRIS-Inflow galaxies as tracing metal-enriched inflowing gas, such as recycled gas from previous ejections (Section 3.4.1).

- At a conservative level, the detection of three galaxies with significant inflows in a sample of 134 implies a covering fraction of $\approx$2% $\pm$ 1%. Based on the full statistical power of the sample, the maximum covering fraction of cool inflowing gas at $v_{\rm 80,red}$ = 350 km s^{-1} is 20% and at $v_{\rm max,red}$ = 550 km s^{-1} is 12%.

- Galaxies with higher sSFR have an increased inflow covering fraction, relative to those with lower sSFR. The larger covering fraction may be due to thicker filaments from the IGM or an increase in the amount of recycling gas in the CGM (Section 3.4.2).

Inflows of pristine gas from the IGM are required for galaxies to sustain their SFRs throughout their evolution. Here, we have presented three galaxies with significant inflows in a large sample of $z \sim 2$ galaxies that push the limits of current ground-based facilities, with full night ($\sim$7.5 hrs) observations needed to obtain sufficiently high SNR spectra. These spectra, however, can only give a glimpse into the complex nature of filamentary inflows and recycling gas. To build a better understanding of inflows, higher resolution spectroscopic data and multiple sightlines through the CGM are necessary to constrain the frequency and geometry of inflows and outflows around individual galaxies. The increased sensitivity of the next generation of 30-m extremely large telescopes will enable observations of faint background galaxies, increasing the density of sightlines through the CGM. In combination

with deep IFU spectroscopy, studies will be able to probe the distribution and kinematics of cool gas throughout the CGM, which may allow one to differentiate between pristine gas accretion and enriched recycled material.

3.6 Appendix

Here we present plots of the MOSFIRE and LRIS spectra of the three galaxies with detected inflows. In each panel, the top row shows strong rest-optical emission lines, while the bottom row shows LIS metal absorption lines.

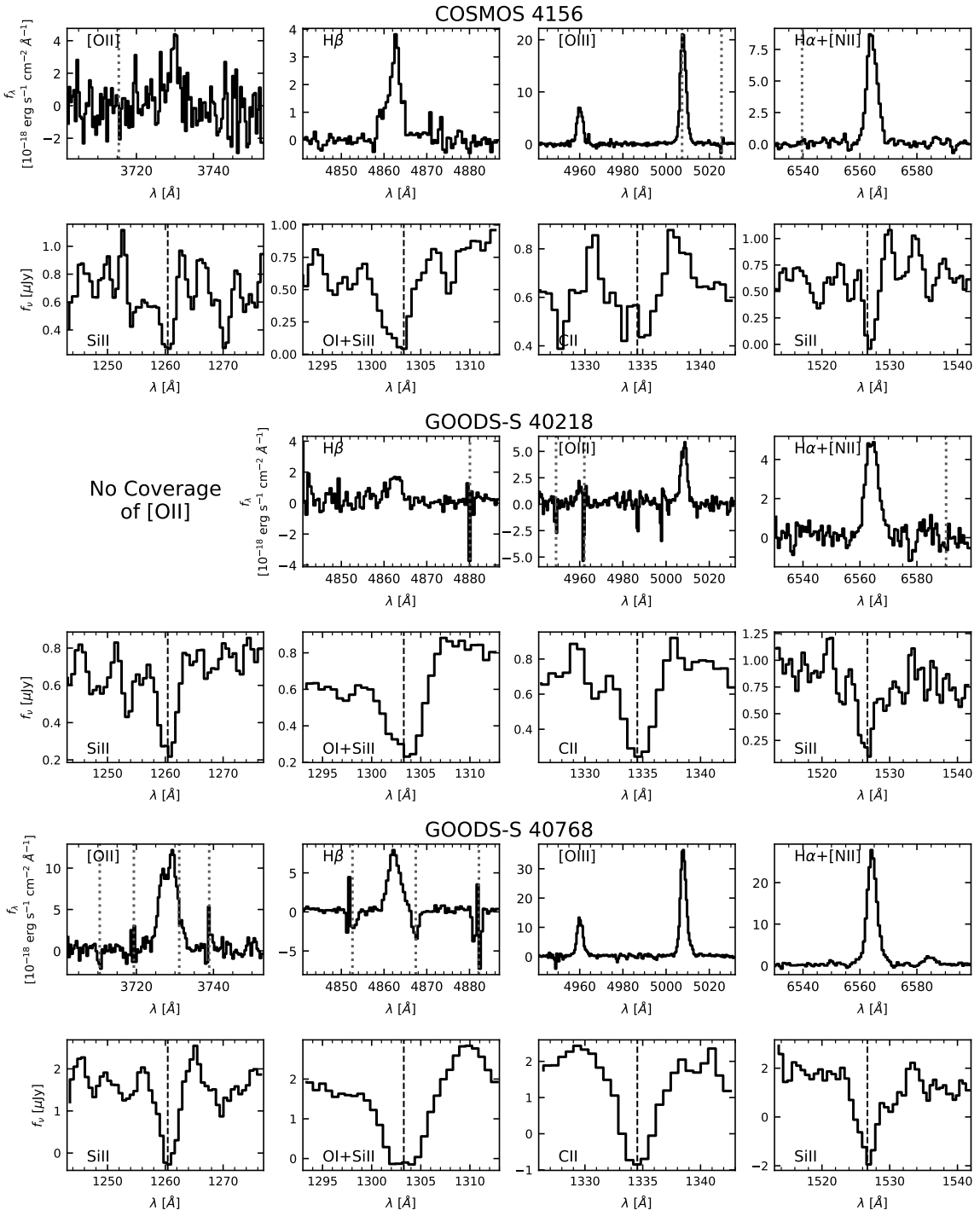

Figure 3.7: Plots of strong rest-optical emission and rest-UV absorption lines of the LRIS-Inflow galaxies from MOSFIRE and LRIS, respectively. Dotted vertical lines mark sky lines. Dashed vertical lines mark the systemic absorption line center. GOODS-S 40218 does not coverage of [OII].

Chapter 4

The MOSDEF Survey: Properties of Warm Ionized Outflows at $z = 1.4 - 3.8$[1]

Abstract We use the large spectroscopic data set of the MOSFIRE Deep Evolution Field survey to investigate the kinematics and energetics of ionized gas outflows. Using a sample of 598 star-forming galaxies at redshift $1.4 < z < 3.8$, we decompose Hα and [O III] emission lines into narrow and broad components, finding significant detections of broad components in 10% of the sample. The ionized outflow velocity from individual galaxies appears independent of galaxy properties, such as stellar mass, star-formation rate (SFR), and star-formation-rate surface density ($\Sigma_{\rm SFR}$). Adopting a simple outflow model, we es-

[1]This chapter contains a draft of an article that has been submitted for publication by Oxford University Press in the Monthly Notices of the Royal Astronomical Society written by Andrew Weldon, Naveen A. Reddy, Alison L. Coil, Alice E. Shapley, Brian Siana, Mariska Kriek, Bahram Mobasher, Zhiyuan Song, and Michael A. Wozniak.

timate the mass-, energy- and momentum-loading factors of the ionized outflows, finding modest values with averages of 0.33, 0.04, and 0.22, respectively. The larger momentum- than energy-loading factors, for the adopted physical parameters, imply that these ionized outflows are primarily momentum-driven. We further find a marginal correlation (2.5σ) between the mass-loading factor and stellar mass in agreement with predictions by simulations, scaling as $\eta_m \propto M_\star^{-0.45}$. This shallow scaling relation is consistent with these ionized outflows being driven by a combination of mechanical energy generated by supernovae explosions and radiation pressure acting on dusty material. In a majority of galaxies, the outflowing material does not appear to have sufficient velocity to escape the gravitational potential of their host, likely recycling back at later times. Together, these results suggest that the ionized outflows traced by nebular emission lines are negligible, with the bulk of mass and energy carried out in other gaseous phases.

4.1 Introduction

Large-scale galactic outflows have long been recognized as a key process in galaxy evolution. Early theoretical models of galaxy formation required outflows of mass and energy to prevent gas from excessively cooling, causing overly efficient star formation and an overproduction of stellar mass (White & Rees, 1978b; Dekel & Silk, 1986; White & Frenk, 1991). Modern models of galaxy evolution and simulations rely on intense, galactic-scale outflows to suppress star formation and reproduce observed properties of galaxies, such as the galaxy mass function and the sizes of galactic disks and bulges (e.g., Guedes et al., 2011; Davé et al., 2011). Beyond suppressing star-formation, outflows modulate the metallicity

within galaxies, enriching the circumgalactic medium (CGM) and possibly the intergalactic medium (IGM) with metals (e.g., Tremonti et al., 2004; Dalcanton, 2007; Finlator & Davé, 2008). At late-times, $z \lesssim 1$, recycled gas from past outflows may fuel a significant fraction of star-formation in galaxies (Oppenheimer et al., 2010; Henriques et al., 2013; Anglés-Alcázar et al., 2017). Outflows also appear to be an important factor in the creation of low-column-density channels in the ISM, allowing for the escape of ionizing photons (e.g., Gnedin et al., 2008; Leitet et al., 2013; Ma et al., 2016; Reddy et al., 2016; Gazagnes et al., 2018; Reddy et al., 2022).

Despite advances in numerical modeling, a complete description of galactic-scale outflows and their impacts on galaxy evolution is challenging for simulations due to the wide scale range of outflows. Large-scale cosmological hydrodynamical suites such as EAGLE (Schaye et al., 2015) and Illustris TNG (Pillepich et al., 2018) do not resolve the small scales required to capture relevant feedback processes that generate outflows. Instead, these models employ sub-grid processes for feedback, which vary between simulations. On the other hand, high-resolution "local patch" simulations capture the interaction between stellar feedback and the multi-phase ISM but lack the size needed to track the long-term evolution of outflows (e.g., Girichidis et al., 2016, 2018; Li et al., 2017; Kim & Ostriker, 2018; Kim et al., 2020). In either case, observational constraints on how the properties of outflows scale with the stellar mass, star-formation rate, and other properties of their host across galaxy populations are essential.

Quantifying the impact of outflows on galaxy evolution based on observational data has been an active area of research for well over a decade. Multi-wavelength observations

have shown that galactic outflows have a multi-phase structure, with outflows detected in hot X-ray ($\sim 10^{6-7}$ K) emitting gas, from emission and absorption lines tracing warm ($\sim 10^4$ K) and cool ($\sim 10^3$ K) gas, and down to cold ($\lesssim$100 K) molecular and dust outflows in radio observations (see reviews by Heckman & Thompson, 2017; Rupke, 2018; Veilleux et al., 2020). In typical star-forming galaxies, outflows are theorized to be driven by energy injected into the ISM by supernovae; radiation pressure acting on cool, dusty material; cosmic rays; or a combination of these mechanisms (Ipavich, 1975; Chevalier & Clegg, 1985; Murray et al., 2005, 2011). Galactic-scale outflows are then expected to play a major role in galaxy evolution at $z \sim 1 - 3$, during the peak of the cosmic star-formation history ("Cosmic Noon"; Madau & Dickinson, 2014), when feedback from star formation and AGN was maximized.

At these redshifts, outflows are a common feature of star-forming galaxies, with blueshifted rest-UV interstellar absorption lines tracing cool, neutral/low-ionization outflows (e.g., Shapley et al., 2003; Steidel et al., 2010; Weldon et al., 2022) and broad components of rest-optical emission lines tracing warm, ionized outflows (hereafter ionized outflows; e.g., Genzel et al., 2011, 2014; Newman et al., 2012; Freeman et al., 2019; Concas et al., 2022). Observations of cool outflows have found that outflow velocity increases with several galactic properties, such as stellar mass, star-formation rate (SFR), and star-formation-rate surface density ($\Sigma_{\rm SFR}$) (e.g., Rubin et al., 2010; Steidel et al., 2010; Martin et al., 2012; Rubin et al., 2014; Chisholm et al., 2015; Weldon et al., 2022). Absorption lines are sensitive to gas along the entire line of sight, including both high- and low-density gas from current and past outflows, thus they likely trace material ejected over long timescales.

Estimates of mass outflow rates from absorption lines will then depend on the metallicity of the outflowing gas, the outflow geometry, and the absorption contribution from the ISM and faint satellite galaxies, which are often unconstrained by absorption line observations (e.g., Weiner et al., 2009; Heckman et al., 2015). On the other hand, the underlying broad components of strong rest-optical emission lines likely trace denser outflowing gas near the launching points of the outflows, providing a snapshot of current outflow activity. The mass outflow rates traced by emission lines depend on similar unconstrained (e.g., outflow geometry) and other properties that may be estimated from emission lines (e.g., the electron density of the outflowing gas). However, due to the difficulty of detecting faint broad components in typical $z \gtrsim 1$ galaxies, studies are primarily limited to local galaxies, small samples, gravitationally lensed galaxies, or high S/N composite spectra to infer average outflow properties (Newman et al., 2012; Davies et al., 2019; Freeman et al., 2019; Swinbank et al., 2019; Förster Schreiber et al., 2019; Concas et al., 2022; Reichardt Chu et al., 2022b,c).

The mass-loading factor (η_m) is a key characteristic of outflows, which represents the amount of mass they remove normalized by the galaxy's star-formation rate and, in star-forming galaxies, is thought of as a proxy for outflow efficiency. Simple analytical arguments and numerical simulations predict an anti-correlation between the mass-loading factor and outflow velocity or stellar mass of galaxies, which scales steeper if the outflows are energy-driven and shallower if they are momentum-driven (e.g., Murray et al., 2005; Oppenheimer & Davé, 2008; Muratov et al., 2015). Observations of ionized outflows in local galaxies find such trends, suggesting that outflows are more efficient at removing material from the

shallower potential wells of lower-mass galaxies (e.g., Heckman et al., 2015; Chisholm et al., 2017; McQuinn et al., 2019; Marasco et al., 2023). In addition to the mass-loading factor, outflows are characterized by the amount of energy and momentum they carry with respect to the amounts generated by supernovae and stellar winds. However, at high redshifts, there are few constraints on the mass-, energy-, and momentum-loading factors of outflows in typical star-forming galaxies.

In this paper, we expand upon the work of Freeman et al. (2019) to characterize the properties of ionized gas outflows from individual star-forming galaxies at $z \sim 2$ using the complete MOSFIRE Deep Evolution Field survey (MOSDEF; Kriek et al., 2015). The MOSDEF survey obtained rest-optical spectra for ∼1500 high-redshift galaxies, most with multiple emission lines for which we can investigate outflows in several emission lines (i.e, Hβ, [O III], Hα, and [N II]) from a large sample of galaxies. Our goals for this study are to constrain the kinematics and loading factors of ionized gas outflows and to explore how these properties are related to galactic properties, such as stellar mass, SFR, and $\Sigma_{\rm SFR}$. The outline of this paper is as follows. In Section 4.2, we introduce the sample, measurements of galaxy properties, and the methodology of fitting galaxy spectra to characterize the presence of outflows. Section 4.4, presents our main results on the correlations between measured galaxy properties, ionized outflow velocities, and mass-loading factors. We discuss the physical context behind these results in Section 4.5 and summarize our conclusions in Section 4.6. Throughout this paper, we adopt a standard cosmology with $\Omega_\Lambda = 0.7$, $\Omega_M = 0.3$, and $\rm H_0 = 70$ km s^{-1}Mpc^{-1}. All wavelengths are presented in the vacuum frame.

4.2 Data and Measurements

4.2.1 MOSDEF Survey

Galaxies analyzed in this paper were drawn from the MOSDEF survey, which targeted ≈1500 H-band selected galaxies and AGNs at redshifts $1.4 \leq z \leq 3.8$ in the CANDELS fields (Grogin et al., 2011; Koekemoer et al., 2011). The survey obtained moderate-resolution ($R \sim 3000$–3600) rest-optical spectra using the Multi-Object Spectrometer for Infra-Red Exploration (MOSFIRE; McLean et al., 2012a) on the Keck I telescope. Galaxies were targeted for spectroscopy based on pre-existing spectroscopic, grism, or photometric redshifts that placed them in three redshift ranges ($z = 1.37 - 1.70$, $z = 2.09 - 2.61$, and $z = 2.95 - 3.80$). This selection optimized the coverage of several strong rest-frame optical emission lines ([O II]$\lambda\lambda$3727,3730, Hβ, [O III]$\lambda\lambda$4960,5008, Hα, [N II]$\lambda\lambda$6550,6585, and [S II]$\lambda\lambda$6717,6732) that lie in the YJHK transmission windows. The final MOSDEF sample spans ranges of star-formation rate ($1 < \mathrm{SFR} < 200$ M$_\odot$ yr^{-1}) and stellar mass ($10^9 < M_\star < 10^{11}$ M$_\odot$) typical for galaxies at $z \sim 1.4 - 3.8$, with the majority of galaxies having detections of multiple rest-frame optical emission lines. For full details regarding the MOSDEF survey (targeting, data reduction, and sample properties), we refer readers to Kriek et al. (2015).

Emission-line fluxes were measured by simultaneously fitting a line with the best-fit SED model for the continuum and a Gaussian function for the line (see Reddy et al., 2022, for a complete description of the SED modeling). For multiple lines that lie in close proximity, multiple Gaussians were fit, such as the [O II] doublet and Hα and the [N II] doublet, which were fitted with two and three Gaussians, respectively. Systemic redshifts

were derived from the strongest emission line, usually Hα or [O III]λ5008, and were used to fit the other rest-frame optical nebular emission lines. Further details on emission-line measurements and slit loss corrections are given in Kriek et al. (2015) and Reddy et al. (2015).

Galaxy sizes and inclinations were estimated from the effective radius ($R_{\rm E}$), within which half the total light of the galaxy is contained, and the axis ratio (b/a), respectively, measured by van der Wel et al. (2014)[2] using GALFIT (Peng et al., 2010) on HST/F160W images from the CANDELS survey.

4.2.2 Sample Selection

In our analysis, we search for underlying, broad rest-optical emission components from star-forming galaxies, tracing ionized outflowing gas. The parent MOSDEF sample contains 878 galaxies with [O III] and 759 with Hα detections. Several criteria are applied to the parent MOSDEF sample to create a sample conducive for measuring broad emission. First, 94 [O III] and 104 Hα detections from active galactic nuclei (AGNs) identified by IR colors, X-ray emission, and/or the [N II]/Hα line ratio were removed (Coil et al., 2015; Azadi et al., 2017, 2018; Leung et al., 2019). Next, we removed: detections with S/N $<$ 10; detections that were affected by bright skylines; and detections that lay close to the edge of their spectra, reducing the sample to 431 galaxies with [O III] and 514 with Hα detections. Finally, galaxies may have broad line components simply from rotation and velocity dispersion. As such, to isolate outflowing broad emission, we limit the narrow emission to FWHM $<$ 275 km s^{-1} (see Section 4.3) and remove detections with FWHM $>$

[2] https://users.ugent.be/~avdrwel/research.html

275 km s^{-1} from a single Gaussian fit. These criteria result in a final sample of 598 galaxies (hereafter the "MOSDEF-ionized" sample), of which 391 (435) have [O III] (Hα) detections. There are 228 galaxies with both an [O III] and Hα detection.

4.2.3 Galaxy Properties

In this study, we investigate the properties of ionized outflows against several global galaxy properties (e.g., stellar mass, SFR, star-formation-rate surface density). Stellar masses ($M_\star$), SFRs, ages, and color excesses were derived from spectral energy distribution (SED) modeling. Here, we briefly describe the models used and refer readers to Reddy et al. (2015) for more details. The models were created adopting a Bruzual & Charlot (2003b, hereafter BC03) stellar population synthesis model, Chabrier (2003) initial mass function, constant star formation histories (SFH), Small Magellanic Cloud (SMC) attenuation curve (Fitzpatrick & Massa, 1990; Gordon et al., 2003), and sub-solar metallicity ($Z_* = 0.28 Z_\odot$). A lower age limit of 50 Myr was imposed, based on the typical dynamical timescale of $z \sim 2$ galaxies (Reddy et al., 2012). The combination of the steeper SMC attenuation curve, which has been found to best reproduce the dust obscurations of typical star-forming galaxies at $z \sim 2$ based on far-infrared data (Reddy et al., 2018a), and sub-solar metallicity provide self-consistent SFRs with those derived using other methods (Reddy et al., 2018b; Theios et al., 2019). The best-fit stellar population parameters and their errors were obtained by perturbing the photometry, refitting the models, and taking the median and dispersion in the resulting parameters, respectively.

Blueshifted interstellar absorption lines tracing cool, neutral/low-ionization gas outflows are ubiquitous in $z \gtrsim 2$ star-forming galaxies (e.g., Shapley et al., 2003; Steidel

et al., 2010). Observations suggest that the velocity of cool outflows increases with the SFR and $\Sigma_{\rm SFR}$ of a galaxy (e.g., Steidel et al., 2010; Martin et al., 2012; Rubin et al., 2014; Weldon et al., 2022). As the broad components of rest-optical emission lines likely trace denser outflowing gas near the launching points of the outflows, they provide a snapshot of current outflow activity, thus their velocity may also scale with SFR and $\Sigma_{\rm SFR}$. We calculate Hα SFRs (SFR[Hα]) from Hα and Hβ flux measurements corrected for dust using the Balmer decrement. Following the methodology presented in Reddy et al. (2015), Hα luminosities are corrected for attenuation assuming a Cardelli et al. (1989) Galactic extinction curve and converted to SFRs using the conversion factor from Reddy et al. (2018b), 3.236×10^{-42} $M_{\odot}$ yr^{-1} ergs^{-1} s, for a BC03 stellar population synthesis model and sub-solar metallicity adopted for the SED fitting. SFR[Hα] is calculated for objects with significant detections (S/N $>$ 3) of Hα and Hβ. As discussed in previous studies, there is a general agreement between SFR[SED] and SFR[Hα] for MOSDEF galaxies (e.g., Reddy et al., 2015; Shivaei et al., 2016; Azadi et al., 2018; Reddy et al., 2022).

When an ionized outflow is detected, SFR[Hα] should be derived from the narrow flux component tracing gas within the galaxy. The Hα SFRs above are then overestimates as they use Hα and Hβ fluxes measured from single-Gaussian fits. As the stellar continuum is unlikely affected by emission from an outflow, SFR[SED] should be insensitive to the presence of outflowing gas. On the other hand, when detected in Hα, we can correct SFR[Hα] by multiplying it by the narrow-to-single Hα flux ratio. For these reasons, in our analysis, we have chosen to focus on SFR[SED] when discussing outflows detected in [O III] and SFR[Hα] when detected in Hα.

Along with the star-formation rate, the mechanisms that drive outflows may be enhanced in regions of compact star formation. We define the star-formation-rate surface density as $\Sigma_{\rm SFR} = {\rm SFR}/(2\pi R_{\rm E}^2)$. Additionally, at a given $\Sigma_{\rm SFR}$, outflows may be more effectively launched from a shallow galaxy potential (i.e., low stellar mass) relative to a deep potential (Pucha et al., 2022; Reddy et al., 2022). To examine the frequency of galaxies with observed outflows on both $\Sigma_{\rm SFR}$ and the galaxy potential, we define the specific star-formation-rate surface density as $\Sigma_{\rm sSFR} = {\rm SFR}/(2\pi R_{\rm E}^2 M_\star)$

4.3 Searching for Broad Emission Lines

4.3.1 Fitting Individual Galaxies

We search for ionized gas outflows by decomposing Hβ, [O III]$\lambda\lambda$4960,5008 and Hα, [N II]$\lambda\lambda$6550,6585 into narrow Gaussian components, tracing virial motions within the galaxy, and broad Gaussian components tracing the ionized outflowing gas. In the most general case, simultaneously fitting narrow and broad Gaussians to each set of three emission lines would require 19 free parameters. Motivated by previous studies (e.g., Genzel et al., 2011, 2014; Newman et al., 2012), we adopt the following assumptions: (1) the narrow components of each line share the same FWHM (FWHM$_{\rm na}$) and redshift, (2) the broad components of each line share the same FWHM (FWHM$_{\rm br}$) and velocity offset from the narrow component ($\Delta v_{\rm br}$), and (3) the [O III]λ5008/[O III]λ4960 and [N II]λ6585/[N II]λ6550 flux ratios are 2.98 and 2.93, respectively (Osterbrock, 1989). Therefore, each fit has nine free parameters; five shared by each line (FWHM$_{\rm na}$, FWHM$_{\rm br}$, $\Delta v_{\rm br}$, narrow component

redshift, and constant background) and four controlling the narrow and broad component amplitudes ($A_{\rm na}$ and $A_{\rm br}$).

For each set of lines, we perform two preliminary fits and one final fit. The first preliminary fit uses a linear continuum and single Gaussians to fit the emission lines using `curve fit`, a non-linear least squares fitting routine from the `scipy.optimize` subpackage. We use this fit to subtract off the linear continuum and normalize the spectra by the peak of the brightest line for each set of lines ([O III] or Hα). Next, using the normalized spectra, we fit each emission line with a narrow and broad Gaussian with `curve fit`. The resulting values of the second fit are used as initial values for the final fit, which is done using `emcee`, a Python Markov chain Monte Carlo (MCMC) Ensemble sampler (Foreman-Mackey et al., 2013). We take the median values of the resulting posterior probability distributions for all the model parameters. The errors on the parameters are estimated using the 16th and 84th percentiles.

In order to properly study ionized outflows, we must be certain that the broad components trace a kinematically distinct feature from the rotation of the host galaxy, thus we place physically motivated restrictions on the free parameters. In particular, we restricted the FWHM$_{\rm na}$ to values between 80 and 275 km s^{-1} and FWHM$_{\rm br}$ to values between 300 and 800 km s^{-1}. The lower limit on FWHM$_{\rm na}$ is the average skyline FWHM of the MOSDEF-ionized galaxies, while a majority of galaxies (90%) exhibit an FWHM $<$ 275 km s^{-1} when fitting [O III] or Hα with a single Gaussian component. The additional 25 km s^{-1} separation between FWHM$_{\rm na}$ and FWHM$_{\rm br}$ helps ensure that the broad component is not an artefact from a better fit to the narrow emission by using two Gaussian components.

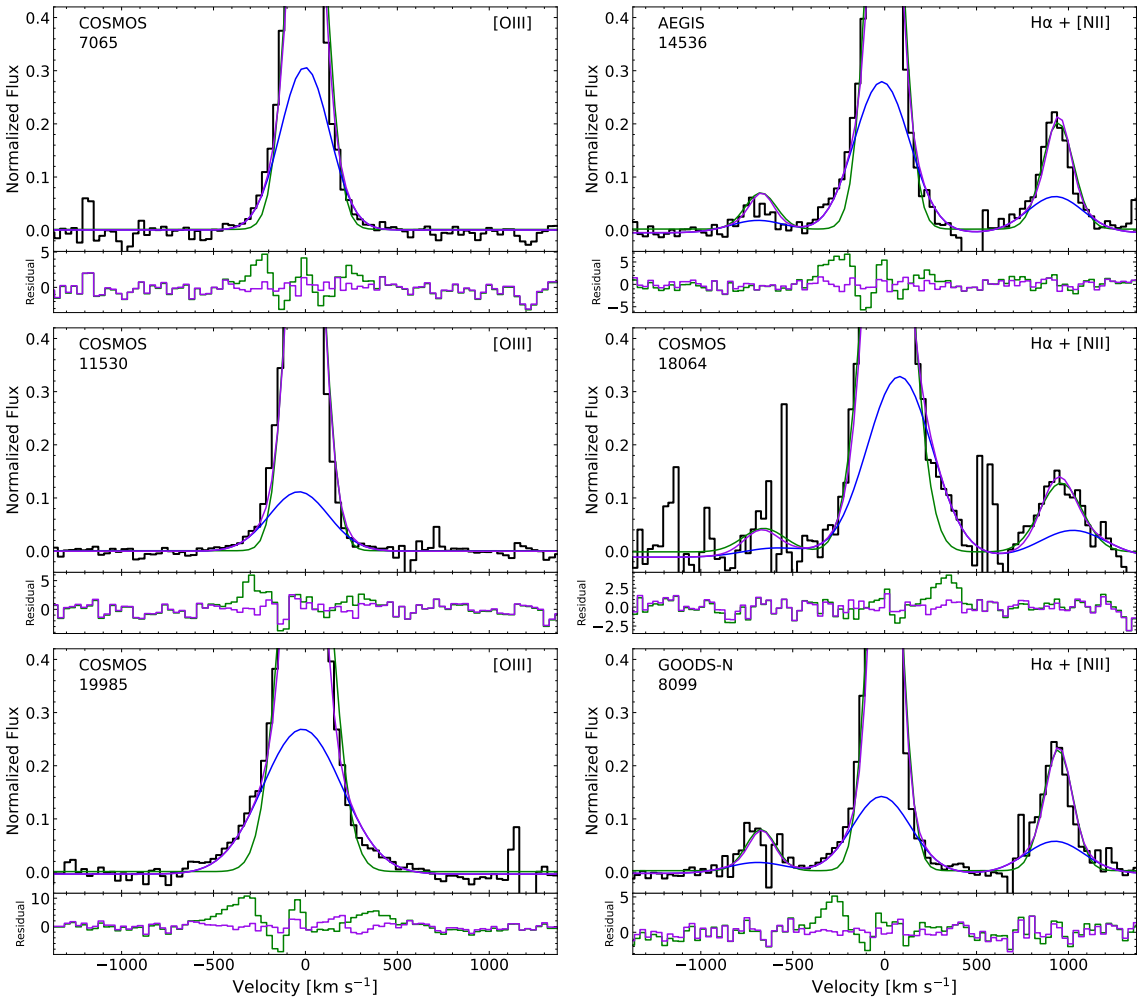

Figure 4.1: Examples of fits for individual spectra with large ΔBIC values. The field and 3D-HST v4.1 catalog ID is given in the upper left. Each line is normalized such that the strongest line peak is unity. The single Gaussian fit is shown in green, the overall fit for the narrow+broad components is shown in purple, and the broad component is shown in blue. The bottom plot in each panel shows the residuals after subtracting the best-fit single (green) and narrow+broad fit (purple) from the spectrum. The "wave" pattern, an underestimation flux at the peak and overestimation in the wing(s), in the residuals shows that a single Gaussian does not fit the observed line profiles well.

Typical values of $\mathrm{FWHM_{br}}$ for ionized outflows from star-forming galaxies are 300–600 km $\mathrm{s^{-1}}$ (Genzel et al., 2011; Newman et al., 2012; Wood et al., 2015). The centroids of the narrow and broad components are limited to within ±100 km $\mathrm{s^{-1}}$ of their initial values, as found by similar studies (Newman et al., 2012; Wood et al., 2015; Davies et al., 2019; Concas et al., 2022).

To determine whether a broad component is detected, we evaluate the improvement over a single Gaussian fit using the Bayesian Information Criterion (BIC; Schwarz, 1978) and the amplitude of the broad component. Following a similar procedure as for the double Gaussian fit, we fit each set of lines with single Gaussians: the spectra are first normalized using an initial fit, then refitted, the results of which serve as the initial values for a MCMC fitting process.[3] The BIC is defined as:

$$\mathrm{BIC} = \chi^2 + k\ln(n)\,, \tag{4.1}$$

where χ^2 is the chi squared of the fit, k is the number of parameters used in the fit, and n is the number of points used in the fit. Following similar studies, we adopt $\Delta\mathrm{BIC} = \mathrm{BIC_{single}} - \mathrm{BIC_{double}} > 10$ as "very strong" evidence against a single Gaussian fit (e.g., Swinbank et al., 2019; Avery et al., 2021; Concas et al., 2022). Additionally, to ensure that the broad component is not an artefact, we require that the broad component amplitude of [O III] or Hα is robustly measured ($\mathrm{A_{br}} - 3\sigma_{\mathrm{A_{br}}} > 0$) as evidence for the detection of a broad component. Figure 4.1 presents fits for six galaxies that show strong evidence for a broad component.

[3]For the single fits there are five free parameters: constant background, redshift, FWHM, and two amplitudes ($A_{\mathrm{H}\beta}$ and $A_{[\mathrm{O\,III}]}$ or $A_{\mathrm{H}\alpha}$ and $A_{[\mathrm{N\,II}]}$).

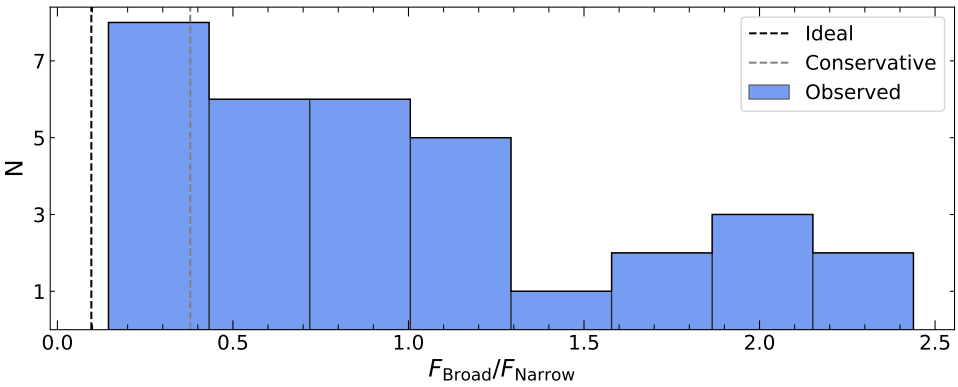

Figure 4.2: The distribution of broad-to-narrow Hα flux ratios for galaxies with a detected broad Hα emission component. The grey (black) vertical dashed line is the minimum flux ratio required for a broad component to be detected using the fitting procedure in Section 4.3 for a broad component with $\Delta v_{\rm br}$ = 10 km s^{-1} ($\Delta v_{\rm br}$ = 90 km s^{-1}) and a Hα signal-to-noise ratio of 25 (100).

4.3.2 Detectability of Broad Components

The detection of an underlying broad component depends on several factors. A broad component may be indistinguishable from that of HII regions at low velocities and small velocity offsets. At the same time, low S/N could prevent the detection of a broad component in the faint, high-velocity wings of an emission line, where the broad component may be the strongest. To quantify the detectability of a broad component, we create simulated Hα emission lines where we can control the parameters of the broad component and signal-to-noise ratio (SNR) of the line.

For this test, we considered two cases with fixed values for $\Delta v_{\rm br}$ and line SNR. In the first case ("conservative"), the broad component had a small velocity offset, $\Delta v_{\rm br}$ = 10 km s^{-1}, and line SNR = 25, the average value of galaxies in the MOSDEF-ionised sample. In the second case ("ideal"), the broad component had a large velocity offset, $\Delta v_{\rm br}$ = 90 km s^{-1} and line SNR = 100. For each case, 110 single Hα emission lines were simulated,

with 11 different $\mathrm{FWHM_{br}}$ between 300 and 500 km $\mathrm{s^{-1}}$ and 10 normalized A_{br} between 0.05 and 0.5, which span the range of measured broad components from individual detected galaxies. The values for the simulated narrow components are randomly selected between the measured narrow component values of individual detected galaxies. We adopt the same resolution and wavelength as a Hα line of a $z \sim 2.3$ galaxy. Following the same fitting process and selection criteria as for individual galaxies in Section 2.4.1, we fit the simulated lines with two Gaussians and a single Gaussian and determined which simulated spectra have a detected broad component.

The results of these tests are shown in Figure 4.2. We find that the lowest detectable broad component has an integrated flux of 10% and 38% of the narrow component for the "ideal" and "conservative" cases, respectively. Not surprisingly, for individual detections, their broad component flux lies above these limits of the fitting process. For all of the galaxies, their broad flux is greater than the "ideal" limit, while 75% are above the "conservative" limit. We note, however, that the detection of the broad component is a function of both Δv_{br} and line SNR. Here, we explored two extreme cases, but varying the values may lead to different limits.

4.3.3 Composite Spectra

Decomposing emission lines into narrow and broad components is often limited by the S/N of a galaxy's spectra. The high-velocity wings of an emission line, where the broad component may be the strongest, are typically dominated by noise. In order to investigate ionized outflows across a wide range of properties, we construct high S/N composite spectra in bins of several galactic properties. We follow a similar method as Weldon et al. (2022)

for constructing composite spectra. In brief, galaxies in the MOSDEF-ionized sample were grouped together into equal-number bins based on various physical properties (e.g., stellar mass, SFR, $\Sigma_{\rm SFR}$). The science and error spectra of individual galaxies were shifted to the rest frame, converted to luminosity density, interpolated onto a grid with a wavelength spacing of $\Delta\lambda = 0.5$Å, and normalized by either the [O III] or Hα luminosity, depending on the line of interest, measured from the science spectrum. The composite spectrum at each wavelength point was computed as the weighted average with 3σ outlier rejection of the luminosity densities of individual spectra at the same wavelength point, where the weights are $1/\sigma\left(\lambda\right)^2$ and $\sigma\left(\lambda\right)$ is the value of the error spectrum at wavelength λ. The line-fitting process for the composite spectra is the same as for individual galaxies. The spectra are first normalized using an initial fit, then refitted, the results of which serve as the initial values for an MCMC fitting process. However, when fitting the Hα and [N II] doublet, we include the faint [S II]$\lambda\lambda$6716,6731 doublet (see Section 4.4.3).

4.4 Results

With the decomposition of rest-optical emission lines into narrow and broad components for individual galaxies and stacked spectra in hand, we are in a position to investigate the properties of the ionized outflows against galactic physical properties. The occurrence of ionized outflows is discussed in Section 4.4.1. Section 4.4.2 focuses on trends between ionized outflow velocity and galactic properties. Section 4.4.3 discusses the mass-loading factor of the ionized outflows and its relations with galactic properties. The energetics of the ionized outflows are discussed in Section 4.4.4.

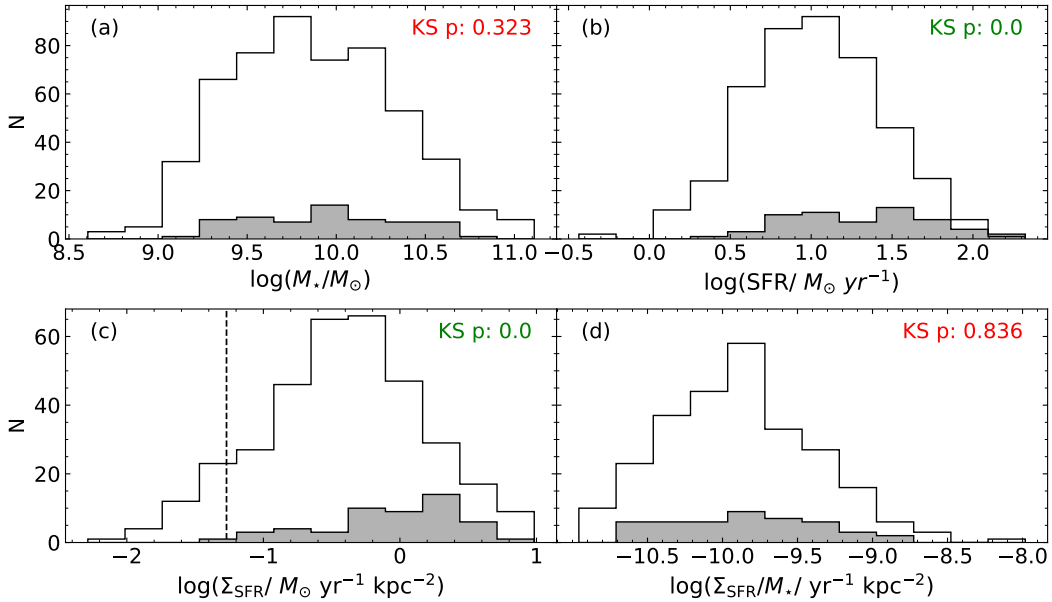

Figure 4.3: The distribution of various galactic properties. Panel (a): stellar mass, Panel (b): SFR, Panel (c): $\Sigma_{\rm SFR}$, Panel (d): $\Sigma_{\rm sSFR}$. Solid gray and open bars represent the 62 galaxies with detected broad components and the remaining galaxies, respectively. The p-value of a KS test between galaxies with a broad component and the remaining galaxies is shown in the upper corners of each panel. The vertical dashed line in panel (c) marks the $\Sigma_{\rm SFR}$ threshold proposed by Heckman (2002) for launching an outflow.

4.4.1 Occurrence

As discussed in Section 4.2.2, the MOSDEF-ionized sample consists of 598 galaxies, with 392 [O III] and 435 Hα detections. Of these, there is significant evidence for broad emission in 39 of the 391 (10%) [O III] detections and in 33 of the 435 (7%) Hα detections. Overall, a broad component is detected in 62 (10%) of the MOSDEF-ionized galaxies. These galaxies typically have a S/N > 50[4], highlighting the difficulty of decomposing rest-optical emission lines into multiple components.

In Figure 4.3, we show the distributions of various galactic properties for the subset of galaxies with evidence of ionized outflows and the remaining MOSDEF-ionized galaxies. To quantitatively test whether the galaxies with detected ionized outflows are drawn from the same parent distribution as the remaining galaxies, we perform a Kolmogorov–Smirnov (KS) test. Unsurprisingly, the detection of ionized outflows is strongly tied to signatures of elevated star-formation activity (SFR and $\Sigma_{\rm SFR}$). This connection is expected as, in star-forming galaxies, the injection of energy and momentum associated with the late stages of massive stellar evolution are theorized to drive galactic-scale outflows. Additionally, nearly all of the galaxies with ionized outflows have an $\Sigma_{\rm SFR}$ above the $\sim$0.05 $M_\odot$ yr^{-1} kpc^{-2} threshold (dashed-line in panel (c) of Figure 4.3) proposed by Heckman (2002)[5], which is interpreted as the point where energy and momentum can overcome the gravity of the galaxy disk and launch an outflow. Alternatively, the apparent difference between the galactic properties of the outflowing and remaining galaxies may reflect limitations in our fitting technique. Outflows from galaxies with lower SFR or $\Sigma_{\rm SFR}$ could be missed if their

[4]We take the S/N as the flux of a single Gaussian divided by the error in the flux for either [O III] or Hα.

[5]Heckman (2002) propose a 0.1 $M_\odot$ yr^{-1} kpc^{-2} threshold based on local starbursts galaxies. For a Chabrier (2003) IMF assumed in our study, this threshold becomes 0.05 $M_\odot$ yr^{-1} kpc^{-2}.

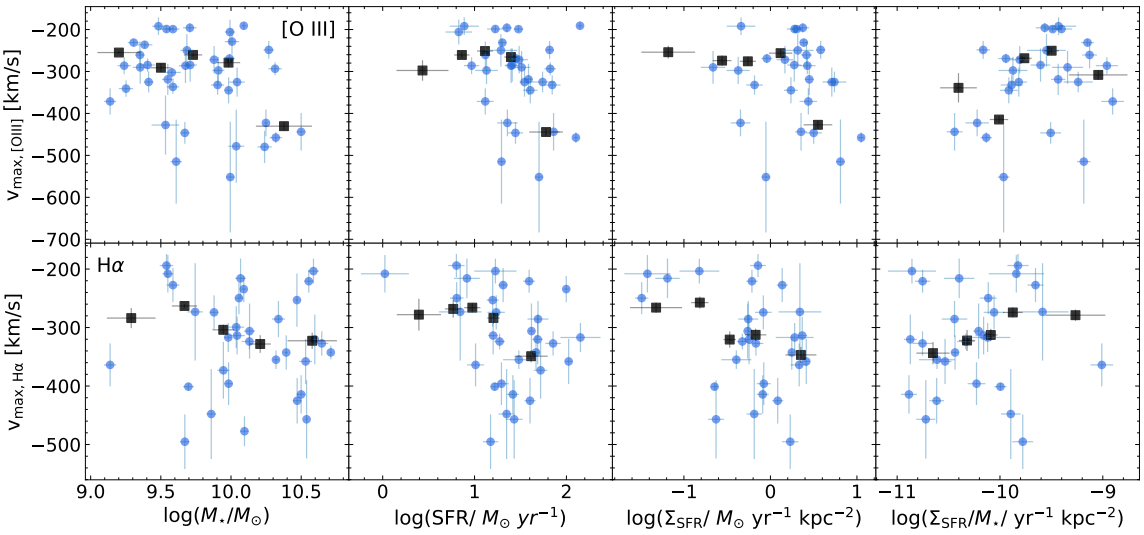

Figure 4.4: Maximum outflow velocity versus various galactic properties. *left*: stellar mass, *left center*: SFR, *right center*: $\Sigma_{\rm SFR}$, *right*: $\Sigma_{\rm sSFR}$. Top (bottom) rows are plotted versus [O III] (Hα) $v_{\rm max}$. Individual galaxies are shown as blue circles, while results from composite spectra are shown as black squares.

velocity is low (FWHM$_{\rm br}$ < 300 km s^{-1}), such that the emission from the broad component is indistinguishable from that of HII regions. Likewise, the detection of a distinct broad emission component likely requires a high SNR of the desired line, and galaxies with strong rest-optical emission lines are also associated with higher star-formation properties. We explore possible dependencies of ionized gas outflow properties on galactic properties in the following sections.

4.4.2 Outflow Velocity

A fundamental property of outflowing gas is its velocity. As stellar feedback in star-forming galaxies likely drives their outflows, correlations between outflow velocity and star-formation properties should naturally arise. Several studies have found that the velocity of cool, neutral gas outflows traced by low-ionization UV absorption lines increases with the

star-formation rate and star-formation-rate surface density of the host galaxy (e.g., Chen et al., 2010; Steidel et al., 2010; Martin et al., 2012; Rubin et al., 2014; Chisholm et al., 2015; Heckman et al., 2015; Bordoloi et al., 2016; Weldon et al., 2022). However, fewer studies have explored how the velocity of warm ionized gas outflows varies with SFR, $\Sigma_{\rm SFR}$, and other properties of the host galaxy (Swinbank et al., 2019; Davies et al., 2019; Avery et al., 2021; Couto et al., 2021; Davis et al., 2023).

We estimate the maximum outflow velocity from the broad component following previous studies as $v_{\rm max} = \Delta v_{\rm br} - 2\sigma_{\rm br}$, where $\sigma_{\rm br}$ is the Gaussian sigma value of the broad component (see Genzel et al., 2011, 2014; Wood et al., 2015). Figure 4.4 presents $v_{\rm max}$ derived from [O III] and Hα as a function of stellar mass, SFR, $\Sigma_{\rm SFR}$, and $\Sigma_{\rm sSFR}$. Considering individual galaxies (blue circles), we find no significant correlations between $v_{\rm max}$ and properties of the host galaxy, which may be due to limitations in our fitting technique (Section 4.5.3). On the other hand, the composite spectra (black squares) exhibit clear trends with velocity. The highest stellar mass, SFR, and $\Sigma_{\rm SFR}$ bins appear to have gas at significantly larger $V_{\rm max,[O\,III]}$ compared to the lowest bins. Similarly, $V_{\rm max,H\alpha}$ appears faster in the higher (lower) $\Sigma_{\rm SFR}$ ($\Sigma_{\rm sSFR}$) bin compared to the lowest (highest) bin. The sudden increase in $V_{\rm max,[O\,III]}$ in the highest galactic properties bins may reflect different initial conditions of the outflowing gas. The [O III]–emitting zone is likely more compacted compared to the HII region, due to the higher ionization potential of OII than HI – 35 eV and 13.6 eV, respectively. Removing the [O III] gas from a smaller, more tightly bound region then likely requires more extreme conditions (i.e., higher SFR, $\Sigma_{\rm SFR}$). The trend of galaxies with higher SFR and $\Sigma_{\rm SFR}$ hosting faster outflows agrees with the picture of

outflows driven by feedback from star-formation. Although, these global trends are quite weak, with $V_{\rm max,H\alpha} \propto \Sigma_{\rm SFR}^{0.07\pm0.03}$. On smaller 1 – 2 kpc scales, Davies et al. (2019) measured broad Hα components in composites of IFU Hα observations from 28 $z \sim 2.3$ galaxies and found $\Sigma_{\rm SFR}$ and outflows are closely, with $v_{\rm out} \propto \Sigma_{\rm SFR}^{0.34\pm0.10}$. Conversely, the $V_{\rm max,H\alpha}$ trend with $\Sigma_{\rm sSFR}$ suggests that – at a fixed $\Sigma_{\rm SFR}$ – faster outflows are launched from high-mass galaxies relative to low-mass ones. However, the observed trend is quite weak, with $V_{\rm max,H\alpha}$ increasing only by $\sim$80 km s^{-1} across the roughly 1.5 dex range in $\Sigma_{\rm sSFR}$ for the composite spectra.

4.4.3 Mass-Loading Factor

In this section, we turn towards estimating the mass-loading factor of the ionized outflows, focusing on galaxies with a detected broad Hα component. While a similar analysis is possible for the [O III] line, there are additional dependencies (i.e., the chemical enrichment of the outflowing gas) that further complicate the derived values. Previous studies have found that the mass-loading factor derived from [O III] is consistent with but systematically lower than values derived from Hα (see Carniani et al., 2015; Marasco et al., 2020; Concas et al., 2022).

Adopting the simple outflow model described in Genzel et al. (2011) and Newman et al. (2012), we estimate the mass outflow rate ($\dot{M}_{\rm out}$) of the galaxies. This model is based on three main assumptions: (1) the geometry of the outflow is multi-conical or spherical with constant velocity and mass loss, (2) the gas in the broad component is photoionized and in case B recombination with an electron temperature of T_e=10^4K, and (3) the electron density

of the broad component does not vary significantly with radius. Under these conditions the mass outflow rate can be calculated as:

$$\dot{M}_{\rm out} = \frac{1.36 m_H}{\gamma_{\rm H\alpha} n_e} \left(L_{\rm H\alpha,\ Broad}\right) \frac{V_{\rm out}}{R_{\rm out}} \tag{4.2}$$

where m_H is the atomic mass of hydrogen, $\gamma_{\rm H\alpha}(T_e) = 3.56{\times}10^{-25} T_4^{-0.91}$ erg cm^{-3} s^{-1} is the Hα emissivity at an electron temperature $T_4 = 10^4$K, n_e is the electron density of the outflow, $L_{\rm H\alpha,Broad}$ is the extinction corrected Hα luminosity of the broad component, $V_{\rm out}$ is the velocity of the outflow, and $R_{\rm out}$ is the radial extent of the outflow.

We adopt this model as the observations are not resolved and to facilitate comparisons with similar studies in the literature. However, varying the assumptions of the model can have noticeable effects on $\dot{M}_{\rm out}$. For example, the inverse dependence of $\gamma_{\rm H\alpha}$ on electron temperature creates a temperature dependence for $\dot{M}_{\rm out}$. Sanders et al. (2020) preformed direct measurements of T_e from the [O III]λ4363 line for four star-forming galaxies in the MOSDEF survey. They found an ISM T_e of $\sim$14000 $-$ 17000 K, with a value of 15400 K for a composite of the four galaxies. If we assume this higher electron temperature for the outflowing gas, $\dot{M}_{\rm out}$ would increase by a factor of 1.5. At higher temperatures, the gas responsible for the broad component may be dominated by collisional ionization, rather than photonized. Genzel et al. (2011) considered collisional ionisation at $T_e = 2{\times}10^4$ K and found that the inferred $\dot{M}_{\rm out}$ decreased by a factor of 2, with the difference decreasing at lower temperatures.

In principle, the electron density of the outflowing gas can be calculated from the broad [S II]λ6717/[S II]λ6732 line ratio (Osterbrock, 1989; Sanders et al., 2016). Using

the composite spectra, we attempt to measure this ratio directly. However, the broad components of the [S II] doublet are not well constrained in any of the composite spectra. Instead, we follow a similar approach as Förster Schreiber et al. (2019) and search for broad components in a composite spectrum of the 33 galaxies with detected broad Hα components. In this new composite, the broad components of the [S II] doublet are well constrained. Using the relationship from Sanders et al. (2016), we estimate an electron density of 420^{+260}_{-200} cm^{-3}, consistent within the large uncertainties of the 300 – 500 cm^{-3} range of $n_{e,\mathrm{broad}}$ reported for ionized outflows in local and high-z star-forming galaxies (e.g., Arribas et al., 2014; Ho et al., 2014; Förster Schreiber et al., 2019; Fluetsch et al., 2021). The intrinsic Hα luminosity of the broad component is measured individually for each galaxy by scaling the total corrected Hα luminosity by the broad-to-single Hα ratio ($\mathrm{F_{broad}/F_{Single}}$). For V_{out}, we adopted the maximum velocity from Section 4.4.2. We take the radial extent of the outflows to be their hosts' effective radii, $R_{\mathrm{out}} = R_{\mathrm{E}}$, motivated by high-resolution adaptive optics SINFONI observations of ionized gas outflows in high redshift star-forming galaxies indicating that outflows typically extend over the half-light radius (Newman et al., 2012; Förster Schreiber et al., 2014).

The mass-loading factor (η_m) represents the amount of mass removed by an outflow per stellar mass formed, and, for star-formation driven outflows, is thought of as a diagnostic of outflow efficiency. Specifically, η_m is defined as the outflow rate normalized by the star formation rate: $\eta_m = \dot{M}_{\mathrm{out}}/\mathrm{SFR}$. An estimate of the SFR can be obtained from the narrow

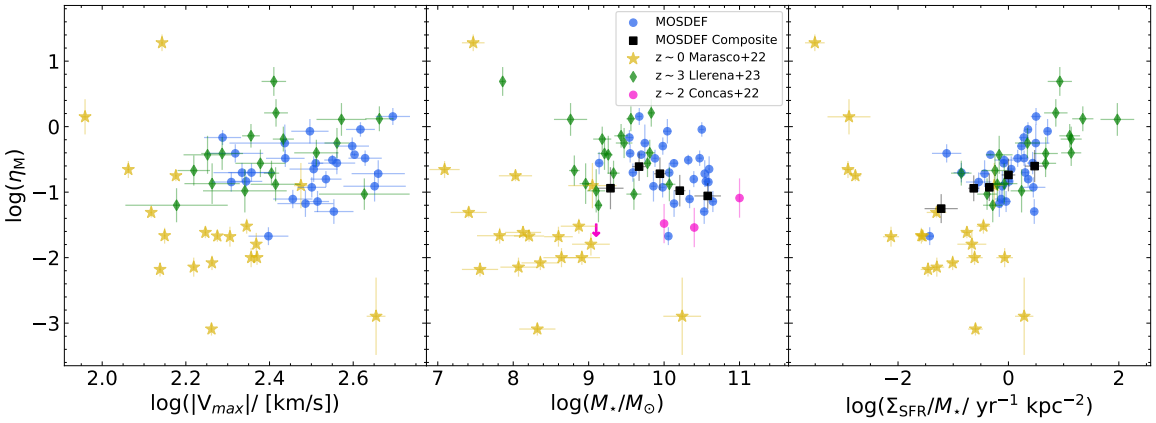

Figure 4.5: Mass-loading factor versus various galactic properties, compared with values from the literature. *left*: outflow velocity, *center*: stellar mass, *right*: $\Sigma_{\rm SFR}$. Individual MOSDEF galaxies are shown as blue circles, while results from composite spectra are shown as black squares. Markers show observational results including low-mass star-forming galaxies at $z \sim 3$ from Llerena et al. (2023, green diamonds), local starburst dwarf galaxies from Marasco et al. (2023, yellow stars), and composites of $z \sim 2$ star-forming galaxies from Concas et al. (2022, pink circles).

Gaussian component of Hα tracing the ongoing star formation activity in the galaxy disk:

$$\mathrm{SFR}_{\mathrm{Narrow}} = 3.236 \times 10^{-42} \left(L_{\mathrm{H}\alpha} \frac{F_{\mathrm{Narrow}}}{F_{\mathrm{Single}}} \right) [M_{\odot}/yr] \tag{4.3}$$

where the first term is the conversion factor between Hα luminosity and SFR from Reddy et al. (2018b) (Section 4.2.3) and $F_{\mathrm{Narrow}}/F_{\mathrm{Single}}$ is the fraction of the total flux in the narrow component. When divided by the narrow component Hα SFR and simplified, Equation 4.2 can be written as

$$\eta_m \approx 3.05 \left(\frac{100\ \mathrm{cm}^{-3}}{n_e} \right) \left(\frac{V_{\mathrm{max}}}{300\ \mathrm{km\ s}^{-1}} \right) \left(\frac{\mathrm{kpc}}{R_{\mathrm{E}}} \right) \left(\frac{F_{\mathrm{Broad}}}{F_{\mathrm{Narrow}}} \right) \tag{4.4}$$

where $F_{\mathrm{Broad}}/F_{\mathrm{Narrow}}$ is the broad-to-narrow flux ratio. Table 4.2 lists the mass-loading factor for galaxies with a detected broad Hα component, finding η_m ranging from 0.02

– 1.44, with a median of 0.23. Uncertainties on η_m are taken as the dispersion of 1000 realizations after perturbing $v_{\rm max}$, $R_{\rm E}$, and $F_{\rm Broad}/F_{\rm Narrow}$ by their errors.[6] We do not include errors in the electron density and temperature assumed, and including these errors would increase the error on η_m by ∼0.2 dex.

The values we estimate for $\eta_m$are similar to those of other recent studies of ionized outflows. Swinbank et al. (2019) stacked Hα emission of ∼530 star-forming galaxies at $z \sim 1$ and found $\eta_m \sim 0.1$–0.4. Similarly, at $z \sim 2$, Davies et al. (2019) and Förster Schreiber et al. (2019) stacked Hα emission from star-forming galaxies finding $\eta_m \sim 0.3$–0.5 and $\eta_m \sim 0.1 - 0.2$, respectively. Recently, Llerena et al. (2023) investigate ionized outflows in a sample of low-mass ($7.8 < \log(M_\star/M_\odot) < 10.2$) star-forming galaxies at $z \sim 3$ and found a wide range of η_m, from 0.1 to 4.9. However, there is debate about the typical value of η_m in star-forming galaxies, with some studies reporting values less than 0.1 (Concas et al., 2022; Marasco et al., 2023). The tension in η_m between various studies is likely due to different assumptions when estimating $\dot{M}_{\rm out}$, or differences in the methodology used to measure ionized outflows (see discussion in Concas et al., 2022).

Here, we explore which, if any, internal galaxy properties correlate with the mass-loading factor. Of particular interest is how η_m potentially scales with the (1) ionized outflow velocity, (2) stellar mass, and/or (3) $\Sigma_{\rm SFR}$. Regarding the first two properties, simple analytical arguments and numerical simulations predict an anti-correlation between the mass-loading factor and the outflow velocity or stellar mass of galaxies, suggesting that outflows are more efficient at removing material from the shallower potential wells

[6]The uncertainty in $R_{\rm E}$, adopted as the radial extent of the outflows, is likely smaller than true uncertainty in R_{out}.

of lower-mass galaxies (Murray et al., 2005; Oppenheimer & Davé, 2008; Muratov et al., 2015). Additionally, the scaling relation between η_m and outflow velocity or stellar mass is predicted to depend on the driving mechanism of the outflow, which scales steeper if the outflows are energy-driven and shallower if they are momentum-driven (see Section 4.5.1). At the same time, one might expect a correlation with $\Sigma_{\rm SFR}$, which traces the concentration of star formation in a galaxy, as regions with higher $\Sigma_{\rm SFR}$ will be more efficient at injecting energy and momentum into the ISM from overlapping supernovae or stellar winds from massive stars, resulting in conditions amenable for outflows.

Figure 4.5 presents the variation of the mass-loading factor as a function of $v_{\rm max}$, stellar mass, and $\Sigma_{\rm SFR}$ with similar results from the literature. In the MOSDEF-ionized sample, we find that η_m is not significantly correlated with $v_{\rm max}$, while marginally correlated with both stellar mass (2.5σ) and $\Sigma_{\rm SFR}$ (2.2σ). Galaxies with lower masses appear to have larger η_m than higher mass galaxies, with η_m decreasing by a factor of 0.6 over a mass range $\log(M_\star/M_\odot) = 9$ – 10.7. Although, at a fixed stellar mass, there is a large range in η_m, which may reflect the variation in outflow efficiency amongst different outflow phases for individual galaxies. On the other hand, galaxies with *higher* $\Sigma_{\rm SFR}$ appear to have larger η_m than lower $\Sigma_{\rm SFR}$ galaxies, with η_m increasing 1.8 dex over an $\Sigma_{\rm SFR}$ range $\log(\Sigma_{\rm SFR}/M_\odot$ yr^{-1} kpc^{-2}) = -1.4 – 0.7.

A negative relation between η_m and stellar mass is predicted by analytical arguments and simulations. Observations, however, have yielded ambiguous results, as shown in Fig 4.5. Studies that measure ionized outflows in composite spectra tend to find a roughly constant relation between η_m and stellar mass, while studies of individual galaxies generally

find the expected negative correlation between η_m and stellar mass. At $z \sim 2$, Concas et al. (2022) reported relatively low mass-loading factors that exhibit little variation among three stellar mass bins below $10^{11} M_{\odot}$, but increases ∼0.2 dex towards the highest mass bin – likely due to increased AGN activity in more massive systems. Meanwhile, Llerena et al. (2023) and Marasco et al. (2023) found that η_m decreases with stellar mass for individual $z \sim 3$ star-forming and local dwarf starburst galaxies, respectively. However, the mass-loading factors of Marasco et al. (2023) are offset towards significantly lower values compared to the MOSDEF-ionized sample. This discrepancy may be due to differing methodologies used to parameterize the outflow velocity, varying assumptions about the outflow geometry, or it may suggest a possible redshift evolution of the mass-loading factor.

The correlation between η_m and $\Sigma_{\rm SFR}$ agrees with the simple outflow picture: galaxies with higher $\Sigma_{\rm SFR}$ are more effective in driving outflows. However, this relation is likely caused by an underlying correlation between $\Sigma_{\rm SFR}$, η_m, and $R_{\rm E}$. With our adopted definitions, $\Sigma_{\rm SFR} \propto {R_{\rm E}}^{-2}$ and $\eta_m \propto {R_{\rm E}}^{-1}$, thus a positive relation would naturally arise. A similar positive relationship is found by Llerena et al. (2023) who also derived $\Sigma_{\rm SFR}$ and η_m using effective radii. Conversely, Marasco et al. (2023) derived η_m with outflow radii measured directly from their sample – independent of the effective radius – and found a strong negative correlation between η_m and $\Sigma_{\rm SFR}$.

4.4.4 Outflow Energetics

In addition to mass, outflows are characterized by the amount of energy and momentum they remove from the ISM. In Appendix 4.7.1, we present a derivation for the

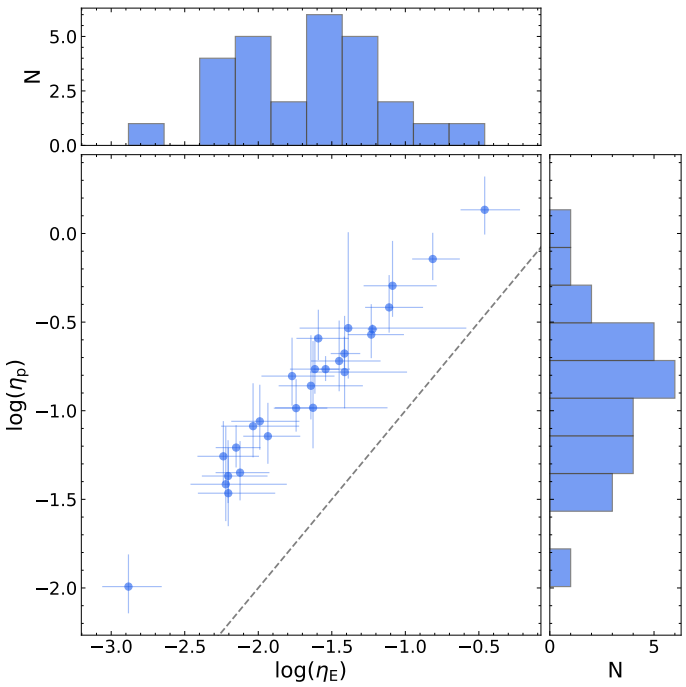

Figure 4.6: Momentum-loading factor versus energy-loading factor. The dashed line marks the one-to-one line. In all of the galaxies, the outflows appear to carry away more momentum than kinetic energy from the ISM.

energy and momentum outflow rates and reference rates of energy and momentum produced within galaxies. Briefly, the energy and momentum outflow rates are calculated from the mass outflow rate (Equation 4.2). Reference rates are calculated following similar analytic arguments as Murray et al. (2005), focusing on the injection of energy and momentum from type IIa supernovae. Dividing the outflow rates by the reference rates and simplifying, the energy- and momentum-loading factors of the outflowing ionized gas are given by:

$$\eta_E = 0.27 \left(\frac{100\ \mathrm{cm}^{-3}}{n_e}\right) \left(\frac{V_{\mathrm{max}}}{300\ \mathrm{km\ s}^{-1}}\right)^3 \left(\frac{\mathrm{kpc}}{R_{\mathrm{E}}}\right) \left(\frac{F_{\mathrm{Broad}}}{F_{\mathrm{Narrow}}}\right) \tag{4.5}$$

$$\eta_p = 1.76 \left(\frac{100\ \mathrm{cm}^{-3}}{n_e}\right) \left(\frac{V_{\mathrm{max}}}{300\ \mathrm{km\ s}^{-1}}\right)^2 \left(\frac{\mathrm{kpc}}{R_{\mathrm{E}}}\right) \left(\frac{F_{\mathrm{Broad}}}{F_{\mathrm{Narrow}}}\right) \tag{4.6}$$

Directly comparing Equation 4.5 and 4.6, we find that the ratio of the momentum- to energy-loading factor is simply:

$$\frac{\eta_p}{\eta_E} = 6.5 \left(\frac{300 \text{ km s}^{-1}}{V_{\rm max}} \right) \tag{4.7}$$

For the sample, $v_{\rm max}$ ranges between $\sim$200 – 500 km s^{-1}, suggesting that these ionized outflows carry away more momentum than kinetic energy from the ISM, with η_p/η_E ranging from $\sim$4 to 10. We further test this result by varying the various physical parameters within a factor of 2 from their adopted values (see Appendix 4.7.1). Considering the most favorable case, η_p remains larger than η_E by about a factor of 2.

Taken at face value, the larger momentum-loading factors suggest that the ionized outflows are primarily momentum driven. However, the comparison between momentum- and energy-loading factors is highly model dependent. There are other sources of energy and/or momentum within the galaxy not accounted in our analytic reference rates (e.g., cosmic rays, winds from massive stars), such that η_E and η_p are likely upper limits. For example, in Figure 4.6, there are a few galaxies with abnormally high energy- and momentum-loading factors ($\eta_E > 0.1$, $\eta_p \sim 1$), which would suggest that their ionized outflows remove nearly all of the energy and momentum produced.[7] Additionally, the assumptions made in our calculations may be incorrect. Based on high-resolution "local patch" simulations of supernovae in the ISM, Kim & Ostriker (2015) argue that the momentum injected by supernovae is better represented by the spherical momentum at the end of the Sedov-Taylor stage when an SN blast wave cools and a shell forms, rather than the initial injected mo-

[7]High-resolution hydrodynamical simulations find that the energy from supernovae is rapidly thermalized and radiated away, with effectively $\sim$10% transferred to the ISM to drive outflows (Creasey et al., 2013).

mentum. If we adopted this convention, η_p decreases by $\sim$0.72 dex, such that η_p and η_E are about equal. In Section 4.5.1, we further investigate the primary driving mechanism of the ionized outflows.

4.5 Discussion

4.5.1 Driving Mechanism

While there is a general picture of the origin of outflows and their role in galaxy evolution, the physical mechanism(s) that generates and sustains outflows remains an open question. In star-forming galaxies, outflows could be launched by momentum injected into the ISM by supernovae, or by radiation pressure acting on dust grains accelerating gas coupled to the dust ("momentum−driven"; Murray et al., 2005, 2011). In addition to injecting momentum, mechanical energy released from multiple, overlapping supernovae thermalizes a large fraction of nearby gas forming a hot over-pressured bubble that sweeps up ambient ISM material until it is ejected from the galaxy ("energy−driven"; Chevalier & Clegg, 1985). Finally, cosmic rays produced by supernovae can transfer momentum to gas after scattering off of magnetic inhomogeneities in the ISM as they diffuse out of a galaxy (see discussions in Heckman & Thompson, 2017; Zhang, 2018). Simple analytic arguments predict that for purely momentum-driven outflows the mass-loading factor scales as $\eta_m \propto V_{\rm out}^{-1}$ and $\eta_m \propto M_\star^{-1/3}$. Similarly, for purely energy-driven outflows: $\eta_m \propto V_{\rm out}^{-2}$ and $\eta_m \propto M_\star^{-2/3}$ (Murray et al., 2005). As these mechanisms are likely dominate under different

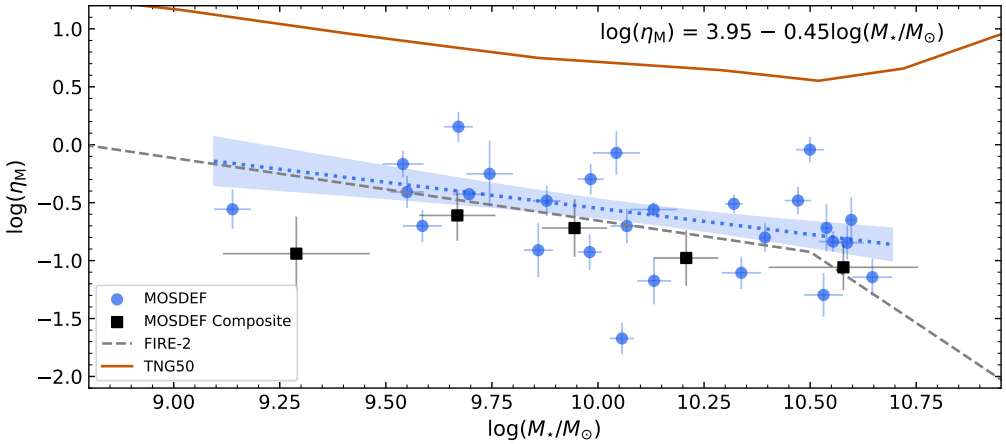

Figure 4.7: Mass-loading factor as a function of stellar mass, compared with predictions from simulations. Individual MOSDEF galaxies are shown as blue circles, while results from composite spectra are shown as black squares. The dotted blue line and shaded region (68% confidence intervals) is the best-fit line to the MOSDEF-ionized galaxies. The functional form of the line is listed in the upper-right corner. Lines show theoretical predictions from the FIRE-2 Pandya et al. (2021, dashed grey) and Illustris TNG50 Nelson et al. (2019, solid orange) cosmological simulations.

galactic conditions, outflows could be driven by a combination of mechanical energy, radiation pressure, and cosmic rays.

Here, we investigate the marginally-correlated trend of $\eta_m$with stellar mass. Figure 4.7 presents the best-fit linear regression in logarithmic space for galaxies with detected Hα outflows:

$$\log(\eta_{\rm M}) = (3.95 \pm 0.54) - (0.45 \pm 0.06)\log(M_\star/M_\odot) \tag{4.8}$$

The power-law index of -0.45 is intermediate between the $M_\star^{-2/3}$ and $M_\star^{-1/3}$ dependence predicted for energy- or momentum-driven outflows, suggesting that these ionized outflows are driven by a combination of mechanical energy and radiation pressure.

In Figure 4.7, we also show the comparison between our derived η_m–$M_\star$ relation to theoretical predictions from Illustris TNG50 (Nelson et al., 2019; Pillepich et al., 2019) and

Feedback in Realistic Environments (FIRE; Hopkins et al., 2014, 2018, 2023) cosmological simulations. In particular, we focus on the TNG50 values derived from outflowing gas at a fixed distance of 10 kpc from the galaxy with a radial velocity > 0 km s^{-1} and the FIRE-2 values for warm ($10^3 < T < 10^5$ K) outflowing gas at a fixed thickness of 0.1–0.2$R_{\rm vir}$[8] (Pandya et al., 2021). We note that this is not a direct comparison, as the simulations measure η_m at $\sim$4$\times$ larger distances than the effective radii used in our derivation of η_m. As the properties of the outflowing gas (e.g., density, velocity) change with distance, η_m would also vary with distance. For example, Nelson et al. (2019) measured lower η_m at larger distances (see their Figure 5).

Below $\log(M_\star/M_\odot) \approx 10.5$, there is general agreement of a negative correlation between stellar mass and η_m. Unsurprisingly, the theoretical values from TNG50 are larger than the observed MOSDEF-ionized mass-loading factors. In these types of large-volume simulations, small scales are not resolved, instead relying on sub-grid recipes to describe stellar feedback, which may overpredict the efficiency of stellar feedback. Additionally, the TNG50 values represent the total mass-loading factor of all phases, rather than our values which only trace ionized outflows from rest-optical emission lines. On the other hand, there is remarkable ($\sim 1\sigma$) agreement between our derived relation and the theoretical prediction from FIRE-2. Pandya et al. (2021) reported a broken power law dependence between η_m and stellar mass, with a shallower (-0.54$\pm$0.05) slope below and steeper (-2.45$\pm$0.3) slope above $\log(M_\star/M_\odot)\sim$10.5. Although, at $\log(M_\star/M_\odot) \sim 10.5$, we do not see strong evidence for a sudden drop in η_m. The broken power law relation may be due to decreasing ISM resolution

[8]The average $R_{\rm vir}$ of our sample is 100 kpc – estimated using the stellar-to-halo mass relation of Behroozi et al. (2019)

in the FIRE-2 simulations towards higher stellar masses, such that η_m is underestimated. However, we caution our derived relation is determined from a *marginal* correlation between η_m and stellar mass.

4.5.2 Fate and impact of ionized outflows

The impact of outflows on their hosts' evolution is directly related to the amount of material that escapes from the gravitational potential well of their host. Here, we investigate whether the ionized outflows have sufficient speeds to escape the gravitational potential of their host or whether the gas is retained and likely recycled as a part of a galactic fountain. For an isothermal gravitational potential truncated at $r_{\rm max}$, the escape velocity at radius r is

$$v_{\rm esc}(r) = v_{\rm circ}\sqrt{2\left[1 + \ln\left(r_{\rm max}/r\right)\right]} \tag{4.9}$$

where $v_{\rm circ}$ is the circular velocity of the galaxy, taken from Price et al. (2020). Briefly, for galaxies with resolved and detected rotation measured from their 2D spectra, circular velocities are calculated as $v_{\rm circ}(1.3R_{\rm E}) = \sqrt{V(1.3R_{\rm E})^2 + 4.4\sigma^2_{V,0}}$, where $\sigma_{V,0}$ is the intrinsic galaxy velocity dispersion.[9] Otherwise, circular velocities are inferred using integrated velocity dispersions and the best-fit ensemble V/σ from galaxies without detected rotation.

Figure 4.8 shows the maximum ionized outflow velocity as a function of circular velocity. To gauge whether the gas escapes, we adopt a rather conservative threshold of $r_{\rm max}/r = 33$ ($v_{\rm esc} = 3v_{\rm circ}$), such that outflowing gas likely has enough velocity to escape or is retained (Veilleux et al., 2005, 2020). In the top panel, we find that outflows detected

[9]We take $r = 1.3R_{\rm E}$ for the radius for galaxy's circular velocity as a conservative choice, as this is the radius where an exponential rotation curve peaks.

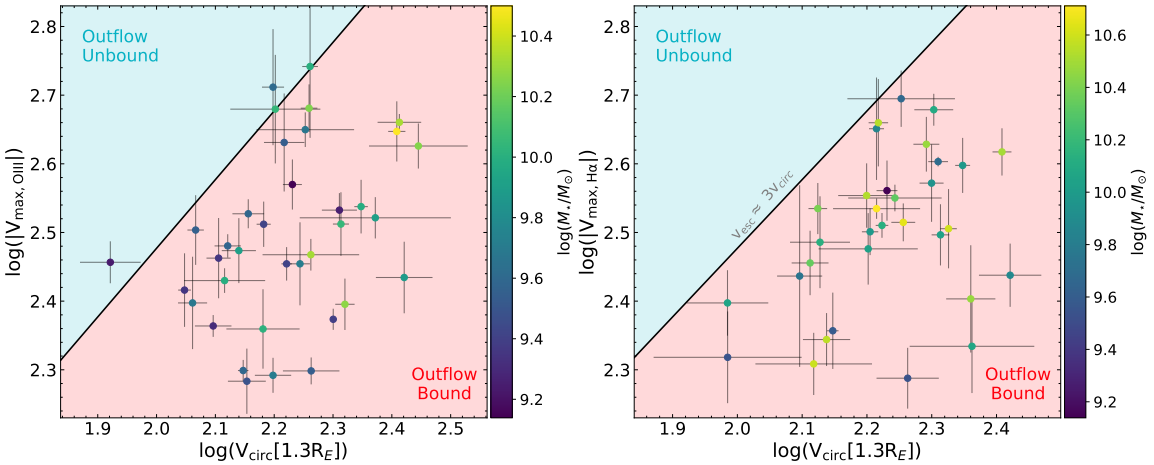

Figure 4.8: Maximum ionized outflow velocity versus circular velocity. *Left*: [O III] *Right*: Hα. The line denotes the gas velocity required to escape the gravitational potential assuming an isothermal gravitation potential that extends to a maximum radius of $r_{\rm max}$, see Equation 4.9. Outflowing gas above $3v_{\rm circ}$ ($r_{\rm max}$ / r = 33) likely has enough velocity to escape, while below $3v_{\rm circ}$ the gas is likely retained. Objects are color coded according to their stellar mass.

in [O III] appear to escape from four and are retained by 32 galaxies, while outflows detected in Hα are retained in all of the galaxies. In addition, we do not find that outflows from shallower potential wells lie closer to the $v_{\rm esc} = 3v_{\rm circ}$ line (i.e., more easily removed) compared to outflows from deeper potential wells. It thus seems that the ionized outflows studied in this work are predominantly retained, recycling back onto the galaxy as part of a galactic fountain, rather than escaping into the IGM. However, these outflows could still potentially contribute to heating the CGM, reducing the rate at which gas can accrete and suppressing star formation.

Multi-wavelength observations and multi-phase simulations have investigated the contribution of ionized outflows to the total mass and energy outflow rates. On the observation side, studies on molecular, neutral, and ionized outflows in local AGNs, ULIRGs, and starburst galaxies (e.g., Cicone et al., 2014; Carniani et al., 2015; Leroy et al., 2015; Rupke

et al., 2017; Fluetsch et al., 2019, 2021) have found that the molecular and neutral phases typically dominate the mass outflow rate. Similarly, local patch and zoom-in simulations predict that the majority of outflowing energy (mass) is carried in the hot (cold) phase (Kim & Ostriker, 2018; Kim et al., 2020; Pandya et al., 2021). In the MOSDEF-ionized sample, the high fraction of warm, ionized outflows retained and their modest mass-, energy-, and momentum-loading factors suggest their contribution may be negligible, even during the peak of cosmic star-formation. However, without observations of other outflow phases (i.e., hot, neutral, molecular), we cannot constrain the contribution of these outflows to the total mass, energy, and momentum outflow rates.

4.5.3 Significance of Outflow Velocity and Galactic Properties

As discussed in Section 4.4.1, in individual galaxies, neither the maximum ionized outflow velocity derived from broad [O III] or Hα emission components appear to correlate significantly with any galactic property. In particular, the lack of a relation between outflow velocity and star formation properties appears to be in tension with the picture of stellar feedback driven outflows, as the level of star formation activity should set the amount of energy and momentum injected into the ISM. However, this apparent lack of observed relations may be due to contributions to the broad component from turbulent motions and/or the limited dynamic range of properties probed by galaxies with detected broad components in the MOSDEF sample.

Turbulence

Throughout this paper, we have adopted the interpretation that the broad component of rest-optical emission lines is a tracer of ionized gas entrained in star-formation driven outflows. However, the broad emission component may originate from other sources. Here, we consider whether shocks can explain the observed broad emission components within the sample.

Outflows can produce widespread shocks throughout a galaxy by injecting mechanical energy into the ISM. As shocked regions have high electron temperatures and ionization states (e.g., Dopita & Sutherland, 1996), collisional excitation and ionization from shocks can produce a variety of optical emission lines, creating broad emission line components. In slow shocks (V $<$ 200 km s^{-1}), the shock front moves faster than the photoionization front, producing relatively weak high ionization lines, but strong low ionization lines. Conversely, in fast shocks (V $>$ 200 km s^{-1}) a supersonic photoionization front pre-ionizes the gas – known as a precursor – which produces strong high ionization lines. The emission line ratios of shocked gas differ from those of gas photoionized in HII regions, often with higher [N II]/Hα and [O III]/Hβ ratios similar to gas photoionized by AGN (e.g., Allen et al., 2008; Alarie & Morisset, 2019).

If the broad components arise from shocked gas, the width of the broad component would trace the velocity of the shock rather than the velocity of outflowing material. To investigate whether shocks can explain the broad components, we consider MAPPINGS V (Sutherland & Dopita, 2017; Sutherland et al., 2018) fully radiative shock models from the

3MdBs[10] database (Alarie & Morisset, 2019). This database provides simulated emission line ratios for shock gas, the precursor, and a combination of shock and precursor for multiple grids. To facilitate comparisons between our observations and the models, we use the low metallicity grid, matched to the broad range of metallicities, $6.64 < 12+\log(\mathrm{O/H}) < 9.28$, used by Gutkin et al. (2016). This grid spans a large range in shock parameters – for each metallicity – with shock velocities of $V_s = 100$ – 1000 km s^{-1}, magnetic field parameters of $\mathrm{B_o} = 10^{-4}$ – 10 μG, and pre-shock densities of $\mathrm{n_o} = 1$ – 10000 cm^{-3}.

For this analysis, we focus on the composite spectra binned by stellar mass, as the broad components of Hβ and [N II] are not robustly detected in individual galaxies, and mass is estimated independently from the Hα line, thus unlikely influenced by broad emission. The widths of the broad components for each mass bin are larger than 200 km s^{-1}, thus we consider the shock+precursor models. Additionally, we restrict the models to those that have a pre-shock density $\leq$100 cm^{-3} and to shock velocities within 50 km s^{-1} of the broad component width of a mass bin.

To determine whether shocks can explain the observed broad components in the composite spectra, we consider their (1) broad emission line ratios, (2) inferred electron density, and (3) emitting areas. We first compare the measured broad emission line ratios – [O III]/Hβ and [N II]/Hα – from each mass bin to the predicted shocked+precursor model ratios, keeping the ten models per bin, which best match the observations. Figure 4.9 shows the BPT diagram for the five stellar mass bins and their best-matched models. A majority of the best-matched models for the lowest, second-lowest, and highest mass bins (red, blue, and orange diamonds) are inconsistent with the observed line ratio(s) by $\geq 3\sigma$.

[10] http://3mdb.astro.unam.mx/

On the other hand, there are models that can reproduce the observed line ratios of the middle and second-highest mass bins (green and purple diamonds) within their uncertainties. In addition to directly comparing line ratios, we can use them to infer other physical properties. If the broad emission arises due to shocks, the electron density measured from the broad [S II]λ6717/[S II]λ6732 line ratio would come from the post-shock recombination regions where the gas densities are expected to be higher than the pre-shock densities (e.g., Allen et al., 2008). We measure the electron density from the [S II] ratio of the ten best-matched models for each mass bin using the relationship from Sanders et al. (2016). For the upper three mass bins, the inferred electron densities from the models span over two orders of magnitude, with a majority of the models within 1.5σ of $n_e = 420$ cm^{-3} derived in Section 4.4.3. Conversely, the inferred electron densities in the two lowest mass bins are consistently larger – ranging from $\sim$4000 to 7000 cm^{-3}. Finally, the database also provides the predicted Hβ luminosity per unit area for the different models. Using the best-matched models, we calculate the emitting area required to produce the observed broad component Hβ luminosity. For the two lowest mass bins, the required emitting areas are $\sim$2 kpc^2, consistently smaller than the average size of the galaxies in the composite – 8 and 13 kpc^2, respectively. On the other hand, for the three upper mass bins, the emitting areas are larger, ranging from 4 to 20$\times$ than their average sizes.

These comparisons show that no shock model simultaneously agrees with the observed broad component line ratios, sample electron density, or the average area of the composite spectra. The best-matched [O III]/Hβ or [N II]/Hα model line ratios are inconsistent with the observed broad line ratios in the lowest, second-lowest, and highest mass

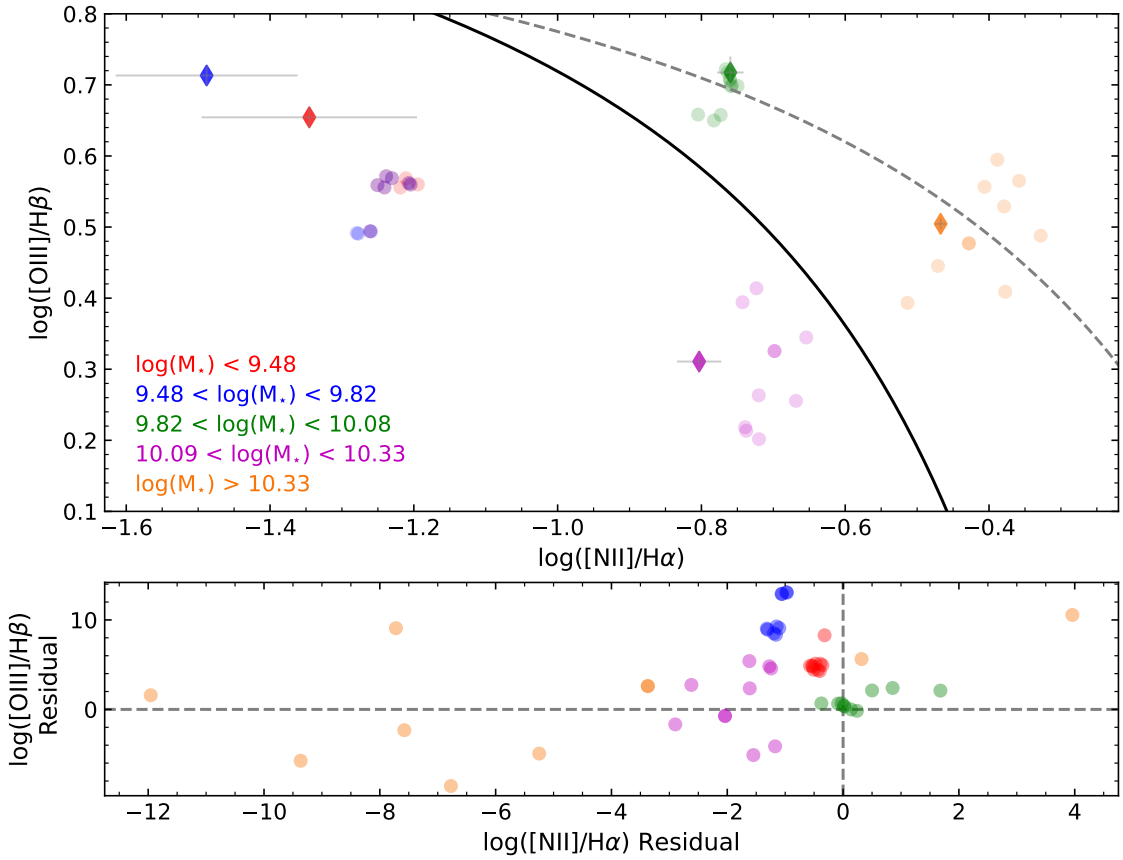

Figure 4.9: BPT diagram for composite spectra binned by stellar mass and shocked+precursor models from the 3MdBs database (Alarie & Morisset, 2019). The broad component and ten best shocked+precursor model emission line ratios are shown as diamonds and transparent circles. The solid black line separates star-forming galaxies and AGN (Kauffmann et al., 2003). The dashed gray line is the "maximum starburst" line, where above this line lie AGN from Kewley et al. (2001). The bottom panel shows the residuals after subtracting the shocked+precursor models from the observed broad component line ratios.

bins, the inferred model electron densities for the lowest and second-lowest mass bins are $\gtrsim$ 15$\times$ higher than the value we derived in Section 4.4.3, and the emitting area to reproduce the broad Hβ luminosity is $\gtrsim 4\times$ the average area of galaxies in the middle, second-highest, and highest mass bins. We therefore conclude that shocks alone cannot produce the broad emission components observed in this study.

This analysis, however, does not rule out other possible origins for the broad emission component. The broad emission may be a mixture of outflowing gas, shocked gas, and other turbulent motions, such as turbulent mixing layers between hot and cold outflow phases. Recent studies that trace outflows using both blueshifted rest-UV absorption lines and broad components of rest-optical emission lines in individual galaxies have found that the two tracers are kinematically similar, thus the broad components can measure the kinematics of outflowing gas (Perrotta et al., 2021; Avery et al., 2022).

Other Physical Origins of Scatter

In addition to effect of turbulent motions, the lack of correlations between ionized outflow velocity and galactic properties may be due to line-of-sight affects or the small dynamic range probe by the sample (see discussion in Davies et al., 2019). If the observations are not well aligned with the outflowing material, then the derived velocities would not capture the true velocities. This in turn would increase the scatter between outflow velocity and galaxy properties and mask any potential correlations. Similarly, if relationships between outflow velocity and properties are weak, then they may not be captured over the small dynamic range probe by our sample. Decomposing rest-optical emission lines into separate narrow and broad components is challenging, with the detection of a broad

component requiring high signal-to-noise in the desired line. However, galaxies with strong nebular emission lines are also associated with elevated star-formation properties. Outflows from galaxies with low star-formation properties would be missed if their velocity is low ($\mathrm{FWHM_{br}} < 300$ km s^{-1}), such that the emission from the broad component is indistinguishable from that of HII regions. As shown in Figure 4.3, the galaxies with a detected broad component appear to be biased toward higher SFR and Σ_{SFR} compared to the remaining MOSDEF-ionized galaxies. In comparison, at low redshifts, Arribas et al. (2014) measured ionized outflows in luminous and ultra-luminous infrared galaxies and found that outflow velocity scales weakly with both SFR and Σ_{SFR}, covering three order-of-magnitude in SFR and Σ_{SFR}. Similarly, Xu et al. (2022) found the ionized outflow velocity scales weakly with SFR in local low-mass (10^4 – 10^7 $M_\odot$) galaxies. In addition to probing larger dynamic ranges, both of these studies detect broad components in lower SFR (Σ_{SFR}) galaxies, with a majority below 10 $M_\odot$ yr^{-1} (1 $M_\odot$ yr^{-1} kpc^{-2}). However, the weak scaling relations found by these studies suggest that the outflows are primarily energy-driven, as opposed to the mix of energy- and momentum-driven found for our sample (Section 4.5.1). In this case, the scaling between ionized outflow velocity and star-formation properties should be steeper than for a pure energy-driven outflow, thus a relation between ionized outflow velocity and star-formation properties may be captured over a smaller dynamic range. If the outflows are driven by a mix of energy and momentum, then the dynamic range probed by our sample is unlikely the reason why we find no correlation between outflow velocity and star-formation properties.

4.6 Conclusions

We have presented an analysis on the kinematics and energetics of ionized gas outflows within a sample of 598 typical star-forming galaxies at $z = 1.4 - 3.8$. Using the extensive spectroscopic dataset of the MOSDEF survey, we decompose strong nebular emission lines of individual galaxies and composite spectra into narrow and broad Gaussian components, tracing virial motions within the galaxy and outflowing gas. Maximum ionized outflow velocities are derived from the FWHM of the broad components, with a mean $v_{\rm max}$ = -320 ± 90 km s^{-1}. Using $v_{\rm max}$ in the outflow model described in Genzel et al. (2011), we estimate the mass-, energy- and momentum-loading factors of the ionized gas outflows. Our main conclusions are as follows:

- There is significant evidence for broad emission components in 10% (7%) of [O III] (Hα) detections, with their incidence becoming more prevalent among systems with higher SFR and $\Sigma_{\rm SFR}$.

- In individual galaxies, the maximum ionized outflow velocity is not significantly correlated with any galactic property. Composite spectra binned by stellar mass, SFR, and $\Sigma_{\rm SFR}$ show clear trends with $v_{\rm max}$, such that faster outflows are found in bins of higher galactic properties.

- The ionized outflows appear to remove more momentum than kinetic energy from the ISM, with $\eta_p/\eta_E\approx6.5$, suggesting that the outflows are primarily momentum-driven. However, these results are model-dependent, and it is likely that there are non-negligible contributions from mechanical energy.

- The mass-loading factor is marginally correlated (2.5σ) with stellar mass, scaling as $\eta_m \propto M_\star^{-0.45}$. This scaling is intermediate between the $M_\star^{-2/3}$ and $M_\star^{-1/3}$ dependence predicted for energy- or momentum-drive outflows, suggesting that these ionized outflows are driven by a combination of these mechanisms, with a larger contribution from radiation pressure acting on cool, dusty material.

- We find $\sim 1\sigma$ agreement between our derived $\eta_m - M_\star$ relation and the theoretical prediction from the FIRE-2 simulations for warm outflowing gas, measured at a larger radial distance.

- 11% (0%) of [O III] (Hα) maximum outflow velocities are larger than the escape velocity from the gravitational potential of their host, suggesting that the ionized outflows are often retained and likely setup a galactic fountain.

Obtaining robust constraints on the properties of outflows across different phases is crucial to understand their impact on galaxy evolution. Here, we have studied ionized outflows from typical $z \sim 2$ galaxies traced by broad components of rest-optical emission lines, finding that these outflows appear to play a negligible role, even during the peak of cosmic star-formation activity. A majority of the ionized outflows likely remain bound to the host galaxy, and their properties (e.g., $v_{\rm max}$, η_m) are independent or weakly correlated with galactic properties. However, these results are based upon simple models and assumptions on the geometry and physical condition of the outflowing gas. To build a better understanding of outflows, higher resolution spectroscopic data and spatially resolved imaging is necessary to constrain the geometry, extent, and conditions of outflowing gas.

Future progress will greatly benefit from such observations, probing both a wider dynamic range of galaxy properties and tracers of other outflow phases.

4.7 Appendix

4.7.1 Derivation of Energy and Momentum Rates

In this section, we derive equations for the energy- and momentum-loading factors of an outflow. A loading factor is the ratio of how much of a quantity (mass, energy, momentum, etc.) is carried out in an outflow relative to the amount produced within a galaxy, thus we define loading factor (η) as:

$$\eta_X = \frac{\dot{X}_{\rm out}}{\dot{X}_{\rm ref}} \tag{4.10}$$

where "out" and "ref" refer to the outflow rate and reference rate of the galaxy, respectively.

The energy and momentum outflow rates are easily calculated from the mass outflow rate (Section 4.4.3) as:

$$\dot{E}_{\rm out} = \frac{1}{2}\dot{M}_{\rm out}V_{\rm out}^2 \qquad\qquad \dot{p}_{\rm out} = \dot{M}_{\rm out}V_{\rm out} \tag{4.11}$$

On the other hand, estimating the reference energy and momentum rates is non-trivial due to the wide range of physical processes that can generate energy and momentum.

Focusing on type IIa supernovae, the total energy injected into the ISM from supernovae is:

$$\dot{E}_{\rm ref} = \dot{E}_{\rm SN} = \dot{N}_{\rm SN} E_{\rm SN} \approx 3.17 \times 10^{41} \left(\frac{\rm SFR_{narrow}}{M_\odot \ {\rm yr}^{-1}} \right) [{\rm erg/s}] \tag{4.12}$$

where $\dot{N}_{\rm SN}$ is the supernova rate, taken as one SN occurs per $100 {\rm M}_\odot$ formed, and $E_{\rm SN} = 10^{51}$ ergs is the mechanical energy released by a Type IIa SN.

Following the analytical arguments of Murray et al. (2005), for star-forming galaxies, we consider momentum injection from supernovae and a central starburst:

$$\begin{aligned} \dot{p}_{\rm ref} \rightarrow \dot{p}_{\rm SN} + \dot{p}_{\rm starburst} &\approx \sqrt{2 E_{\rm SN} M_{\rm ej}} \dot{N}_{\rm SN} + L_{\rm bol}/c \\ &\approx 3.285 \times 10^{33} \left(\frac{\rm SFR_{narrow}}{M_\odot \ {\rm yr}^{-1}} \right) [{\rm cm \ g \ s}^{-2}] \end{aligned} \tag{4.13}$$

where $M_{\rm ej} = 10 {\rm M}_\odot$ is the mean ejected mass from a Type II SN, and $L_{\rm bol}$ is the bolometric luminosity of the galaxy. We assume that $L_{\rm bol} \sim {\rm SFR} \times 10^{10}$ $L_\odot$ (Kennicutt, 1998).

Alternatively, based on high resolution "local path" simulations of supernovae in the ISM, Kim & Ostriker (2015) argue that the $\dot{p}_{\rm sn}$ is better represented by the spherical momentum at the end of the Sedov-Taylor stage when an SN blast wave cools and a shell forms, rather than the initial injected momentum as in Equation 4.13. If this convention is adopted then:

$$\begin{aligned} \dot{p}_{\rm ref} \rightarrow \dot{p}_{\rm SN} + \dot{p}_{\rm starburst} &\approx \dot{N}_{\rm SN} \frac{E_{\rm SN}}{v_{\rm cool}} + L_{\rm bol}/c \approx \\ &1.71 \times 10^{34} \left(\frac{\rm SFR_{narrow}}{M_\odot \ {\rm yr}^{-1}} \right) [{\rm cm \ g \ s}^{-2}] \end{aligned} \tag{4.14}$$

where $v_{\rm cool} = 200$ km s^{-1} is the terminal velocity of the supernova remnant after it has shocked and swept up ambient ISM material.

4.7.2 Results

In this Appendix, we provide tables of the ionized gas outflow properties detected in [O III] and Hα.

Table 4.1: Properties of the ionized gas outflows based on [O III] modeling

FIELD	V4ID	z	$\log(M_\star/M_\odot)$	log(SFR[SED])	$\log(\Sigma_{\rm SRF[SED]})$	$\rm FWHM_{br}$ [km s^{-1}]	$V_{\rm off}$ [km s^{-1}]	$V_{\rm max}$ [km s^{-1}]
(1)	(2)	(3)	(4)	(5)	(6)	(7)	(8)	(9)
AEGIS	3668	2.19	9.99±0.04	1.38±0.03	-0.12±0.03	$305.60^{+9.17}_{-4.20}$	$-9.56^{+8.80}_{-10.33}$	$-269.11^{+11.75}_{-10.93}$
AEGIS	4711	2.18	9.31±0.04	0.76±0.03	-0.15±0.04	$303.21^{+5.34}_{-2.43}$	$26.40^{+8.43}_{-7.14}$	$-231.12^{+9.58}_{-7.43}$
AEGIS	6315	2.23	9.48±0.04	0.87±0.04	-0.36±0.06	$326.70^{+23.51}_{-17.53}$	$85.45^{+9.94}_{-13.54}$	$-192.02^{+22.31}_{-20.12}$
AEGIS	10832	2.30	9.59±0.05	0.98±0.03	-0.60±0.05	$307.94^{+13.57}_{-5.97}$	$-75.15^{+14.24}_{-14.03}$	$-336.70^{+18.32}_{-14.91}$
AEGIS	12311	2.13	9.99±0.04	0.87±0.03	...[a]	$325.64^{+34.51}_{-18.84}$	$70.63^{+18.28}_{-19.42}$	$-205.95^{+34.54}_{-25.16}$
AEGIS	12512	2.32	10.25±0.01	0.84±0.01	-0.87±0.02	$424.79^{+33.49}_{-30.55}$	$-61.81^{+16.20}_{-17.32}$	$-422.60^{+32.73}_{-31.20}$
AEGIS	14957	2.30	9.91±0.04	0.68±0.03	-0.83±0.06	$338.23^{+42.29}_{-25.36}$	$-10.28^{+14.97}_{-15.03}$	$-297.55^{+38.91}_{-26.26}$
AEGIS	15737	2.30	9.59±0.05	1.06±0.03	-0.11±0.05	$302.44^{+3.77}_{-1.83}$	$57.84^{+7.07}_{-6.31}$	$-199.03^{+7.76}_{-6.50}$
AEGIS	18543	2.14	9.35±0.03	0.93±0.04	0.23±0.05	$327.0^{+48.10}_{-20.22}$	$17.06^{+15.20}_{-12.50}$	$-260.67^{+43.59}_{-21.24}$
AEGIS	22931	2.30	9.41±0.03	1.00±0.03	0.00±0.05	$334.46^{+31.09}_{-21.55}$	$-41.02^{+9.32}_{-11.68}$	$-325.08^{+28.0}_{-21.71}$
AEGIS	22935	2.37	9.71±0.05	0.90±0.03	-0.08±0.06	$304.97^{+8.30}_{-3.73}$	$63.15^{+10.96}_{-9.66}$	$-195.87^{+13.03}_{-10.16}$
AEGIS	25817	2.29	9.68±0.05	0.95±0.03	...[a]	$371.98^{+47.02}_{-41.06}$	$29.60^{+18.67}_{-15.98}$	$-286.33^{+44.08}_{-38.36}$
AEGIS	30758	2.13	9.24±0.05	0.63±0.03	0.08±0.06	$317.29^{+26.89}_{-13.04}$	$-16.65^{+10.07}_{-11.66}$	$-286.14^{+24.96}_{-16.08}$
AEGIS	35056	1.65	9.25±0.05	0.50±0.05	...[a]	$314.73^{+18.56}_{-10.59}$	$-73.53^{+14.88}_{-15.19}$	$-340.84^{+21.68}_{-17.65}$
COSMOS	3626	2.32	9.61±0.04	1.20±0.02	0.72±0.04	$563.13^{+129.91}_{-97.07}$	$-36.57^{+26.09}_{-28.79}$	$-514.85^{+113.38}_{-87.33}$
COSMOS	6283	2.22	9.55±0.04	1.02±0.03	-0.11±0.04	$333.73^{+54.21}_{-25.29}$	$-35.38^{+12.33}_{-19.14}$	$-318.82^{+47.66}_{-28.77}$
COSMOS	6750	2.13	9.99±0.03	1.08±0.02	-0.67±0.03	$555.26^{+170.20}_{-137.63}$	$-80.12^{+22.35}_{-14.34}$	$-551.71^{+146.27}_{-117.77}$
COSMOS	7065	3.26	9.41±0.05	1.29±0.03	0.28±0.08	$325.84^{+20.15}_{-15.56}$	$-7.90^{+4.77}_{-5.29}$	$-284.64^{+17.77}_{-14.24}$
COSMOS	9971	2.41	10.27±0.04	1.46±0.02	0.23±0.04	$327.87^{+22.75}_{-16.37}$	$29.92^{+15.03}_{-12.01}$	$-248.55^{+24.48}_{-18.37}$
COSMOS	10550	3.59	9.53±0.10	0.93±0.04	-0.14±0.19	$487.81^{+88.40}_{-67.77}$	$-13.33^{+20.69}_{-26.04}$	$-427.64^{+77.88}_{-63.17}$

FIELD	V4ID	z	$\log(M_\star/M_\odot)$	log(SFR[SED])	$\log(\Sigma_{\rm SRF[SED]})$	$\rm FWHM_{br}$ [km s^{-1}]	$V_{\rm off}$ [km s^{-1}]	$V_{\rm max}$ [km s^{-1}]
(1)	(2)	(3)	(4)	(5)	(6)	(7)	(8)	(9)
COSMOS	11530	2.10	9.14±0.04	0.93±0.04	0.25±0.06	$391.85^{+38.19}_{-31.46}$	$-38.60^{+8.88}_{-11.0}$	$-371.40^{+33.63}_{-28.90}$
COSMOS	12476	1.51	9.98±0.03	1.06±0.04	-0.31±0.04	$397.88^{+37.68}_{-31.78}$	$-6.93^{+9.13}_{-10.11}$	$-344.86^{+33.28}_{-28.82}$
COSMOS	18064	1.65	9.88±0.03	1.06±0.03	-0.25±0.03	$431.96^{+38.40}_{-37.31}$	$94.97^{+3.63}_{-7.50}$	$-271.91^{+32.82}_{-32.57}$
COSMOS	19439	2.47	10.31±0.05	0.90±0.02	...[a]	$314.28^{+20.70}_{-10.47}$	$-26.56^{+8.20}_{-8.30}$	$-293.49^{+19.40}_{-12.17}$
COSMOS	19985	2.19	10.32±0.05	1.61±0.03	0.55±0.03	$525.70^{+14.50}_{-14.14}$	$-11.07^{+3.68}_{-4.0}$	$-457.56^{+12.86}_{-12.66}$
COSMOS	22576	3.26	9.38±0.06	1.27±0.04	0.40±0.06	$307.98^{+10.55}_{-5.77}$	$25.22^{+4.81}_{-4.63}$	$-236.36^{+10.17}_{-6.74}$
COSMOS	22838	3.36	10.24±0.05	1.12±0.02	0.20±0.07	$474.56^{+45.50}_{-37.63}$	$-76.70^{+15.30}_{-14.57}$	$-479.75^{+41.56}_{-35.12}$
COSMOS	22862	3.12	10.01±0.05	1.70±0.03	...[a]	$353.63^{+34.33}_{-28.37}$	$71.54^{+15.63}_{-14.0}$	$-228.81^{+33.08}_{-27.87}$
GOODS-N	1975	2.36	9.69±0.05	1.17±0.03	0.20±0.05	$340.86^{+54.59}_{-29.14}$	$39.82^{+16.69}_{-13.81}$	$-249.68^{+49.28}_{-28.34}$
GOODS-N	16060	1.52	10.04±0.06	1.12±0.05	0.29±0.05	$381.20^{+44.41}_{-32.01}$	$-1.54^{+12.62}_{-11.78}$	$-325.30^{+39.78}_{-29.63}$
GOODS-N	22065	3.13	9.58±0.06	1.17±0.03	0.13±0.04	$306.93^{+11.35}_{-5.13}$	$-41.61^{+8.93}_{-10.22}$	$-302.29^{+13.14}_{-11.11}$
GOODS-N	22235	2.43	9.54±0.05	1.12±0.03	0.17±0.04	$304.05^{+6.11}_{-3.01}$	$59.46^{+8.46}_{-7.72}$	$-198.78^{+9.93}_{-8.13}$
GOODS-N	24328	2.41	9.35±0.05	1.24±0.04	-0.94±0.11	$380.65^{+43.42}_{-40.67}$	$33.14^{+16.66}_{-14.98}$	$-290.16^{+40.46}_{-37.65}$
GOODS-N	27035	2.42	9.67±0.03	1.06±0.03	0.12±0.05	$416.74^{+30.97}_{-27.45}$	$-92.45^{+9.60}_{-5.44}$	$-446.40^{+28.0}_{-23.94}$
GOODS-N	30053	2.25	10.50±0.03	1.08±0.02	-0.42±0.03	$510.27^{+52.94}_{-47.01}$	$-10.41^{+14.81}_{-13.81}$	$-443.80^{+47.34}_{-42.25}$
GOODS-N	34699	2.20	10.04±0.06	1.43±0.03	0.21±0.04	$567.82^{+104.20}_{-90.32}$	$4.06^{+29.38}_{-25.61}$	$-478.21^{+93.25}_{-80.88}$
GOODS-N	35924	2.43	9.90±0.05	0.98±0.03	-1.05±0.04	$353.50^{+25.66}_{-22.43}$	$-31.95^{+10.21}_{-11.01}$	$-332.18^{+24.07}_{-22.0}$
GOODS-S	40768	2.30	10.09±0.02	1.58±0.01	...[a]	$302.48^{+4.12}_{-1.85}$	$65.98^{+8.98}_{-7.66}$	$-190.92^{+9.64}_{-7.82}$
GOODS-S	45531	2.31	9.71±0.05	0.90±0.02	-0.24±0.04	$352.36^{+56.27}_{-32.24}$	$14.60^{+12.66}_{-12.54}$	$-284.67^{+49.44}_{-30.12}$

(1): CANDELS field (2): 3D-HST v4 catalogue ID (3): Redshift measured by MOSDEF Survey (4): Stellar Mass (5): Star-formation rate from SED fitting (6): Star-formation-rate surface density (7): Full width half max of the broad [O III] component (8): Velocity offset between the broad and narrow [O III] components (9): Maximum outflow velocity.

[a] Galaxy does not have a robust $R_{\rm E}$ measurement.

Table 4.2: Properties of the ionized gas outflows based on Hα modeling

FIELD	V4ID	z	$\log(M_\star/M_\odot)$	log(SFR[Hα])	$\log(\Sigma_{\rm SRF[H\alpha]})$	FWHM$_{\rm br}$ [km s^{-1}]	$V_{\rm off}$ [km s^{-1}]
(1)	(2)	(3)	(4)	(5)	(6)	(7)	(8)
AEGIS	3658	2.17	9.86±0.03	1.43±0.08	-0.11±0.08	$461.09^{+95.90}_{-74.36}$	$-56.21^{+25.92}_{-26.55}$
AEGIS	8907	1.59	10.06±0.03	0.87±0.07	-1.43±0.08	$314.60^{+24.10}_{-11.06}$	$17.53^{+25.49}_{-20.49}$
AEGIS	10386	1.67	10.60±0.01	1.99±0.05	0.05±0.06	$392.99^{+50.06}_{-42.97}$	$13.52^{+17.51}_{-14.14}$
AEGIS	11930	1.57	9.70±0.04	1.54±0.04	-0.33±0.05	$359.54^{+6.20}_{-6.19}$	$-95.68^{+4.42}_{-3.0}$
AEGIS	14536	1.57	10.13±0.06	1.51±0.06	-0.09±0.06	$357.73^{+15.25}_{-14.4}$	$-19.99^{+4.54}_{-5.02}$
AEGIS	15737	2.30	9.59±0.05	1.48±0.05	0.30±0.06	$327.22^{+36.76}_{-19.68}$	$50.49^{+18.61}_{-14.43}$
AEGIS	17556	1.40	10.13±0.04	1.72±0.03	-0.16±0.03	$360.59^{+65.28}_{-41.06}$	$0.20^{+13.64}_{-13.57}$
AEGIS	26886	1.64	10.07±0.04	1.26±0.14	-0.85±0.14	$344.91^{+39.11}_{-28.85}$	$77.06^{+15.47}_{-19.96}$
AEGIS	27627	1.67	10.54±0.01	1.63±0.10	-0.43±0.10	$437.90^{+85.75}_{-68.67}$	$-84.99^{+16.10}_{-10.64}$
AEGIS	35764	2.37	10.47±0.03	1.80±0.07	0.28±0.08	$392.37^{+48.92}_{-40.65}$	$-91.85^{+11.25}_{-6.04}$
AEGIS	39567	1.58	10.55±0.03	1.82±0.07	0.01±0.07	$320.71^{+24.19}_{-14.97}$	$51.56^{+11.30}_{-9.48}$
COSMOS	3185	2.17	9.74±0.06	1.01±0.26	0.50±0.28	$397.59^{+117.34}_{-69.38}$	$64.47^{+23.33}_{-27.25}$
COSMOS	6754	2.12	9.55±0.04	0.33±0.24	-1.12±0.25	$329.68^{+37.72}_{-21.28}$	$71.96^{+18.0}_{-21.83}$
COSMOS	11530	2.10	9.14±0.04	1.12±0.10	0.44±0.10	$337.50^{+46.48}_{-26.18}$	$-77.23^{+23.74}_{-16.04}$
COSMOS	12476	1.51	9.98±0.03	1.61±0.08	0.24±0.08	$449.34^{+47.37}_{-36.29}$	$-14.34^{+8.65}_{-8.55}$
COSMOS	13701	2.17	10.65±0.05	1.98±0.09	-0.04±0.09	$308.53^{+15.82}_{-6.5}$	$-65.10^{+17.09}_{-19.91}$
COSMOS	18064	1.65	9.88±0.03	1.49±0.09	0.17±0.09	$420.22^{+33.58}_{-28.61}$	$82.91^{+11.18}_{-13.07}$
COSMOS	27945	2.02	10.10±0.03	...[a]	...	$447.48^{+28.44}_{-31.03}$	$-97.20^{+5.51}_{-2.09}$
GOODS-N	328	2.27	10.53±0.05	2.08±0.04	0.47±0.04	$322.53^{+66.75}_{-17.79}$	$-83.99^{+17.43}_{-11.25}$
GOODS-N	7652	2.27	10.59±0.04	1.51±0.20	-0.54±0.20	$315.10^{+25.55}_{-11.22}$	$64.12^{+14.21}_{-14.55}$
GOODS-N	8099	1.49	10.39±0.01	1.78±0.04	0.36±0.04	$377.52^{+33.72}_{-29.5}$	$-21.98^{+11.24}_{-12.56}$
GOODS-N	12345	2.27	10.34±0.05	1.82±0.11	-0.13±0.11	$331.89^{+43.44}_{-23.18}$	$-3.62^{+12.67}_{-12.06}$
GOODS-N	16060	1.52	10.04±0.06	1.54±0.05	0.71±0.06	$367.17^{+45.56}_{-27.57}$	$-1.86^{+7.95}_{-9.03}$
GOODS-N	22235	2.43	9.54±0.05	1.23±0.09	0.28±0.09	$313.61^{+20.69}_{-9.96}$	$72.38^{+14.80}_{-15.0}$
GOODS-N	23869	2.24	10.32±0.02	1.80±0.16	-0.08±0.16	$317.01^{+15.23}_{-11.14}$	$-85.73^{+12.80}_{-9.65}$
GOODS-N	27035	2.42	9.67±0.03	1.45±0.09	0.50±0.10	$474.07^{+58.06}_{-50.36}$	$-92.57^{+10.62}_{-5.47}$
GOODS-N	28061	2.20	9.98±0.03	2.32±0.20	0.45±0.21	$317.56^{+28.75}_{-13.19}$	$-47.24^{+14.38}_{-20.20}$
GOODS-N	30053	2.25	10.50±0.03	1.86±0.07	0.35±0.07	$452.85^{+37.16}_{-32.66}$	$-29.71^{+13.36}_{-14.87}$
GOODS-N	30564	2.48	10.47±0.01	1.62±0.07	...[b]	$382.87^{+53.60}_{-43.9}$	$72.10^{+17.68}_{-20.24}$
GOODS-N	34699	2.20	10.04±0.06	...[a]	...	$382.97^{+43.54}_{-36.98}$	$25.95^{+11.46}_{-10.21}$
GOODS-S	40768	2.30	10.09±0.02	2.15±0.03	...[b]	$320.96^{+30.67}_{-15.34}$	$38.31^{+12.31}_{-9.46}$
GOODS-S	46938	2.33	9.95±0.04	1.95±0.07	...[b]	$446.84^{+58.20}_{-49.03}$	$6.37^{+16.21}_{-16.79}$
UDS	16873	1.47	10.71±0.01	...[a]	...	$304.89^{+7.96}_{-3.68}$	$-83.58^{+11.19}_{-10.02}$

FIELD	V4ID	$V_{\rm max}$ [km s^{-1}]	$\dot{M}_{\rm out}$ [$M_\odot$ yr^{-1}]	$\log(\eta_M)$	$\log(\eta_E)$	$\log(\eta_p)$
(1)	(2)	(9)	(10)	(11)	(12)	(13)
AEGIS	3658	$-447.83^{+85.47}_{-68.50}$	$2.53^{+1.38}_{-1.10}$	$-0.91^{+0.27}_{-0.19}$	$-1.63^{+0.51}_{-0.26}$	$-0.98^{+0.38}_{-0.23}$
AEGIS	8907	$-249.68^{+32.69}_{-22.54}$	$0.13^{+0.04}_{-0.04}$	$-1.67^{+0.14}_{-0.13}$	$-2.88^{+0.23}_{-0.18}$	$-1.99^{+0.18}_{-0.15}$
AEGIS	10386	$-320.25^{+45.98}_{-39.14}$	$10.32^{+3.11}_{-2.94}$	$-0.65^{+0.23}_{-0.16}$	$-1.64^{+0.35}_{-0.22}$	$-0.86^{+0.29}_{-0.19}$
AEGIS	11930	$-401.04^{+6.88}_{-6.05}$	$5.58^{+0.58}_{-0.58}$	$-0.43^{+0.02}_{-0.02}$	$-1.22^{+0.03}_{-0.03}$	$-0.54^{+0.03}_{-0.03}$
AEGIS	14536	$-323.82^{+13.72}_{-13.22}$	$4.74^{+0.75}_{-0.74}$	$-0.56^{+0.06}_{-0.06}$	$-1.54^{+0.09}_{-0.08}$	$-0.77^{+0.07}_{-0.07}$
AEGIS	15737	$-227.42^{+36.35}_{-22.08}$	$3.81^{+1.06}_{-0.99}$	$-0.70^{+0.15}_{-0.13}$	$-1.99^{+0.27}_{-0.19}$	$-1.06^{+0.21}_{-0.16}$
AEGIS	17556	$-306.06^{+57.09}_{-37.42}$	$2.63^{+1.08}_{-0.94}$	$-1.17^{+0.23}_{-0.18}$	$-2.22^{+0.41}_{-0.24}$	$-1.41^{+0.33}_{-0.21}$
AEGIS	26886	$-215.88^{+36.64}_{-31.60}$	$1.28^{+0.50}_{-0.48}$	$-0.70^{+0.16}_{-0.13}$	$-2.04^{+0.31}_{-0.22}$	$-1.09^{+0.24}_{-0.18}$
AEGIS	27627	$-456.90^{+74.59}_{-59.29}$	$4.52^{+1.89}_{-1.66}$	$-0.72^{+0.23}_{-0.18}$	$-1.41^{+0.42}_{-0.23}$	$-0.78^{+0.32}_{-0.20}$
AEGIS	35764	$-425.10^{+43.04}_{-35.05}$	$11.97^{+2.98}_{-2.75}$	$-0.48^{+0.13}_{-0.11}$	$-1.23^{+0.22}_{-0.16}$	$-0.57^{+0.17}_{-0.13}$
AEGIS	39567	$-220.82^{+23.45}_{-15.86}$	$5.11^{+1.05}_{-1.04}$	$-0.84^{+0.09}_{-0.08}$	$-2.15^{+0.17}_{-0.14}$	$-1.21^{+0.13}_{-0.11}$
COSMOS	3185	$-273.22^{+102.35}_{-64.92}$	$3.03^{+3.43}_{-2.36}$	$-0.25^{+0.34}_{-0.23}$	$-1.39^{+0.80}_{-0.33}$	$-0.53^{+0.54}_{-0.28}$
COSMOS	6754	$-208.05^{+36.75}_{-28.34}$	$0.30^{+0.19}_{-0.18}$	$-0.41^{+0.15}_{-0.12}$	$-1.77^{+0.29}_{-0.21}$	$-0.80^{+0.22}_{-0.17}$
COSMOS	11530	$-363.88^{+46.06}_{-27.42}$	$2.78^{+1.16}_{-1.03}$	$-0.56^{+0.18}_{-0.16}$	$-1.45^{+0.28}_{-0.19}$	$-0.72^{+0.23}_{-0.17}$
COSMOS	12476	$-395.98^{+41.16}_{-31.98}$	$9.99^{+2.60}_{-2.49}$	$-0.30^{+0.14}_{-0.12}$	$-1.11^{+0.23}_{-0.16}$	$-0.42^{+0.18}_{-0.14}$
COSMOS	13701	$-327.14^{+21.74}_{-20.66}$	$4.80^{+1.82}_{-1.58}$	$-1.14^{+0.17}_{-0.16}$	$-2.12^{+0.20}_{-0.17}$	$-1.35^{+0.18}_{-0.16}$
COSMOS	18064	$-274.01^{+30.64}_{-27.59}$	$5.20^{+1.54}_{-1.47}$	$-0.48^{+0.14}_{-0.12}$	$-1.61^{+0.24}_{-0.17}$	$-0.77^{+0.19}_{-0.14}$
COSMOS	27945	$-477.26^{+24.78}_{-26.44}$	...[c]	...[c]	...[c]	...[c]
GOODS-N	328	$-357.92^{+59.31}_{-18.84}$	$5.24^{+2.19}_{-1.91}$	$-1.30^{+0.21}_{-0.17}$	$-2.20^{+0.32}_{-0.21}$	$-1.47^{+0.26}_{-0.19}$
GOODS-N	7652	$-203.50^{+25.94}_{-17.39}$	$2.00^{+1.17}_{-1.08}$	$-0.85^{+0.16}_{-0.13}$	$-2.24^{+0.24}_{-0.18}$	$-1.26^{+0.20}_{-0.15}$
GOODS-N	8099	$-342.62^{+30.77}_{-28.03}$	$6.79^{+1.62}_{-1.52}$	$-0.80^{+0.13}_{-0.11}$	$-1.74^{+0.21}_{-0.15}$	$-0.99^{+0.16}_{-0.13}$
GOODS-N	12345	$-285.50^{+39.01}_{-23.09}$	$3.52^{+1.37}_{-1.23}$	$-1.11^{+0.15}_{-0.13}$	$-2.21^{+0.27}_{-0.18}$	$-1.37^{+0.20}_{-0.15}$
GOODS-N	16060	$-313.71^{+39.51}_{-25.10}$	$13.52^{+3.59}_{-3.56}$	$-0.07^{+0.21}_{-0.16}$	$-1.09^{+0.30}_{-0.20}$	$-0.29^{+0.25}_{-0.18}$
GOODS-N	22235	$-193.97^{+22.97}_{-17.22}$	$4.18^{+1.06}_{-1.04}$	$-0.17^{+0.13}_{-0.10}$	$-1.59^{+0.21}_{-0.15}$	$-0.59^{+0.16}_{-0.12}$
GOODS-N	23869	$-354.98^{+18.19}_{-13.52}$	$8.58^{+3.53}_{-3.54}$	$-0.51^{+0.09}_{-0.08}$	$-1.41^{+0.11}_{-0.09}$	$-0.68^{+0.10}_{-0.08}$
GOODS-N	27035	$-495.20^{+50.44}_{-43.12}$	$16.43^{+4.28}_{-4.27}$	$0.16^{+0.14}_{-0.11}$	$-0.46^{+0.24}_{-0.16}$	$0.13^{+0.19}_{-0.14}$
GOODS-N	28061	$-316.96^{+28.34}_{-23.10}$	$15.37^{+10.42}_{-8.94}$	$-0.93^{+0.17}_{-0.14}$	$-1.93^{+0.22}_{-0.17}$	$-1.14^{+0.19}_{-0.16}$
GOODS-N	30053	$-414.32^{+34.27}_{-31.47}$	$21.43^{+4.18}_{-4.35}$	$-0.04^{+0.12}_{-0.10}$	$-0.81^{+0.18}_{-0.14}$	$-0.14^{+0.15}_{-0.12}$
GOODS-N	30564	$-253.08^{+48.84}_{-42.42}$	...[c]	...[c]	...[c]	...[c]
GOODS-N	34699	$-299.32^{+38.72}_{-33.03}$	...[c]	...[c]	...[c]	...[c]
GOODS-S	40768	$-234.29^{+28.81}_{-16.10}$	...[c]	...[c]	...[c]	...[c]
GOODS-S	46938	$-373.14^{+52.02}_{-44.91}$	...[c]	...[c]	...[c]	...[c]
UDS	16873	$-342.52^{+13.07}_{-10.50}$	...[c]	...[c]	...[c]	...[c]

(1): CANDELS field (2): 3D-HST v4 catalogue ID (3): Redshift measured by MOSDEF Survey (4): Stellar Mass (5): Star-formation rate from SED fitting (6): Star-formation-rate surface density (7): Full width half max of the broad Hα component (8): Velocity offset between the broad and narrow Hα components (9): Maximum outflow velocity (10): Mass outflow rate (11): Mass loading factor (12): Energy loading factor (13): Momentum loading factor

[a] Galaxy does not have a significant detection of Hβ

[b] Galaxy does not have a robust $R_{\rm E}$ measurement

[c] Property could not be measured, due to lack of SFR or $R_{\rm E}$.

Chapter 5

The MOSDEF-KCWI Survey: Spectral Properties of Lyα halos around $z \sim 2$ star-forming galaxies[1]

Abstract We present Keck Cosmic Web Imager integral field observations of extended Lyα emission in the circumgalactic medium of 27 typical star-forming galaxies at $z \sim 2$, drawn from the MOSFIRE Deep Evolution Field survey. Using composite spectra in two bins of star-formation rate (SFR), star-formation-rate surface density ($\Sigma_{\rm SFR}$), and other galactic properties, we measure spatial variations in the Lyα profile across three regions in the Lyα halo. We find single-peaked, redshifted profiles are ubiquitous within a central 7 kpc radii region. Further out in the halo (7 – 14 kpc and 14 – 21 kpc), the Lyα profile of

[1]This chapter contains a draft of an article that has been submitted for publication by the American Astronomical Society in the Astrophysical Journal written by Andrew Weldon, Zhiyuan Song, Naveen A. Reddy, and Alice E. Shapley.

the resonantly scattered emission exhibits more diversity, either transitioning to a double-peaked profile or remaining single-peaked across the halo. We find a shorter scale-length of the Lyα halo surface-brightness profile for composite halos with faster winds. The composites have a similar average inclination, suggesting those with faster winds clear channels in the ISM, reducing the fraction of Lyα resonantly scattered to large radii. A uniform expanding shell radiative transfer model reproduces the shape, but not the normalization of the observed double-peaked Lyα profiles. Models that adopt a more realistic, clumpy ISM are likely needed to reproduce both the shape and normalization of the Lyα profiles.

5.1 Introduction

The faint and diffuse nature of the CGM has made studying its structure with direct observations difficult. Halos of Lyα emission extending several kpc around galaxies are frequently used to probe the distribution and kinematics of neutral gas in the CGM. These Lyα halos are theorized to be powered by either: (1) resonant scattering of Lyα photons produced within star-forming regions and/or AGN by neutral hydrogen gas in the CGM (Dijkstra et al., 2006; Zheng et al., 2011; Steidel et al., 2011) or (2) in situ ionization or collisional emission in the CGM from inflowing gas (Dijkstra et al., 2006; Faucher-Giguère et al., 2010; Goerdt et al., 2010; Rosdahl & Blaizot, 2012; Lake et al., 2015), outflowing gas (Dijkstra & Kramer, 2012; Orsi et al., 2012), or a nearby ionizing source (Adelberger et al., 2006; Mas-Ribas & Dijkstra, 2016). In either case, the resonant scattering of Lyα photons as they escape the ISM yields important clues on the kinematics, clumpiness, column densities

of neutral hydrogen, and dust content within the CGM (e.g., see Ouchi et al., 2020, and the references therein).

Detecting Lyα halos around $z \gtrsim 2$ star-forming galaxies is difficult due to their faint emission coupled with sensitivity limitations. At these redshifts, Lyα halos were initially observed using stacked, narrowband images (Hayashino et al., 2004; Steidel et al., 2011), while individual spectroscopic detections were limited to local galaxies, gravitationally lensed galaxies, and/or AGNs (e.g., Swinbank et al., 2007; Christensen et al., 2012; Hayes et al., 2013; Hayes, 2015; Cantalupo et al., 2014). The Lyα profile from these sources is typically redshifted relative to the systemic velocity, likely due to backscattering from a receding outflow. If the Lyα optical depth is relatively low, the emission profile will typically be double-peaked, exhibiting a dominant red and secondary blue peak, with the peak separation depending on the neutral hydrogen column density (Verhamme et al., 2006, 2017; Henry et al., 2015; Gronke & Dijkstra, 2016).

Recently, with the arrival of the Multi-Unit Spectroscopic Explorer (MUSE; Bacon et al., 2010) at the ESO-VLT and the Keck Cosmic Web Imager (KCWI; Morrissey et al., 2018), studies have investigated variations in Lyα emission across the halo in gravitationally lensed (Patrício et al., 2016; Claeyssens et al., 2019; Solimano et al., 2022) and unlensed (Leclercq et al., 2020; Erb et al., 2022) galaxies at $z > 2$. Studies of single-peaked Lyα profiles have found that the Lyα line becomes redder and narrower at large radii (Claeyssens et al., 2019; Leclercq et al., 2020; Solimano et al., 2022). For double-peaked profiles,

Erb et al. (2022) found that the velocity separation between the blue and red peaks decreases, while the blue-to-red peak flux ratio increases towards the outskirts of the halo.

However, most Lyα halo studies have focused on bright halos that surround Lyα emitters (LAEs). As only $\approx$ 20% of star-forming galaxies with R<25.5 at $z \sim 2-3$ are LAEs (e.g., Shapley et al., 2003; Reddy et al., 2008; Cassata et al., 2015), it is still unknown whether the trends seen in Lyα emission across the halo are present within the larger galaxy population. In this paper, we analyze the spectral properties of extended Lyα emission from 27 star-forming galaxies, without preselection on the down-the-barrel Lyα emission, using integral field (IFU) spectroscopy from KCWI. This sample is a blind search for Lyα halos in typical star-forming galaxies drawn from the MOSFIRE Deep Evolution Field (MOSDEF; Kriek et al., 2015). The paper is structured as follows. In Section 5.2, we describe the sample, observations, data reduction, and measurements of physical properties. Section 5.3 describes how the Lyα profiles were fit and line properties measured in regions across the halos. We present our main results on the variation in the Lyα profile in Section 5.4, their physical implications on the CGM in Section 5.5, and summarize our conclusions in Section 5.6. Throughout this paper, we adopt a standard cosmology with $\Omega_\Lambda = 0.7$, $\Omega_M = 0.3$, and $H_0 = 70$ km s^{-1}Mpc^{-1}. All wavelengths are presented in the vacuum frame.

5.2 Data

5.2.1 MOSDEF Survey

Our analysis utilizes rest-optical spectra from the MOSDEF Survey which targeted $\approx$1500 H-band selected galaxies and AGNs at redshifts $1.4 \leq z \leq 3.8$. The survey obtained

moderate-resolution ($R \sim 3000$–3600) near-infrared spectra using the Multi-Object Spectrometer for Infra-Red Exploration (MOSFIRE; McLean et al., 2012b) spectrograph over 48.5 nights between 2012 - 2016. Galaxies were targeted for spectroscopy based on pre-existing spectroscopic, grism, or photometric redshifts that placed them in three redshift ranges ($z = 1.37 - 1.70$, $z = 2.09 - 2.61$, and $z = 2.95 - 3.80$) where strong rest-frame optical emission lines (e.g., Hβ, [O III], Hα, [N II]) lie in the $YJHK$ transmission windows. For full details regarding the MOSDEF survey (targeting, data reduction, and sample properties), we refer readers to Kriek et al. (2015).

Emission-line fluxes were measured by simultaneously fitting a line with the best-fit SED model for the continuum and a Gaussian function (see Reddy et al., 2022, for a complete description of the SED modeling). For multiple lines that lie in close proximity, multiple Gaussians were fit, such as the [O II] doublet and Hα and the [N II] doublet, which were fit with two and three Gaussians, respectively. Systemic redshifts were derived from the strongest emission line, usually Hα or [O III]λ5008, and were used to fit the other rest-frame optical nebular emission lines. Further details on emission-line measurements and slit loss corrections are given in Kriek et al. (2015) and Reddy et al. (2015).

5.2.2 MOSDEF-KCWI Spectroscopy

In this study, we use a sample of galaxies drawn from the MOSDEF survey with follow-up KCWI IFU observations. Here, we briefly summarize the sample and refer readers to Song et al. (2024) for more details. From the MOSDEF Survey, objects were prioritized for KCWI observations based on strong detections of Hα, Hβ, and [O III] at $\geq 3\sigma$, and either a detection or upper limit on [N II]. In addition, several objects observed as part

of the MOSDEF survey were also included within the KCWI field-of-view. Objects were observed with KCWI over eight nights in 2018 – 2020. The medium slicer with the BL grating, central wavelength of 4500 Å, was used, resulting in a $16\farcs5 \times 20\farcs0$ field of view and a spectral resolution $R \sim 1800$. The typical integration time per pointing was ~ 5 hours, and the average seeing was $\sim 1\farcs0$. In total, 40 galaxies were followed up with KCWI.

The reduction of the KCWI data is discussed in more detail in Chen et al. (2021) and Song et al. (2024), but here we provide a brief overview. Individual exposures were reduced using the KCWI Data Reduction Pipeline, which performs overscan subtraction, cosmic ray removal, scattered light subtraction, wavelength calibration, flat-fielding, sky-subtraction, differential atmospheric refraction correction, and flux calibration. Additional low frequency background structures, due to imperfect sky-subtraction, were removed using a 3D boxcar filter to create a median-filtered cube.[2] Next, we removed any remaining low-frequency residuals from imperfect sky background subtraction by forming a median-filtered cube after masking obvious continuum and extended emission line sources using a running 3D boxcar filter. The final product of the pipeline were 3D data cubes assembled from the 2D spectra of all slices. Data cubes of multiple exposures of the same target were rotated to the north-up direction, drizzled onto a common 3D grid, and averaged, creating the final data cube for each target.

Several criteria were applied to the parent MOSDEF-KCWI sample for our analysis on Lyα halos of typical, star-forming galaxies at $z \sim 2$. We remove 10 objects without secure systemic redshifts from MOSDEF spectroscopy. Specifically, objects must have more than

[2]The typical dimensions of the 3D boxcar filter were 100 Å(100 pixels) in the wavelength direction, 16 pixels along slices, and 1 pixel perpendicular to the slices.

one emission line with an integrated line flux with S/N $\geq$ 2. One galaxy with an active galactic nuclei (AGN) identified by IR colors, X-ray emission, and/or the [N II]/Hα line ratio was removed (Coil et al., 2015; Azadi et al., 2017, 2018; Leung et al., 2019). Finally, two objects at $z_{\rm sys}$ = 3.2 and 3.4 were removed as the KCWI observations lacked coverage of Lyα. These criteria result in a final sample of 27 galaxies.

5.2.3 MOSDEF-LRIS Spectroscopy

In addition to KCWI IFU observations, 16 galaxies have rest-UV slit spectroscopy as part of follow-up observations to the MOSDEF survey with the Keck Low Resolution Imaging Spectrometer (LRIS; Oke et al., 1995; Steidel et al., 2003). Observations were performed over nine nights in 2017 and 2018 in the COSMOS, GOODS-S, GOODS-N, and AEGIS fields using the Keck Low Resolution Imaging Spectrometer to obtain low-resolution ($R \sim 800 - 1300$) optical spectra. The instrumental setup provided continuous spectral coverage from the atmospheric cut-off at 3100Å up to a typical wavelength of ∼7000Å, depending on the position of the slit within the spectroscopic field of view. Objects for follow-up LRIS spectroscopy were prioritized based on strong detections of rest-optical emission lines (Hβ, [O III], Hα, and [N II]), with higher priority given to objects with confirmed spectroscopic redshift at $1.90 \leq z \leq 2.65$. For full details regarding the follow-up LRIS observations (sample selection, data collection, and reduction), we refer readers to Topping et al. (2020) and Reddy et al. (2022).

5.2.4 Stellar Population Properties

In this study, we consider several global galaxy properties (e.g., star-formation rate, stellar mass, star-formation-rate surface density). As part of the MOSDEF survey, SED fits are available for all of the KCWI galaxies. Here, we briefly describe the models and refer readers to Reddy et al. (2015) for more details. The models were created adopting a Bruzual & Charlot (2003a, hereafter BC03) stellar population synthesis model, Chabrier (2003) initial mass function, constant star formation histories (SFH), Small Magellanic Cloud (SMC) extinction curve (Fitzpatrick & Massa, 1990; Gordon et al., 2003), and sub-solar metallicity ($Z_* = 0.28 Z_\odot$). A lower age limit of 50 Myr was imposed, based on the typical dynamical timescale of $z \sim 2$ galaxies (Reddy et al., 2012). The combination of the steeper SMC attenuation curve, which has been found to best reproduce the dust obscurations of typical star-forming galaxies at $z \sim 2$ based on far-infrared data (Reddy et al., 2018a), and sub-solar metallicity provide self-consistent SFRs with those derived using other methods (Reddy et al., 2018b; Theios et al., 2019). The best-fit stellar population parameters and their errors were obtained by perturbing the photometry, refitting the models, and taking the median and dispersion in the resulting parameters, respectively.

Radiative transfer models of Lyα emission have shown that redshifted, single-peaked profiles are a signature of Lyα photons backscattering from a receding galactic outflow (e.g., Dijkstra et al., 2006; Verhamme et al., 2006). Observations suggest that outflow velocity may scale with the SFR, SFR surface density ($\Sigma_{\rm SFR}$), and specific SFR surface density ($\Sigma_{\rm sSFR}$) of a galaxy (e.g., see Weldon et al., 2022, and references therein). Together, these results suggest that the Lyα profile may vary significantly between galaxies with dif-

ferent SFR, $\Sigma_{\rm SFR}$, or $\Sigma_{\rm sSFR}$. To make full use of the statistical power of the sample, we have chosen to focus on SFR[SED] when discussing SFR as 9 galaxies (33%) lack significant Hα and/or Hβ detections necessary for dust-corrected SFRs based on these nebular lines. The star-formation-rate surface density and specific star-formation-rate surface density are defined as $\Sigma_{\rm SFR} = {\rm SFR}/(2\pi R_{\rm E}^2)$ and $\Sigma_{\rm sSFR} = {\rm SFR}/(2\pi R_{\rm E}^2 M_\star)$, where SFR and $M_\star$ are the star-formation rate and stellar mass from SED fitting, and $R_{\rm E}$ is the effective radius, within which half the total light of the galaxy is contained, measured by van der Wel et al. (2014)[3] using GALFIT (Peng et al., 2010) on HST/F160W images from the CANDELS survey.

5.3 Resolved spectroscopy of the Lyα halos

In this section, we describe the technique for measuring spatial variations in the Lyα profile across the extended, diffuse halos. To quantify changes in the profile, we measure six parameters: the peak velocity shift ($\Delta v_{\rm off}$), the full-width half maximum (FWHM), and the asymmetry parameter ($a_{\rm asym}$) for single-peaked profiles or the peak separation ($\Delta v_{\rm peaks}$), blue-to-red peak flux ratio ($f_{\rm b-r}$), and trough flux ratio ($f_{\rm tr}$) for double-peaked profiles. We also describe the methods to measure outflow velocities from low-ionization interstellar metal absorption lines and create 2D Lyα images.

5.3.1 Fitting Lyα emission

In order to investigate the variation in the Lyα halo, we first divide each galaxy into three regions: a central continuum region ($\leq$7.3 kpc radii), an inner halo (7.3 – 14.6 kpc), and an outer halo (14.6 – 21.9 kpc). The size of these regions are set to the seeing

[3] https://users.ugent.be/~avdrwel/research.html

Table 5.1: Global properties of the galactic property stacks

Property	Bin	Mean	Min	Max
$\log(\mathrm{SFR}/M_\odot\ \mathrm{yr}^{-1})$	Lower	0.66±0.08	0.02	1.04
	Higher	1.30±0.05	1.06	1.61
$\log(\Sigma_{\mathrm{SFR}}/M_\odot\ \mathrm{kpc}^2\ \mathrm{yr}^{-1})$	Lower	-0.80±0.08	-1.21	-0.47
	Higher	0.05±0.09	-0.40	0.55
$\log(\Sigma_{\mathrm{sSFR}}/\ \mathrm{kpc}^2\ \mathrm{yr}^{-1})$	Lower	-10.38±0.06	-10.71	-10.18
	Higher	-9.62±0.10	-10.07	-9.03
Δv_{LIS} [km s^{-1}]	Lower	-168±27	-304	-101
	Higher	3±20	-93	68

of the KCWI observations.[4] The 1D spectra are taken as the sum of fluxes within each of the three regions, while the error is calculated by summing the uncertainty per pixel in quadrature. Next, to increase the S/N of the halos, galaxies are divided into "lower" ($x < x_{\mathrm{median}}$) and "higher" ($x > x_{\mathrm{median}}$) bins, where "x" corresponds to the value of a given galaxy property, see Table 5.1. Composite spectra are constructed by shifting each galaxy's extracted 1D spectra into the rest frame, converting flux density to luminosity density, interpolating onto a common wavelength grid, and taking the unweighted average of the spectra for all galaxies contributing to the composite. However, one galaxy (COSMOS 1908) exhibits a strong, double-peaked Lyα profile, which would bias any composite spectra that included it. As such, in Section 5.4.2, we analyze this galaxy separately from the composite Lyα profiles.

Next, we fit the Lyα line in each bin and region, performing two sets of fits: a single asymmetric Gaussian,

$$f(\lambda) = A\mathrm{exp}\left(\frac{-(\lambda-\lambda_0)^2}{2\sigma(\lambda)^2}\right) \tag{5.1}$$

[4] 7.3 kpc corresponds to 0.″9 at $\langle z \rangle = 2.4$; the seeing of the KCWI observations.

and a double asymmetric Gaussian,

$$f(\lambda) = A_{\rm blue}\ \exp\left(\frac{-(\lambda-\lambda_{0,\rm blue})^2}{2\sigma_{\rm blue}(\lambda)^2}\right) + A_{\rm red}\ \exp\left(\frac{-(\lambda-\lambda_{0,\rm red})^2}{2\sigma_{\rm red}(\lambda)^2}\right) \tag{5.2}$$

where A, λ, and $\sigma(\lambda)$ are the amplitude, peak wavelength, asymmetric line width of the single, blue, or red components, respectively. The asymmetric line width is defined as $\sigma(\lambda) = a(\lambda - \lambda_0) + d$, where a and d describe the asymmetry and width of the profile, respectively. Asymmetric Gaussians may provide a more robust peak position than a symmetric Gaussian profile, and have been used to fit single-peaked (Shibuya et al., 2014; Leclercq et al., 2020) and double-peaked (Erb et al., 2022) Lyα profiles at $z \gtrsim 2$.

For both cases, we perform two preliminary fits and one final fit. The first preliminary fit uses a linear continuum with a single or double asymmetric Gaussian to fit the Lyα emission using `curve fit`, a non-linear least squares fitting routine from the `scipy.optimize` subpackage. We use this fit to subtract off the linear continuum and normalize the spectra by the peak of the Lyα emission. Next, we fit the normalized spectra again with `curve fit`. The resulting values of this second fit are used as initial values for the final fit, which is done using `emcee`, a Python Markov chain Monte Carlo (MCMC) Ensemble sampler (Foreman-Mackey et al., 2013). We take the median values of the resulting posterior probability distributions for all the model parameters. The errors on the parameters are estimated using the 16th and 84th percentiles. Using the best-fit single- and double-peaked models, we perform a χ^2 difference test, adopting the double-peaked model for the Lyα profile when the significant <0.05, otherwise adopting the single-peaked model.

For single-peaked profiles, we derive the he peak velocity shift ($\Delta v_{\rm off}$) and FWHM from the fitted parameters. Using the modeled peak wavelength, $\Delta v_{\rm off}$ is taken as the velocity difference of the peak to the zero velocity. From Equation 5.1, we derive the analytic expression for the full width at half maximum of the line as

$$\mathrm{FWHM} = \frac{2\sqrt{2\ln 2}\,d}{1 - 2\ln 2\,a_{\rm asym}^2} \tag{5.3}$$

Uncertainties on the peak offset and FWHM are taken as the dispersion of 200 realizations after perturbing the fitted parameters by their errors.

For double-peaked profiles, we measure the peak separation ($\Delta v_{\rm peaks}$), blue-to-red peak flux ratio ($f_{\rm b-r}$), and trough flux ($f_{\rm tr}$) of the line profile. Using the modeled blue and red wavelengths, $\Delta v_{\rm peaks}$ is taken as the velocity difference of the two peaks. The blue (red) peak flux is measured by integrating the normalized observed profile between the points where the data meets the error spectrum on the blue (red) side and the trough between the peaks. The trough flux[5] represents the depth of the trough between the peaks and is taken as the ratio of emission within $\pm$ 100 km s^{-1} of the trough centroid to total line emission (Erb et al., 2022). Flux uncertainties are derived by perturbing the spectra by its error spectrum to generate 1000 realizations, remeasuring the fluxes from these realizations, and calculating the dispersion from the realizations. The peak separation uncertainty is taken as the dispersion of 200 realizations after perturbing the fitted parameters by their errors.

[5]We note that trough flux depends on spectral resolution; i.e., in a lower-resolution spectrum, it becomes more challenging to discriminate between the peaks in the Lyman-alpha profile, decreasing the depth of the trough and increasing the trough flux. However, we do not expect this to affect our analysis, as we are performing a relative comparison of objects whose spectra all have a similar resolution.

Table 5.2: Low- and high-ionization metal absorption lines

Line	$\lambda_{\rm rest}$[a](Å)	$f_{\rm osc}$[b]
Si II	1260.42	1.220
O II	1302.17	0.052
C II	1334.53	0.129
Si II	1526.71	0.133
Si IV	1393.76	0.513
Si IV	1402.77	0.255
C IV	1548.20	0.190
C IV	1550.77	0.095

[a] Rest-frame vacuum wavelength, taken from the Atomic Spectra Database website of the National Institute of Standards and Technology (NIST; Kramida et al., 2022).
[b] Oscillator strength from the NIST Atomic Spectra Database.

5.3.2 Fitting Absorption lines

In addition to the Lyα emission line, the KCWI datacubes provide coverage of several low-ionization (LIS) metal absorption lines. Due to large-scale galaxy outflows, these absorption lines are Doppler shifted away from systemic redshift ($z_{\rm sys}$) measured from strong rest-frame optical emission lines. Outflow velocities derived from these lines provide an independent check as to whether the velocities from radiative transfer models are reliable. We use a similar procedure as described in Section 5.3.1 to fit *symmetric* Gaussians to LIS absorption lines in the central region of each bin. Each line is first normalized from an initial fit using a linear continuum and Gaussian, which is then refitted with `emcee`. We manually inspect the fits to each line and exclude lines if the fits were poor. The final $z_{\rm LIS}$ is taken as the average z from all available interstellar absorption lines. Using the mean systemic

redshift of the bin ($z_{\rm mean}$), we measure centroid velocities from the redshift difference:

$$\Delta v_{\rm LIS} = \frac{c(z_{\rm LIS} - z_{\rm mean})}{1 + z_{\rm mean}} \tag{5.4}$$

Uncertainties in $\Delta v_{\rm LIS}$ are determined by perturbing the spectra by their corresponding error spectra, refitting the lines, and recalculating $z_{\rm LIS}$ for 200 realizations.

Additionally, the relative strength of low- and high-ionization (HIS) metal absorption lines can provide insight on the presence of low-column-density channels. As LIS and HIS metal absorption lines are typically saturated in star-forming galaxies with properties similar of those in our sample (e.g., Shapley et al., 2003), their equivalent widths are sensitive to the gas covering fraction rather than the column density of gas. In order to measure the equivalent widths of the LIS and HIS features (W_λ) in the central region, we construct "mean" absorption profiles. For each LIS or HIS transition (see Table 5.2), the spectral region within $\pm$5000 km s^{-1} of the rest-frame wavelength is interpolated onto a common velocity grid and normalized to its local continuum, taken as the median flux in two regions bracketing the transition, -5000 – -1000 km s^{-1} and 1000 – 5000 km s^{-1}. The mean absorption profile is then taken as the weighted average of the profiles. An effective rest-frame equivalent width is measured for the profile via direct integration according to the following expression:

$$W_\lambda = \int_{\lambda_1}^{\lambda_2} \left(1 - \frac{f_\lambda}{f_{\rm cont}}\right) d\lambda, \tag{5.5}$$

where λ_1 and λ_2 correspond to $\pm$1000 km s^{-1} from the rest-frame line center, f_λ is the

observed spectral flux density, and $f_{\rm cont}$ is the local continuum. The uncertainty on W_λ is estimated by perturbing the mean profile by its error and remeasuring W_λ for 200 realizations.

5.3.3 2D Lyα Images

Along with 1D spectra, the KCWI IFU data cubes can be used to create pseudo-narrowband Lyα surface brightness images. We create 2D Lyα emission images of each galaxy from the 3D data cubes using a similar method, as described in Song et al. (2024). We first identify the spatial peak of the Lyα emission in each data cube, then extract the summed one-dimensional spectra from a square 9x9 pixel (2.″7x2.″7) region centered on this peak. The continuum level bluewards (1160–1180 Å; $c_{\rm blue}$) and redwards (1269–1279 Å; $c_{\rm red}$) of Lyα are calculated by averaging the spectrum within these windows. Next, two-dimensional images of Lyα and the red side continuum are constructed by collapsing the cube along the wavelength axis over the regions 1210 - 1220 Å and 1269 - 1279 Å[6], respectively. The red-side continuum image is then scaled by the average value of the blue- and red-side continuum creating an underlying continuum image. Finally, the underlying continuum image is subtracted from the Lyα image to create an emission-only Lyα image. Uncertainty images for the continuum and emission-only Lyα images are estimated from the 2D Lyα and red-side continuum variance images.

[6]This region was chosen to avoid N V features at ∼1240Å and Si II absorption at 1260Å.

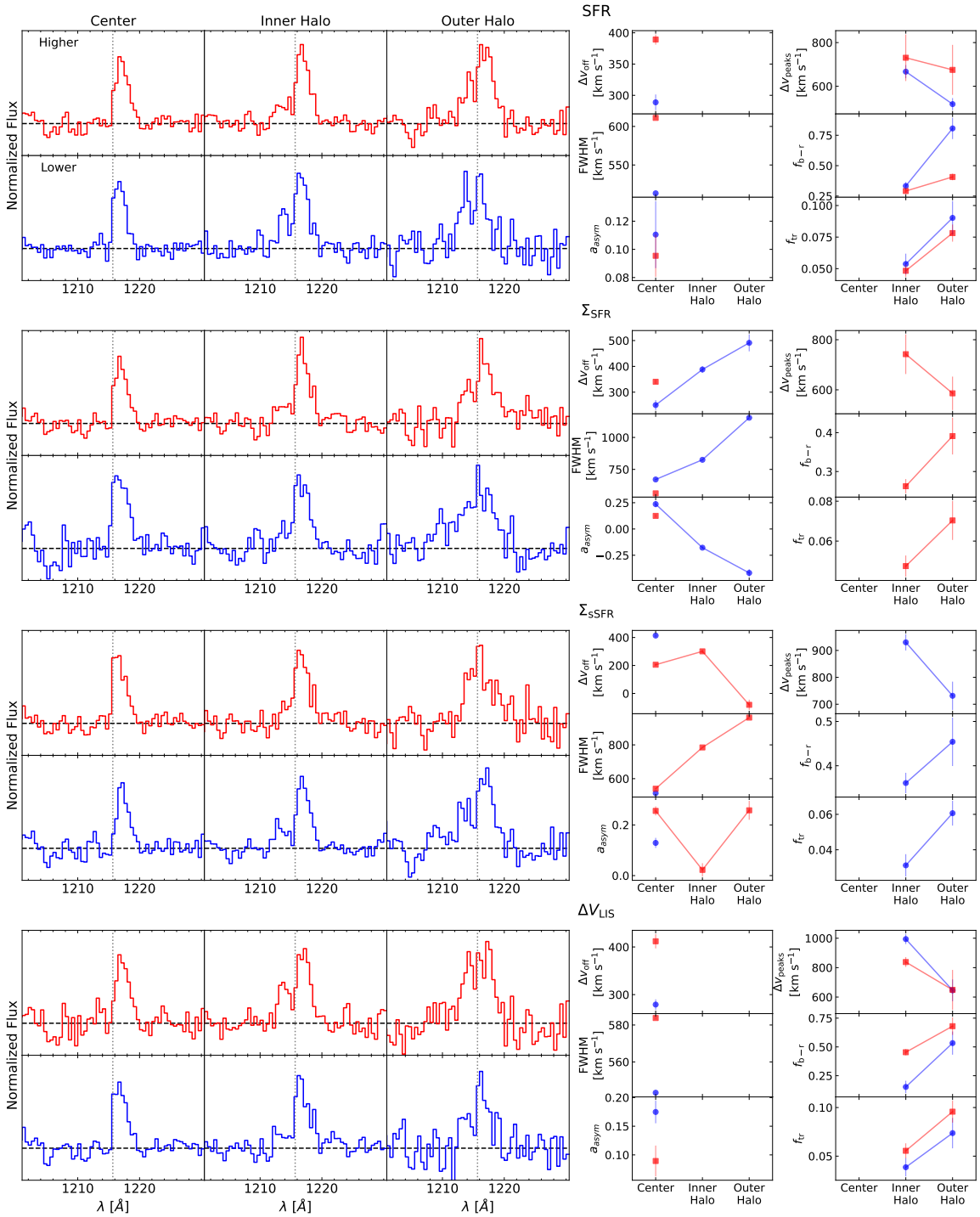
Center
Inner Halo
Outer Halo
Higher
Lower
Normalized Flux
λ [Å]
SFR
Σ_SFR
Σ_sSFR
ΔV_LIS
Δv_off [km s⁻¹]
FWHM [km s⁻¹]
a_asym
Δv_peaks [km s⁻¹]
f_0−r
f_tr

Figure 5.1: Lyα spectral profiles and derived properties across the Lyα halo in bins of (from top to bottom) SFR, $\Sigma_{\rm SFR}$, $\Sigma_{\rm sSFR}$, and $\Delta v_{\rm LIS}$. *Left*: The Lyα profile in three regions. Distance from the center increases from left to right, starting in a central continuum region ($\leq$7.3 kpc radii), to an inner halo (7.3 – 14.6 kpc), and an outer halo (14.6 – 21.9 kpc). The bottom row of each panel (blue) displays the "lower" bin, while the top row (red) is the "higher" bin. *Right*: The properties of the single- or double-peaked Lyα profiles. The panels in the left column are the peak velocity shift ($\Delta v_{\rm off}$), FWHM, and the asymmetry parameter ($a_{\rm asym}$) for single-peaked profiles, while in the right column are the peak separation ($\Delta v_{\rm peaks}$), blue-to-red peak flux ratio ($f_{\rm b-r}$), and trough flux ratio ($f_{\rm tr}$) for double-peaked profiles. Filled blue circles and red squares are values measured from the observed "lower" and "higher" binned profiles, respectively. The error bars are typically smaller than the symbol size.

5.4 Results

5.4.1 Spatial Lyα Emission

Figure 5.1 presents the 1D composite Lyα profiles and their properties in three regions across the halo in two bins of SFR, $\Sigma_{\rm SFR}$, $\Sigma_{\rm sSFR}$, and $\Delta v_{\rm LIS}$, respectively. The first interesting feature we find is a redshifted, single-peaked Lyα profile in the central region – regardless of the property or bin. Moving outwards to the inner and outer halo regions, the profiles exhibit more diversity between the various properties and bins. The Lyα profile transitions from single- to double-peaked in both bins of SFR and $\Delta v_{\rm LIS}$. On the other hand, the profiles of the $\Sigma_{\rm SFR}$ and $\Sigma_{\rm sSFR}$ bins appear to have opposite trends with distance. The profiles in the higher $\Sigma_{\rm SFR}$ and lower $\Sigma_{\rm sSFR}$ bins transition to double-peaked, while the profiles in the lower $\Sigma_{\rm SFR}$ and higher $\Sigma_{\rm sSFR}$ bins remain single-peaked across the halo.

In bins that transition to double-peaked profiles in the inner and outer halo regions, the peak separation decreases and the blue-to-red peak and trough flux ratios increase between the inner and outer regions. These trends are similar to those presented in Erb et al. (2022) who measured the properties of double-peaked Lyα profiles in 12 relatively low-mass ($M_\star \sim 10^9\ M_\odot$), extreme emission line galaxies at $z \sim 2$. In the lower $\Sigma_{\rm SFR}$ and higher $\Sigma_{\rm sSFR}$ bins, their single-peak profiles generally become broader and more blueward asymmetric between the central and outer halo regions. These trends of a strengthening blue-side suggest that the profile may be doubled-peaked, but due to the faintness in the outer halo, the blue peak is unresolved.

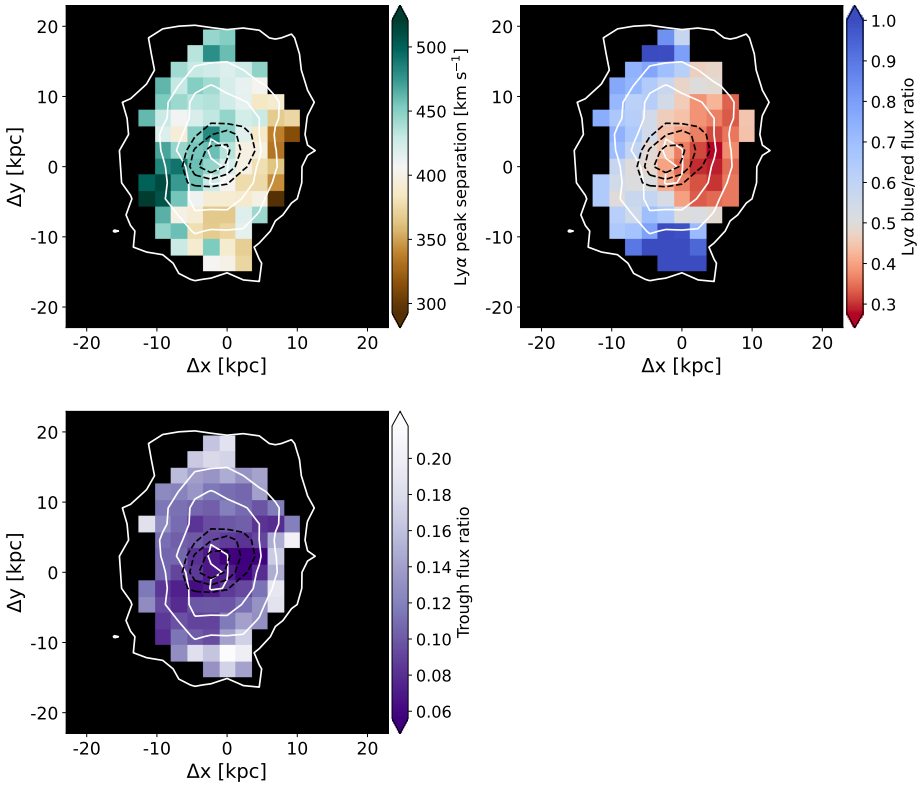

Figure 5.2: Variation in the double-peaked Lyα profile of COSMOS 1908 across the Lyα halo. *Upper Left*: Map of the Lyα peak separation. *Upper Right*: Map of the Lyα blue-to-red peak flux ratio. *Lower Right*: Map of the trough flux ratio. The solid white (black dashed) contours indicate the surface brightness of the Lyα halo (galaxy).

5.4.2 Case Study: COSMOS 1908

In this section, we discuss the velocity structure of the bright, extended Lyα halo around COSMOS 1908. The rest-optical spectrum of COSMOS 1908 reveals several striking physical properties, such as a high specific SFR, low-metallicity, young age, and dust-free ISM; properties typical of $z \gg 3$ galaxies thought to have ionized the Universe. Weak LIS absorption lines suggest a hard radiation field associated with low-metallicity star formation. Additionally, with the detection of the auroral [O III]λ4363 line, Sanders et al. (2016) estimated an electron-temperature-based metallicity, representing one of the highest redshift direct measurements prior to the launch of JWST.

The high signal-to-noise of the Lyα halo allows for the construction of reliable maps of the Lyα profile across the halo using individual spaxels. In particular, as COSMOS 1908 exhibits strong doubled-peak Lyα emission, we focus on the velocity separation of the peaks, the blue-to-red peak and trough flux ratios. For each spaxel with a S/N > 3.5, we fit the profile with two asymmetric Gaussian functions, following the same method as for composite spectra described in Section 5.3.1. The flux of the blue and red peaks is measured by integrating each side of the line between the trough between the peaks and the points at which the S/N drops below unity. The flux ratio and uncertainty are taken as the mean and standard deviation of 1000 perturbations of the spectra by its error spectrum. The peak separation is calculated using the fitted red and blue peak wavelengths, while its uncertainty is taken as the dispersion of 200 realizations after perturbing the fitted parameters by their errors.

Maps of the peak separation, peak and trough flux ratios are shown in Figure 5.2. There is a clear variation in the Lyα profile across the halo. The largest peak separations of $\sim$550–600 km s^{-1} occur in the eastern and central regions of the halo, while the smallest separations of $\sim$325 km s^{-1} along the western edge. On the other hand, the peak flux ratio is dominated by the red peak in the western region, transitioning to the blue peak along the northern and southern outskirts of the halo. The trough flux ratio appears to be minimal near the center of the halo and increases almost uniformly outwards. A dominant red-peak Lyα profile is widely interpreted as a signature of Lyα photons backscattering off a receding galactic outflow on the far side of a galaxy. However, LIS absorption lines, which trace large-scale galactic outflows, are not observed in COSMOS 1908. The low peak flux ratio in the western region then may imply the presence of low-column-density channels or a low covering fraction of neutral gas cleared by previous outflow events. Radiative transfer models indicate that the velocity separation of the blue and red peaks is due to the column density of neutral hydrogen – with peak separation increasing with column density (e.g., Gronke & Dijkstra, 2016; Verhamme et al., 2017). The low peak separations along the western edge of the 2D map appear to support a scenario of channels or a low covering fraction easing Lyα escape from the galaxy.

The smaller peak separations, larger blue-to-red peak and trough flux ratios towards the outskirts of the halo are broadly consistent with the trends seen in the composite spectra between the inner and outer halo regions. To gain further insight into the connection between individual spaxels and their location within the halo, we perform Spearman correlation tests between their properties and the distance from the Lyα surface brightness

peak. The peak and trough flux ratios are significantly correlated ($> 3\sigma$) and peak separation is not correlated with distance. Increasing blue-peak strength towards the outskirts of the halo agrees with Erb et al. (2022) who found strong ($> 5\sigma$) and significant correlations for peak flux ratio and peak separation, respectively, in 8/12 of their Lyα halos of $z \sim 2$ galaxies, suggesting stronger correlations may only be found over a relatively large Lyα halo. The relationship between distance and Lyα profile properties is discussed in more detail in Section 5.5.

5.4.3 Lyα surface brightness profiles and scale lengths

A complementary approach to investigate Lyα halos is to study their 2D surface brightness. Using the same sample as in this study, Song et al. (2024) examined how the extent of Lyα halos varies with the properties of the host galaxy. The authors found that the scale length of the halo is smaller for composite halos with lower SFR and $\Sigma_{\rm SFR}$, suggesting that the fraction of Lyα that escapes "down-the-barrel" is larger, possibly due to a lower neutral gas covering fraction. Here, we extend the analysis of Song et al. (2024) by considering the impact that outflow velocity may have on the size of the Lyα halo.

Galaxies are divided into "faster" ($\Delta v_{\rm LIS} < \Delta v_{\rm LIS,\ median}$) and "slower" ($\Delta v_{\rm LIS} > \Delta v_{\rm LIS,\ median}$) centroid outflow velocity bins. Composite 2D images are taken as the unweighted mean of each galaxy's Lyα emission-only image (Section 5.3.3), while individual uncertainty images are summed in quadrature to calculate the uncertainty of the composite image. We use the Python package `photutils` to calculate the surface brightness flux

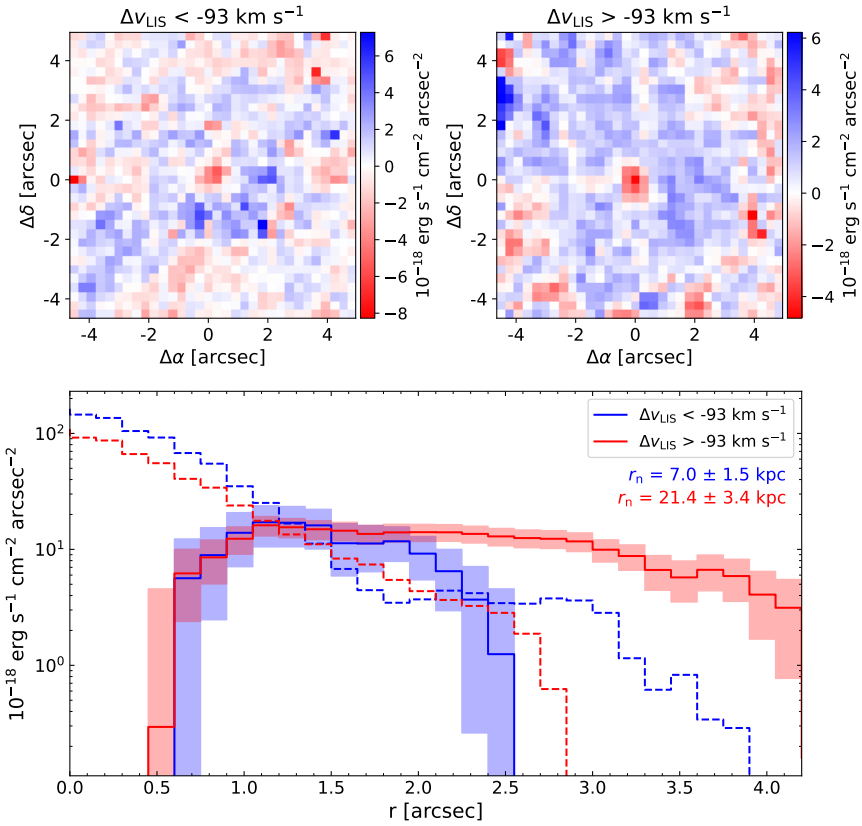

Figure 5.3: *Top*: Composite Lyα emission surface brightness images of the "faster"and "slower" $\Delta v_{\rm LIS}$ bins. *Bottom*: Surface brightness profiles of composite Lyα images. The blue (red) solid line and shaded region are Lyα surface brightness profile and 1σ error of the "faster" ("slower") bin. The blue (red) dashed lines indicate the surface brightness profiles of the continuum images of the "faster" ("slower") bin.

density and its uncertainty in annuli with radii r = 0 to 4.″5 (18 pixel) and a width of 0.″15 (0.5 pixel).

The surface brightness profile of the Lyα halo is usually described by a decreasing exponential model (Steidel et al., 2011):

$$S\left(r\right) = C_n e^{-r/r_n} \tag{5.6}$$

where C_n is a constant and r_n is the scale length. However, as the surface brightness profiles are not monotonically decreasing, we fit the profiles with Equation 5.6 from the peak of the profile out to 4.″5. Figure 5.3 shows the composite Lyα halo of the "faster" and "slower" outflow velocity bins. The surface brightness profiles of both bins have a non-monotonic shape with a peak at r $\sim$1.2 arcsec and a deficiency of Lyα emission within a $\sim$0.6 arcsec radius. However, the scale length of the Lyα halo for the "faster" outflow velocity bin (7.0$\pm$1.4 kpc) is smaller than for the "slower" outflow velocity bin (21.4$\pm$3.3 kpc) – a 4σ difference. The difference in the scale length may be due to the "faster" outflow velocity bin containing galaxies with outflows oriented along our line-of-sight or stronger outflows. In either case, low-column-density channels created by the outflows would ease the escape of Lyα photons and decrease the scale length of the Lyα halo. To test between these cases, we calculate the average inclination of galaxies in both bins under the assumption that the outflows are preferentially launched perpendicular to the "disk" of the galaxy. The average inclinations of the "faster" and "slower" bins are similar within their uncertainties, 54$\pm$6° and 52$\pm$5°, respectively. The difference in halo scale length then seems to support a physical picture where the "faster" outflow velocity bin hosts stronger outflows, which create low-density channels that facilitate the escape of Lyα photons.

To investigate the presence of low-column-density channels along our line-of-sight, we compare the equivalent widths of LIS and HIS lines in the central region as proxies for neutral and ionized metal covering fractions. If the W_λ of LIS lines is weaker than that of HIS lines, it would imply that the covering fraction of neutral gas is lower, possibly due to outflows creating channels in the ISM. We find that the "faster" outflow velocity bin has

marginally lower LIS and higher HIS EWs (-1.6 ± 0.2 and -2.0 ± 0.2) compared to the "slower" outflow velocity bin (-2.3 ± 0.2, -1.1 ± 0.3), with 2.5σ differences, suggesting that the "faster" bin may have a lower neutral gas covering fraction towards us. On the other hand, the effect of low-column-density channels along our line-of-sight is not observed in the Lyα profile. There is a deficiency of Lyα emission in the surface brightness profile at small distances, suggesting that Lyα photons are scattered out toward larger radii along our line-of-sight. In the central region of the Lyα line profile (Figure 5.1), the peak of Lyα emission is shifted several 100 km s^{-1} from rest rather than emerging near the line center ($\lesssim$ 100 km s^{-1}) expected for Lyα photons escaping through low-column-density channels (e.g., Behrens et al., 2014; Verhamme et al., 2015; Dijkstra et al., 2016; Rivera-Thorsen et al., 2017). Taken together, we argue that the low-column-density channels in the "faster" outflow velocity bin do not lie along our line-of-sight.

5.5 Discussion

5.5.1 Variations within Lyα Halos

This study allows for the analysis of Lyα emission both spatially across Lyα halos and with the galactic properties of the host. Of particular interest is how the shape of the profiles (i.e., single- or double-peaked) varies individually across the halo and between galactic property bins. A generic expectation is that Lyα photons that undergo scattering – those that interact with neutral gas before escaping – will produce a double-peaked spectral profile. In the central region of all the halos, however, the Lyα profile is single-

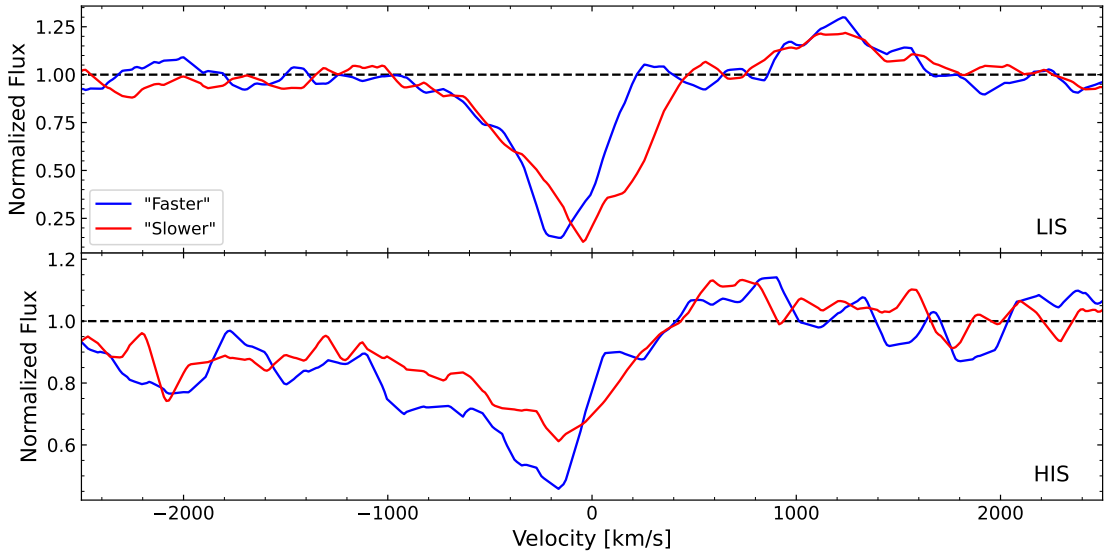

Figure 5.4: Composite spectra of low-ionization (Top) and high-ionization (Bottom) interstellar metal absorption lines for the two bins of outflow velocity. The blue (red) lines are the spectra for the "faster" ("slower") bin. The "faster" outflow velocity bin has marginally lower LIS and higher HIS EWs compared to the "slower" outflow velocity bin, suggesting that the "faster" bin may have a lower neutral gas covering fraction.

peaked, suggesting that the photons escape with few scatterings. The mechanical feedback associated with star formation can result in strong gas outflows, which, in turn, can create low-column-density channels in the ISM. The presence of such channels would allow Lyα photons to escape with relatively few scatterings, thus giving rise to a single-peaked profile near the line center ($\lesssim$ 100 km s^{-1}; e.g., Behrens et al., 2014; Verhamme et al., 2015; Dijkstra et al., 2016; Rivera-Thorsen et al., 2017). Although, these channels would have to lie along our line-of-sight in order in order for the single-peaked profiles to be observable. At the same time, Lyα photons may also backscatter off a receding gas outflow on the far side of a galaxy, which then shifts their frequency out of resonance, allowing them to pass back through the galaxy without additional scatterings (e.g., Dijkstra et al., 2006; Verhamme et al., 2006). Given the high average inclinations (>50°) of the composites and Lyα peak

velocity offsets (>200 km s^{-1}) observed in the central region, the single-peaked profiles are likely due to backscattering, suggesting the presence of strong outflows among all of the composites.

Farther out in the halo, a double-peaked profile is more likely to arise as Lyα photons have a greater chance to undergo multiple scatterings while trying to escape. Indeed, for 6/8 composite halos, the profiles transition to a double-peaked profile in the inner and outer halo regions. In the lower SFR, $\Sigma_{\rm sSFR}$, and higher $\Delta v_{\rm LIS}$ (i.e., slower) bins, this transition may be due to slower outflows, as expected for lower star-formation activity bins, allowing for more blueshifted Lyα photons to escape. On the other hand, double-peaked profiles are also observed in the higher SFR, $\Sigma_{\rm SFR}$, and lower $\Delta v_{\rm LIS}$ (i.e., faster) bins, which likely host strong outflows relative to their counterparts. The transition in these bins may suggest that the primary factor shaping their observed profile is not the kinematics, but rather the distribution of neutral gas. Alternatively, the transition in the higher $\Sigma_{\rm SFR}$ bin may indicate that outflowing gas experiences a sudden decrease in velocity – possibly due to gravitational deceleration or moving through the stationary medium.

In bins that exhibit double-peaked profiles in both the inner and outer halo regions, the peak separation decreases and the blue-to-red peak and trough flux ratios increase between the inner and outer regions. These changes may be related to the geometry of the halo. The decrease in peak separation can be naturally explained by lower HI column densities, as the covering fraction of HI decreases at large radii due to the increased physical volume of the halo (Rudie et al., 2012). Similarly, a Lyα photon would travel through less of the CGM along our line-of-sight the farther its last scattering occurs in the halo,

thus the profile would suffer from less extinction at line center, increasing the trough flux ratio. Finally, a strengthening blue peak in the outer region may be due to the preferential scattering of blue-shifted Lyα photons to larger radii (Zheng et al., 2010) or a decrease in the average projected outflow velocity with distance (Li et al., 2022).

5.5.2 Radiative Transfer Modeling

Lyα emission is a powerful observational tool, tracing the structure and kinematics of neutral gas that is otherwise challenging to observe. However, the complex radiative transfer of Lyα impedes the physical interpretation of the emergent line profile. Several radiative transfer models have been developed to connect observed Lyα profiles to properties of neutral gas within the CGM. The most widely used model is the "shell" model, in which the emergent Lyα profile arises from photons resonantly scattering off of an expanding, homogeneous neutral gas shell surrounding the central Lyα source. Despite the simple geometry employed, these models are able to reproduce a wide range of observed Lyα profiles, such as single- and double-peaked profiles from Lyman break galaxies (LBGs), Lyα emitters (LAEs), damped Lyα systems (DLAs) and Green Pea galaxies (e.g., Verhamme et al., 2008; Vanzella et al., 2010; Krogager et al., 2013; Hashimoto et al., 2015; Yang et al., 2016, 2017), providing insight on the properties of HI. In general, the strength of the blue peak increases with decreasing shell velocity, while the peak separation decreases with decreasing HI column density (e.g., Verhamme et al., 2015). However, discrepancies persist between the modeled parameters and observational constraints from interstellar absorption and nebular emission lines (e.g., Kulas et al., 2012; Leitherer et al., 2013; Hashimoto et al., 2015; Orlitová et al., 2018). In particular, the outflow velocity of the shell is often lower

than those derived from LIS interstellar absorption metal lines, the intrinsic Lyα line widths are broader than observed Balmer lines, and the range of velocities suggested by the widths of LIS lines are not consistent with a thin shell model (Steidel et al., 2010; Kulas et al., 2012). These inconsistencies have motivated the use of alternate models that employ more realistic gas structures. One such model is the "clumpy" model, which consists of cool ($\sim 10^4$ K) neutral hydrogen clumps moving within a static, hot ($\sim 10^6$ K), highly ionized inter-clump medium (ICM) (e.g., Neufeld, 1991; Hansen & Oh, 2006; Dijkstra & Kramer, 2012; Laursen et al., 2013; Duval et al., 2014; Gronke & Dijkstra, 2016). Recent studies have shown that the clumpy models can reproduce Lyα profiles of Lyα blobs (Li et al., 2021, 2022) and spatially resolved double-peaked profiles of LAEs (Erb et al., 2022).

To quantify the physical properties of gas across the Lyα halo, we fit the composite spectra using the radiative transfer model `zELDA` (Gurung-López et al., 2022), an open-source Python module. Based on the radiative transfer Monte Carlo code LyaRT (Orsi et al., 2012), `zELDA` fits the observed Lyα profiles from a grid of LyaRT outputs using a MCMC methodology. Several simple geometries are available in `zELDA`, such as the "shell" model (e.g., Verhamme et al., 2006; Schaerer et al., 2011; Gronke et al., 2015), galactic wind (Orsi et al., 2012; Gurung-López et al., 2019), and moving slabs (Schaerer & Verhamme, 2008). As we are studying composite spectra averaged over many galaxies viewed from different angles with different neutral gas covering fractions, we apply the widely studied thin shell model. The free parameters are the outflow expansion velocity, $V_{\rm exp}$, the HI column density, $\log(N_{\rm H})$, and the dust optical depth, τ. As with fitting the Lyα profile (Section 5.3.1), we take the median values of the resulting posterior probability distributions

as the best-fit model parameters and the 16th (84th) percentile as the lower (higher) error of each parameter.

Figure 5.5 shows the best-fit shell models to the composite spectra (black lines) and the variation in the profile properties across the halo (open black circles and squares). The properties of the modeled Lyα profile were derived using the same methods described in Section 5.3.1. In the central region, the thin shell model reproduces the redshifted peak but appears to overpredict the observed profile with the addition of an extremely faint blue peak. In the inner and outer halo regions, the thin shell model predicts a double-peaked profile regardless of the property or bin. As with the observed double-peaked profiles, between the inner and outer halo, $\Delta v_{\rm peaks}$ decreases, while $f_{\rm b-r}$ and $f_{\rm tr}$ increase for the modeled Lyα profiles.

Next, we turn to how the properties of the neutral gas predicted by `zELDA` vary in the Lyα halo, and their possible connection to the observed profiles. In Section 5.5.1, we attributed the transition in profile shape and trends of double-peaked profile properties to differences in the neutral gas velocity or column density. With the thin-shell modeling in hand, we are now able to investigate these possibilities.

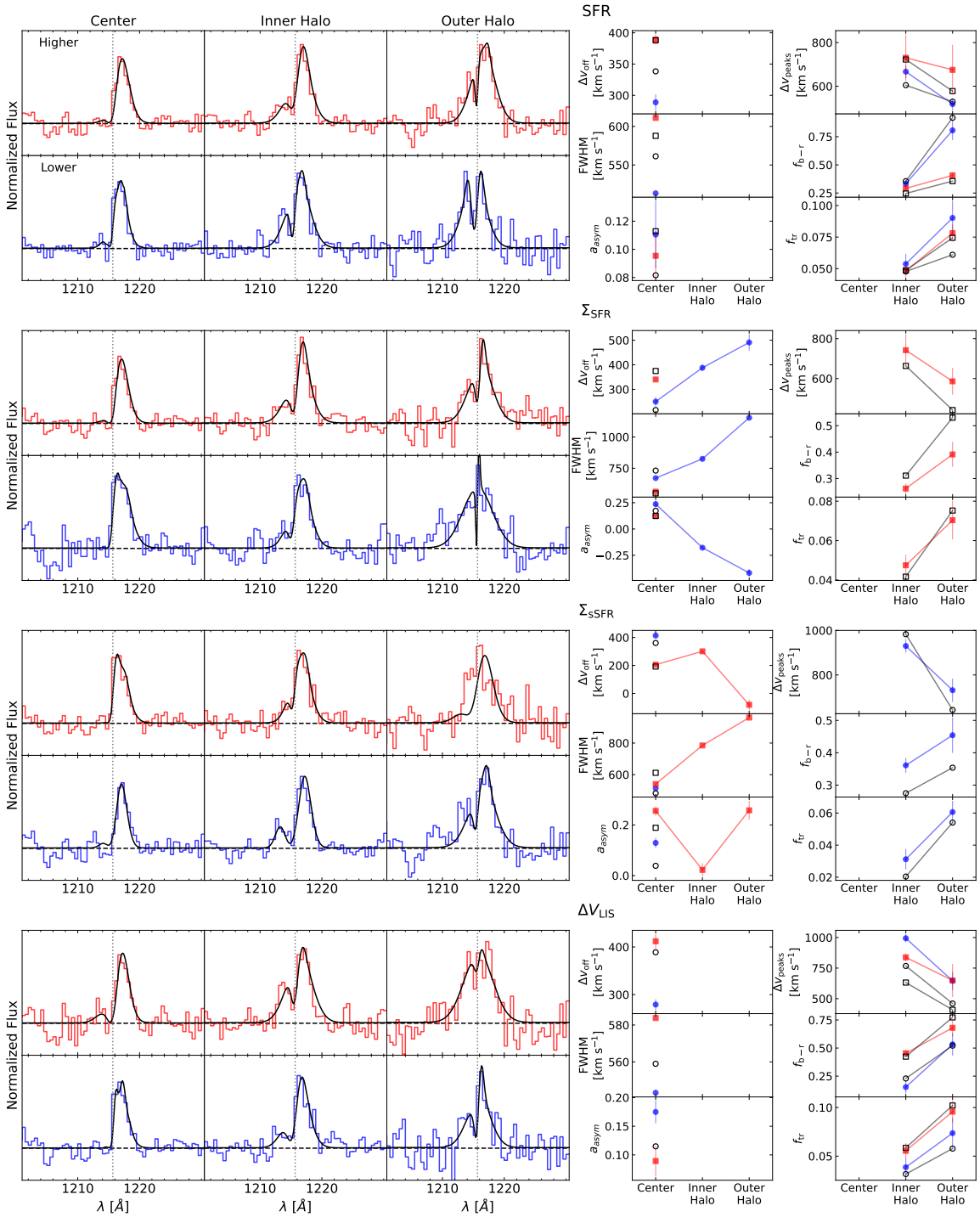
Center
Inner Halo
Outer Halo
Higher
Lower
Normalized Flux
SFR
Σ_{SFR}
Σ_{sSFR}
ΔV_{LIS}
Δv_{off} [km s^{-1}]
FWHM [km s^{-1}]
a_{asym}
Δv_{peaks} [km s^{-1}]
f_{b-r}
f_{fr}
λ [Å]
1210
1220
Center
Inner Halo
Outer Halo

Figure 5.5: Lyα spectral profiles and derived properties across the Lyα halo in bins of various galactic properties. *Left*: The Lyα profile in three regions. Distance from the center increases from left to right. The bottom row of each panel (blue) displays the "lower" bin, while the top row (red) is the "higher" bin. The black line is the best-fit shell model from `zELDA`. *Right*: The properties of the single- or double-peaked Lyα profiles. The panels in the left column are the peak velocity shift ($\Delta v_{\rm off}$), FWHM, and the asymmetry parameter ($a_{\rm asym}$) for single-peaked profiles, while in the right column are the peak separation ($\Delta v_{\rm peaks}$), blue-to-red peak flux ratio ($f_{\rm b-r}$), and trough flux ratio ($f_{\rm tr}$) for double-peaked profiles. Filled blue and open black circles are measured from the observed and best-fit shell model "lower" bin, respectively. Filled red and open black squares are measured from the observed and best-fit shell model "higher" bin, respectively. The error bars are typically smaller than the symbol size.

Table 5.3 reports the best-fit values of the properties of the gas predicted by `zELDA` and the chi-squared of the best fit. As shown in previous studies, by fitting the Lyα profile alone, the shell model cannot provide reliable constraints on the dust optical depth but can constrain the shell expansion velocity and HI column density (e.g., Gronke et al., 2015; Gurung-López et al., 2022); thus, we only report on the expansion velocity and column density.

We first consider the transition to double-peaked profiles in the lower SFR, $\Sigma_{\rm sSFR}$, and higher (i.e., "slower") outflow velocity bins. The double-peaked profiles may be the result of lower neutral gas kinematics in the inner halo region due to weaker outflows. Indeed, the shell expansion velocity decreases in the inner halo region for the lower SFR and $\Sigma_{\rm sSFR}$ bins, as expected for lower star-formation activity driving weaker outflows. On the other hand, $V_{\rm exp}$ increases in the inner halo region of the higher outflow velocity bin. Although, $V_{\rm exp}$ in the central and inner halo regions of each of these bins agree within 1σ, suggesting that the kinematics of neutral gas is not the primary factor in reshaping their Lyα profile. The transition may be due instead to changes in the distribution of neutral gas. The column density of the thin shell between the central and inner halo regions in the lower SFR and $\Sigma_{\rm sSFR}$ bins varies slightly (1.6σ and 0.3σ), while decreasing significantly (3.4σ) in the higher outflow velocity bin. The distribution of neutral gas within the CGM appears to have a large role in shaping the Lyα profile in the higher outflow velocity bin. Although, changes in the thin shell expansion velocity and column density cannot explain the transition to double-peaked profiles in bins of lower SFR and $\Sigma_{\rm sSFR}$.

Table 5.3: Best fit parameters of zELDA models

Quantity	Bin	Region	$V_{\rm exp}$ [km s^{-1}]	$\log(N_{\rm H}$ [cm^{-2}]	$\chi^2_{\rm r}$
SFR	Lower	Cont.	300^{+18}_{-72}	$19.2^{+0.5}_{-0.2}$	7
		Inner	230^{+18}_{-15}	$18.5^{+0.4}_{-0.2}$	5
		Outer	2^{+20}_{-2}	$20.1^{+0.1}_{-1.0}$	6
	Higher	Cont.	190^{+25}_{-21}	$20.1^{+0.1}_{-0.1}$	13
		Inner	220^{+26}_{-40}	$19.0^{+0.4}_{-0.6}$	2
		Outer	260^{+20}_{-17}	$17.7^{+0.2}_{-0.3}$	7
$\Sigma_{\rm SFR}$	Lower	Cont.	310^{+85}_{-32}	$20.0^{+0.1}_{-0.3}$	4
		Inner	320^{+16}_{-22}	$18.7^{+0.2}_{-0.2}$	8
		Outer	50^{+43}_{-34}	$17.6^{+0.7}_{-0.4}$	7
	Higher	Cont.	200^{+60}_{-30}	$20.0^{+0.1}_{-0.2}$	15
		Inner	200^{+20}_{-20}	$19.0^{+0.2}_{-0.2}$	8
		Outer	130^{+40}_{-40}	$18.2^{+0.4}_{-0.5}$	3
$\Sigma_{\rm sSFR}$	Lower	Cont.	60^{+100}_{-40}	$20.5^{+0.8}_{-2.7}$	17
		Inner	20^{+200}_{-2}	$21.1^{+0.1}_{-1.8}$	5
		Outer	260^{+30}_{-250}	$18.3^{+0.3}_{-0.3}$	5
	Higher	Cont.	280^{+30}_{-18}	$19.8^{+0.1}_{-0.1}$	14
		Inner	300^{+18}_{-20}	$18.3^{+0.3}_{-0.3}$	10
		Outer	210^{+560}_{-180}	$19.9^{+0.8}_{-2.5}$	9
$\Delta v_{\rm LIS}$	Lower	Cont.	200^{+30}_{-6}	$19.9^{+0.1}_{-0.1}$	15
		Inner	230^{+18}_{-18}	$19.3^{+0.1}_{-0.1}$	7
		Outer	110^{+40}_{-52}	$18.6^{+0.4}_{-0.4}$	4
	Higher	Cont.	130^{+80}_{-90}	$20.1^{+0.9}_{-0.4}$	7
		Inner	200^{+40}_{-60}	$18.6^{+0.2}_{-0.2}$	6
		Outer	40^{+100}_{-25}	$17.9^{+1.0}_{-0.6}$	9

Expansion velocity, $V_{\rm exp}$, and HI column density, $\log(N_{\rm H})$, of the zELDA models. The last column provides an estimation of the goodness of the fit in terms of reduced χ^2. The numbers in the fourth and fifth columns correspond to the 50th percentile, while uncertainties are reported at the 16th and 84th percentiles.

Next, we consider the transition to double-peaked profiles in the higher SFR, $\Sigma_{\rm SFR}$, and lower (i.e., "faster") outflow velocity bins. As these bins likely host faster outflows, this transition may indicate a rapid decrease in $V_{\rm exp}$. However, between the central and inner halo regions, $V_{\rm exp}$ remains constant in the higher $\Sigma_{\rm SFR}$ bin and increases slightly in the higher SFR and lower outflow velocity bins, 0.6σ and 0.9σ, respectively. On the other hand, there is a marginal (2.7σ) and significant (3.5σ and 4.2σ) decrease in the column density of the shell for the higher SFR, $\Sigma_{\rm SFR}$, and lower outflow velocity bins, respectively. The distribution of neutral gas in the CGM appears to be the primary factor shaping the Lyα profiles in these regions.

In addition to the overall shape of the profile (i.e., single- or double-peaked), variations in the properties of the Lyα profile (e.g., $\Delta v_{\rm peaks}$, $f_{\rm b-r}$) across the halo will depend on the distribution of neutral gas in the CGM. Here, we investigate the decrease (increase) in peak separation (blue-to-red flux ratio) between the inner and outer halo regions where both the observations and `zELDA` models exhibit double-peaked profiles. In general, both $V_{\rm exp}$ and $\log(N_{\rm H})$ decrease between the inner and outer halo regions. We argue that $V_{\rm exp}$ controls the blue-to-red flux ratio, and $\log(N_{\rm H})$ sets the peak separation. In this framework, photons emerging from the outer halo would undergo (1) fewer resonant scatterings due to the decrease in column density and (2) experience smaller resonant shifts due to the slower expansion velocity of the shell.[7] With fewer scatterings, the photons could escape closer to the systemic redshift, thus decreasing the peak separation. Smaller resonant shifts would allow more photons to escape in the blue wing of Lyman-alpha, as they would appear farther

[7] A possible explanation for the decrease in shell expansion velocity could be the increasing significance of gravitational deceleration at large radii (e.g., Thompson et al., 2016; Chen et al., 2020).

from resonance in the reference frame of the expanding, blueshifted shell approaching the observer. However, in the SFR and lower $\Sigma_{\rm sSFR}$ bins, $V_{\rm exp}$ or $\log(N_{\rm H})$ *increases* in the outer halo, while the trends in peak separation and blue-to-red flux ratio remain unchanged. Similarly, the best-fit shell models are unable to recreate profiles with similar physical properties. The peak separation is consistently underpredicted, while the blue-to-red and trough flux ratios vary between under- and overpredicted. These discrepancies suggest that the geometry of the shell model may be too simplistic, even for these less extreme Lyα halos, and that more realistic (e.g., clumpy ISM) models should be considered to extract robust physical information from the Lyα profile.

5.6 Conclusions

We have presented results on the spectral properties of Lyα emission in a sample of 27 star-forming galaxies using KCWI integral field spectroscopy. These objects represent a search for Lyα halos in typical star-forming galaxies with no preselection based on the down-the-barrel Lyα emission. Composite spectra were constructed in three regions across the Lyα halo in bins of various galaxy properties, and fitted with single and double asymmetric Gaussian profiles. To quantify changes in the Lyα profile across the halo, the red peak velocity offset, FWHM, and asymmetry in single-peaked profiles, or the peak separation, blue-to-red peak flux ratio, and trough flux ratio in double-peaked profiles were measured. This study allowed us to further push the analysis of spatially resolved Lyα halos towards the larger galaxy population at $z \sim 2$. Our main results are as follows:

- Redshifted single-peaked Lyα profiles are ubiquitous within a central region, while the profiles in the inner and outer halos are more diverse. In the SFR, $\Delta v_{\rm LIS}$, lower $\Sigma_{\rm sSFR}$, and higher $\Sigma_{\rm SFR}$ bins, the profiles transition to double-peaked profiles. Between the inner and outer halo regions, the peak separation decreases, while the blue-to-red peak and trough flux ratios increase. On the other hand, the higher $\Sigma_{\rm sSFR}$ and lower $\Sigma_{\rm SFR}$ bins remain single-peaked, and becoming broader and more blueward asymmetric at large radii.

- For the brightest halo in the sample, COSMOS 1908, we measured the properties of the Lyα profile in individual spaxels. The halo displays large azimuthal variations in peak separation, with both regions of narrow and large separation near the outskirts of the halo. The blue-to-red peak and trough fluxes are significantly correlated with distance, increasing towards the outskirts of the halo, similar to the composite spectra.

- We investigated the effect of outflow velocity on the Lyα surface brightness profile. The "faster" outflow bin appears to have a smaller Lyα halo than that of the "slower" bin. This may be due to outflows clearing channels in the ISM/CGM, aiding in the escape of Lyα photons. Considering the EW of LIS and HIS lines, the faster bin has stronger (weaker) HIS (LIS) than the slower bin, suggesting a lower neutral gas covering fraction. However, the deficiency of Lyα in the surface brightness profiles at small distances and large velocity offset of the Lyα profiles suggest that the low-column-density channels do not lie along our line of sight.

- We fitted the composite spectra with a uniform expanding shell radiative transfer model. The model reproduces the redshifted single-peaked profile in the central re-

gion, and predicts double-peaked profiles in the inner and outer halo regions, regardless of property or bin. When both the the observations and `zELDA` models exhibit double-peaked profiles, the shell expansion velocity and HI column density decrease as distance increases. However, the properties derived from the modeled profiles can be significantly different than those from the observed profiles. These discrepancies suggest that the geometry of the shell model is too simplistic. To derive physical insights from the Lyα profile, models that employ realistic neutral gas distributions should be considered.

The emergent Lyα profile encodes a wealth of information about neutral gas within the CGM, where many processes crucial to galaxy evolution are regulated. Here, we have studied the spatial variation within Lyα halos in a small sample of typical star-forming galaxies with KCWI observations. This study gives us a glimpse into the complexity of recovering physical information from Lyα profiles in typical $z \sim 2$ star-forming galaxies. To build a better understanding of the connection between gas properties and the shape of the Lyα profile, larger and deeper samples of galaxies and the continuing development of realistic radiative transfer models are crucial. As integral field observations push towards individual galaxies with lower masses, lower star-formation rates, and higher star-formation-rate surface densities, we expect that use of Lyα halos as probes of neutral gas kinematics and structure will only continue to grow.

Chapter 6

Conclusions

In order to study the cycling of gas into and out of galaxies, this work has taken advantage of the spectroscopic coverage of the MOSDEF Survey and follow-up campaigns with LRIS and KCWI. The combination of rest-UV and rest-optical spectra allowed outflows and inflows to be studied on an individual galaxy basis for star-forming galaxies at $z = 1.42$ – 3.48. In Chapter 2, the relation between cool, low-ionized gas outflows and their host galaxies was investigated to determine the primary driving mechanism of the outflows, the low detection rate of gas inflows was explored in Chapter 3, strong rest-optical emission lines were decomposed in Chapter 4 to constrain the loading factors of warm, ionized gas outflows, and variations in the Lyα emission line profile across composite Lyα halos were investigated in Chapter 5 to quantify the distribution and kinematics of neutral CGM gas.

6.1 Gas flows and Galaxy Evolution

To place the conclusions of this dissertation into the larger context of galaxy evolution, we return to the questions presented in Section 1.3. For star-forming galaxies at $z \sim 2$:

1. What are the properties of their outflows?

In Chapter 2, the outflow velocity of cool, low-ionized outflows traced by rest-UV absorption lines was measured for individual galaxies. Comparing outflow velocity to global galactic properties revealed that only the maximum outflow velocity was marginally correlated with SFR, such that galaxies hosting faster outflows have higher SFRs. The large fraction of outflows among galaxies at high ($>45°$) inclinations, even within a rotation-dominated sub-sample, suggests that the outflows are not well collimated. Instead, the outflows likely have large covering fractions and, thus, are observable at high inclinations. Limitations in the down-the-barrel observations can explain the lack of a correlation between outflow velocity and $\Sigma_{\rm SFR}$. The outflowing gas could uncouple from changes in $\Sigma_{\rm SFR}$ at large distances from galaxies, outflows and $\Sigma_{\rm SFR}$ may be related on local scales rather than the global scales observed, or the global $v_{\rm out}$–$\Sigma_{\rm SFR}$ relation may be weak and undetectable within the $\Sigma_{\rm SFR}$ range probed by the sample. Within the sample, there was no strong evidence of a threshold $\Sigma_{\rm SFR}$ or $\Sigma_{\rm sSFR}$ value necessary to launch an outflow.

In Chapter 4, [O III] and Hα emission lines were decomposed into narrow components tracing motion within galaxies and broad components tracing warm, ionized gas outflows. Significant evidence for broad emission was found in $\sim$10% of the sample and was more prevalent among galaxies with higher SFRs and $\Sigma_{\rm SFR}$. The maximum ionized outflow

velocity, however, did not exhibit significant correlations with any galactic property and was below the escape velocity of their host in a majority of the galaxies. Moving beyond velocity, the mass-, energy-, and momentum-loading factors of the ionized outflows were derived using the simple outflow model of Genzel et al. (2011) and found to be modest, with the mass-loading factor marginally correlated with stellar mass. These results suggest that the contribution of ionized outflows may be negligible, even during the peak of cosmic star-formation.

Together, these two outflow phases hint at the multi-scale nature of outflows. Absorption lines tracing cool outflowing gas are sensitive to both high- and low-density gas, while broad emission line components trace warmer, denser outflowing gas. This difference in density sensitivity likely leads to a difference in scales probed, with emission lines tracing gas closer to the launching sites of outflows compared to absorption lines. Within this context, our results suggest that outflows are connected to the regions that launch them rather than the global properties of their host. Cool outflows have almost no correlations with the properties of their host galaxies, while warm outflows, tracing gas on smaller scales, in composite spectra exhibit clear trends with several galactic properties. However, the trends presented in this work need to be confirmed over a larger range of galactic properties with outflows detected with absorption and emission line tracers (see Section 6.2).

2. What is the primary driving mechanism of their outflows?

The primary outflow driving mechanism is predicted to affect how the velocity and mass-loading factor of outflows scale with the SFR and stellar mass of galaxies. In Chapter

2, the scaling between the maximum outflow velocity of cool, low-ionized gas outflows and SFR agreed with predictions for outflows primarily driven by mechanical energy injected by supernovae, as opposed to radiation pressure acting on dusty material. On the other hand, the scaling of the mass-loading factor of warm, ionized gas outflows with stellar mass in Chapter 4 was intermediate between the predicted dependence for energy- or momentum-driven outflows, suggesting that ionized outflows are driven by a combination of these mechanisms. Together, these results indicate that different physical mechanisms may be responsible for driving different outflow phases.

3. What is the covering fraction of inflows?

At a conservative level, the detection of three galaxies with robust measurements of inflowing gas traced by red-shifted rest-UV low-ionization absorption lines from a sample of 134 galaxies in Chapter 3 implies that along a random sightline through a galaxy, the chance of encountering inflowing gas is $\approx 2\% \pm 1\%$. The three inflow galaxies were found to have higher sSFR and $\Sigma_{\rm SFR}$ compared to the remaining sample. However, no property was unique within a larger sample of "inflowing" galaxies that included galaxies with heavily redward skewed absorption line profiles - indicating a large fraction of inflowing gas. The low detection rate of inflowing gas is likely related to the geometry and covering fraction of inflowing gas. Within the entire sample, higher sSFR galaxies were found to have an enhanced inflow covering fraction at a given inflow velocity relative to those with lower sSFR, possibly due to thicker filaments from the IGM or an increase in the amount of recycling gas in the CGM.

4. What are the kinematics and distribution of neutral gas within their circumgalatic mediums?

In Chapter 5, redshifted single-peaked Lyα line profiles were found to be ubiquitous within a central region of composite Lyα halos, while farther out, the profile either remained single-peaked or transitioned to double-peaked. These profiles were fit with a uniform expanding thin shell radiative transfer model to connect the properties of neutral gas to the observed profiles. The model reproduced the observed redshifted single-peaked profile within the central region and predicted double-peaked profiles in the inner and outer halo regions, regardless of galactic property. When both the observed and modeled profiles double-peaked, the neutral gas shell expansion velocity and column density generally decreased with distance. However, the large errors in the modeled properties and discrepancies between the best-fit models and the observed profiles suggest that the geometry of the shell model is too simplistic and that more realistic gas distribution models should be considered.

6.2 Future Work

The work presented in this dissertation provides a glimpse into the complexities that arise while studying gas cycling around $z \sim 2$ star-forming galaxies with direct observations. As such, there are several directions for future work that will be critical to furthering our understanding of outflows and inflows during this important epoch. A persistent observational limitation at $z \sim 2$ is the relatively limited range in galactic properties probed, often missing galaxies at the extreme ends of parameter space (e.g., very high or low stellar

masses and SFRs). In the local Universe, samples that span several orders of magnitude in stellar mass, SFR, or $\Sigma_{\rm SFR}$ have shown that outflow velocity scales weakly with these properties (e.g., Martin, 2005; Heckman et al., 2015). As discussed in Chapter 2, the lack of correlations found between the velocity of cool, low-ionized gas outflows and galactic properties is likely a result of the limited range of properties probed by the MOSDEF Survey, highlighting the need for a large parameter space to establish clear relations. Alternatively, the properties of outflows may strongly couple to the regions that launch them rather than the "global" properties of their host (e.g., Bordoloi et al., 2016). The upcoming arrival of wide-field, massive multiplexing spectrographs on ground-based 8-10m telescopes, such as MOONS on VLT and PFS on Subrau, will be of major importance for such work. Surveys with these instruments will enable us to probe a wider range of galactic properties and better constrain how outflow velocity scales with galactic properties, providing insight into the nature of outflows (global or local) and their primary driving mechanism (energy- or momentum-driven).

Another limitation of current observational studies is probing the multi-phase nature of outflows. Multi-wavelength observations have demonstrated that outflows are multi-phased, spanning up to six orders of magnitude in temperature ($10 - 10^7$ K). Beyond the local Universe, however, studies are often limited to a single gas tracer, which only probes a single outflow phase. Studying various outflow phases simultaneously from individual high redshift galaxies will help constrain the total effect outflows have on galaxy evolution. Progress on this front will require spectroscopic surveys with multiple instruments providing broad wavelength coverage. Large rest-optical surveys with wide-field, massive multiplexing

spectrographs will greatly increase the number of known galaxies with detections of warm, ionized gas outflows. Smaller, targeted follow-up campaigns with different instruments can then probe other outflow phases of those galaxies.

Another area that requires attention is constraining the properties of gas flows beyond their kinematics. The effects that gas flows into and out of galaxies will have depend on several properties of the gas, such as their metallicity, electron density, covering fraction, etc. Current studies can begin to estimate these properties under simple models and with various assumptions. However, properly constraining these properties in high-redshift galaxies will require the development of models to extract information from subtle signatures in observed line profiles and observations along multiple sightlines through galaxies to break degeneracies in the modeling, which will not be feasible in the foreseeable future.

Bibliography

Adelberger, K. L., Steidel, C. C., Kollmeier, J. A., & Reddy, N. A. 2006, ApJ, 637, 74, doi: 10.1086/497896

Alarie, A., & Morisset, C. 2019, Rev. Mexicana Astron. Astrofis., 55, 377, doi: 10.22201/ia.01851101p.2019.55.02.21

Alexandroff, R. M., Heckman, T. M., Borthakur, S., Overzier, R., & Leitherer, C. 2015, ApJ, 810, 104, doi: 10.1088/0004-637X/810/2/104

Allen, M. G., Groves, B. A., Dopita, M. A., Sutherland, R. S., & Kewley, L. J. 2008, ApJS, 178, 20, doi: 10.1086/589652

Anglés-Alcázar, D., Faucher-Giguère, C.-A., Kereš, D., et al. 2017, MNRAS, 470, 4698, doi: 10.1093/mnras/stx1517

Arribas, S., Colina, L., Bellocchi, E., Maiolino, R., & Villar-Martín, M. 2014, A&A, 568, A14, doi: 10.1051/0004-6361/201323324

Astropy Collaboration, Robitaille, T. P., Tollerud, E. J., et al. 2013, A&A, 558, A33, doi: 10.1051/0004-6361/201322068

Astropy Collaboration, Price-Whelan, A. M., Sipőcz, B. M., et al. 2018, AJ, 156, 123, doi: 10.3847/1538-3881/aabc4f

Astropy Collaboration, Price-Whelan, A. M., Lim, P. L., et al. 2022, ApJ, 935, 167, doi: 10.3847/1538-4357/ac7c74

Avery, C. R., Wuyts, S., Förster Schreiber, N. M., et al. 2021, MNRAS, 503, 5134, doi: 10.1093/mnras/stab780

—. 2022, MNRAS, 511, 4223, doi: 10.1093/mnras/stac190

Azadi, M., Coil, A. L., Aird, J., et al. 2017, ApJ, 835, 27, doi: 10.3847/1538-4357/835/1/27

Azadi, M., Coil, A., Aird, J., et al. 2018, ApJ, 866, 63, doi: 10.3847/1538-4357/aad3c8

Bacon, R., Accardo, M., Adjali, L., et al. 2010, in Society of Photo-Optical Instrumentation Engineers (SPIE) Conference Series, Vol. 7735, Ground-based and Airborne Instrumentation for Astronomy III, ed. I. S. McLean, S. K. Ramsay, & H. Takami, 773508, doi: 10.1117/12.856027

Baldwin, J. A., Phillips, M. M., & Terlevich, R. 1981, PASP, 93, 5, doi: 10.1086/130766

Barden, M., Jahnke, K., & Häußler, B. 2008, ApJS, 175, 105, doi: 10.1086/524039

Bauermeister, A., Blitz, L., & Ma, C.-P. 2010, ApJ, 717, 323, doi: 10.1088/0004-637X/717/1/323

Behrens, C., Dijkstra, M., & Niemeyer, J. C. 2014, A&A, 563, A77, doi: 10.1051/0004-6361/201322949

Behroozi, P., Wechsler, R. H., Hearin, A. P., & Conroy, C. 2019, MNRAS, 488, 3143, doi: 10.1093/mnras/stz1182

Bian, F., Kewley, L. J., & Dopita, M. A. 2018, ApJ, 859, 175, doi: 10.3847/1538-4357/aabd74

Bordoloi, R., Rigby, J. R., Tumlinson, J., et al. 2016, MNRAS, 458, 1891, doi: 10.1093/mnras/stw449

Bordoloi, R., Lilly, S. J., Knobel, C., et al. 2011, ApJ, 743, 10, doi: 10.1088/0004-637X/743/1/10

Bouché, N., Hohensee, W., Vargas, R., et al. 2012, MNRAS, 426, 801, doi: 10.1111/j.1365-2966.2012.21114.x

Bouché, N., Murphy, M. T., Kacprzak, G. G., et al. 2013, Science, 341, 50, doi: 10.1126/science.1234209

Bouché, N., Finley, H., Schroetter, I., et al. 2016, ApJ, 820, 121, doi: 10.3847/0004-637X/820/2/121

Bruzual, G., & Charlot, S. 2003a, MNRAS, 344, 1000, doi: 10.1046/j.1365-8711.2003.06897.x

—. 2003b, MNRAS, 344, 1000, doi: 10.1046/j.1365-8711.2003.06897.x

Calabrò, A., Pentericci, L., Talia, M., et al. 2022, A&A, 667, A117, doi: 10.1051/0004-6361/202244364

Calzetti, D., Armus, L., Bohlin, R. C., et al. 2000, ApJ, 533, 682, doi: 10.1086/308692

Calzetti, D., Kinney, A. L., & Storchi-Bergmann, T. 1994, ApJ, 429, 582, doi: 10.1086/174346

Cantalupo, S., Arrigoni-Battaia, F., Prochaska, J. X., Hennawi, J. F., & Madau, P. 2014, Nature, 506, 63, doi: 10.1038/nature12898

Cardelli, J. A., Clayton, G. C., & Mathis, J. S. 1989, ApJ, 345, 245, doi: 10.1086/167900

Carniani, S., Marconi, A., Maiolino, R., et al. 2015, A&A, 580, A102, doi: 10.1051/

0004-6361/201526557

Carr, C., & Scarlata, C. 2022, ApJ, 939, 47, doi: 10.3847/1538-4357/ac93fa

Cassata, P., Tasca, L. A. M., Le Fèvre, O., et al. 2015, A&A, 573, A24, doi: 10.1051/0004-6361/201423824

Chabrier, G. 2003, PASP, 115, 763, doi: 10.1086/376392

Chen, Y., Steidel, C. C., Hummels, C. B., et al. 2020, MNRAS, 499, 1721, doi: 10.1093/mnras/staa2808

Chen, Y., Steidel, C. C., Erb, D. K., et al. 2021, MNRAS, 508, 19, doi: 10.1093/mnras/stab2383

Chen, Y.-M., Tremonti, C. A., Heckman, T. M., et al. 2010, AJ, 140, 445, doi: 10.1088/0004-6256/140/2/445

Chevalier, R. A., & Clegg, A. W. 1985, Nature, 317, 44, doi: 10.1038/317044a0

Chisholm, J., Tremonti, C. A., Leitherer, C., & Chen, Y. 2017, MNRAS, 469, 4831, doi: 10.1093/mnras/stx1164

Chisholm, J., Tremonti, C. A., Leitherer, C., et al. 2015, ApJ, 811, 149, doi: 10.1088/0004-637X/811/2/149

Chisholm, J., Tremonti Christy, A., Leitherer, C., & Chen, Y. 2016, MNRAS, 463, 541, doi: 10.1093/mnras/stw1951

Christensen, C. R., Davé, R., Governato, F., et al. 2016, ApJ, 824, 57, doi: 10.3847/0004-637X/824/1/57

Christensen, L., Laursen, P., Richard, J., et al. 2012, MNRAS, 427, 1973, doi: 10.1111/j.1365-2966.2012.22007.x

Cicone, C., Maiolino, R., Sturm, E., et al. 2014, A&A, 562, A21, doi: 10.1051/0004-6361/201322464

Claeyssens, A., Richard, J., Blaizot, J., et al. 2019, MNRAS, 489, 5022, doi: 10.1093/mnras/stz2492

Coil, A. L., Aird, J., Reddy, N., et al. 2015, ApJ, 801, 35, doi: 10.1088/0004-637X/801/1/35

Concas, A., Popesso, P., Brusa, M., Mainieri, V., & Thomas, D. 2019, A&A, 622, A188, doi: 10.1051/0004-6361/201732152

Concas, A., Maiolino, R., Curti, M., et al. 2022, MNRAS, 513, 2535, doi: 10.1093/mnras/stac1026

Couto, G. S., Hughes, T. M., Boquien, M., et al. 2021, A&A, 654, A128, doi: 10.1051/0004-6361/202141490

Creasey, P., Theuns, T., & Bower, R. G. 2013, MNRAS, 429, 1922, doi: 10.1093/mnras/sts439

Croton, D. J., Springel, V., White, S. D. M., et al. 2006, MNRAS, 365, 11, doi: 10.1111/j.1365-2966.2005.09675.x

Daddi, E., Valentino, F., Rich, R. M., et al. 2021, A&A, 649, A78, doi: 10.1051/0004-6361/202038700

Dalcanton, J. J. 2007, ApJ, 658, 941, doi: 10.1086/508913

Danovich, M., Dekel, A., Hahn, O., Ceverino, D., & Primack, J. 2015, MNRAS, 449, 2087, doi: 10.1093/mnras/stv270

Davé, R., Finlator, K., & Oppenheimer, B. D. 2011, MNRAS, 416, 1354, doi: 10.1111/j.

1365-2966.2011.19132.x

Davies, R. L., Förster Schreiber, N. M., Übler, H., et al. 2019, ApJ, 873, 122, doi: 10.3847/1538-4357/ab06f1

Davis, J. D., Tremonti, C. A., Swiggum, C. N., et al. 2023, ApJ, 951, 105, doi: 10.3847/1538-4357/accbbf

Dekel, A., & Birnboim, Y. 2006, MNRAS, 368, 2, doi: 10.1111/j.1365-2966.2006.10145.x

Dekel, A., & Silk, J. 1986, ApJ, 303, 39, doi: 10.1086/164050

Dekel, A., Birnboim, Y., Engel, G., et al. 2009, Nature, 457, 451, doi: 10.1038/nature07648

Diamond-Stanic, A. M., Coil, A. L., Moustakas, J., et al. 2016, ApJ, 824, 24, doi: 10.3847/0004-637X/824/1/24

Dijkstra, M., Gronke, M., & Venkatesan, A. 2016, ApJ, 828, 71, doi: 10.3847/0004-637X/828/2/71

Dijkstra, M., Haiman, Z., & Spaans, M. 2006, ApJ, 649, 14, doi: 10.1086/506243

Dijkstra, M., & Kramer, R. 2012, MNRAS, 424, 1672, doi: 10.1111/j.1365-2966.2012.21131.x

Dopita, M. A., & Sutherland, R. S. 1996, ApJS, 102, 161, doi: 10.1086/192255

Du, X., Shapley, A. E., Martin, C. L., & Coil, A. L. 2016, ApJ, 829, 64, doi: 10.3847/0004-637X/829/2/64

Du, X., Shapley, A. E., Reddy, N. A., et al. 2018, ApJ, 860, 75, doi: 10.3847/1538-4357/aabfcf

Du, X., Shapley, A. E., Topping, M. W., et al. 2021, ApJ, 920, 95, doi: 10.3847/1538-4357/

ac1273

Duval, F., Schaerer, D., Östlin, G., & Laursen, P. 2014, A&A, 562, A52, doi: 10.1051/0004-6361/201220455

Erb, D. K., Li, Z., Steidel, C. C., et al. 2022, arXiv e-prints, arXiv:2210.02465, doi: 10.48550/arXiv.2210.02465

Erb, D. K., Pettini, M., Steidel, C. C., et al. 2016, ApJ, 830, 52, doi: 10.3847/0004-637X/830/1/52

Erb, D. K., Steidel, C. C., Shapley, A. E., et al. 2006, ApJ, 647, 128, doi: 10.1086/505341

Erb, D. K., Steidel, C. C., Trainor, R. F., et al. 2014, ApJ, 795, 33, doi: 10.1088/0004-637X/795/1/33

Everett, J. E., & Zweibel, E. G. 2011, ApJ, 739, 60, doi: 10.1088/0004-637X/739/2/60

Faucher-Giguère, C.-A., Hopkins, P. F., Kereš, D., et al. 2015, MNRAS, 449, 987, doi: 10.1093/mnras/stv336

Faucher-Giguère, C.-A., & Kereš, D. 2011, MNRAS, 412, L118, doi: 10.1111/j.1745-3933.2011.01018.x

Faucher-Giguère, C.-A., Kereš, D., Dijkstra, M., Hernquist, L., & Zaldarriaga, M. 2010, ApJ, 725, 633, doi: 10.1088/0004-637X/725/1/633

Faucher-Giguère, C.-A., Kereš, D., & Ma, C.-P. 2011, MNRAS, 417, 2982, doi: 10.1111/j.1365-2966.2011.19457.x

Ferrara, A., & Ricotti, M. 2006, MNRAS, 373, 571, doi: 10.1111/j.1365-2966.2006.10978.x

Finlator, K., & Davé, R. 2008, MNRAS, 385, 2181, doi: 10.1111/j.1365-2966.2008.

12991.x

Fitzpatrick, E. L., & Massa, D. 1990, ApJS, 72, 163, doi: 10.1086/191413

Fluetsch, A., Maiolino, R., Carniani, S., et al. 2019, MNRAS, 483, 4586, doi: 10.1093/mnras/sty3449

—. 2021, MNRAS, 505, 5753, doi: 10.1093/mnras/stab1666

Foreman-Mackey, D., Hogg, D. W., Lang, D., & Goodman, J. 2013, PASP, 125, 306, doi: 10.1086/670067

Förster Schreiber, N. M., & Wuyts, S. 2020, ARA&A, 58, 661, doi: 10.1146/annurev-astro-032620-021910

Förster Schreiber, N. M., Genzel, R., Newman, S. F., et al. 2014, ApJ, 787, 38, doi: 10.1088/0004-637X/787/1/38

Förster Schreiber, N. M., Übler, H., Davies, R. L., et al. 2019, ApJ, 875, 21, doi: 10.3847/1538-4357/ab0ca2

Freeman, W. R., Siana, B., Kriek, M., et al. 2019, ApJ, 873, 102, doi: 10.3847/1538-4357/ab0655

Fu, H., Xue, R., Prochaska, J. X., et al. 2021, ApJ, 908, 188, doi: 10.3847/1538-4357/abdb32

Fumagalli, M., Hennawi, J. F., Prochaska, J. X., et al. 2014, ApJ, 780, 74, doi: 10.1088/0004-637X/780/1/74

Fumagalli, M., Prochaska, J. X., Kasen, D., et al. 2011, MNRAS, 418, 1796, doi: 10.1111/j.1365-2966.2011.19599.x

Gazagnes, S., Chisholm, J., Schaerer, D., et al. 2018, A&A, 616, A29, doi: 10.1051/

0004-6361/201832759

Genzel, R., Newman, S., Jones, T., et al. 2011, ApJ, 733, 101, doi: 10.1088/0004-637X/733/2/101

Genzel, R., Förster Schreiber, N. M., Rosario, D., et al. 2014, ApJ, 796, 7, doi: 10.1088/0004-637X/796/1/7

Girichidis, P., Naab, T., Hanasz, M., & Walch, S. 2018, MNRAS, 479, 3042, doi: 10.1093/mnras/sty1653

Girichidis, P., Walch, S., Naab, T., et al. 2016, MNRAS, 456, 3432, doi: 10.1093/mnras/stv2742

Gnedin, N. Y., Kravtsov, A. V., & Chen, H.-W. 2008, ApJ, 672, 765, doi: 10.1086/524007

Goerdt, T., & Ceverino, D. 2015, MNRAS, 450, 3359, doi: 10.1093/mnras/stv786

Goerdt, T., Dekel, A., Sternberg, A., et al. 2010, MNRAS, 407, 613, doi: 10.1111/j.1365-2966.2010.16941.x

Gordon, K. D., Clayton, G. C., Misselt, K. A., Landolt, A. U., & Wolff, M. J. 2003, ApJ, 594, 279, doi: 10.1086/376774

Grand, R. J. J., van de Voort, F., Zjupa, J., et al. 2019, MNRAS, 490, 4786, doi: 10.1093/mnras/stz2928

Grogin, N. A., Kocevski, D. D., Faber, S. M., et al. 2011, ApJS, 197, 35, doi: 10.1088/0067-0049/197/2/35

Gronke, M., Bull, P., & Dijkstra, M. 2015, ApJ, 812, 123, doi: 10.1088/0004-637X/812/2/123

Gronke, M., & Dijkstra, M. 2016, ApJ, 826, 14, doi: 10.3847/0004-637X/826/1/14

Guedes, J., Callegari, S., Madau, P., & Mayer, L. 2011, ApJ, 742, 76, doi: 10.1088/0004-637X/742/2/76

Gurung-López, S., Gronke, M., Saito, S., Bonoli, S., & Orsi, Á. A. 2022, MNRAS, 510, 4525, doi: 10.1093/mnras/stab3554

Gurung-López, S., Orsi, Á. A., Bonoli, S., Baugh, C. M., & Lacey, C. G. 2019, MNRAS, 486, 1882, doi: 10.1093/mnras/stz838

Gutkin, J., Charlot, S., & Bruzual, G. 2016, MNRAS, 462, 1757, doi: 10.1093/mnras/stw1716

Hansen, M., & Oh, S. P. 2006, MNRAS, 367, 979, doi: 10.1111/j.1365-2966.2005.09870.x

Harris, C. R., Millman, K. J., van der Walt, S. J., et al. 2020, Nature, 585, 357, doi: 10.1038/s41586-020-2649-2

Hashimoto, T., Ouchi, M., Shimasaku, K., et al. 2013, ApJ, 765, 70, doi: 10.1088/0004-637X/765/1/70

Hashimoto, T., Verhamme, A., Ouchi, M., et al. 2015, ApJ, 812, 157, doi: 10.1088/0004-637X/812/2/157

Hayashino, T., Matsuda, Y., Tamura, H., et al. 2004, AJ, 128, 2073, doi: 10.1086/424935

Hayes, M. 2015, PASA, 32, e027, doi: 10.1017/pasa.2015.25

Hayes, M., Östlin, G., Schaerer, D., et al. 2013, ApJ, 765, L27, doi: 10.1088/2041-8205/765/2/L27

Heckman, T. M. 2002, in Astronomical Society of the Pacific Conference Series, Vol. 254, Extragalactic Gas at Low Redshift, ed. J. S. Mulchaey & J. T. Stocke, 292. https:

//arxiv.org/abs/astro-ph/0107438

Heckman, T. M., Alexandroff, R. M., Borthakur, S., Overzier, R., & Leitherer, C. 2015, ApJ, 809, 147, doi: 10.1088/0004-637X/809/2/147

Heckman, T. M., Armus, L., & Miley, G. K. 1990, ApJS, 74, 833, doi: 10.1086/191522

Heckman, T. M., Lehnert, M. D., Strickland, D. K., & Armus, L. 2000, ApJS, 129, 493, doi: 10.1086/313421

Heckman, T. M., & Thompson, T. A. 2017, in Handbook of Supernovae, ed. A. W. Alsabti & P. Murdin (Springer International Publishing), 2431, doi: 10.1007/978-3-319-21846-5_23

Henriques, B. M. B., White, S. D. M., Thomas, P. A., et al. 2013, MNRAS, 431, 3373, doi: 10.1093/mnras/stt415

Henry, A., Scarlata, C., Martin, C. L., & Erb, D. 2015, ApJ, 809, 19, doi: 10.1088/0004-637X/809/1/19

Ho, I. T., Kewley, L. J., Dopita, M. A., et al. 2014, MNRAS, 444, 3894, doi: 10.1093/mnras/stu1653

Ho, I. T., Medling, A. M., Bland-Hawthorn, J., et al. 2016, MNRAS, 457, 1257, doi: 10.1093/mnras/stw017

Ho, S. H., Martin, C. L., & Turner, M. L. 2019, ApJ, 875, 54, doi: 10.3847/1538-4357/ab0ec2

Hopkins, P. F., Kereš, D., Oñorbe, J., et al. 2014, MNRAS, 445, 581, doi: 10.1093/mnras/stu1738

Hopkins, P. F., Murray, N., Quataert, E., & Thompson, T. A. 2010, MNRAS, 401, L19,

doi: 10.1111/j.1745-3933.2009.00777.x

Hopkins, P. F., Wetzel, A., Kereš, D., et al. 2018, MNRAS, 480, 800, doi: 10.1093/mnras/sty1690

Hopkins, P. F., Wetzel, A., Wheeler, C., et al. 2023, MNRAS, 519, 3154, doi: 10.1093/mnras/stac3489

Hou, A., Parker, L. C., Harris, W. E., & Wilman, D. J. 2009, ApJ, 702, 1199, doi: 10.1088/0004-637X/702/2/1199

Hummels, C. B., Smith, B. D., & Silvia, D. W. 2017, ApJ, 847, 59, doi: 10.3847/1538-4357/aa7e2d

Hunter, J. D. 2007, Computing in Science & Engineering, 9, 90, doi: 10.1109/MCSE.2007.55

Ipavich, F. M. 1975, ApJ, 196, 107, doi: 10.1086/153397

Jaskot, A. E., Oey, M. S., Scarlata, C., & Dowd, T. 2017, ApJ, 851, L9, doi: 10.3847/2041-8213/aa9d83

Jones, T., Stark, D. P., & Ellis, R. S. 2012, ApJ, 751, 51, doi: 10.1088/0004-637X/751/1/51

Kacprzak, G. G., Churchill, C. W., Ceverino, D., et al. 2010, ApJ, 711, 533, doi: 10.1088/0004-637X/711/2/533

Kacprzak, G. G., Churchill, C. W., & Nielsen, N. M. 2012, ApJ, 760, L7, doi: 10.1088/2041-8205/760/1/L7

Katz, N., & White, S. D. M. 1993, ApJ, 412, 455, doi: 10.1086/172935

Kauffmann, G., Heckman, T. M., Tremonti, C., et al. 2003, MNRAS, 346, 1055, doi: 10.1111/j.1365-2966.2003.07154.x

Kennicutt, R. C., J. 1983, ApJ, 272, 54, doi: 10.1086/161261

Kennicutt, Robert C., J. 1989, ApJ, 344, 685, doi: 10.1086/167834

—. 1998, ARA&A, 36, 189, doi: 10.1146/annurev.astro.36.1.189

Kereš, D., Katz, N., Fardal, M., Davé, R., & Weinberg, D. H. 2009, MNRAS, 395, 160, doi: 10.1111/j.1365-2966.2009.14541.x

Kereš, D., Katz, N., Weinberg, D. H., & Davé, R. 2005, MNRAS, 363, 2, doi: 10.1111/j.1365-2966.2005.09451.x

Kewley, L. J., Dopita, M. A., Sutherland, R. S., Heisler, C. A., & Trevena, J. 2001, ApJ, 556, 121, doi: 10.1086/321545

Kim, C.-G., & Ostriker, E. C. 2015, ApJ, 802, 99, doi: 10.1088/0004-637X/802/2/99

—. 2018, ApJ, 853, 173, doi: 10.3847/1538-4357/aaa5ff

Kim, C.-G., Ostriker, E. C., Somerville, R. S., et al. 2020, ApJ, 900, 61, doi: 10.3847/1538-4357/aba962

Kimm, T., Slyz, A., Devriendt, J., & Pichon, C. 2011, MNRAS, 413, L51, doi: 10.1111/j.1745-3933.2011.01031.x

Koekemoer, A. M., Faber, S. M., Ferguson, H. C., et al. 2011, ApJS, 197, 36, doi: 10.1088/0067-0049/197/2/36

Kornei, K. A., Shapley, A. E., Erb, D. K., et al. 2010, ApJ, 711, 693, doi: 10.1088/0004-637X/711/2/693

Kornei, K. A., Shapley, A. E., Martin, C. L., et al. 2012, ApJ, 758, doi: 10.1088/0004-637X/758/2/135

Kramida, A., Ralchenko, Y., Reader, J., & NIST ASD Team. 2022, NIST Atomic Spectra

Database (version 5.10), [Online]. Available: https://physics.nist.gov/asd [Thu Jun 01 2023]. National Institute of Standards and Technology, Gaithersburg, MD

Kriek, M., Shapley, A. E., Reddy, N. A., et al. 2015, ApJS, 218, 15, doi: 10.1088/0067-0049/218/2/15

Krogager, J.-K., Fynbo, J. P. U., Ledoux, C., et al. 2013, MNRAS, 433, 3091, doi: 10.1093/mnras/stt955

Kulas, K. R., Shapley, A. E., Kollmeier, J. A., et al. 2012, ApJ, 745, 33, doi: 10.1088/0004-637X/745/1/33

Lake, E., Zheng, Z., Cen, R., et al. 2015, ApJ, 806, 46, doi: 10.1088/0004-637X/806/1/46

Larson, R. B. 1974, MNRAS, 169, 229, doi: 10.1093/mnras/169.2.229

Laursen, P., Duval, F., & Östlin, G. 2013, ApJ, 766, 124, doi: 10.1088/0004-637X/766/2/124

Law, D. R., Steidel, C. C., Shapley, A. E., et al. 2012, ApJ, 759, 29, doi: 10.1088/0004-637X/759/1/29

Leclercq, F., Bacon, R., Verhamme, A., et al. 2020, A&A, 635, A82, doi: 10.1051/0004-6361/201937339

Leitet, E., Bergvall, N., Hayes, M., Linné, S., & Zackrisson, E. 2013, A&A, 553, A106, doi: 10.1051/0004-6361/201118370

Leitherer, C., Chandar, R., Tremonti, C. A., Wofford, A., & Schaerer, D. 2013, ApJ, 772, 120, doi: 10.1088/0004-637X/772/2/120

Leitherer, C., Schaerer, D., Goldader, J. D., et al. 1999, ApJS, 123, 3, doi: 10.1086/313233

Leroy, A. K., Walter, F., Brinks, E., et al. 2008, AJ, 136, 2782, doi: 10.1088/0004-6256/

136/6/2782

Leroy, A. K., Walter, F., Martini, P., et al. 2015, ApJ, 814, 83, doi: 10.1088/0004-637X/814/2/83

Leung, G. C. K., Coil, A. L., Aird, J., et al. 2019, ApJ, 886, 11, doi: 10.3847/1538-4357/ab4a7c

Li, M., Bryan, G. L., & Ostriker, J. P. 2017, ApJ, 841, 101, doi: 10.3847/1538-4357/aa7263

Li, Z., Steidel, C. C., Gronke, M., & Chen, Y. 2021, MNRAS, 502, 2389, doi: 10.1093/mnras/staa3951

Li, Z., Steidel, C. C., Gronke, M., Chen, Y., & Matsuda, Y. 2022, MNRAS, 513, 3414, doi: 10.1093/mnras/stac958

Llerena, M., Amorín, R., Pentericci, L., et al. 2023, arXiv e-prints, arXiv:2303.01536, doi: 10.48550/arXiv.2303.01536

Ma, X., Hopkins, P. F., Kasen, D., et al. 2016, MNRAS, 459, 3614, doi: 10.1093/mnras/stw941

Madau, P., & Dickinson, M. 2014, ARA&A, 52, 415, doi: 10.1146/annurev-astro-081811-125615

Marasco, A., Cresci, G., Nardini, E., et al. 2020, A&A, 644, A15, doi: 10.1051/0004-6361/202038889

Marasco, A., Belfiore, F., Cresci, G., et al. 2023, A&A, 670, A92, doi: 10.1051/0004-6361/202244895

Martin, C. L. 2005, ApJ, 621, 227, doi: 10.1086/427277

Martin, C. L., Shapley, A. E., Coil, A. L., et al. 2012, ApJ, 760, 127, doi: 10.1088/

0004-637X/760/2/127

Mas-Ribas, L., & Dijkstra, M. 2016, ApJ, 822, 84, doi: 10.3847/0004-637X/822/2/84

McKee, C. F., & Ostriker, J. P. 1977, ApJ, 218, 148, doi: 10.1086/155667

McLean, I. S., Steidel, C. C., Epps, H., et al. 2010, in Society of Photo-Optical Instrumentation Engineers (SPIE) Conference Series, Vol. 7735, Ground-based and Airborne Instrumentation for Astronomy III, ed. I. S. McLean, S. K. Ramsay, & H. Takami, 77351E, doi: 10.1117/12.856715

McLean, I. S., Steidel, C. C., Epps, H. W., et al. 2012a, in Society of Photo-Optical Instrumentation Engineers (SPIE) Conference Series, Vol. 8446, Ground-based and Airborne Instrumentation for Astronomy IV, ed. I. S. McLean, S. K. Ramsay, & H. Takami, 84460J, doi: 10.1117/12.924794

McLean, I. S., Steidel, C. C., Epps, H. W., et al. 2012b, in Society of Photo-Optical Instrumentation Engineers (SPIE) Conference Series, Vol. 8446, Ground-based and Airborne Instrumentation for Astronomy IV, ed. I. S. McLean, S. K. Ramsay, & H. Takami, 84460J, doi: 10.1117/12.924794

McQuinn, K. B. W., van Zee, L., & Skillman, E. D. 2019, ApJ, 886, 74, doi: 10.3847/1538-4357/ab4c37

Meléndez, M., Veilleux, S., Martin, C., et al. 2015, ApJ, 804, 46, doi: 10.1088/0004-637X/804/1/46

Mitchell, P. D., Schaye, J., & Bower, R. G. 2020, MNRAS, 497, 4495, doi: 10.1093/mnras/staa2252

Mo, H. J., Mao, S., & White, S. D. M. 1998, MNRAS, 295, 319, doi: 10.1046/j.1365-8711.

1998.01227.x

Mo, H. J., & White, S. D. M. 2002, MNRAS, 336, 112, doi: 10.1046/j.1365-8711.2002.05723.x

Morganti, R., Oosterloo, T., Oonk, J. B. R., Frieswijk, W., & Tadhunter, C. 2015, A&A, 580, A1, doi: 10.1051/0004-6361/201525860

Morrissey, P., Matuszewski, M., Martin, D. C., et al. 2018, ApJ, 864, 93, doi: 10.3847/1538-4357/aad597

Muratov, A. L., Kereš, D., Faucher-Giguère, C.-A., et al. 2015, MNRAS, 454, 2691, doi: 10.1093/mnras/stv2126

Murray, N., Ménard, B., & Thompson, T. A. 2011, ApJ, 735, 66, doi: 10.1088/0004-637X/735/1/66

Murray, N., Quataert, E., & Thompson, T. A. 2005, ApJ, 618, 569, doi: 10.1086/426067

Nakajima, K., Fletcher, T., Ellis, R. S., Robertson, B. E., & Iwata, I. 2018, MNRAS, 477, 2098, doi: 10.1093/mnras/sty750

Nelson, D., Pillepich, A., Springel, V., et al. 2019, MNRAS, 490, 3234, doi: 10.1093/mnras/stz2306

Neufeld, D. A. 1991, ApJ, 370, L85, doi: 10.1086/185983

Newman, S. F., Genzel, R., Förster-Schreiber, N. M., et al. 2012, ApJ, 761, 43, doi: 10.1088/0004-637X/761/1/43

Oke, J. B., Cohen, J. G., Carr, M., et al. 1995, PASP, 107, 375, doi: 10.1086/133562

Oosterloo, T., Raymond Oonk, J. B., Morganti, R., et al. 2017, A&A, 608, A38, doi: 10.1051/0004-6361/201731781

Oppenheimer, B. D., & Davé, R. 2006, MNRAS, 373, 1265, doi: 10.1111/j.1365-2966.2006.10989.x

—. 2008, MNRAS, 387, 577, doi: 10.1111/j.1365-2966.2008.13280.x

Oppenheimer, B. D., Davé, R., Kereš, D., et al. 2010, MNRAS, 406, 2325, doi: 10.1111/j.1365-2966.2010.16872.x

Orlitová, I., Verhamme, A., Henry, A., et al. 2018, A&A, 616, A60, doi: 10.1051/0004-6361/201732478

Orsi, A., Lacey, C. G., & Baugh, C. M. 2012, MNRAS, 425, 87, doi: 10.1111/j.1365-2966.2012.21396.x

Osterbrock, D. E. 1989, Astrophysics of gaseous nebulae and active galactic nuclei

Osterbrock, D. E., & Ferland, G. J. 2006, Astrophysics of gaseous nebulae and active galactic nuclei

Ouchi, M., Ono, Y., & Shibuya, T. 2020, ARA&A, 58, 617, doi: 10.1146/annurev-astro-032620-021859

Pandya, V., Fielding, D. B., Anglés-Alcázar, D., et al. 2021, MNRAS, 508, 2979, doi: 10.1093/mnras/stab2714

Patrício, V., Richard, J., Verhamme, A., et al. 2016, MNRAS, 456, 4191, doi: 10.1093/mnras/stv2859

Peeples, M. S., Corlies, L., Tumlinson, J., et al. 2019, ApJ, 873, 129, doi: 10.3847/1538-4357/ab0654

Peng, C. Y., Ho, L. C., Impey, C. D., & Rix, H.-W. 2010, AJ, 139, 2097, doi: 10.1088/0004-6256/139/6/2097

Perrotta, S., George, E. R., Coil, A. L., et al. 2021, ApJ, 923, 275, doi: 10.3847/1538-4357/ac2fa4

Pettini, M., & Pagel, B. E. J. 2004, MNRAS, 348, L59, doi: 10.1111/j.1365-2966.2004.07591.x

Pettini, M., Rix, S. A., Steidel, C. C., et al. 2002, ApJ, 569, 742, doi: 10.1086/339355

Pillepich, A., Springel, V., Nelson, D., et al. 2018, MNRAS, 473, 4077, doi: 10.1093/mnras/stx2656

Pillepich, A., Nelson, D., Springel, V., et al. 2019, MNRAS, 490, 3196, doi: 10.1093/mnras/stz2338

Pointon, S. K., Kacprzak, G. G., Nielsen, N. M., et al. 2019, ApJ, 883, 78, doi: 10.3847/1538-4357/ab3b0e

Price, S. H., Kriek, M., Barro, G., et al. 2020, ApJ, 894, 91, doi: 10.3847/1538-4357/ab7990

Prochaska, J. X., & Wolfe, A. M. 2009, ApJ, 696, 1543, doi: 10.1088/0004-637X/696/2/1543

Prusinski, N. Z., Erb, D. K., & Martin, C. L. 2021, AJ, 161, 212, doi: 10.3847/1538-3881/abe85b

Pucha, R., Reddy, N. A., Dey, A., et al. 2022, AJ, 164, 159, doi: 10.3847/1538-3881/ac83a9

Reddy, N. A., Pettini, M., Steidel, C. C., et al. 2012, ApJ, 754, 25, doi: 10.1088/0004-637X/754/1/25

Reddy, N. A., Steidel, C. C., Pettini, M., et al. 2008, ApJS, 175, 48, doi: 10.1086/521105

Reddy, N. A., Steidel, C. C., Pettini, M., Bogosavljević, M., & Shapley, A. E. 2016, ApJ, 828, 108, doi: 10.3847/0004-637X/828/2/108

Reddy, N. A., Kriek, M., Shapley, A. E., et al. 2015, ApJ, 806, 259, doi: 10.1088/0004-637X/806/2/259

Reddy, N. A., Oesch, P. A., Bouwens, R. J., et al. 2018a, ApJ, 853, 56, doi: 10.3847/1538-4357/aaa3e7

Reddy, N. A., Shapley, A. E., Sanders, R. L., et al. 2018b, ApJ, 869, 92, doi: 10.3847/1538-4357/aaed1e

Reddy, N. A., Shapley, A. E., Kriek, M., et al. 2020, ApJ, 902, 123, doi: 10.3847/1538-4357/abb674

Reddy, N. A., Topping, M. W., Shapley, A. E., et al. 2022, ApJ, 926, 31, doi: 10.3847/1538-4357/ac3b4c

Rees, M. J., & Ostriker, J. P. 1977, MNRAS, 179, 541, doi: 10.1093/mnras/179.4.541

Reichardt Chu, B., Fisher, D. B., Nielsen, N. M., et al. 2022a, MNRAS, 511, 5782, doi: 10.1093/mnras/stac420

—. 2022b, MNRAS, 511, 5782, doi: 10.1093/mnras/stac420

Reichardt Chu, B., Fisher, D. B., Bolatto, A. D., et al. 2022c, ApJ, 941, 163, doi: 10.3847/1538-4357/aca1bd

Rivera-Thorsen, T. E., Dahle, H., Gronke, M., et al. 2017, A&A, 608, L4, doi: 10.1051/0004-6361/201732173

Roberts-Borsani, G. W., & Saintonge, A. 2019, MNRAS, 482, 4111, doi: 10.1093/mnras/sty2824

Roberts-Borsani, G. W., Saintonge, A., Masters, K. L., & Stark, D. V. 2020, MNRAS, 493, 3081, doi: 10.1093/mnras/staa464

Rosdahl, J., & Blaizot, J. 2012, MNRAS, 423, 344, doi: 10.1111/j.1365-2966.2012.20883.x

Rubin, K. H. R., Prochaska, J. X., Koo, D. C., & Phillips, A. C. 2012, ApJ, 747, L26, doi: 10.1088/2041-8205/747/2/L26

Rubin, K. H. R., Prochaska, J. X., Koo, D. C., et al. 2014, ApJ, 794, 156, doi: 10.1088/0004-637X/794/2/156

Rubin, K. H. R., Weiner, B. J., Koo, D. C., et al. 2010, ApJ, 719, 1503, doi: 10.1088/0004-637X/719/2/1503

Rudie, G. C., Steidel, C. C., Trainor, R. F., et al. 2012, ApJ, 750, 67, doi: 10.1088/0004-637X/750/1/67

Rupke, D. 2018, Galaxies, 6, 138, doi: 10.3390/galaxies6040138

Rupke, D. S. N., Gültekin, K., & Veilleux, S. 2017, ApJ, 850, 40, doi: 10.3847/1538-4357/aa94d1

Saintonge, A., Catinella, B., Tacconi, L. J., et al. 2017, ApJS, 233, 22, doi: 10.3847/1538-4365/aa97e0

Sanders, R. L., Shapley, A. E., Kriek, M., et al. 2016, ApJ, 816, 23, doi: 10.3847/0004-637X/816/1/23

Sanders, R. L., Shapley, A. E., Reddy, N. A., et al. 2020, MNRAS, 491, 1427, doi: 10.1093/mnras/stz3032

Sato, T., Martin, C. L., Noeske, K. G., Koo, D. C., & Lotz, J. M. 2009, ApJ, 696, 214,

doi: 10.1088/0004-637X/696/1/214

Scannapieco, E., Silk, J., & Bouwens, R. 2005, ApJ, 635, L13, doi: 10.1086/499271

Schaerer, D., Hayes, M., Verhamme, A., & Teyssier, R. 2011, A&A, 531, A12, doi: 10.1051/0004-6361/201116709

Schaerer, D., & Verhamme, A. 2008, A&A, 480, 369, doi: 10.1051/0004-6361:20078913

Schaye, J., Crain, R. A., Bower, R. G., et al. 2015, MNRAS, 446, 521, doi: 10.1093/mnras/stu2058

Schmidt, M. 1963, ApJ, 137, 758, doi: 10.1086/147553

Schwarz, G. 1978, Annals of Statistics, 6, 461

Shapley, A. E., Steidel, C. C., Pettini, M., & Adelberger, K. L. 2003, ApJ, 588, 65, doi: 10.1086/373922

Sharma, M., & Nath, B. B. 2012, ApJ, 750, 55, doi: 10.1088/0004-637X/750/1/55

Shibuya, T., Ouchi, M., Nakajima, K., et al. 2014, ApJ, 788, 74, doi: 10.1088/0004-637X/788/1/74

Shivaei, I., Reddy, N. A., Shapley, A. E., et al. 2015, ApJ, 815, 98, doi: 10.1088/0004-637X/815/2/98

Shivaei, I., Kriek, M., Reddy, N. A., et al. 2016, ApJ, 820, L23, doi: 10.3847/2041-8205/820/2/L23

Shivaei, I., Reddy, N. A., Siana, B., et al. 2018, ApJ, 855, 42, doi: 10.3847/1538-4357/aaad62

Shivaei, I., Reddy, N., Rieke, G., et al. 2020, ApJ, 899, 117, doi: 10.3847/1538-4357/aba35e

Silk, J. 1977, ApJ, 211, 638, doi: 10.1086/154972

Solimano, M., González-López, J., Aravena, M., et al. 2022, ApJ, 935, 17, doi: 10.3847/1538-4357/ac7c1a

Sommer-Larsen, J. 1991, MNRAS, 249, 368, doi: 10.1093/mnras/249.2.368

Song, Z., Reddy, N. A., Chen, Y., et al. 2024, arXiv e-prints, arXiv:2405.13122. https://arxiv.org/abs/2405.13122

Steidel, C. C., Adelberger, K. L., Shapley, A. E., et al. 2003, ApJ, 592, 728, doi: 10.1086/375772

Steidel, C. C., Bogosavljević, M., Shapley, A. E., et al. 2011, ApJ, 736, 160, doi: 10.1088/0004-637X/736/2/160

Steidel, C. C., Erb, D. K., Shapley, A. E., et al. 2010, ApJ, 717, 289, doi: 10.1088/0004-637X/717/1/289

Stewart, K. R., Kaufmann, T., Bullock, J. S., et al. 2011, ApJ, 738, 39, doi: 10.1088/0004-637X/738/1/39

Strickland, D. K., & Heckman, T. M. 2009, ApJ, 697, 2030, doi: 10.1088/0004-637X/697/2/2030

Strickland, D. K., & Stevens, I. R. 2000, MNRAS, 314, 511, doi: 10.1046/j.1365-8711.2000.03391.x

Sugahara, Y., Ouchi, M., Lin, L., et al. 2017, ApJ, 850, 51, doi: 10.3847/1538-4357/aa956d

Sutherland, R., Dopita, M., Binette, L., & Groves, B. 2018, MAPPINGS V: Astrophysical plasma modeling code, Astrophysics Source Code Library, record ascl:1807.005

Sutherland, R. S., & Dopita, M. A. 2017, ApJS, 229, 34, doi: 10.3847/1538-4365/aa6541

Swinbank, A. M., Bower, R. G., Smith, G. P., et al. 2007, MNRAS, 376, 479, doi: 10.1111/j.1365-2966.2007.11454.x

Swinbank, A. M., Harrison, C. M., Tiley, A. L., et al. 2019, MNRAS, 487, 381, doi: 10.1093/mnras/stz1275

Tacconi, L. J., Genzel, R., Saintonge, A., et al. 2018, ApJ, 853, 179, doi: 10.3847/1538-4357/aaa4b4

The Astronomy and Astrophysics Decadal Survey. 2021, Pathways to Discovery in Astronomy and Astrophysics for the 2020s, National Academies of Sciences, Engineering, and Medicine (Washington, DC: The National Academies Press), doi: 10.17226/26141

Theios, R. L., Steidel, C. C., Strom, A. L., et al. 2019, ApJ, 871, 128, doi: 10.3847/1538-4357/aaf386

Thompson, T. A., Quataert, E., & Murray, N. 2005, ApJ, 630, 167, doi: 10.1086/431923

Thompson, T. A., Quataert, E., Zhang, D., & Weinberg, D. H. 2016, MNRAS, 455, 1830, doi: 10.1093/mnras/stv2428

Topping, M. W., Shapley, A. E., Reddy, N. A., et al. 2020, MNRAS, 495, 4430, doi: 10.1093/mnras/staa1410

Trainor, R. F., Steidel, C. C., Strom, A. L., & Rudie, G. C. 2015, ApJ, 809, 89, doi: 10.1088/0004-637X/809/1/89

Tremonti, C. A., Heckman, T. M., Kauffmann, G., et al. 2004, ApJ, 613, 898, doi: 10.1086/423264

Tumlinson, J., Peeples, M. S., & Werk, J. K. 2017, ARA&A, 55, 389, doi: 10.1146/annurev-astro-091916-055240

van den Bergh, S. 1962, AJ, 67, 486, doi: 10.1086/108757

van der Wel, A., Bell, E. F., Häussler, B., et al. 2012, ApJS, 203, 24, doi: 10.1088/0067-0049/203/2/24

van der Wel, A., Franx, M., van Dokkum, P. G., et al. 2014, ApJ, 788, 28, doi: 10.1088/0004-637X/788/1/28

Vanzella, E., Giavalisco, M., Inoue, A. K., et al. 2010, ApJ, 725, 1011, doi: 10.1088/0004-637X/725/1/1011

Vasan G. C., K., Jones, T., Sanders, R. L., et al. 2022, arXiv e-prints, arXiv:2209.05508. https://arxiv.org/abs/2209.05508

Veilleux, S., Cecil, G., & Bland-Hawthorn, J. 2005, ARA&A, 43, 769, doi: 10.1146/annurev.astro.43.072103.150610

Veilleux, S., Maiolino, R., Bolatto, A. D., & Aalto, S. 2020, A&A Rev., 28, 2, doi: 10.1007/s00159-019-0121-9

Verhamme, A., Orlitová, I., Schaerer, D., & Hayes, M. 2015, A&A, 578, A7, doi: 10.1051/0004-6361/201423978

Verhamme, A., Orlitová, I., Schaerer, D., et al. 2017, A&A, 597, A13, doi: 10.1051/0004-6361/201629264

Verhamme, A., Schaerer, D., Atek, H., & Tapken, C. 2008, A&A, 491, 89, doi: 10.1051/0004-6361:200809648

Verhamme, A., Schaerer, D., & Maselli, A. 2006, A&A, 460, 397, doi: 10.1051/0004-6361:20065554

Virtanen, P., Gommers, R., Oliphant, T. E., et al. 2020, Nature Methods, 17, 261, doi: 10.

1038/s41592-019-0686-2

Weiner, B. J., Coil, A. L., Prochaska, J. X., et al. 2009, ApJ, 692, 187, doi: 10.1088/0004-637X/692/1/187

Weldon, A., Reddy, N. A., Topping, M. W., et al. 2022, MNRAS, 515, 841, doi: 10.1093/mnras/stac1822

—. 2023, MNRAS, 523, 5624, doi: 10.1093/mnras/stad1615

White, S. D. M., & Frenk, C. S. 1991, ApJ, 379, 52, doi: 10.1086/170483

White, S. D. M., & Rees, M. J. 1978a, MNRAS, 183, 341, doi: 10.1093/mnras/183.3.341

—. 1978b, MNRAS, 183, 341, doi: 10.1093/mnras/183.3.341

Wood, C. M., Tremonti, C. A., Calzetti, D., et al. 2015, MNRAS, 452, 2712, doi: 10.1093/mnras/stv1471

Xu, Y., Ouchi, M., Rauch, M., et al. 2022, ApJ, 929, 134, doi: 10.3847/1538-4357/ac5e32

Yang, H., Malhotra, S., Gronke, M., et al. 2016, ApJ, 820, 130, doi: 10.3847/0004-637X/820/2/130

—. 2017, ApJ, 844, 171, doi: 10.3847/1538-4357/aa7d4d

Zabl, J., Bouché, N. F., Schroetter, I., et al. 2019, MNRAS, 485, 1961, doi: 10.1093/mnras/stz392

Zhang, D. 2018, Galaxies, 6, 114, doi: 10.3390/galaxies6040114

Zheng, Z., Cen, R., Trac, H., & Miralda-Escudé, J. 2010, ApJ, 716, 574, doi: 10.1088/0004-637X/716/1/574

Zheng, Z., Cen, R., Weinberg, D., Trac, H., & Miralda-Escudé, J. 2011, ApJ, 739, 62, doi: 10.1088/0004-637X/739/2/62